An Engineering Approach to Understanding the Bone-Tumor Microenvironment: *In Vitro* Modeling and Drug Delivery Strategies to Improve Bone-Metastatic Patient Outcomes

By

Joseph Paul Vanderburgh

Dissertation

Submitted to the Faculty of the

Graduate School of Vanderbilt University

in partial fulfillment of the requirements

for the degree of

DOCTOR OF PHILOSOPHY
in

Chemical and Biomolecular Engineering
May 10, 2019

Nashville, Tennessee

Approved:

Professor Scott A. Guelcher

Professor Craig L. Duvall

Professor Ethan S. Lippmann

Professor Julie A. Rhoades

Professor John T. Wilson

ACKNOWLEDGMENTS

I would like to thank my advisor Dr. Scott Guelcher for his guidance over the past 5 years. I am grateful for all the ideas generated during our discussions, the opportunity to conduct cutting-edge and collaborative biomedical research in his lab, and his supervision and advice that has helped me become a better scientist, worker, and person. I am also very thankful to him for the opportunity to disseminate my work within Vanderbilt, across the country, and even abroad. It has been a pleasure to conduct this research under his tutelage, and I am confident that the experience I've gained at Vanderbilt will serve me well in the next chapter of my career. I would also like to thank the members of my PhD committee: Dr. Craig Duvall, Dr. Ethan Lippmann, Dr. Julie Rhoades, and Dr. John Wilson. Their counsel and insights were invaluable in improving the content, impact, and rigor of this work. I would especially like to thank Dr. Craig Duvall and Dr. Julie Rhoades for their extensive collaboration with the Guelcher lab that made all this work possible. Dr. Duvall and Dr. Rhoades were instrumental in teaching me the foundations of drug delivery and cancer biology, respectively, and I believe this breadth of experience has made me a better scientist.

Thank you also to the Guelcher Laboratory members whom I've had the pleasure of working with during my tenure at Vanderbilt. Katarzyna (Kasia) Zienkiewicz has been instrumental to not only keeping the Guelcher Laboratory in pristine condition, but also providing mentorship and relentless help with experiments even when my projects didn't align with her expertise. I am very thankful to Kasia for making my time in the Guelcher Laboratory so enjoyable. Thank you to Guelcher group peers who have already moved on to their post-PhD careers including Dr. Drew Harmata, Dr. Ruijing Guo, Dr. Anne Talley, Dr. Sichang Lu, and Dr. Madison McGough. They have been great role models and coworkers during my time at Vanderbilt. I would also like to thank my contemporaries in the Guelcher lab including Tom Spoonmore, Lauren Boller, Dustin Groff, Greg Lowen, and David Florian for all their support in and outside the lab. I couldn’t have asked for a better group to work with for 5 years. I would also like to thank the undergraduate students, Cody Dykes and Sean Wang, that I had the pleasure of working with during my time at Vanderbilt. I would especially like to thank Dr. Shanik Fernando for introducing me to the 3D printing project that comprises an entire chapter of this dissertation.

This work represents a highly collaborative effort that could not have been undertaken in the Guelcher Laboratory alone. I would like to thank Dr. Mukesh Gupta, Dr. Thomas Werfel and Taylor Kavanaugh from the Duvall Lab for their aide in teaching me polymer synthesis and nano/microparticle preparation and characterization techniques that laid the groundwork for two chapters of this dissertation. I would also like to thank Alyssa Merkel, Kristin Kwakwa, Erik Beadle and Dr. Shellese Cannonier in the Rhoades Lab for their expertise, collaboration, and patience with me while I tried to learn cancer biology. Thank you to Josh Johnson (Vanderbilt Center for Bone Biology) and Sasidhar Uppuganti (Nyman Lab) for their help and expertise in histology and μCT. I would also like to acknowledge the Vanderbilt Institute for Nanoscale Science and Engineering for access to DLS, TEM, and SEM, and thank you to the incredible Kate Moyer for her aide in TEM and STEM-EDS.

I am also grateful for all the funding sources that supported this research. This work was supported in part by the National Institutes of Health (R01CA163499), the Veterans Administration (1I01BX001957) and the Department of Defense (W81XWH-15-1-0627, W81XWH-15-1-0622).

Finally, I would like to thank my family and Kate Moyer for their constant support and love throughout this endeavor. They are the motivation behind everything I do.

TABLE OF CONTENTS

Page

CHAPTER

LIST OF TABLES

LIST OF FIGURES

Figure Page

CHAPTER 1

I. INTRODUCTION

Breast cancer remains the second leading cause of cancer-related deaths among female cancer patients.[1] Despite advances in early screening and adjuvant therapy, many breast cancer subtypes remain elusive and currently lack any targeted therapies. Metastasis is the major prognostic factor for breast cancer patient survival, and breast tumors have a striking propensity for metastasis to bone with over 70% of patients presenting with bone metastases at post-mortem.[2] Once tumors reach the bone, they secrete various osteolytic factors that contribute to what is colloquially known as the "vicious cycle", which describes the positive feedback loop mechanism induced by tumors in stimulating osteoclastogenesis and subsequent bone destruction.[3] Patients presenting with bone metastases often experience significant skeletal complications including bone pain, increased risk of pathological fracture, reduction in mobility, and surgery to replace tumor-laden bone in addition to chemotherapy for cancer treatment, and thus treating tumor-induced bone disease (TIBD) remains a large clinical challenge.[4,5] Current treatment strategies for TIBD include antiresorptives such as bisphosphonates and the RANKL inhibitor, denosumab. While these agents inhibit osteoclast activity and subsequent bone resorption, they have no effect on tumor burden nor do they selectively obstruct the vicious cycle, and thus do not improve overall survival.[6–8]

Biological research into the underlying mechanisms contributing to tumor progression in bone has illuminated multiple pathways involved in bone-related tumor progression. While most of this research has traditionally been conducted in 2D tissue culture plates, the importance of studying cell behavior in 3D has been stressed in recent years.[9] 3D culture has yielded important findings in the behavior of tumor cells in the presence of bone. One such finding, shown in both 2D and 3D, is that the expression of parathyroid hormone-related protein (PTHrP), an osteoclast-promoting cytokine, is dependent on mechanically transduced signaling. This suggests that 3D matrix rigidity plays a role in tumor progression in bone.[10] Furthermore, others have shown that pore size, curvature, and geometry affect bone cell activity.[11–13] Collectively, these findings suggest that the 3D bone microenvironment (μEN) surface, mechanical, and topological properties affect the autocrine, paracrine, and mechanotransduction signaling of tumor and bone cells that contribute to TIBD. Further, perfusion of cells and media through 3D matrices can support long term culture by increased nutrient transport and waste removal, more closely mimic the shear and mechanical forces experienced *in vivo* which can drive osteoblast differentiation,[14] and even support blood vessel growth when endothelial progenitors are present.[15] Thus, the increasing recognition of the physical, cellular, and dynamic properties of the μEN as significant factors contributing to disease progression has motivated the investigation of new techniques for fabrication of more complex, biomimetic 3D *in vitro* models.

On the pharmacological front, therapeutic targeting of the molecular mechanisms involved in tumor metastasis to bone is a constantly developing field of study. As the mechanisms themselves are becoming elucidated through our deeper understanding of the signaling pathway networks involved in TIBD, new targets for intracellular inhibition or promotion are becoming apparent. Previous studies from our group have shown that matrix rigidity in the bone μEN triggers tumor cells to adopt a bone-destructive phenotype by altering TGF-β signaling within the cell.[16] This suggests multiple targets for preventing TIBD, including TGF-β, p38 MAPK, PTHrP, and Gli2. Concurrently, major strides have been made in biocompatible polymer science towards improving the pharmacokinetic properties of potential therapeutic agents that otherwise have poor *in vivo* characteristics. These advances have been predicated upon the tailored design of polymers to impart specific, application-based properties on the drug delivery system to improve cargo loading and retention, increase circulation time, provide environmentally-responsive release mechanisms, and/or convey site-specific targeting.

1.1. Specific Aims

The overarching goal of this work is to develop 3D *in vitro* modeling and drug delivery strategies to better understand TIBD progression in bone. This goal was achieved through completion of the following aims.

Aim I: Fabricate Tissue-Engineered Bone Constructs (TEBCs) that recapitulate the physicochemical, mechanical, and morphological properties of human trabecular bone and incorporate into bioreactor model to provide a means for studying TIBD.

Much work in recent years has been dedicated to understanding how the 3D microenvironment affects cell behavior. The skeleton is a unique organ due to its load-bearing responsibility and matrix rigidity orders of magnitude higher than that of most soft tissue. Previous work in our lab has demonstrated that both rigidity and pore size of substrates affect osteoblast proliferation and differentiation. We thus hypothesized that recapitulating trabecular bone microstructure *in vitro* could provide a means to study how cellular behavior is influenced by bone microarchitecture. Further, we hypothesized that incorporation of these trabecular-bone templated constructs into perfusion bioreactor culture with key cell types involved in TIBD could allow the study of disease progression *in vitro* to help bridge the gap between 2D cell culture and animal models. To this end, the development of tissue-engineered bone constructs (TEBCs) that recapitulate the mechanical, topological, and physicochemical properties of trabecular bone utilizing a polyurethane composite bone-like material (PUR-nHA) will be described. *In vitro* perfusion bioreactor studies will further show that culture of bone and tumor cells on TEBCs provide a viable model of tumor-induced bone resorption.

Aim II: Encapsulate Gli-inhibitor, GANT58, into nanoparticle carrier (GANT58-NP) and assess its efficacy in mouse models of bone metastasis

Aberrant activation of the transcription factor Gli2 in tumors has been implicated in driving TIBD. Gli2 is a developmental protein that is not normally expressed in healthy adult tissues, yet is expressed in many metastatic tumors. Thus, Gli2 is a compelling target for therapeutic inhibition. Small molecule inhibitors of Gli proteins have been developed, and the molecule GANT58 has demonstrated significant knockdown of Gli2 and PTHrP *in vitro*. However, the hydrophobicity of GANT58 has precluded its systemic bioavailability in its free form. The objective of this aim is to utilize a polymer nanoparticle formulation to encapsulate GANT58 and enable its systemic bioavailability *in vivo* to study its efficacy in blocking TIBD.

Aim III: Develop bone-targeted nanoparticle (BTNP) carrier to improve GANT58 efficacy in vivo.

Bone-targeting of polymeric carriers has been successfully implemented in previous studies for encapsulation of hydrophobic small molecules to improve their *in vivo* delivery to bone. In this aim, we develop a novel bone-targeted carrier for improved GANT58 delivery to the bone-tumor microenvironment. We hypothesized that bone-targeted delivery of the Gli-inhibitor would not only improve its efficacy, but also provide a pretreatment platform to enable GANT58 to block tumor establishment in addition to bone destruction.

In vitro studies will optimize bone-targeted nanoparticle formulation and assess bone-binding affinity. *In vivo* studies will then investigate GANT58 efficacy when encapsulated in new bone-targeted carrier and delivered systemically.

1.2. Approach

Chapter 1 of this work provides an introduction into TIBD and justification behind the undertaking of this project and the goals of this dissertation. **Chapter 2** gives background information on the use of 3D printing for *in vitro* modeling and how 3D *in vitro* models are being used for studying cancer in bone. An overview of 3D printing methods that have been successfully used for *in vitro* models of both hard and soft tissue will be presented, followed by a discussion of current technologies where specific examples of successful implementation of 3D printing for *in vitro* modeling will be highlighted. A more focused discussion on 3D models in tumor-induced bone disease will follow.

Chapter 3 of this work discusses the development of trabecular bone-templated tissue engineered constructs and implementation into a perfusion bioreactor *in vitro* model of TIBD. TEBCs were developed through a tandem μCT-3D printing process and evaluated for their mechanical, surface, and structural properties. Human mesenchymal stem cells (hMSCs) behavior was then investigated on TEBCs of different anatomical sites. TEBCs were then incorporated into a perfusion bioreactor model to create a 3D *in vitro* model of TIBD. Cellular and resorption outcomes were evaluated after extended perfusion culture of bone and tumor cells. This fully-humanized TEBC-based 3D model could help bridge the gap between traditional 2D culture and animal models. This chapter addresses **Aim I**.

Chapter 4 of this work describes the formulation and characterization of GANT58-loaded polymeric nanoparticles (GANT58-NPs) and assessment of GANT58-NP efficacy in blocking TIBD in mouse models of bone metastasis. GANT58-NPs micelles were characterized and subsequent *in vitro* studies evaluated GANT58-NP efficacy and mechanism of action. GANT58-NPs were then tested *in vivo* and bone outcomes were evaluated by µCT and x-ray, while tumor outcomes were evaluated histologically. Results from *in vivo* models led to the development of a novel bone-targeted nanoparticle (BTNP) chemistry described in **Chapter 5**. The BTNPs were thoroughly characterized for BTNP morphology, size, surface properties, and bone-binding affinity via a combinatorial library of BTNP formulations. The lead candidate formulation loaded with GANT58 (GANT58-BTNP) was evaluated *in vivo* in an intracardiac mouse model of early bone metastasis. Results from this study are anticipated to guide further preclinical studies for GANT58 as a tumor-mediated osteoclast inhibitor.

Chapter 6 summarizes the overall findings of this dissertation and **Chapter 7** outlines future directions based on these findings.

This research strategy aims to engineer novel in vitro models and drug delivery strategies to both understand and treat TIBD. These chapters build on one another to address current limitations in simulating and treating TIBD and culminate in novel techniques that hold potential in improving bone metastatic patient outcomes.

References

(1) American Cancer Society. Breast Cancer Facts & Figures 2017-2018. *Atlanta: American Cancer Society, Inc.* 2017, pp 1–44.

(2) GD, R. Mechanisms of Bone Metastasis. *N Engl j Med* **2004**, *350* (16), 1655–1664.

(3) Ignatiadis, M.; Sotiriou, C. Luminal Breast Cancer: From Biology to Treatment. *Nat Rev Clin Oncol* **2013**, *10* (9), 494–506.

(4) Onishi, T.; Hayashi, N.; Theriault, R. L.; Hortobagyi, G. N.; Ueno, N. T. Future Directions of Bone-Targeted Therapy for Metastatic Breast Cancer. *Nature Reviews Clinical Oncology*. 2010.

(5) Cannonier, S. A.; Sterling, J. A. The Role of Hedgehog Signaling in Tumor Induced Bone Disease. *Cancers (Basel).* **2015**, *7* (3), 1658–1683.

(6) Gnant, M.; Pfeiler, G.; Dubsky, P. C.; Hubalek, M.; Greil, R.; Jakesz, R.; Wette, V.; Balic, M.; Haslbauer, F.; Melbinger, E.; et al. Adjuvant Denosumab in Breast Cancer (ABCSG-18): A Multicentre, Randomised, Double-Blind, Placebo-Controlled Trial. *Lancet* **2015**, *386* (9992), 433–443.

(7) Fusco, V.; Galassi, C.; Berruti, A.; Ciuffreda, L.; Ortega, C.; Ciccone, G.; Angeli, A.; Bertetto, O. Osteonecrosis of the Jaw after Zoledronic Acid and Denosumab Treatment. *Journal of Clinical Oncology*. 2011.

(8) Bamias, A.; Kastritis, E.; Bamia, C.; Moulopoulos, L. A.; Melakopoulos, I.; Bozas, G.; Koutsoukou, V.; Gika, D.; Anagnostopoulos, A.; Papadimitriou, C.; et al. Osteonecrosis of the Jaw in Cancer after Treatment with Bisphosphonates: Incidence and Risk Factors. *J. Clin. Oncol.* **2005**, *23* (34), 8580–8587.

(9) Griffith, L. G.; Swartz, M. A. Capturing Complex 3D Tissue Physiology in Vitro. *Nat. Rev. Mol. Cell Biol.* **2006**, *7* (3), 211–224.

(10) Sterling, J. A.; Guelcher, S. A. Bone Structural Components Regulating Sites of Tumor Metastasis. *Curr. Osteoporos. Rep.* **2011**, *9* (2), 89–95.

(11) Zadpoor, A. A. Bone Tissue Regeneration: The Role of Scaffold Geometry. *Biomater. Sci.* **2015**, *3* (2), 231–245.

(12) Guo, R.; Merkel, A. R.; Sterling, J. A.; Davidson, J. M.; Guelcher, S. A. Substrate Modulus of 3D-Printed Scaffolds Regulates the Regenerative Response in Subcutaneous Implants through the Macrophage Phenotype and Wnt Signaling. *Biomaterials* **2015**, *73*, 85–95.

(13) Ferlin, K. M.; Prendergast, M. E.; Miller, M. L.; Kaplan, D. S.; Fisher, J. P. Influence of 3D Printed Porous Architecture on Mesenchymal Stem Cell Enrichment and Differentiation. *Acta Biomater.* **2016**, *32*, 161–169.

(14) Bancroft, G. N.; Sikavitsas, V. I.; van den Dolder, J.; Sheffield, T. L.; Ambrose, C. G.; Jansen, J. A.; Mikos, A. G. Fluid Flow Increases Mineralized Matrix Deposition in 3D Perfusion Culture of Marrow Stromal Osteoblasts in a Dose-Dependent Manner. *Proc. Natl. Acad. Sci. U. S. A.* **2002**, *99* (20), 12600–12605.

(15) Papadimitropoulos, A.; Scherberich, A.; Güven, S.; Theilgaard, N.; Crooijmans, H. J. A.; Santini, F.; Scheffler, K.; Zallone, A.; Martin, I. A 3D in Vitro Bone Organ Model Using Human Progenitor Cells. *Eur. Cells Mater.* **2011**, *21*, 445–458.

(16) Page, J. M.; Merkel, A. R.; Ruppender, N. S.; Guo, R.; Dadwal, U. C.; Cannonier, S. A.; Basu, S.; Guelcher, S. A.; Sterling, J. A. Matrix Rigidity Regulates the Transition of Tumor Cells to a Bone-Destructive Phenotype through Integrin B3 and TGF-β Receptor Type II. *Biomaterials* **2015**, *64*, 33–44.

CHAPTER 2

II. BACKGROUND

2.1. 3D Printing of Tissue Engineered Constructs for *In Vitro* Modeling of Disease Progression and Drug Screening

Adapted from:
Vanderburgh, J, Sterling, JA, Guelcher, SA. "3D Printing of Tissue Engineered Constructs for *in vitro* Modeling of Disease Progression and Drug Screening." *Ann Biomed Eng*. 2017;45(1):164-179.

2.1.1. Abstract

2D cell culture and preclinical animal models have traditionally been implemented for investigating the underlying cellular mechanisms of human disease progression. However, the increasing significance of 3D versus 2D cell culture has initiated a new era in cell culture research in which 3D *in vitro* models are emerging as a bridge between traditional 2D cell culture and *in vivo* animal models. Additive manufacturing (AM, also known as 3D printing), defined as the layer-by-layer fabrication of parts directed by digital information from a 3D computer-aided design (CAD) file, offers the advantages of simultaneous rapid prototyping and biofunctionalization as well as the precise placement of cells and extracellular matrix with high resolution. In this review, we highlight recent advances in 3D printing of tissue engineered constructs (TECs) that recapitulate the physical and cellular properties of the tissue microenvironment for investigating mechanisms of disease progression and for screening drugs.

2.1.2. Introduction

For decades biologists have relied on a combination of cell culture and mouse models for elucidating the underlying cellular mechanisms that lead to human diseases. While these models have their limitations, they have enabled major discoveries and greatly improved understanding of diseases. However, traditional cell culture and mouse models are limited in their ability to recapitulate the complex tissue microenvironment (μEN). Thus, the increasing recognition of the physical and cellular properties of the μEN as an important factor contributing to disease progression has motivated the investigation of new techniques for fabrication of more complex 3D systems that more accurately mimic the tissue μEN.

Animal models are an established approach for studying the mechanisms of disease progression. However, the clinical translatability of these animal models to human disease has been questioned, since the μEN in animals differs from that in humans. The efficacy and toxicity of drugs evaluated in animal studies do not always predict the response in human patients. For example, liver toxicity of experimental drugs that was not discovered in preclinical studies is a leading cause of clinical trial failures.[1] Animal models also present uncontrollable variables that limit quantitative analysis of the mechanisms of interest in understanding disease progression at the molecular level. Furthermore, the cost and ethical concerns associated with animal testing have motivated research on less expensive, higher throughput, and more humane alternatives.[2]

Cells more closely mimic *in vivo* behavior when grown in 3D conditions, and a number of 3D culture systems have been reported that more accurately predict the cellular response compared to 2D culture.[3–9] Tissue Engineered Constructs (TECs) have emerged as more physiologically relevant 3D *in vitro* models of organogenesis, disease progression, and drug screening due to their ability to recapitulate the physical and cellular properties of the tissue μEN. Despite the advances in TECs utilizing conventional scaffold techniques, the inability of traditional methods to reproducibly fabricate structures with precise architectural features and spatial location of cells has motivated the search for new alternatives. Additive manufacturing (AM, also known as 3D printing), defined as the layer-by-layer fabrication of parts directed by digital information from a 3D computer-aided design (CAD) file[10], offers the advantages of simultaneous rapid prototyping and biofunctionalization as well as the precise placement of cells and biomaterials with high resolution. In this review, we highlight recent advances in AM technology for 3D printing of TECs to investigate mechanisms of disease progression and screen drugs.

2.1.3. 3D Tissue-Engineered Constructs (TECs) for Modeling Disease Progression and Drug Efficacy

3D *in vitro* models have been proposed as a bridge between cell culture and *in vivo* modeling[11] and even between animal modeling and human trials.[12] Early studies with 3D culture largely involved either explanted host tissue or natural biopolymers such as collagen, cell-extracted native extracellular matrix, or polyacrylamide gels. The explanted tissue models assumed very simple architectures, often layers less than 1 mm thick that simply allowed for cells to migrate in 3D.[7] However, the use of native tissues *in vitro* often necessitates arduous extraction and preparation techniques that limits the ease of application. The need for more precise control over mechanical, chemical, and surface properties, as well as simple preparation techniques engendered a new approach for developing TECs. While initial studies targeted *in vivo* implantation of TECs in regenerative medicine applications, TECs have recently been investigated as *in vitro* tools for understanding molecular mechanisms and testing drug candidates prior to human trials. These *in vitro* models have potentially far-reaching effects in the fields of drug development and molecular biology that could reduce the need for organ and tissue implants.[13]

Conventional scaffold synthesis methods employing synthetic and natural polymers include gas foaming, freeze-drying, phase separation, particulate leaching, liquid molding, fiber bonding, and electrospinning.[14] These techniques have been used to create scaffolds with rigidity, strength, surface properties, porosities, and degradation kinetics targeted to host tissue.[15,16] Spheroid cell culture has also been utilized to simulate *in vivo* cell morphology and behavior by facilitating aggregation of cells in a non-anchored environment. Spheroid culture is achieved either by using attachment-resistant cell culture surfaces with constant agitation, or by culturing cells in droplets that are hanging from a surface, also known as the hanging drop technique.[17] Spheroid cultures of tumor cells form hollow cores in which the central cells experience a hypoxic environment and become quiescent, similar to how tumor cells in the necrotic core behave *in vivo.*[18] Spheroid cultures have exhibited proper differentiation abilities and chemical gradients, as well as the ability to resemble avascular tumor nodules and micrometastases.[19] A significant limitation of spheroid culture is its inability to control spheroid size and architecture.[17]

Considerable progress has been made in designing scaffolds specifically for *in vitro* models using conventional synthetic scaffolds and spheroid cell culture to mimic a variety of tissue and organ types. A skin-replicating model has been developed to model melanoma for studying disease mechanisms and drug screening utilizing collagen scaffolds and tumor cell spheroids.[20] A liver-like model utilizing an immortalized hepatoma cell line and ECM-derived hydrogel has been reported to not only recover hepatocyte function in 3D but also provide a means of high-throughput screening of drugs to assess liver toxicity *in vitro*.[21]

Other *in vitro* models have been developed for organs including bone[22], myocardium[23], trachea[24], vessels[25], nerves[26], cartilage[27], and cornea.[28]

Despite these successes, traditional synthesis methods still lack control of some essential factors contributing to *in vivo* cellular function, in particular the tissue micro-architecture and precise placement of cells within the construct. The architecture in the tissue milieu of interest has proven to play a large role in cell differentiation, proliferation, metabolic activity, and motility.[29–31] Thus, creating the appropriate architecture in addition to the chemical and mechanical properties of the specific tissue is necessary if *in vivo* conditions are to be accurately simulated.

2.1.4. Fabrication of 3D Scaffolds by Additive Manufacturing (AM)

Since the advent of AM in the late 1980s, many techniques have been developed to create micro-scale precision 3D structures from a variety of source materials. In addition to the plethora of techniques, the industry's Moore's law-type increase in speed, precision, and cost reduction has made it an appealing tool to create TECs with defined mechanical, topological, and cellular properties. Anatomically accurate models can be reliably and economically created by using medical imaging in conjunction with the computer-aided design (CAD) technology employed by most AM machines. The ability to create structures that can be tailored to an individual patient's anatomy through medical imaging has made AM an emerging regenerative medicine approach for organ replacement. However, AM is also being increasingly applied to create *in vitro* models of disease progression and drug screening, which has potential to advance drug discovery.

AM, also known as rapid prototyping (RP), layer manufacturing, 3D printing, and solid freeform fabrication, refers to the fabrication of parts by addition of layers that is directed by a CAD file, most frequently in the stereolithography (STL) file format created by 3D Systems.[10] It can be inferred from this broad definition that there are many ways to achieve layer-by-layer manufacturing, and indeed there are a growing number of commercially available techniques. An American Society of the International Association for Testing and Materials (ASTM International) committee categorized AM techniques into seven groups: binder jetting, directed energy deposition, material extrusion, material jetting, powder bed fusion, sheet lamination, and vat polymerization.[32] While these terms describe the general techniques used, not all are applicable to biomaterials applications. Currently, four AM technologies have been predominantly used for TECs: stereolithography, fused deposition modeling, material jetting (inkjetting), and bioprinting.

Stereolithography (SLA) is widely considered the first AM technique developed.[33] SLA is a form of vat polymerization that utilizes photopolymerization to solidify a liquid monomer resin layer by layer. The liquid monomer is contained in a vat with a moveable base such that a UV laser, directed by a CAD file, selectively "draws" a layer of the desired part onto the liquid in the container. The UV light crosslinks the monomer to solidify the polymer in the location of UV exposure. After a layer is finished, the base drops the height of the previously polymerized layer and the process repeats. The base-lowering step is often accompanied by the sweep of a recoater blade to ensure there is a fresh, uniform layer of liquid monomer. Thus the part is built bottom-up, usually accompanied by support material to hold the part in place and prevent lateral deformation during the blade sweep or vertical deformation due to gravity. After completion, the part is washed in a chemical bath to remove any uncured monomer resin, the support material is removed, and the resulting part is post-cured in a UV oven.

While the bottom-up approach is the most abundantly used technology, an increasing number of SLA machines utilize a top-down approach in which the UV light is directed upward from under the vat and the base moves up as each layer is finished. Top-down manufacturing has multiple advantages, including a smooth polymerization surface, elimination of the need for a recoater blade, reduction in the volume of monomer, and elimination of atmospheric exposure, which mitigates oxygen inhibition.[34] Another advancement in SLA technology, called microstereolithography (μSLA), can achieve sub-micron features using focused light spot scanning. The major drawback to this process is that many photo masks must be used in parallel, which makes processing time and cost unfeasible. However, the use of a single dynamic mask (normally in the form of a digital micromirror display (DMD)) and a reducing lens has achieved sub-micron features at speeds comparable to normal SLA.[35]

The lack of available photo-sensitive resins useable in SLA machines is often considered one of the major limitations of the technology. In addition to being capable of photopolymerization, the resin must be a low-viscosity liquid. Despite these restrictions, SLA has found use in biomedical applications as a means to create patient-specific models of body parts for use as surgical guides, implantable devices, and tissue engineered grafts. Major advancements in SLA resins have made this shift toward biomedical devices possible. TECs fabricated from biodegradable resins such as poly(propylene fumarate), poly(ε-caprolactone), and poly(lactide) have been successfully evaluated in animals and shown to support cell adhesion and growth *in vitro*.[34] These resins have also been augmented with ceramic particles such as β-tricalcium phosphate (β-TCP) or hydroxyapatite to fabricate bone-like TECs.[36] Despite the advances in polymer resins available to SLA technology, the major limitation to the progress of SLA in tissue engineering applications is its restriction to a single resin per structure.[34]

Fused deposition modeling (FDM)[37] is a material extrusion technique in which a filament is drawn through a computer-guided nozzle, heated above the glass transition temperature (T_g), extruded, and deposited in a layer-by-layer fashion to construct the part in a bottom-up fashion. Material is drawn by two rollers into a heating element, and the resulting semi-molten filament is then extruded through the nozzle tip and deposited. By remaining intact, the filament creates "roads" of deposited material rather than individual "dots". Multiple parameters, including FDM head speed, nozzle tip width, roller speed, direction of deposition, and material temperature, can be adjusted to tailor the resulting product to desired specifications.[38] Furthermore, multiple materials may be used in a single print by the addition of separate nozzles and filaments to allow for more versatility in design. In most commercial cases, a second material is used as support material to build support for any structure on the part that exhibits an overhang angle less than 45°.[39] While the primary use of a second material is for support, this also allows for multi-composition structures with different chemical and mechanical properties for the construction of hierarchical designer scaffolds.[40]

Fused deposition modeling most commonly employs thermoplastics with relatively low T_g and high thermal stability. Polylactic acid (PLA), polyamide (PA), acrylonitrile butadiene styrene (ABS), and polycaprolactone (PCL) are commonly used FDM resins.[38] Metal wires, metal-polymer composites, and ceramic-polymer composites have also been utilized.[10] This versatility in resins and capability for use of multiple materials renders FDM an appealing method of scaffold generation for tissue engineering. Multiple groups have created TECs to not only mimic tissue architecture, but also impart appropriate mechanical properties.[41] The major limitation of FDM is its low resolution compared to SLA and inkjet printing. Because FDM relies on semi-molten "roads" of material opposed to drops, the resolution is inherently lower and susceptible to surface imperfections in the resulting part. Therefore, FDM is limited to applications where a tolerance >100 µm is acceptable.[42]

Material jetting is analogous to 2D inkjet printing, in which a CAD-guided nozzle deposits an ink that is heated just past its melting temperature onto a solid base. Upon deposition, the material cools and solidifies in place. Once a layer is complete, the base moves down the height of a single layer and the process continues in a bottom-up fashion until completion. There are two well-established means of depositing the ink droplets: continuous and drop-on-demand (DOD) modes.[43] In the continuous mode, a constant pressure is applied to the ink chamber such that a steady stream of the fluid exits the nozzle. Upon exiting the nozzle, the stream forms droplets due to Rayleigh scattering. In DOD mode, an actuator creates pulses of pressure such that droplets are formed at the exit of the nozzle, and the frequency of pulses can be adjusted. The DOD mode is the most preferred due to the smaller drop size and placement accuracy.[43] Due to the temperature constraints required by material jetting, the type and number of useable materials is fairly limited compared to other AM techniques. Waxy, low molecular weight polymers and acrylate photopolymers are most often used in inkjet printing, which often limits the technique's biomaterials applications to mold castings for use as an indirect means of scaffold generation.

In contrast to the previously described AM technologies, bioprinting is defined more conceptually, which is a topic of current debate. Bioprinting has been defined as "the use of computer-aided transfer processes for patterning and assembling living and non-living materials with a prescribed 2D or 3D organization in order to produce bio-engineered structures serving in regenerative medicine, pharmacokinetic and basic cell biology studies."[44,45] Multiple AM technologies have been applied to bioprinting, which is also referred to as bioplotting, cell writing, laser-assisted bioprinting, and microextrusion.[46,47] Maintaining cell viability during and post-printing is the essential requirement for bioprinting that limits the AM techniques that can be feasibly used. Consequently, it is imperative that sterility of materials and equipment can be maintained during the printing process. Equipment and materials must be capable of being sterilized, most commonly by autoclave, UV light, or ethanol treatment, and it is common to conduct the bioprinting within a laminar flow hood to promote a clean environment. Further, sterility tests are often conducted by printing cell-containing material and culturing in antiobiotic-free media.[48] SLA, material jetting, and material extrusion are the three ASTM-defined techniques that have been proven capable of bioprinting. New techniques not defined by ASTM International, known as laser-guided direct cell printing and laser-induced direct cell printing, utilize a laser to guide and deposit cells onto substrates.[49] System temperature, pressure, surrounding media, matrix or scaffold composition, and associated chemical and solvents are all parameters that must be considered to optimize cell viability. New approaches have been developed to address these restrictions, such as nozzles that use piezoelectric actuators to create droplets to alleviate thermal stress, and the use of near-infrared lasers to limit the risk of overheating cells in the laser-guided technique.[47,50] Cell media must also be supplied before, during, and after printing to ensure sufficient cell nutrition, which has limited the matrix to hydrogels such as Matrigel and PEG gels that are cyto-compatible and nano-porous. Use of metals, ceramics, and composite materials with high mechanical properties are thus restricted to cell-seeding after scaffold preparation as opposed to direct bioprinting.[50] While bioprinting is growing both in efficiency and complexity of constructs, the inability of this approach to fabricate sophisticated tissue architectures is a significant limitation.

2.1.5. 3D Models of Disease Progression and Drug Screening

The design of TECs that mimic the μEN, facilitate studies on the spatio-temporal dynamics of disease progression, and assess drug response has been recognized as a pressing need.[51] Compared to more conventional fabrication techniques, advances in AM have enabled more precise control over topological properties[52] such as porosity, pore size, pore shape, and curvature, as well as precise placement of cells.[8] Consequently, 3D printing is emerging as a powerful tool for recapitulating the mechanical, topological, and cellular properties of both hard and soft tissue. In this section, the design of 3D-printed TECs for modeling disease progression and drug response in a variety of tissue types are reviewed.

In a transformative study, viable human bone grafts that recapitulate the temporomandibular joint (TMJ) were fabricated from decellularized trabecular bone.[53] Clinical CT images of the joint were digitized and imported into a computer-aided design (CAD) tool, which was used to machine a TMJ-shaped graft. Human mesenchymal stem cells (MSCs) were cultured on the grafts in a perfusion bioreactor for 5 weeks, resulting in the formation of lamellar bone. While this study represented an important step toward *in vitro* culture of patient-specific bone grafts, recent advances in AM have aimed to fabricate clinically sized, anatomically shaped bone grafts from synthetic materials. In a follow-up study, anatomically shaped PCL scaffolds were printed by FDM from CT scans of the maxilla and the mandible in human patients (Fig. 1A).[54] AM has also been applied to manufacture TECs in which a scaffold and bioreactor chamber are fabricated simultaneously as a custom-designed device designed to match a patient's anatomy (Fig. 1B).[55] A 3-cm section of an ovine tibia was imaged by μCT, from which a computational 3D model was generated that captured the anatomical features of the tibia. Using a computed-aided design (CAD) tool, a shell wall was then created that enabled fluid flow. The resulting device was printed by FDM in a single step using two thermoplastic polymers: poly(lactic acid) (PLA) for the scaffold and acrylonitrile butadiene styrene (ABS) for the bioreactor (Fig. 1B). Primary human osteoblasts were dynamically seeded in the bioreactor and cultured under bi-directional perfusion. The cells maintained viability for up to 6 weeks.

Trabecular bone is differentiated from other tissues by its rod- and plate-like trabeculae spaced 600 – 800 μm apart and its rigid mineralized ECM (93 - 365 MPa[56]), which is several orders of magnitude higher than that of soft tissue.[57] The progression of tumor-induced bone disease has been modeled *in vitro* using 3D scaffolds for metastatic breast cancer[58], prostate cancer[59],and Ewing sarcoma.[60] In these studies, cell culture on collagen or polymer scaffolds demonstrated that the 3D microenvironment substantially alters the tumor response to anti-cancer drugs compared to 2D monoculture. However, the substrate modulus and pore size of these scaffolds fabricated by conventional methods are generally not representative of trabecular bone. A templated-Fused Deposition Modeling (t-FDM) approach has recently been reported for fabrication of 3D scaffolds with tunable substrate moduli and pore sizes representative of trabecular bone (Fig. 1C).[29] While pore sizes > 100 μm can be printed using FDM, the small number of thermoplastic polymers that can be printed limits the range of substrate moduli that can be achieved. In the t-FDM approach, a template is printed by FDM which is subsequently filled with a two-component reactive poly(ester urethane) with substrate moduli ranging from 20 MPa (collagen fibrils) to 266 MPa (trabecular bone) (Fig. 1C). Thus, the t-FDM method enables independent control of mechanical and topological properties. Rat bone marrow-derived mesenchymal stem cells (MSCs) were cultured on the 3D scaffolds for up to 21 days. Expression of markers of osteogenic differentiation, including the transcription factor *Runx2*, increased with increasing substrate rigidity and decreasing pore size. Furthermore, matrix mineralization increased with increasing substrate modulus and decreasing pore size, as assessed by Alizarin red staining and SEM imaging. Taken together, these findings highlight the utility of FDM methods for fabricating TECs for use in regenerative medicine and mechanistic studies investigating the effects of the μEN on cell fate.

Healing of damaged cartilage is often incomplete due to lack of vascularity and low cell density in cartilage tissue. Consequently, TEC approaches have aimed to promote cartilage regeneration through *ex vivo* engineering of cartilage tissue for implantation. However, limited clinical success has been achieved due to inferior mechanical and structural properties of the implanted or regenerated tissue.[61] Furthermore, zonal organization and integration of implanted articular cartilage tissue remains a challenge for clinical success.[62] Researchers have shifted focus toward recapitulating the 3D structural properties of the *in vitro* μEN to not only improve the tissue quality of *ex vivo* cartilage for implantation, but also to investigate the cellular mechanisms involved in proper cartilage development.

In a recent study, a form of material extrusion bioprinting was used to fabricate hybrid constructs of PCL and chondrocyte-encapsulated alginate hydrogels.[63] In this bioprinting system, called a multihead deposition system (MHDS), PCL was printed as the structural component and chondrocyte-containing hydrogels as the functional component for regeneration. Additionally, the growth factor TGF-β was incorporated in the chondrocyte hydrogels to promote cartilage tissue formation, which showed enhanced ECM formation compared to the hydrogels not supplemented with TGF-β *in vitro.* The scaffolds were implanted into the subcutaneous dorsal spaces of nude mice tissue invasion and formation was observed. Histochemical staining showed that the engineered tissue supplemented with TGF-β exhibited improved cartilage formation with minimal adverse tissue response. This study highlights 3D bioprinting as a viable method for fabrication of TECs that direct cartilage regeneration *in vivo*.

An AM technique has also been used to create an *in vitro* biomimetic 3D μEN to probe the signaling pathways involved in chondrogenesis as a tool to discover potential biomarkers for drug testing. In this study, a material jetting bioprinting system was used to deposit hydrogels containing human MSCs, TGF-β, and BMP-2 to create scaffolds with varying concentrations and gradients of the growth factors not feasible by conventional scaffold synthesis to assess their effect on fibrocartilage development.[64] An extensive quantitative real-time polymerase chain reaction (qRT-PCR) and pathway network analysis was conducted to assess the differentiation of the hMSCs based on the supplied conditions as well as the differentiation-related pathways involved in the model. The results showed that both osteogenesis and chondrogenesis-related genes were up-regulated in the bioprinted constructs that contained both growth factors as opposed to the constructs without growth factors. Furthermore, the pathway and network analysis showed that multiple bone- and cartilage-related differentiation pathways, including TGF-β, Wnt, and BMP pathways were all active in the model. This study highlights the capability of using AM techniques to recapitulate the structure and function of cells involved in bone and cartilage development, and further poses a tool for future research in drug discovery.

The creation of vascularized 3D tissues *in vitro* would significantly advance the fields of tissue engineering and high-throughput drug screening. A number of challenges must be overcome for 3D bioprinting to achieve its full potential, including the development of new biomaterials that recapitulate the properties of the matrix and the fabrication of vascular trees with capillaries and microvessels that provide adequate blood supply.[49] Recent studies have addressed these key technological limitations. Biomaterials used to prepare bioprinting inks typically lack the complexity of natural extracellular matrix, and therefore cannot recapitulate the cell-ECM interactions in the native tissue μEN. To address this limitation, tissue-specific bioinks have been prepared from decellularized ECM (dECM) from adipose, cartilage, and heart tissue (Fig. 2A).[65] Porcine cartilage and heart tissue, as well as human adipose tissue, were decellularized and dissolved in pH-adjusted solutions that gelled at 37°C. Bioinks were used to bioprint structures encapsulating either human adipose-derived stem cells (hASCs) or human interior turbinate tissue-derived MSCs (hTMSCs) that supported the formation of structured 3D tissues. The printed scaffolds enhanced cell viability, commitment of the stem cells to a specific differential lineage, and deposition of new extracellular matrix compared to collagen controls. Due to the ability to print specific cells and ECMs, the dECM approach exhibits considerable potential for modeling disease progression and drug response for a broad variety of tissue types. Another recent study has applied 3D bioprinting to prepare constructs incorporating multiple cell types, ECM, and well-developed vasculature.[66] A custom 3D bioprinter with four independently controlled print heads was designed to concomitantly print cells, ECM, and vasculature. Gelatin methacrylate (GelMA) was used to print the cell-laden ECM, which was subsequently photo-crosslinked after printing. An aqueous solution of a poly(ethylene oxide) (PEO)-poly(propylene oxide) (PPO) triblock copolymer comprised the fugitive ink for bioprinting the microvascular network. After printing, the ink was removed by cooling to temperatures below 4°C to yield hierarchical, bifurcated vascular networks embedded in the ECM (Fig. 2B). In a proof-of-concept experiment, human neonatal dermal fibroblasts (HNDFs) and mouse 10T1/2s fibroblasts bioprinted in the vascularized constructs remained viable for up to 1 week in culture and lined the bioprinted channels (Fig. 2C). This new vascularization approach is scalable for mechanistic and high-throughput drug screening assays related to wound healing and angiogenesis, in which the 3D constructs could be printed in standard tissue culture plates.

Autologous split skin grafts (SSG) are the clinical “gold standard” for repair of cutaneous defects. However, autologous grafting is associated with scarring and is insufficient for extensive surgeries where a considerable amount of skin is needed.[67] Therefore, other directions in tissue engineering research have been taken to alleviate the need for autograft in repairing skin. *In vitro* platforms capable of producing tissue-engineered skin both for implants to replace autologous grafts and as models for drug and topical chemical compound screening have also been an area of extensive research. AM techniques have been utilized to recapitulate the hierarchical and layered nature of skin. A direct cell printing method of 3D bioprinting was utilized to create multi-layered TECs containing fibroblasts (FB), keratinocytes (KC), and a collagen-based hydrogel as the structural component to mimic skin layers.[68] A stratified skin layer was created by depositing a coat of sodium bicarbonate, a crosslinking agent, after the deposition of a layer of collagen and the desired cell type. The sodium bicarbonate crosslinks the recently deposited layer, fixing the cells within and allowing for the deposition of a new layer on top. Cell viability, proliferation and stratified structure of both the FBs and KCs were maintained after printing. Further, the authors proposed the use of this model to print additional cell lines such as melanomas and epithelial cells as a means of modeling skin disease for study of disease progression or a high-throughput drug-screening tool. In another study, the t-FDM scaffolds described in the Bone section above (Fig. 1C) were implanted subcutaneously in rats to investigate the effects of substrate modulus on cutaneous wound healing.[69] Scaffolds with a modulus comparable to collagen fibrils minimized scar formation, Wnt signaling in fibroblasts, and polarization of macrophages toward the restorative phenotype compared to scaffolds that were more compliant or rigid.

The development of robust, reliable *in vitro* liver models is an area of continuous research due to the liver's role in drug metabolism and associated toxicity.[70] In the past, most *in vitro* models relied on 2D monolayer hepatic culture, but 3D models utilizing AM techniques combined with perfusion culture are proving more capable of reliably modeling *in vivo* liver behavior. A direct cell printing approach in conjunction with perfusion culture has been developed to create a biomimetic liver micro-organ as a drug-screening tool.[71,72] The direct cell writing (DCW) system utilized four nozzles capable of operating in extrusion or droplet mode to deposit alginate hydrogels encapsulating HepG2 liver cells. These alginate-encapsulated cells were printed into a three-layer TEC that mimicked the liver sinusoidal shape that was incorporated into a microchip device that allow for media circulation. Results showed that over 80% of HepG2 cells in the cross-linked, bioprinted construct remained viable after three days. Furthermore, viability was maintained after 24-hour perfusion flow, indicating that the perfusion system did not affect cell viability and could be used to perfuse a drug of interest through the system and assess its pharmacokinetic behavior. A more recent study utilizing the DCW process incorporated both hepatic and epithelial cells in Matrigel to more closely mimic the liver sinusoid hierarchical structure.[73] In addition to successfully printing the dual-cellular construct, a radiation drug (amifostine) was perfused through the micro-organ system to test its efficacy in protecting cells from radiation damage. Results indicated that the drug caused a marked decrease in radiation damage compared to untreated cells.

Another study utilized an organ-on-a-chip device, LiverChip (CN Bio Innovations), and co-culture of hepatocytes and Kepffer cells to assess hydrocortisone pharmacokinetic behavior in an inflammation-induced liver environment.[74] The LiverChip is a microfluidic bioreactor model designed to recapitulate the liver capillary bed under perfusion and employs 12 bioreactors in series with 3D scaffolds capable of seeding cells. Endotoxin lipopolysaccharide (LPS) was introduced into the LiverChip co-culture to promote an inflammatory response by the cultured cells. Hydrocortisone, an anti-inflammatory drug, was then introduced into the perfusion medium and its disappearance and metabolism were determined using a form of liquid chromatography-mass spectrometry (LC-MS). The half-life, rate of elimination, clearance, and area-under-the-curve were assessed based on the LC-MS data, and an *in vitro/in vivo* correlation was established to extrapolate *in vivo* behavior from the *in vitro* culture. These results and correlations suggest that this *in vitro* system could be used as a tool to investigate drug metabolism and predict *in vivo* toxicology. Scaffolds that more closely mimic liver architecture and promote enhanced hepatocyte culture have also been investigated. Using SLA, PEG-based, photo-polymerizable hydrogels have been fabricated to improve hepatocyte cell seeding, proliferation, and duration of perfusion cultures in liver models (Fig. 3).[75]

Capturing the complex structural organization of the brain and nervous system has been a major obstacle in creating *in vitro* models that could accelerate the development of new therapies for neurological disorders.[76] Microfluidic mixing has been integrated with hydrogel functionalization to fabricate hydrogels with spatially controlled gradients of matrix and cells representative of glioblastomas[77], which could potentially support studies investigating how spatiotemporal gradients regulate tumor cell fate. Compared to conventional approaches, 3D printing offers the advantage of simultaneous rapid prototyping and biofunctionalization as well as high-throughput production capacity, which has been applied to design TECs that recapitulate the function of glial cell-axon interfaces.[78] This TEC was prepared by 3D printing of three components: (1) microchannels to provide axonal guidance, (2) a sealant layer to prohibit exchange of fluids between chambers, and (3) a top tri-chamber to isolate different cell types. A 3D model of the central nervous system (CNS) was built by culturing hippocampal neurons in chamber 1, superior cervical ganglion (SCG) cells in chamber 2, and Schwann cells in chamber 3. When the peripheral (SCG) neurons were infected with pseudorabies virus (PRV), the viral particles were transported to the Schwann and hippocampal cells at a rate of 2 $\mu m\ s^{-1}$. However, a bottleneck in the spread of the virus was observed. Thus, the 3D CNS model enabled two key findings related to transmission of viral infection in the central nervous system: (1) Schwann cells and hippocampal neurons are resistant to infection, and (2) Schwann cells transmit the infection response through axonal interaction. Furthermore, the CNS TEC enabled quantitative measurements of the transport rate of viral particles. These findings underscore the significance of the model for interrogation of the nervous system's response to pathogens or therapies.

Until recently, the study of neuronal tissue was limited mainly to monolayer culture or to simple hydrogel scaffolds that lack the layered architecture exhibited by the human cortex.[79] A syringe-based ink bioprinting technique has been employed to create layered, neuronal cell-encapsulated hydrogels to mimic layered human brain tissue.[80] A hand-held reactive bioextrusion technique was used to plot freeform 3D layers of gellan gum (GG) encapsulating cortical neurons and glial cells. To increase cell adhesion and proliferation, the GG gels were modified with an RGD peptide sequence and made into a bio-ink formulation to allow for bioprinting. Encapsulated neuronal and glial cells were shown to remain viable and proliferate within the cross-linked hydrogel, and importantly they exhibited appropriate morphologies and axonal development. This strategy for producing layers of different brain tissue cell subtypes provides a potential means of understanding neurodegenerative diseases to drug testing.

In vitro models of the biological barriers in the lung are critical for the development of new drugs and drug carriers for pulmonary delivery.[81] 3D *in vitro* models potentially enable the identification of physiological characteristics of the lung μEN that must be considered in the design of novel carriers. Consequently, more accurate models of the air-blood barrier are needed to design carriers that minimize clearance and promote controlled release of the therapeutic. Co-culture models that capture cellular interactions, as well as microfluidic approaches that mimic the effects of fluid flow on the functionality of epithelial cells represent significant advances in the field. 3D bioprinting has been applied to fabricate air-blood tissue barrier analogues comprising endothelial cells, a basement membrane, and epithelial cells.[82] In a layer-by-layer bioprinting approach, A549 alveolar epithelial cells were separated from EA.hy926 endothelial cells by Matrigel, which was used to mimic the basement membrane. Compared to manually-seeded conventional constructs, the bioprinted analogues exhibited a thinner Matrigel layer and more homogeneously distributed monolayers of cells. Furthermore, the bioprinted endothelial cell layer was less permeable than the manually-seeded layer. Due to its ability to recapitulate the features of the alveolar μEN, this automated and more reproducible 3D bioprinted air-blood tissue barrier model is anticipated to provide a more accurate approach to assessing inhalation hazards as well as screening of new therapeutics.

Successful *in vitro* culture of organs requires vascularization of the construct, since cells must be less than 100 – 200 μm from blood vessels and capillaries that supply oxygen and nutrients.[83] Due to its ability to precisely pattern cells and biomaterials, 3D printing of vascular networks is an emerging approach in which 3D printed sacrificial fibers are embedded in hydrogels to generate microchannels. In one study, template agarose fibers were printed by extrusion of the aqueous agarose solution from a glass capillary.[84] After printing of the agarose fibers, a hydrogel was cast over the agarose fibers and photo-crosslinked, followed by removal of the agarose template. HUVECs cultured on GelMA hydrogels formed a confluent monolayer exhibiting high CD31 expression and formation of cell-cell junctions. 3D printing of carbohydrate glass networks has also been utilized to prepare sacrificial templates.[85] Filament size was controlled by varying the velocity of the nozzle through which the carbohydrate glass was extruded. The resulting glass fibers were embedded in cell-laden hydrogels, including agarose, alginate, PEG, fibrin, or Matrigel, and the fibers removed by dissolution. The carbohydrate glass presents the advantages of sufficient strength to provide mechanical support during fabrication and the ability to be removed from the construct after gel encapsulation without harming the cells. Co-culture of 10T1/2 cells and HUVECs in fibrin gels resulted in the formation of three key components of vascularized tissue: the vascular lumen, endothelial cells lining the vascular wall, and the interstitial region. Furthermore, PEG hydrogels with vascular networks enhanced hepatocyte function compared to monolithic gels. In an alternative approach to generating vascular networks, a high-resolution μSLA apparatus capable of patterning biomaterials and cells at resolutions <5 μm was designed to 3D print photo-crosslinked hydrogels with angiogenic patches.[86] Encapsulation of fibroblasts in PEG hydrogels with 3D-printed 100-μm channels enhanced the formation of neovasculature in a chick chorioallantoic membrane (CAM) model. The ability of these 3D printing techniques to control the architecture of the vascular network, as well as the types of cells and matrices used, may facilitate mechanistic studies of the relationship between vascular structure and mass transfer in tissue, as well as studies investigating disease progression and high-throughput drug screening.

Both the physical and cellular μEN play a large role in cancer initiation, promotion, and metastasis; therefore, mimicking the 3D context of the *in vivo* milieu is essential to modeling the appropriate physical, chemical, and mechanical cues that contribute to tumorigenesis.[18]

3D bioprinting has been used to enhance a previously established 3D ovarian cell (OVCAR-5) model. In the original model, cells cultured on Matrigel spontaneously formed micronodules (acini), a commonly assumed physiological morphology *in vivo* representative of adherent micrometastatic disease.[87] To improve upon this model, a cell-patterning platform was developed to print two cell types, fibroblasts (MRC-5) and OVCAR-5, onto Matrigel to miniaturize the model, improve reproducibility, and make it amenable to high throughput screening. Furthermore, 3D cell-printing allowed for spatial control of the cancer and stromal cells to recapitulate their *in vivo* orientation.[88] Cells were printed using a dual-valve dispensing system and CAD program to independently and precisely deposit the MRC-5 and OVCAR-5 cell suspensions onto a bed of Matrigel in a predefined pattern. The patterning platform successfully produced a viable, cocultured system with reliable cell droplet size, cell density, spatial distribution, and appropriate morphological behavior.

A more recent study used bioprinting to create a cervical cancer model and tested chemoresistance of the cultured cervical cancer cells in 3D versus 2D.[89] A 3D cell printer was used to deposit HeLa cervical cancer cells encapsulated in a gelatin, alginate, and fibrinogen hydrogel mixture into a gridded structure. The hydrogel was designed to mimic the ECM in which HeLa cells are known to proliferate. The printing method was capable of printing viable cells contained in the cross-linked matrix, and the cells showed greater proliferation over a 5-day period compared to 2D culture. Furthermore, this study also showed increased matrix metalloproteinase (MMP) expression on 3D culture versus 2D culture, indicating a more metastatic phenotype in the HeLa cells cultured in 3D. Finally, this study compared treatment of a chemotherapeutic, Paclitaxel, between the 3D and 2D culture. While considerable HeLa cell death was exhibited in both groups, the 3D culture showed significant chemoresistance versus 2D.

Other studies have focused on cancer cell migration and motility utilizing AM techniques to pattern hydrogels. One such study utilized a form of SLA discussed previously, DMD-PP, to create honeycomb patterns in hydrogels that mimic vasculature to study migration of cancer cells versus non-cancerous cells.[90] Cancer cell migration speed increased with decreasing diameter of the bioprinted vessels. A similar study used the same SLA method to create PEG scaffolds to investigate how both cell morphology and substrate modulus affect cell migration.[91] Substrate modulus and cell morphology profoundly affected cell migration in 3D, whereas differences in 2D were not as significant. These models for cancer cell migration have the potential to provide insight into tumor behavior, progression, and invasion.

2.1.6. Perspective

AM has profoundly impacted the field of tissue engineering despite its only recent widespread use. While initial studies were motivated by the potential of organ printing for implantation, AM has recently found a niche in creating TECs for *in vitro* models of organogenesis, disease progression, and drug screening. 3D culture using conventional fabrication techniques, such as microfluidics, electrospinning, and porogen leaching, has underscored the need for 3D models that more accurately recapitulate the cellular and physical properties of the tissue μEN compared to 2D cell culture. However, further research has indicated that parameters such as the matrix architecture, spatial arrangement of cells, hierarchical structure of tissues, and cellular cross-talk between adjacent tissues contribute substantially to cell behavior *in vivo*. AM techniques have the potential to bridge this gap between 3D models and *in vivo* milieu due to their ability to precisely control scaffold architecture and spatial arrangement of cells. Furthermore, progress in bioprinting has made possible the deposition of multiple cell types into different hierarchical structures, allowing for more sophisticated models capable of simulating the interaction between different tissue types. As the significance of 3D versus 2D culture has been established, there is a new need to transition high-throughput screening techniques to 3D. The continuously increasing speed of AM machines in addition to its inherent reproducibility renders AM a valuable means of creating scaffolds for high throughput drug screening. Other advantages of AM compared to more conventional techniques include enhanced reproducibility, scalability from the tissue culture well plate to the anatomic scale, and the ability to combine rapid prototyping and biofunctionalization in a single step.

3D *in vitro* models based on AM techniques are still emerging, and thus a number of challenges need to be addressed to fully realize the potential of AM for the design of TECs. While *in vivo* validation of 3D *in vitro* TECs remains an ultimate long-term goal, more achievable and modest shorter term objectives would make substantial contributions to the field, such as the identification of physiological characteristics of the tissue μEN that must be considered in the design of new therapies. Despite the fact that currently available 3D printed TECs cannot recapitulate all the properties of the μEN, they still present a more realistic and stringent μEN for drug screening compared to 2D culture. Consequently, 3D printed TECs have the potential to reduce the need for preclinical testing by more stringently screening drug candidates *in vitro*.

Advances in AM have realized the ability to create TECs with precisely controlled structures beyond the capabilities of conventional approaches, but additional barriers must be overcome before these models can reliably predict drug efficacy or model disease progression in humans. The use of patient-derived cells rather than cell lines could potentially advance the development of personalized medicine, in which patient-specific therapies are identified on the basis of high-throughput *in vitro* drug screening. In addition, many current models rely on static culture, whereas the *in vivo* µEN often experiences fluid flow that can affect cell behavior. Therefore, current models will need to support perfusion culture to more closely mimic the shear forces experienced by cells *in vivo.* Even further, maintaining a physiologic gradient of growth factors and other proteins within the tissues in perfusion culture would more accurately mimic the tissue µEN. Bioprinting has made progress in creating TECs from different cell types; however, scaffold architectures are largely limited to simple constructs, such as grids. Therefore, bioprinting methods capable of constructing more sophisticated architectures could expand complexity and thus more accurately mimic the *in vivo* µEN. More efficient simultaneous bioprinting of cells and biomaterials with tissue-specific mechanical properties could better recapitulate the mechanical, topological, and cellular properties of the µEN, and significant progress is being made in this area. Kang et al. have presented a bioprinting system, called ITOP, capable of fabricating mechanically-stable, functional, human-scale constructs of the mandible, calvarial bone, cartilage, and skeletal muscle by simultaneously plotting cell-laden material with biodegradable structural polymers containing microchannels to allow for nutrient transport.[92] Finally, organs in the human body do not behave independently, but are interconnected and communicate in a complex manner. Consequently, *in vitro* 3D models should ideally capture the cross-talk not just between cells, but also between tissues and organs. For instance, promoting angiogenesis and innervation into TECs in perfusion culture would better replicate the biological forces experienced by the organ of interest. Incorporation of multiple tissues and organs will also require scale-up of the models. This in turn will further necessitate networks of vasculature and other means of nutrient transport throughout the model, and this new complexity will need to be addressed. AM technology has the potential to address many of these limitations, due to the rapid growth in new technologies and approaches. Interdisciplinary research between tissue engineers, molecular biologists, and mechanical and electrical engineers in conjunction with AM technology has the potential to overcome the barriers that limit these models from becoming reliable tools for drug screening and understanding the underlying mechanisms contributing to disease.

2.2. Engineering 3D Models of Tumors and Bone to Understand Tumor-Induced Bone Disease and Improve Treatments

Adapted from:
Kwakwa, KA*, **Vanderburgh, JP***, Guelcher, SA, Sterling, JA. “Engineering 3D Models of Tumors and Bone to Understand Tumor-Induced Bone Disease and Improve Treatments.” *Curr Osteoporos Rep*. 2017;15(4):247-254.

2.2.1. Abstract

Bone is a structurally unique microenvironment that presents many challenges for the development of 3D models for studying bone physiology and diseases, including cancer. As researchers continue to investigate the interactions within the bone microenvironment, the development of 3D models of bone has become critical.

3D models have been developed that replicate some properties of bone, but have not fully reproduced the complex structural and cellular composition of the bone microenvironment.

This review will discuss 3D models including polyurethane, silk, and collagen scaffolds that have been developed to study tumor-induced bone disease. In addition, we discuss 3D printing techniques used to better replicate the structure of bone.

3D models that better replicate the bone microenvironment will help researchers better understand the dynamic interactions between tumors and the bone microenvironment, ultimately leading to better models for testing therapeutics and predicting patient outcomes.

2.2.2. Introduction

Tumor cells frequently reside in the bone microenvironment due to primary (osteosarcomas), invasive (melanoma, myeloma), or metastatic disease (breast, prostate, lung, and renal cancers). Once tumors establish in bone, they interact with the physical microenvironment as well as the resident bone cells to cause bone destruction known as tumor-induced bone disease. While these interactions have been well-established by in vitro and in vivo studies, it has been challenging to investigate dynamic tumor-bone interactions due to a lack of appropriate 3D models. Thus, many groups have developed new models for studying tumor-induced bone disease that use both tumor cells and bone-resident cells (osteoblasts, osteoclasts). The development of these models has relied heavily on collaborations between biologists, clinicians, and engineers. These 3D models have allowed scientists to better understand the signaling pathways that drive tumor-induced bone disease, the interactions between different cell types, and the influence of the physical bone microenvironment. Furthermore, these models can serve as valuable platforms for the discovery and development of novel therapeutics to target tumors in bone. In this review, we will briefly discuss common 3D culture methods used in cancer research (hydrogels, spheroids) while focusing on current 3D models for studying bone and tumor metastasis to bone, specifically tissue-engineered constructs (TECs).

2.2.3. Cancer Models

Since its development in the late 19th century, cell culture has remained an important tool for both basic biology and medical research, including cancer research. Most adherent tumor cells are cultured as a monolayer on two-dimensional (2D) substrates made of polystyrene plastic or glass. Although 2D culture systems are widely used in cancer research, an increasing body of evidence has shown that 2D cell culture does not adequately replicate the complex interactions and spatial organization of cells in the three-dimensional (3D) tumor microenvironment. Moreover, tumor cell behavior (proliferation, migration, gene expression) and response to drug treatment can differ dramatically in conventional 2D culture compared to in vivo cellular responses.[93–95] To address some of these limitations, several 3D cell culture systems have been developed in the last few decades and the adoption of these methods in cancer cell biology is rapidly increasing. Cancer cells grown in 3D more closely resemble those in the tumor microenvironment and thus, have more physiologically relevant responses. To date, the most common 3D cell culture methods in cancer research include extracellular matrix (ECM)-based hydrogels and tumor spheroids.

Due to their soft tissue-like properties, hydrogels have been increasingly used to mimic the 3D extracellular matrix (ECM) of solid tumors including breast, prostate, lung, and colorectal cancers.[96–99] Hydrogels are comprised of crosslinked polymer networks derived from natural or synthetic materials. Natural hydrogels are typically formed from ECM proteins like collagen, laminin, and fibrin as well as other matrix components like hyaluronic acid.[100,101] Collagen type I is a commonly used natural hydrogel since it is the most abundant ECM protein in tumor stroma and has been shown to support tumor growth and increase the expression of genes promoting malignant phenotypes.[102,103] The commercially available Corning® Matrigel® matrix is perhaps the most widely used natural ECM-based hydrogel for 3D culture of tumor cells in vitro. Matrigel® is a reconstituted basement membrane isolated from murine Engelbreth-Holm-Swarm (EHS) sarcoma which contains various ECM proteins (e.g. laminin, collagen IV, heparin sulfate proteoglycans) and endogenous growth factors (e.g. TGF-β, EGF, IGF-1, PDGF).[104] These gels are highly biocompatible and not only modulate tumor cell viability, proliferation, adhesion, and motility, but also sensitivity to therapeutic agents.[105] However, the concentration of proteins and growth factors in natural hydrogels can vary between batches and confounding factors such as undefined matrix components can influence tumor cell behavior.[106]

Alternatively, hydrogels made from synthetic materials such as poly(ethylene glycol) (PEG), poly(lactic acid) (PLA), and poly(vinyl alcohol) (PVA) have relatively well-defined structures with tunable chemical compositions and mechanical properties (e.g. stiffness).[4,107] Synthetic hydrogels also provide 3D architectural support for tumor cells and have been shown to maintain cell viability even in the absence of endogenous matrix components; however, these gels are usually supplemented with ECM proteins, growth factors, and other bioactive molecules in order to optimize tumor cell growth and survival.[108–110] Both natural and synthetic hydrogels can be used alone or in combination with other 3D culture methods including tumor spheroids.

In contrast to 2D monolayers, adherent tumor cells cultured in 3D tend to self-assemble into multicellular aggregates known as spheroids. Tumor spheroids are more mimetic of solid tumors in vivo with respect to cellular heterogeneity, metabolic and proliferative gradients, and gene expression. Specifically, spheroids typically contain a well-oxygenated outer layer of proliferating cells, a hypoxic inner layer of quiescent cells, and a necrotic core.[111,112] Multicellular spheroids may consist of tumor cells alone or as co-cultures with stromal, endothelial, and immune cells. The 3D cell culture methods used to generate tumor spheroids include both scaffold-based (e.g. hydrogels) and scaffold-free (e.g. forced floating, hanging drop) platforms.

Scaffold-based methods for spheroid growth involve embedding or encapsulating tumor cells within natural or synthetic hydrogels that mimic the ECM. As previously discussed, the presence of endogenous matrix proteins and growth factors in these gel matrices not only support the organization of tumor cells into 3D spheroids, but also promote the formation of migratory and invasive structures, significantly alter gene expression patterns, and affect cellular response to anti-tumor drugs.[96–99]

On the other hand, scaffold-free platforms do not use a gel matrix support. Tumor spheroids produced by these methods are generated in suspension culture. One relatively simple approach is the force floating method which utilizes an ultra-low attachment plate to prevent tumor cell adhesion to the surface. Instead, cells aggregate to form multicellular spheroids.[113,114] Another scaffold-free approach is the hanging drop method during which tumor cells in suspension aggregate into spheroids under gravity. Specifically, small aliquots of cell suspension are dispensed onto a Petri dish lid that is subsequently inverted to allow droplets to hang.[115] Various spheroid culture array plates have also been developed to better stabilize hanging drops.[116,117] This 3D tumor culture model generates a large number of spheroids with uniform size and morphology which is suitable for biochemical assays and high-throughput screening of therapeutics.[116,118,119]

2.2.4. Limitations of 3D Cancer Models for Bone

Tumors originating in the breast, prostate, and lung frequently metastasize to other organs, including bone.[120,121] In addition to interacting with bone-resident cells, tumor cells also come into contact with the mineralized bone matrix , which is orders of magnitude more rigid than soft tissues.[122,123] Simple 3D models like hydrogels and tumor spheroids improve upon 2D culture methods used to investigate soft tissue tumors and provide structural support for 3D cell growth and adhesion that resembles that of cells in their native environment. Moreover, hydrogels and other organic ECM components can be combined with more rigid scaffolding materials like ceramics, polymers, and composites to better mimic the bone microenvironment (discussed later in this review). However, used alone, these approaches fail to recapitulate the mechanical and physical properties of bone which should be considered when investigating tumor interactions in bone, especially mechanically responsive genes. Tissue engineering and scaffolding approaches have been employed to develop biomimetic 3D constructs in order to study metastatic tumors in bone.

2.2.5. 3D Bone Models

The field of bone tissue engineering has traditionally been focused on regenerating or repairing bone through the development of bone tissue-engineered constructs (TECs). However, advances toward creating TECs for *in vivo* applications have led to progress in designing biomimetic *in vitro* models for studying bone biology, disease progression, and drug screening in the bone microenvironment. 3D *in vitro* bone models have been proposed to aid in bridging the gap between 2D culture and animal models for diseases and medical conditions such as osteomyelitis,[124] bone fracture healing, [125,126] and, as will be discussed in this review, tumor metastases. In designing such TECs, studies investigating properties of the constructs indicated that characteristics including rigidity,[123,127] pore size,[29,128] pore shape,[129] and curvature[130] all affect cell behavior. Tissue engineers have been working toward creating TECs with precisely controlled physicochemical, mechanical, and structural properties that not only replicate human bone, but also allow for the systematic and parametric study of how these factors influence disease progression and drug response.

The first step in engineering *in vitro* models is designing the appropriate construct considering the *in vivo* microenvironment of interest. Bone stands apart from other non-mineralized tissues in that the rigidity of bone (1.7–2.9 × 10^{10} Pa) is orders of magnitude higher than soft tissues (10^2–10^6 Pa).[122,131] This unique rigidity necessitates TECs with high mechanical properties not attainable by hydrogels and other ECM-mimicking materials. On the other hand, materials used for cancer models vary widely depending on the origin of the tumor, and would ideally exhibit an angiogenic capacity.[3,7] Thus, in designing TECs for bone applications and 3D cancer models, engineers employ various materials and fabrication methods to create biomimetic matrices on which appropriate cell populations may be cultured.

First and foremost, materials must be biocompatible to avoid eliciting adverse cell responses *in vitro.* Since cells can sense and respond to the matrix, these biocompatible materials are carefully chosen for characteristics that will have the desired effect on the cell populations to be introduced. Mechanical properties, bioactivity, biodegradability, and chemical composition are characteristics that must be considered when choosing TEC materials for cancer and bone modeling alike. The robust mechanical properties of materials like ceramics, metals, polymers, and composites have rendered them the predominant materials used in fabricating bone TECs. While 3D models for soft tissue tumors are not necessarily subjected to the stringent rigidity restrictions, conferring ECM-like properties and surface modifications with specific proteins and growth factors are desirable to mimic the cancer microenvironment.[51]

Multiple poly(α-esters) have been used extensively in bone tissue engineering and for cancer models including poly(caprolactone) (PCL),[54,132,133] PLA,[134,135] and poly(lactic-co-glycolic acid) (PLGA).[5,136] These are biocompatible and biodegradable polymers that have other biomaterial applications such as drug delivery. They have also been combined with hydroxyapatite and other ceramics to create composite materials that exhibit more bone-like qualities.[137] However, these materials have drawbacks that can limit their effectiveness in bone applications including slow degradation time (PCL), low mechanical properties (PLGA), and low cell adhesion. Polyurethanes (PUR) are a good alternative due to their tunable rigidity, biodegradability, and physicochemical properties.[138] Furthermore, the ease of PUR processing, high mechanical properties, and biostability makes them attractive materials for biomedical bone implants and other bone-mimicking materials. Poly(propylene fumarate) (PPF) has also been incorporated into TECs due to their biocompatibility, biodegradability, and high mechanical properties.[139,140]

Natural materials have been employed for bone TEC applications as well. Collagen is a versatile material that has obvious appeal for bone applications as it is the main protein constituent of bone and comprises ~10% of bone matrix.[141] Collagen can be prepared into cross-linked solids or gels with varying mechanical properties and is intrinsically resorbable and bioactive. This makes collagen useful for a variety of applications including bone TECs, skin grafts, hydrogels, and sponges for wound healing.[142] Hydroxyapatite (HA) constitutes 50-70% of bone; therefore, HA and other calcium phosphate materials are also appealing for bone applications. Since HA is a ceramic material and not easily formed into 3D structures by conventional means, it is often combined with polymeric materials to create composites that impart both the osteoinductive benefits of HA along with the malleability of polymers. These main components of bone are enticing materials to use for bone TECs due to their physiologic relevance, however, other natural materials have been pursued as bone-like substrates. Silk is another biomaterial used in several biomedical applications because of its mechanical properties and versatility through its receptivity to chemical modifications.[143] Silk can be molecularly engineered to confer specific properties onto the material such as cellular recognition and mineralization, and multiple studies have utilized silk as a biomaterial for studying bone metastases.[144] Researchers have even used bone cells alone to create TECs for studying cancer progression. In one such study, an osteoid matrix was constructed by long-term culture of osteoblasts in a bioreactor system. Subsequent introduction of breast cancer cells revealed important pathological events including microtumor formation and cancer cell filing.[58]

In addition to substrate properties, it is important that biomaterials are able to be manipulated into relevant structures and 3D morphologies. Traditional methods to fabricate porous TECs from natural or synthetic polymers includes gas foaming,[145,146] particulate leaching,[137,147,148] or freeze-drying.[136,149] While these methods are effective in creating porous scaffolds, they lack the control necessary to create specific architectures.

As the importance of structural properties on which cells are grown becomes more evident, biologists and engineers have looked to new avenues for creating TECs with well-defined architectures. Additive manufacturing (AM), also known as 3D printing, is perhaps the most widely used new technology for creating TECs due to its unparalleled ability to create precisely controlled geometries at increasingly fast speeds.[150] AM, defined as the layer-by-layer fabrication of parts directed by digital information from a 3D computer-aided design file, is an umbrella term that describes multiple methods for creating 3D constructs. These methods include fused-deposition modeling,[41,69] stereolithography,[134,151] material jetting (inkjetting),[152] and bioprinting.[63,92] Other AM methods such as selective laser sintering (SLS) have also been implicated for use in biomaterials applications.

In addition to creating TECs with the appropriate physicochemical, structural, and mechanical properties, researchers are using bioreactors to more closely mimic physiologic flow conditions experience by cells *in vivo*. To do this, media is perfused through the TECs and circulated within the system, often using a peristaltic pump. Perfusion culture allows cells to experience physiologic shear conditions which are known to affect cell behavior.[153] Furthermore, perfusion culture allows for the flow of nutrients and other soluble factors that can keep cells viable for longer durations.

2.2.6. 3D Bone-Tumor Models

Collaborations between biologists and engineers have fostered the combining of the discussed biomaterials and fabrication methods to create 3D bone-tumor models using TECs. These biomimetic models not only aim to confer the appropriate cell-cell interactions, but also the appropriate cell-matrix interactions through the creation of TECs with precisely controlled properties that more closely replicate the *in vivo* bone-tumor milieu.

One such study employed a 3D bioreactor culture system to first create a mineralized, multi-layered tissue of osteoblasts and subsequently co-cultured with osteoclasts and metastatic tumor cells to investigate tumor effect on matrix degradation.[154] To create the 3D matrix, MC3T3-E1 murine osteoblasts were cultured for up to 10 months to create a 3D osteoid matrix. Osteoclasts were then introduced to the 3D culture, and subsequent matrix degradation was observed. After addition of fresh MC3T3-E1s, the matrix was reformed, thereby suggesting that bone remodeling was occurring. Finally, metastatic MDA-MB-231 breast cancer cells were added to the 3D co-culture system. By confocal microscopy, it was observed that the cancer cells migrated towards sites of active remodeling which led to further degradation of the matrix. This study not only demonstrates the ability to study the bone remodeling process *in vitro* but also how this process can be disrupted in a diseased state. This system is also amenable to clinically-relevant drug screening since it has a measurable physical outcome (matrix degradation).

In another high-impact study, porous silk fibroin scaffolds prepared directly from the silk fibroin protein of silk worms,[155] were used in a 3D culture system to investigate the response of metastatic tumor cells to external stimuli in the presence of osteoblasts and mesenchymal stem cells (MSC).[156] The silk fibroin scaffolds were hypothesized to be an ideal scaffold for investigating metastatic breast cancer behavior due to its mechanical properties in the range of adipose breast cancer in breast cancer patients, its inherent possession of Asp-Gly-Asp (RGD) peptide sequences known to promote cytocompatibility and cell adhesion, and based on the results of previous studies showing that MSCs undergo osteogenic differentiation on the scaffolds. Co-culture of MG-63 human osteoblast-like cells and MDA-MB-231 human breast cancer cells on the silk scaffolds resulted in a decrease in MG-63 population compared to that of the MDA-MB-231 despite being seeded at a 1:1 ratio. This suggests that the breast cancer cells were inhibiting growth of the osteoblasts, a finding that is supported by previous studies.[157] To take these findings a step further, the effect of the breast cancer cells on matrix mineralization was investigated using the same co-culture. Alizarin red staining and alkaline phosphatase activity indicated that matrix mineralization was lower on the scaffolds containing the breast cancer cells, further confirming the effect of tumor cells on osteoblast viability and function. Further studies in this system indicated that the co-culture significantly increases drug resistance, invasiveness, and angiogenicity.

In a more recent study from the same group, a similar 3D system utilizing silk fibroin scaffolds was used to screen anticancer drugs to understand its effect on the cellular interactions of the co-culture of MDA-MD-231 breast cancer cells and MG-63 osteoblastic cells.[158] A targeted nanoparticle (NP) formulation for the anticancer drug, doxorubicin, was developed using a folate-conjugated silk fibroin polymer. This formulation was then introduced into the 3D co-culture system to test the efficacy of the drug *in vitro* as well as its targeting ability. After 14 days of co-culture, the viability of the cancer cells decreased while osteoblast morphology and density was not much affected by the presence of doxorubicin. Also noted was the IC_{50} of the doxorubicin which was 10-fold higher in the 3D system than 2D, thus illustrating that tumor cell response to drugs can be drastically different in 3D compared to 2D. Further, they found that drug treatment reduced vascular endothelial growth factor (VEGF) expression and glucose consumption, suggesting a down-regulation of angiogenic factors and slowed proliferation of cancer cells, respectively. While the effect of the targeted NP formulation did not necessarily produce notably improved results over free doxorubicin, this study shows that the 3D co-culture system is capable of screening anticancer drugs and outcomes in 3D are notably different than in 2D.

Other studies have incorporated mechanical loading into the model to test how mechanical stress affects bone and cancer cell behavior. One such study employed HA-containing PLGA scaffolds under cyclic compression to investigate the interactions between MDA-MB-231 breast cancer cells and human bone marrow-derived mesenchymal stem cells (hBM-MSCs) in the mechanically stressed environment.[159] Before investigating mechanical loading, HA-containing scaffolds were seeded with hBM-MSCs and treated with tumor-conditioned media to observe how tumor-derived soluble factors influence osteogenic behavior. Interestingly, it was found that alkaline phosphatase (ALP) activity increased in the presence of tumor-conditioned media. This finding runs contrary to previous findings concluding that tumors tend to inhibit osteogenic differentiation. The authors suggest this could be a result of the early timing at which the hBM-MSCs were exposed to the conditioned media. Upon cyclic compression of HA-containing scaffolds seeded with hBM-MSCs and supplemented with conditioned media from mechanically loaded MDA-MD-231, there was no notable effect on ALP activity as seen in the non-loaded case. However, gene expression of the osteogenic marker osteopontin (OPN) significantly increased when the hBM-MSCs and MDA-MB-231s were mechanically loaded, and these findings were corroborated by measuring OPN protein levels. These data suggest that mechanical loading influences the interaction between hBM-MSCs and tumor cells through modulation of OPN levels. This study stresses the important role mechanical loading plays in bone-tumor interactions, which emphasizes the need to further investigate the effects of dynamic mechanical forces on tumor progression in bone.

As stated earlier, additive manufacturing has become a valuable tool for *in vitro* modeling due to its ability to create precise 3D geometries. Considering that bone has a complex and intricate structure, it is perhaps not surprising that 3D printing has started to influence 3D bone-tumor modeling. A recent study utilized a stereolithography 3D printing technique to create HA-composite scaffolds for modeling breast cancer bone metastases.[160] First, a PEG-based ink was printed into several pore geometries including square and hexagonal. After choosing the optimal geometry (small square pores) based on cell proliferation of MDA-MB-231 cells, HA was incorporated into the PEG ink (10% HA) and printed. The breast cancer cells grown on the HA-containing scaffolds proliferated significantly faster than the non-HA scaffolds, suggesting the HA component of bone promotes tumor proliferation. To study tumor cell migration on the HA-containing scaffolds, a non-metastatic breast cancer cell line (MCF-7) was also introduced and compared to the MDA-MB-231 cells. MDA-MB-231 cells cultured on the matrices migrated significantly farther than the MCF-7 in both the HA and non-HA scaffolds. They further tested the efficacy of the chemotherapeutic 5-FU in both the 3D and 2D environment. While 5-FU treatment did show efficacy in both environments, the efficacy was significantly less in 3D culture than in 2D. This study highlights the potential impact that 3D printing can have in *in vitro* modeling. It is evident from this study that curvature affects cell proliferation, therefore, it can be conjectured that 3D architecture may play an important role in tumor progression in bone.

2.2.7. Future of 3D Models

3D models have drastically improved over the past 5 years. However, existing 3D bone models only focus on a few aspects of the bone microenvironment. As researchers continue to study this niche, models will not only begin to incorporate more physical properties (rigidity, fluid flow, compression, pore size) but also different cell types (osteoblasts, osteoclasts, endothelial cells, fibroblasts, immune cells) (**Figure 2.1**). This will be an exceedingly complex undertaking that will likely take many years to accomplish as well as a variety of expertise from different groups. Additionally, researchers have begun modeling dynamic cellular interactions and processes in bone using computational models in order to develop a more complete understanding of the bone microenvironment and to predict outcomes.[161,162] These dynamic 3D models will significantly improve our ability to screen and develop new drugs to treat bone diseases including tumor-induced bone disease. One important objective is to increase usage of patient-derived cells in these 3D models to help predict patient outcomes to novel therapeutics.

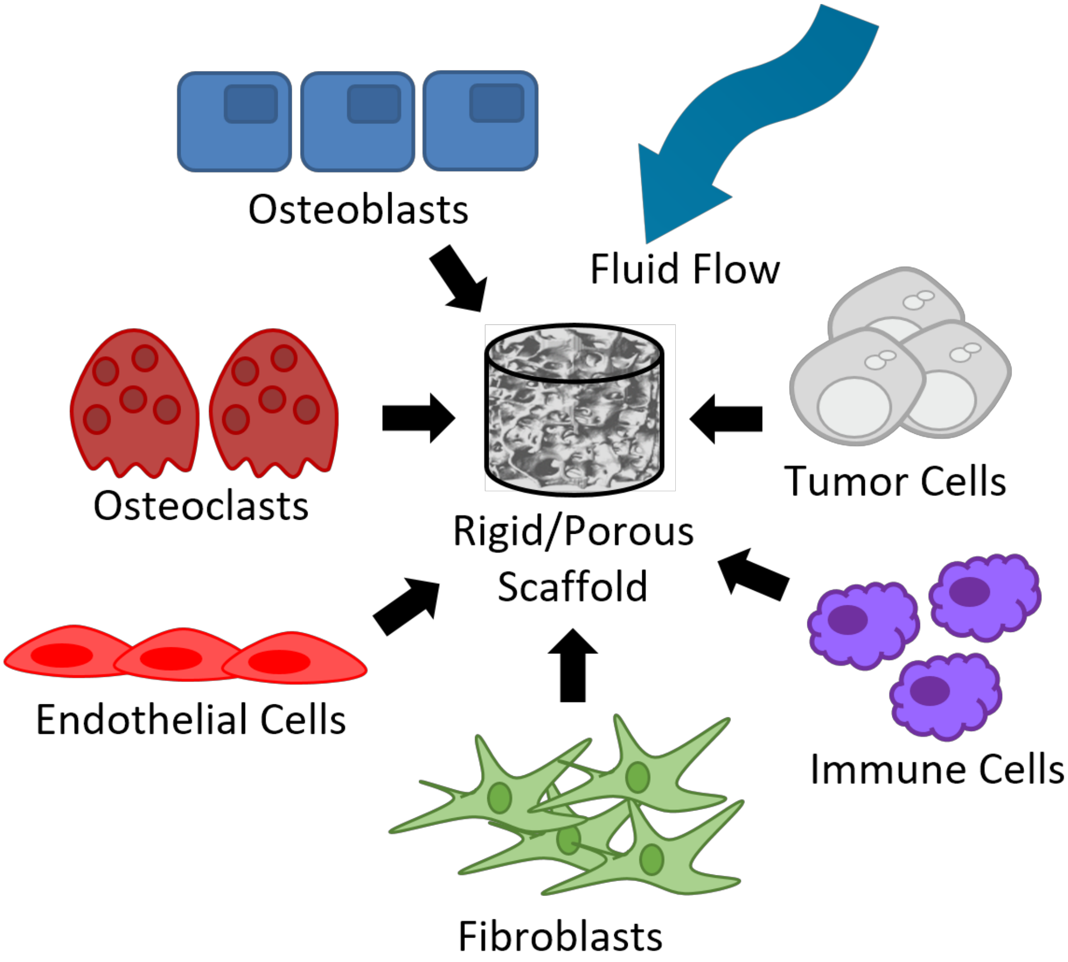

Figure 2.1. The incorporation of additional physical and cellular components in 3D bone models will help increase our understanding of the dynamic interactions in the bone microenvironment.

References

(1) Olson, H.; Betton, G.; Robinson, D.; Thomas, K.; Monro, A.; Kolaja, G.; Lilly, P.; Sanders, J.; Sipes, G.; Bracken, W.; et al. Concordance of the Toxicity of Pharmaceuticals in Humans and in Animals. *Regul. Toxicol. Pharmacol.* **2000**, *32* (1), 56–67.

(2) Andersen, M. E. Calling on Science: Making “Alternatives” the New Gold Standard. *Altex-Alternatives to Anim. Exp.* **2010**, *27* (2), 135–143.

(3) Fischbach, C.; Chen, R.; Matsumoto, T.; Schmelzle, T.; Brugge, J. S.; Polverini, P. J.; Mooney, D. J. Engineering Tumors with 3D Scaffolds. *Nat. Methods* **2007**, *4* (10), 855–860.

(4) Gurski, L. A.; Petrelli, N. J.; Jia, X.; Farach-Carson, M. C. 3D Matrices for Anti-Cancer Drug Testing and Development. *Oncol. Issues* **2010**, *25* (February), 20–25.

(5) Horning, J. L.; Sahoo, S. K.; Vijayaraghavalu, S.; Dimitrijevic, S.; Vasir, J. K.; Jain, T. K.; Panda, A. K.; Labhasetwar, V. 3-D Tumor Model for in Vitro Evaluation of Anticancer Drugs. *Mol. Pharm.* **2008**, *5* (5), 849–862.

(6) Sun, T.; Jackson, S.; Haycock, J. W.; MacNeil, S. Culture of Skin Cells in 3D Rather than 2D Improves Their Ability to Survive Exposure to Cytotoxic Agents. *J. Biotechnol.* **2006**, *122* (3), 372–381.

(7) Yamada, K. M.; Cukierman, E. Modeling Tissue Morphogenesis and Cancer in 3D. *Cell* **2007**, *130* (4), 601–610.

(8) Zadpoor, A. A. Bone Tissue Regeneration: The Role of Scaffold Geometry. *Biomater. Sci.* **2015**, *3* (2), 231–245.

(9) Zhang, D.; Pekkanen-Mattila, M.; Shahsavani, M.; Falk, A.; Teixeira, A. I.; Herland, A. A 3D Alzheimer’s Disease Culture Model and the Induction of P21-Activated Kinase Mediated Sensing in IPSC Derived Neurons. *Biomaterials* **2014**, *35* (5), 1420–1428.

(10) Bandyopadhyay, A.; Bose, S.; Das, S. 3D Printing of Biomaterials. *MRS Bull.* **2015**, *40* (02), 108–115.

(11) Khademhosseini, A.; Langer, R.; Borenstein, J. T.; Vacanti, J. P. Microscale Technologies for Tissue Engineering and Biology. *Proc. Natl. Acad. Sci. U. S. A.* **2006**, *103* (8), 2480–2487.

(12) Griffith, L. G.; Swartz, M. A. Capturing Complex 3D Tissue Physiology in Vitro. *Nat. Rev. Mol. Cell Biol.* **2006**, *7* (3), 211–224.

(13) Griffith, L. G.; Naughton, G. Tissue Engineering--Current Challenges and Expanding Opportunities. *Science* **2002**, *295* (5557), 1009–1014.

(14) Hutmacher, D. Scaffolds in Tissue Engineering Bone and Cartilage. *Biomaterials* **2000**, *21* (24), 2529–2543.

(15) Chung, T. W.; Yang, J.; Akaike, T.; Cho, K. Y.; Nah, J. W.; Kim, S. Il; Cho, C. S. Preparation of Alginate/Galactosylated Chitosan Scaffold for Hepatocyte Attachment. *Biomaterials* **2002**, *23* (14), 2827–2834.

(16) Guelcher, S. A.; Srinivasan, A.; Dumas, J. E.; Didier, J. E.; McBride, S.; Hollinger, J. O. Synthesis, Mechanical Properties, Biocompatibility, and Biodegradation of Polyurethane Networks from Lysine Polyisocyanates. *Biomaterials* **2008**, *29* (12), 1762–1775.

(17) Kimlin, L.; Kassis, J.; Virador, V. 3D in Vitro Tissue Models and Their Potential for Drug Screening. *Expert Opin. Drug Discov.* **2013**, *8* (12), 1455–1466.

(18) Alemany-Ribes, M.; Semino, C. E. Bioengineering 3D Environments for Cancer Models. *Adv. Drug Deliv. Rev.* **2014**, *79–80*, 40–49.

(19) Hirschhaeuser, F.; Menne, H.; Dittfeld, C.; West, J.; Mueller-Klieser, W.; Kunz-Schughart, L. A. Multicellular Tumor Spheroids: An Underestimated Tool Is Catching up Again. *J. Biotechnol.* **2010**, *148* (1), 3–15.

(20) Vörsmann, H.; Groeber, F.; Walles, H.; Busch, S.; Beissert, S.; Walczak, H.; Kulms, D. Development of a Human Three-Dimensional Organotypic Skin-Melanoma Spheroid Model for in Vitro Drug Testing. *Cell Death Dis.* **2013**, *4*, e719.

(21) Ramaiahgari, S. C.; Den Braver, M. W.; Herpers, B.; Terpstra, V.; Commandeur, J. N. M.; Van De Water, B.; Price, L. S. A 3D in Vitro Model of Differentiated HepG2 Cell Spheroids with Improved Liver-like Properties for Repeated Dose High-Throughput Toxicity Studies. *Arch. Toxicol.* **2014**, *88* (5), 1083–1095.

(22) Almela, T.; Brook, I. M.; Moharamzadeh, K. Development of Three-Dimensional Tissue Engineered Bone-Oral Mucosal Composite Models. *J. Mater. Sci. Mater. Med.* **2016**, *27* (4), 65.

(23) Evans, H. J.; Sweet, J. K.; Price, R. L.; Yost, M.; Goodwin, R. L. Novel 3D Culture System for Study of Cardiac Myocyte Development. *Am. J. Physiol. Heart Circ. Physiol.* **2003**, *285* (May 2003), H570–H578.

(24) Macchiarini, P.; Jungebluth, P.; Go, T.; Asnaghi, M. A.; Rees, L. E.; Cogan, T. A.; Dodson, A.; Martorell, J.; Bellini, S.; Parnigotto, P. P.; et al. Clinical Transplantation of a Tissue-Engineered Airway. *Lancet* **2008**, *372* (9655), 2023–2030.

(25) Zanotelli, M. R.; Ardalani, H.; Zhang, J.; Hou, Z.; Nguyen, E. H.; Swanson, S.; Nguyen, B. K.; Bolin, J.; Elwell, A.; Bischel, L. L.; et al. Stable Engineered Vascular Networks from Human Induced Pluripotent Stem Cell-Derived Endothelial Cells Cultured in Synthetic Hydrogels. *Acta Biomater.* **2016**, 1–10.

(26) Kraus, D.; Boyle, V.; Leibig, N.; Stark, G.; Penna, V. The Neuro-Spheroid—A Novel 3D in Vitro Model for Peripheral Nerve Regeneration. *J. Neurosci. Methods* **2015**, *246*, 97–105.

(27) Fernández-Muiños, T.; Recha-Sancho, L.; López-Chicón, P.; Castells-Sala, C.; Mata, A.; Semino, C. E. Bimolecular Based Heparin and Self-Assembling Hydrogel for Tissue Engineering Applications. *Acta Biomater.* **2015**, *16* (1), 35–48.

(28) Abidin, F. Z.; Gouveia, R. M.; Connon, C. J. Application of Retinoic Acid Improves Form and Function of Tissue Engineered Corneal Construct. *Organogenesis* **2015**, *11* (3), 122–136.

(29) Guo, R.; Lu, S.; Page, J. M.; Merkel, A. R.; Basu, S.; Sterling, J. A.; Guelcher, S. A. Fabrication of 3D Scaffolds with Precisely Controlled Substrate Modulus and Pore Size by Templated-Fused Deposition Modeling to Direct Osteogenic Differentiation. *Adv. Healthc. Mater.* **2015**, *4* (12), 1826–1832.

(30) Malda, J.; Woodfield, T. B. F.; van der Vloodt, F.; Wilson, C.; Martens, D. E.; Tramper, J.; van Blitterswijk, C. A.; Riesle, J. The Effect of PEGT/PBT Scaffold Architecture on the Composition of Tissue Engineered Cartilage. *Biomaterials* **2005**, *26* (1), 63–72.

(31) Sanz-Herrera, J. A.; Moreo, P.; García-Aznar, J. M.; Doblaré, M. On the Effect of Substrate Curvature on Cell Mechanics. *Biomaterials* **2009**, *30* (34), 6674–6686.

(32) ASTM International. F2792-12a - Standard Terminology for Additive Manufacturing Technologies. *Rapid Manuf. Assoc.* **2013**, 10–12.

(33) Hull, C. W. Apparatus for Production of Three Dimensional Objects by Stereolithography, 1986.

(34) Melchels, F. P. W.; Feijen, J.; Grijpma, D. W. A Review on Stereolithography and Its Applications in Biomedical Engineering. *Biomaterials* **2010**, *31* (24), 6121–6130.

(35) Sun, C.; Fang, N.; Wu, D. M.; Zhang, X. Projection Micro-Stereolithography Using Digital Micro-Mirror Dynamic Mask. *Sensors Actuators A Phys.* **2005**, *121* (1), 113–120.

(36) Bian, W.; Li, D.; Lian, Q.; Li, X.; Zhang, W.; Wang, K.; Jin, Z. Fabrication of a Bio-Inspired Beta-Tricalcium Phosphate/Collagen Scaffold Based on Ceramic Stereolithography and Gel Casting for Osteochondral Tissue Engineering. *Rapid Prototyp. J.* **2012**, *18* (1), 68–80.

(37) Crump, S. S. Apparatus and Method for Creating Three-Dimensional Objects, 1992.

(38) Zein, I.; Hutmacher, D. W.; Tan, K. C.; Teoh, S. H. Fused Deposition Modeling of Novel Scaffold Architectures for Tissue Engineering Applications. *Biomaterials* **2002**, *23* (4), 1169–1185.

(39) Ahn, S. H.; Montero, M.; Odell, D.; Roundy, S.; Wright, P. K. Anisotropic Material Properties of Fused Deposition Modeling ABS. *Rapid Prototyp. J.* **2002**, *8* (4), 248–257.

(40) Hollister, S. J. Porous Scaffold Design for Tissue Engineering. *Nat. Mater.* **2005**, *4* (7), 518–524.

(41) Hutmacher, D. W.; Schantz, T.; Zein, I.; Ng, K. W.; Teoh, S. H.; Tan, K. C. Mechanical Properties and Cell Cultural Response of Polycaprolactone Scaffolds Designed and Fabricated via Fused Deposition Modeling. *J. Biomed. Mater. Res.* **2001**, *55* (2), 203–216.

(42) Galantucci, L. M.; Lavecchia, F.; Percoco, G. Experimental Study Aiming to Enhance the Surface Finish of Fused Deposition Modeled Parts. *CIRP Ann. - Manuf. Technol.* **2009**, *58* (1), 189–192.

(43) de Gans, B.-J.; Duineveld, P. C.; Schubert, U. S. Inkjet Printing of Polymers: State of the Art and Future Developments. *Adv. Mater.* **2004**, *16* (3), 203–213.

(44) Groll, J.; Boland, T.; Blunk, T.; Burdick, J. a; Cho, D.; Paul, D.; Derby, B.; Forgacs, G.; Li, Q.; Mironov, V. a; et al. Biofabrication : Reappraising the Definition in an Evolving Field. *Biofabrication* **2016**, *8*, 013001.

(45) Guillemot, F.; Mironov, V.; Nakamura, M. Bioprinting Is Coming of Age: Report from the International Conference on Bioprinting and Biofabrication in Bordeaux (3B'09). *Biofabrication* **2010**, *2* (1), 010201.

(46) Derby, B. Printing and Prototyping of Tissues and Scaffolds. *Science* **2012**, *338* (6109), 921–926.

(47) Knowlton, S.; Onal, S.; Yu, C. H.; Zhao, J. J.; Tasoglu, S. Bioprinting for Cancer Research. *Trends Biotechnol.* **2015**, *33* (9), 1–10.

(48) Rimann, M.; Bono, E.; Annaheim, H.; Bleisch, M.; Graf-Hausner, U. Standardized 3D Bioprinting of Soft Tissue Models with Human Primary Cells. *J. Lab. Autom.* **2015**.

(49) Murphy, S. V; Atala, A. 3D Bioprinting of Tissues and Organs. *Nat. Biotechnol.* **2014**, *32* (8), 773–785.

(50) Tasoglu, S.; Demirci, U. Bioprinting for Stem Cell Research. *Trends Biotechnol* **2013**, *31* (1), 10–19.

(51) Schuessler, T. K.; Chan, X. Y.; Chen, H. J.; Ji, K.; Park, K. M.; Roshan-Ghias, A.;

Sethi, P.; Thakur, A.; Tian, X.; Villasante, A.; et al. Biomimetic Tissue-Engineered Systems for Advancing Cancer Research: NCI Strategic Workshop Report. *Cancer Res.* **2014**, *74* (19), 5359–5363.

(52) VanBael, S.; Chai, Y. C.; Truscello, S.; Moesen, M.; Kerckhofs, G.; Van Oosterwyck, H.; Kruth, J. P.; Schrooten, J. The Effect of Pore Geometry on the in Vitro Biological Behavior of Human Periosteum-Derived Cells Seeded on Selective Laser-Melted Ti6Al4V Bone Scaffolds. *Acta Biomater.* **2012**, *8* (7), 2824–2834.

(53) Grayson, W. L.; Fröhlich, M.; Yeager, K.; Bhumiratana, S.; Chan, M. E.; Cannizzaro, C.; Wan, L. Q.; Liu, X. S.; Guo, X. E.; Vunjak-Novakovic, G. Engineering Anatomically Shaped Human Bone Grafts. *Proc. Natl. Acad. Sci. U. S. A.* **2010**, *107* (8), 3299–3304.

(54) Temple, J. P.; Hutton, D. L.; Hung, B. P.; Huri, P. Y.; Cook, C. a.; Kondragunta, R.; Jia, X.; Grayson, W. L. Engineering Anatomically Shaped Vascularized Bone Grafts with HASCs and 3D-Printed PCL Scaffolds. *J. Biomed. Mater. Res. - Part A* **2014**, 4317–4325.

(55) Costa, P. F.; Vaquette, C.; Baldwin, J.; Chhaya, M.; Gomes, M. E.; Reis, R. L.; Theodoropoulos, C.; Hutmacher, D. W. Biofabrication of Customized Bone Grafts by Combination of Additive Manufacturing and Bioreactor Knowhow. *Biofabrication* **2014**, *6* (3), 035006.

(56) Smith, K. E.; Hyzy, S. L.; Sunwoo, M.; Gall, K. A.; Schwartz, Z.; Boyan, B. D. The Dependence of MG63 Osteoblast Responses to (Meth)Acrylate-Based Networks on Chemical Structure and Stiffness. *Biomaterials* **2010**, *31* (24), 6131–6141.

(57) Ruppender, N. S.; Merkel, A. R.; Martin, T. J.; Mundy, G. R.; Sterling, J. A.; Guelcher, S. A. Matrix Rigidity Induces Osteolytic Gene Expression of Metastatic Breast Cancer Cells. *PLoS One* **2010**, *5* (11), 1–10.

(58) Mastro, A. M.; Vogler, E. A. A Three-Dimensional Osteogenic Tissue Model for the Study of Metastatic Tumor Cell Interactions with Bone. *Cancer Res.* **2009**, *69* (10), 4097–4100.

(59) Fitzgerald, K. A.; Guo, J.; Tierney, E. G.; Curtin, C. M.; Malhotra, M.; Darcy, R.; O'Brien, F. J.; O'Driscoll, C. M. The Use of Collagen-Based Scaffolds to Simulate Prostate Cancer Bone Metastases with Potential for Evaluating Delivery of Nanoparticulate Gene Therapeutics. *Biomaterials* **2015**, *66*, 53–66.

(60) Fong, E. L. S.; Lamhamedi-Cherradi, S.-E.; Burdett, E.; Ramamoorthy, V.; Lazar, A. J.; Kasper, F. K.; Farach-Carson, M. C.; Vishwamitra, D.; Demicco, E. G.; Menegaz, B. a; et al. Modeling Ewing Sarcoma Tumors in Vitro with 3D Scaffolds. *Proc. Natl. Acad. Sci. U. S. A.* **2013**, *110* (16), 6500–6505.

(61) Kock, L.; van Donkelaar, C. C.; Ito, K. Tissue Engineering of Functional Articular Cartilage: The Current Status. *Cell Tissue Res.* **2012**, *347* (3), 613–627.

(62) Moreira-Teixeira, L. S.; Georgi, N.; Leijten, J.; Wu, L.; Karperien, M. Cartilage Tissue Engineering. *Endocr. Dev.* **2011**, *21*, 102–115.

(63) Kundu, J.; Shim, J. H.; Jang, J.; Kim, S. W.; Cho, D. W. An Additive Manufacturing-Based PCL-Alginate-Chondrocyte Bioprinted Scaffold for Cartilage Tissue Engineering. *J. Tissue Eng. Regen. Med.* **2015**, *9* (11), 1286–1297.

(64) Gurkan, U. a.; El Assal, R.; Yildiz, S. E.; Sung, Y.; Trachtenberg, A. J.; Kuo, W. P.; Demirci, U. Engineering Anisotropic Biomimetic Fibrocartilage Microenvironment by Bioprinting Mesenchymal Stem Cells in Nanoliter Gel Droplets. *Mol. Pharm.* **2014**, *11* (7), 2151–2159.

(65) Pati, F.; Jang, J.; Ha, D.-H.; Won Kim, S.; Rhie, J.-W.; Shim, J.-H.; Kim, D.-H.; Cho, D.-W. Printing Three-Dimensional Tissue Analogues with Decellularized Extracellular Matrix Bioink. *Nat. Commun.* **2014**, *5*, 3935.

(66) Kolesky, D. B.; Truby, R. L.; Gladman, A. S.; Busbee, T. A.; Homan, K. A.; Lewis, J. A. 3D Bioprinting of Vascularized, Heterogeneous Cell-Laden Tissue Constructs. *Adv. Mater.* **2014**, *26* (19), 3124–3130.

(67) Groeber, F.; Holeiter, M.; Hampel, M.; Hinderer, S.; Schenke-Layland, K. Skin Tissue Engineering — In Vivo and in Vitro Applications. *Adv. Drug Deliv. Rev.* **2011**, *63* (4–5), 352–366.

(68) Lee, W.; Debasitis, J. C.; Lee, V. K.; Lee, J. H.; Fischer, K.; Edminster, K.; Park, J. K.; Yoo, S. S. Multi-Layered Culture of Human Skin Fibroblasts and Keratinocytes through Three-Dimensional Freeform Fabrication. *Biomaterials* **2009**, *30* (8), 1587–1595.

(69) Guo, R.; Merkel, A. R.; Sterling, J. A.; Davidson, J. M.; Guelcher, S. A. Substrate Modulus of 3D-Printed Scaffolds Regulates the Regenerative Response in Subcutaneous Implants through the Macrophage Phenotype and Wnt Signaling. *Biomaterials* **2015**, *73*, 85–95.

(70) LeCluyse, E. L.; Witek, R. P.; Andersen, M. E.; Powers, M. J. Organotypic Liver Culture Models: Meeting Current Challenges in Toxicity Testing. *Crit. Rev. Toxicol.* **2012**, *42* (6), 501–548.

(71) Chang, R.; Nam, J.; Sun, W. Direct Cell Writing of 3D Microorgan for in Vitro Pharmacokinetic Model. *Tissue Eng. Part C. Methods* **2008**, *14* (2), 157–166.

(72) Chang, R.; Emami, K.; Wu, H.; Sun, W. Biofabrication of a Three-Dimensional Liver Micro-Organ as an in Vitro Drug Metabolism Model. *Biofabrication* **2010**, *2* (4), 045004.

(73) Snyder, J. E.; Hamid, Q.; Wang, C.; Chang, R.; Emami, K.; Wu, H.; Sun, W. Bioprinting Cell-Laden Matrigel for Radioprotection Study of Liver by pro-Drug Conversion in a Dual-Tissue Microfluidic Chip. *Biofabrication* **2011**, *3* (3), 034112.

(74) Sarkar, U.; Rivera-Burgos, D.; Large, E. M.; Hughes, D. J.; Ravindra, K. C.; Dyer, R. L.; Ebrahimkhani, M. R.; Wishnok, J. S.; Griffith, L. G.; Tannenbaum, S. R. Metabolite Profiling and Pharmacokinetic Evaluation of Hydrocortisone in a Perfused Three-Dimensional Human Liver Bioreactor. *Drug Metab. Dispos.* **2015**, *43* (7), 1091–1099.

(75) Neiman, J. a. S.; Raman, R.; Chan, V.; Rhoads, M. G.; Raredon, M. S. B.; Velazquez, J. J.; Dyer, R. L.; Bashir, R.; Hammond, P. T.; Griffith, L. G. Photopatterning of Hydrogel Scaffolds Coupled to Filter Materials Using Stereolithography for Perfused 3D Culture of Hepatocytes. *Biotechnol. Bioeng.* **2015**, *112* (4), 777–787.

(76) Taylor, M. P.; Kobiler, O.; Enquist, L. W. Alphaherpesvirus Axon-to-Cell Spread Involves Limited Virion Transmission. *Proc. Natl. Acad. Sci. U. S. A.* **2012**, *109* (42), 17046–17051.

(77) Pedron, S.; Becka, E.; Harley, B. A. Spatially Gradated Hydrogel Platform as a 3D Engineered Tumor Microenvironment. *Adv. Mater.* **2015**, *27* (9), 1567–1572.

(78) Johnson, B.; Lancaster, K.; Hogue, I. B.; Meng, F.; Kong, Y. L.; Enquist, L.; McAlpine, M. 3D Printed Nervous System on a Chip. *Lab Chip* **2015**.

(79) Frega, M.; Tedesco, M.; Massobrio, P.; Pesce, M.; Martinoia, S. Network Dynamics of 3D Engineered Neuronal Cultures: A New Experimental Model for in-Vitro

Electrophysiology. *Sci. Rep.* **2014**, *4*, 1–14.

(80) Lozano, R.; Stevens, L.; Thompson, B. C.; Gilmore, K. J.; Gorkin, R.; Stewart, E. M.; in het Panhuis, M.; Romero-Ortega, M.; Wallace, G. G. 3D Printing of Layered Brain-like Structures Using Peptide Modified Gellan Gum Substrates. *Biomaterials* **2015**, *67*, 264–273.

(81) de Souza Carvalho, C.; Daum, N.; Lehr, C. M. Carrier Interactions with the Biological Barriers of the Lung: Advanced in Vitro Models and Challenges for Pulmonary Drug Delivery. *Adv. Drug Deliv. Rev.* **2014**, *75*, 129–140.

(82) Horváth, L.; Umehara, Y.; Jud, C.; Blank, F.; Petri-Fink, A.; Rothen-Rutishauser, B. Engineering an in Vitro Air-Blood Barrier by 3D Bioprinting. *Sci. Rep.* **2015**, *5*, 7974.

(83) Jain, R. K.; Au, P.; Tam, J.; Duda, D. G.; Fukumura, D. Engineering Vascularized Tissue. *Nat. Biotechnol.* **2005**, *23* (7), 821–823.

(84) Bertassoni, L. E.; Cecconi, M.; Manoharan, V.; Nikkhah, M.; Hjortnaes, J.; Cristino, A. L.; Barabaschi, G.; Demarchi, D.; Dokmeci, M. R.; Yang, Y.; et al. Hydrogel Bioprinted Microchannel Networks for Vascularization of Tissue Engineering Constructs. *Lab Chip* **2014**, *14* (13), 2202–2211.

(85) Miller, J. S.; Stevens, K. R.; Yang, M. T.; Baker, B. M.; Nguyen, D. H. T.; Cohen, D. M.; Toro, E.; Chen, A. A.; Galie, P. A.; Yu, X.; et al. Rapid Casting of Patterned Vascular Networks for Perfusable Engineered Three-Dimensional Tissues. *Nat. Mater.* **2012**, *11* (9), 768–774.

(86) Raman, R.; Bhaduri, B.; Mir, M.; Shkumatov, A.; Lee, M. K.; Popescu, G.; Kong, H.; Bashir, R. High-Resolution Projection Microstereolithography for Patterning of Neovasculature. *Adv. Healthc. Mater.* **2015**.

(87) Rizvi, I.; Celli, J. P.; Evans, C. L.; Abu-Yousif, A. O.; Muzikansky, A.; Pogue, B. W.; Finkelstein, D.; Hasan, T. Synergistic Enhancement of Carboplatin Efficacy with Photodynamic Therapy in a Three-Dimensional Model for Micrometastatic Ovarian Cancer. *Cancer Res.* **2010**, *70* (22), 9319–9328.

(88) Xu, F.; Celli, J.; Rizvi, I.; Moon, S.; Hasan, T.; Demirci, U. A Three-Dimensional in Vitro Ovarian Cancer Coculture Model Using a High-Throughput Cell Patterning Platform. *Biotechnol. J.* **2011**, *6* (2), 204–212.

(89) Zhao, Y.; Yao, R.; Ouyang, L.; Ding, H.; Zhang, T.; Zhang, K.; Cheng, S.; Sun, W. Three-Dimensional Printing of Hela Cells for Cervical Tumor Model *in Vitro*. *Biofabrication* **2014**, *6* (3), 035001.

(90) Huang, T. Q.; Qu, X.; Liu, J.; Chen, S. 3D Printing of Biomimetic Microstructures for Cancer Cell Migration. *Biomed. Microdevices* **2014**, *16* (1), 127–132.

(91) Soman, P.; Kelber, J. a.; Lee, J. W.; Wright, T. N.; Vecchio, K. S.; Klemke, R. L.; Chen, S. Cancer Cell Migration within 3D Layer-by-Layer Microfabricated Photocrosslinked PEG Scaffolds with Tunable Stiffness. *Biomaterials* **2012**, *33* (29), 7064–7070.

(92) Kang, H. W.; Lee, S. J.; Ko, I. K.; Kengla, C.; Yoo, J. J.; Atala, A. A 3D Bioprinting System to Produce Human-Scale Tissue Constructs with Structural Integrity. *Nat. Biotechnol.* **2016**, No. October 2015.

(93) Ma, X. H.; Piao, S.; Wang, D.; Mcafee, Q. W.; Nathanson, K. L.; Lum, J. J.; Li, L. Z.; Amaravadi, R. K. Measurements of Tumor Cell Autophagy Predict Invasiveness, Resistance to Chemotherapy, and Survival in Melanoma. *Clin. Cancer Res.* **2011**, *17* (10), 3478–3489.

(94) Lee, J. M.; Mhawech-Fauceglia, P.; Lee, N.; Parsanian, L. C.; Lin, Y. G.; Gayther, S. A.; Lawrenson, K. A Three-Dimensional Microenvironment Alters Protein Expression and Chemosensitivity of Epithelial Ovarian Cancer Cells in Vitro. *Lab. Investig.* **2013**, *93* (5), 528–542.

(95) Imamura, Y.; Mukohara, T.; Shimono, Y.; Funakoshi, Y.; Chayahara, N.; Toyoda, M.; Kiyota, N.; Takao, S.; Kono, S.; Nakatsura, T.; et al. Comparison of 2D- and 3D-Culture Models as Drug-Testing Platforms in Breast Cancer. *Oncol. Rep.* **2015**, *33* (4), 1837–1843.

(96) Vantangoli, M. M.; Madnick, S. J.; Huse, S. M.; Weston, P.; Boekelheide, K. MCF-7 Human Breast Cancer Cells Form Differentiated Microtissues in Scaffold-Free Hydrogels. *PLoS One* **2015**, *10* (8), 1–20.

(97) Härmä, V.; Virtanen, J.; Mäkelä, R.; Happonen, A.; Mpindi, J. P.; Knuuttila, M.; Kohonen, P.; Lötjönen, J.; Kallioniemi, O.; Nees, M. A Comprehensive Panel of Three-Dimensional Models for Studies of Prostate Cancer Growth, Invasion and Drug Responses. *PLoS One* **2010**, *5* (5), e10431.

(98) Cichon, M. A.; Gainullin, V. G.; Zhang, Y.; Radisky, D. C. Growth of Lung Cancer Cells in Three-Dimensional Microenvironments Reveals Key Features of Tumor Malignancy. *Integr Biol* **2012**, *4* (4), 440–448.

(99) Luca, A. C.; Mersch, S.; Deenen, R.; Schmidt, S.; Messner, I.; Schäfer, K. L.; Baldus, S. E.; Huckenbeck, W.; Piekorz, R. P.; Knoefel, W. T.; et al. Impact of the 3D Microenvironment on Phenotype, Gene Expression, and EGFR Inhibition of Colorectal Cancer Cell Lines. *PLoS One* **2013**, *8* (3), e59689.

(100) Sokol, E. S.; Miller, D. H.; Breggia, A.; Spencer, K. C.; Arendt, L. M.; Gupta, P. B. Growth of Human Breast Tissues from Patient Cells in 3D Hydrogel Scaffolds. *Breast Cancer Res.* **2016**, *18* (19), 1–13.

(101) Xu, X.; Gurski, L. A.; Zhang, C.; Harrington, D. A.; Farach-Carson, M. C.; Jia, X. Recreating the Tumor Microenvironment in a Bilayer, Hyaluronic Acid Hydrogel Construct for the Growth of Prostate Cancer Spheroids. *Biomaterials* **2012**, *33* (35), 9049–9060.

(102) Szot, C. S.; Buchanan, C. F.; Freeman, J. W.; Rylander, M. N. 3D in Vitro Bioengineered Tumors Based on Collagen I Hydrogels. *Biomaterials* **2011**, *32* (31), 7905–7912.

(103) Riching, K. M.; Cox, B. L.; Salick, M. R.; Pehlke, C.; Riching, A. S.; Ponik, S. M.; Bass, B. R.; Crone, W. C.; Jiang, Y.; Weaver, A. M.; et al. 3D Collagen Alignment Limits Protrusions to Enhance Breast Cancer Cell Persistence. *Biophys. J.* **2014**, *107* (11), 2546–2558.

(104) Kleinman, H. K.; Martin, G. R. Matrigel: Basement Membrane Matrix with Biological Activity. *Semin. Cancer Biol.* **2005**, *15*, 378–386.

(105) Lovitt, C. J.; Shelper, T. B.; Avery, V. M. Evaluation of Chemotherapeutics in a Three-Dimensional Breast Cancer Model. *J. Cancer Res. Clin. Oncol.* **2015**, *141* (5), 951–959.

(106) Hughes, C. S.; Postovit, L. M.; Lajoie, G. A. Matrigel: A Complex Protein Mixture Required for Optimal Growth of Cell Culture. *Proteomics* **2010**, *10* (9), 1886–1890.

(107) Chung, I. M.; Enemchukwu, N. O.; Khaja, S. D.; Murthy, N.; Mantalaris, A.; García, A. J. Bioadhesive Hydrogel Microenvironments to Modulate Epithelial Morphogenesis. *Biomaterials* **2008**, *29* (17), 2637–2645.

(108) Gill, B. J.; Gibbons, D. L.; Roudsari, L. C.; Saik, J. E.; Rizvi, Z. H.; Roybal, J. D.;

Kurie, J. M.; West, J. L. A Synthetic Matrix with Independently Tunable Biochemistry and Mechanical Properties to Study Epithelial Morphogenesis and EMT in a Lung Adenocarcinoma Model. *Cancer Res.* **2012**, *72* (22), 6013–6023.

(109) Del Bufalo, F.; Manzo, T.; Hoyos, V.; Yagyu, S.; Caruana, I.; Jacot, J.; Benavides, O.; Rosen, D.; Brenner, M. K. 3D Modeling of Human Cancer: A PEG-Fibrin Hydrogel System to Study the Role of Tumor Microenvironment and Recapitulate the in Vivo Effect of Oncolytic Adenovirus. *Biomaterials* **2016**, *84*, 76–85.

(110) Pradhan, S.; Hassani, I.; Seeto, W. J.; Lipke, E. A. PEG-Fibrinogen Hydrogels for Three-Dimensional Breast Cancer Cell Culture. *J. Biomed. Mater. Res. Part A* **2017**, *105* (A), 236–252.

(111) Feder-Mengus, C.; Ghosh, S.; Reschner, A.; Martin, I.; Spagnoli, G. C. New Dimensions in Tumor Immunology: What Does 3D Culture Reveal? *Trends Mol. Med.* **2008**, *14* (8), 333–340.

(112) Zanoni, M.; Piccinini, F.; Arienti, C.; Zamagni, A.; Santi, S.; Polico, R.; Bevilacqua, A.; Tesei, A. 3D Tumor Spheroid Models for in Vitro Therapeutic Screening: A Systematic Approach to Enhance the Biological Relevance of Data Obtained. *Sci. Rep.* **2016**, *6*, 19103.

(113) Vinci, M.; Gowan, S.; Boxall, F.; Patterson, L.; Zimmermann, M.; Court, W.; Lomas, C.; Mendiola, M.; Hardisson, D.; Eccles, S. a. Advances in Establishment and Analysis of Three-Dimensional Tumor Spheroid-Based Functional Assays for Target Validation and Drug Evaluation. *BMC Biol.* **2012**, *10* (29), 1–20.

(114) Breslin, S.; O'Driscoll, L. Three-Dimensional Cell Culture: The Missing Link in Drug Discovery. *Drug Discov. Today* **2013**, *18* (5–6), 240–249.

(115) Yip, D.; Cho, C. H. A Multicellular 3D Heterospheroid Model of Liver Tumor and Stromal Cells in Collagen Gel for Anti-Cancer Drug Testing. *Biochem. Biophys. Res. Commun.* **2013**, *433* (3), 327–332.

(116) Tung, Y.-C.; Hsiao, A. Y.; Allen, S. G.; Torisawa, Y.; Ho, M.; Takayama, S. High-Throughput 3D Spheroid Culture and Drug Testing Using a 384 Hanging Drop Array. *Analyst* **2011**, *136* (3), 473–478.

(117) Amann, A.; Zwierzina, M.; Gamerith, G.; Bitsche, M.; Huber, J. M.; Vogel, G. F.; Blumer, M.; Koeck, S.; Pechriggl, E. J.; Kelm, J. M.; et al. Development of an Innovative 3D Cell Culture System to Study Tumour - Stroma Interactions in Non-Small Cell Lung Cancer Cells. *PLoS One* **2014**, *9* (3).

(118) Raghavan, S.; Ward, M. R.; Rowley, K. R.; Wold, R. M.; Takayama, S.; Buckanovich, R. J.; Mehta, G. Formation of Stable Small Cell Number Three-Dimensional Ovarian Cancer Spheroids Using Hanging Drop Arrays for Preclinical Drug Sensitivity Assays. *Gynecol. Oncol.* **2015**, *138* (1), 181–189.

(119) Raghavan, S.; Mehta, P.; Horst, E. N.; Ward, M. R.; Rowley, K. R.; Mehta, G. Comparative Analysis of Tumor Spheroid Generation Techniques for Differential in Vitro Drug Toxicity. *Oncotarget* **2016**, *7* (13), 16948–16961.

(120) Aboulafia, A. J.; Levine, A. M.; Schmidt, D.; Aboulafia, D. Surgical Therapy of Bone Metastases. *Semin. Oncol.* **2007**, *34*, 206–214.

(121) Johnson, R. W.; Schipani, E.; Giaccia, A. J. HIF Targets in Bone Remodeling and Metastatic Disease. *Pharmacol. Ther.* **2015**, *150*, 169–177.

(122) Guelcher, S. A.; Sterling, J. A. Contribution of Bone Tissue Modulus to Breast Cancer Metastasis to Bone. *Cancer Microenviron.* **2011**, *4*, 247–259.

(123) Page, J. M.; Merkel, A. R.; Ruppender, N. S.; Guo, R.; Dadwal, U. C.; Cannonier, S.

A.; Basu, S.; Guelcher, S. A.; Sterling, J. A. Matrix Rigidity Regulates the Transition of Tumor Cells to a Bone-Destructive Phenotype through Integrin Β3 and TGF-β Receptor Type II. *Biomaterials* **2015**, *64*, 33–44.
(124) García-Alvarez, R.; Izquierdo-Barba, I.; Vallet-Regí, M. 3D Scaffold with Effective Multidrug Sequential Release against Bacteria Biofilm. *Acta Biomater.* **2016**, *49*, 113–126.
(125) Sundelacruz, S.; Li, C.; Choi, Y. J.; Levin, M.; Kaplan, D. L. Bioelectric Modulation of Wound Healing in a 3D Invitro Model of Tissue-Engineered Bone. *Biomaterials* **2013**, *34* (28), 6695–6705.
(126) Lee, J. H.; Gu, Y.; Wang, H.; Lee, W. Y. Microfluidic 3D Bone Tissue Model for High-Throughput Evaluation of Wound-Healing and Infection-Preventing Biomaterials. *Biomaterials* **2012**, *33* (4), 999–1006.
(127) Chatterjee, K.; Lin-Gibson, S.; Wallace, W. E.; Parekh, S. H.; Lee, Y. J.; Cicerone, M. T.; Young, M. F.; Simon, C. G. The Effect of 3D Hydrogel Scaffold Modulus on Osteoblast Differentiation and Mineralization Revealed by Combinatorial Screening. *Biomaterials* **2010**, *31* (19), 5051–5062.
(128) Sun, L.; Parker, S. T.; Syoji, D.; Wang, X.; Lewis, J. A.; Kaplan, D. L. Direct-Write Assembly of 3D Silk/Hydroxyapatite Scaffolds for Bone Co-Cultures. *Adv. Healthc. Mater.* **2012**, *1* (6), 729–735.
(129) Bidan, C. M.; Kommareddy, K. P.; Rumpler, M.; Kollmannsberger, P.; Fratzl, P.; Dunlop, J. W. C. Geometry as a Factor for Tissue Growth: Towards Shape Optimization of Tissue Engineering Scaffolds. *Adv. Healthc. Mater.* **2013**, *2* (1), 186–194.
(130) Gamsjager, E.; Bidan, C. M.; Fischer, F. D.; Fratzl, P.; Dunlop, J. W. C. Modelling the Role of Surface Stress on the Kinetics of Tissue Growth in Confined Geometries. *Acta Biomater.* **2013**, *9* (3), 5531–5543.
(131) Sterling, J. A.; Guelcher, S. A. Bone Structural Components Regulating Sites of Tumor Metastasis. *Curr. Osteoporos. Rep.* **2011**, *9* (2), 89–95.
(132) Williams, J. M.; Adewunmi, A.; Schek, R. M.; Flanagan, C. L.; Krebsbach, P. H.; Feinberg, S. E.; Hollister, S. J.; Das, S. Bone Tissue Engineering Using Polycaprolactone Scaffolds Fabricated via Selective Laser Sintering. *Biomaterials* **2005**, *26* (23), 4817–4827.
(133) Petrie Aronin, C. E.; Cooper, J. A.; Sefcik, L. S.; Tholpady, S. S.; Ogle, R. C.; Botchwey, E. A. Osteogenic Differentiation of Dura Mater Stem Cells Cultured in Vitro on Three-Dimensional Porous Scaffolds of Poly(??-Caprolactone) Fabricated via Co-Extrusion and Gas Foaming. *Acta Biomater.* **2008**, *4* (5), 1187–1197.
(134) Guillaume, O.; Geven, M. A.; Sprecher, C. M.; Stadelmann, V. A.; Grijpma, D. W.; Tang, T. T.; Qin, L.; Lai, Y.; Alini, M.; de Bruijn, J. D.; et al. Surface-Enrichment with Hydroxyapatite Nanoparticles in Stereolithography-Fabricated Composite Polymer Scaffolds Promotes Bone Repair. *Acta Biomater.* **2017**.
(135) Gay, S.; Arostegui, S.; Lemaitre, J. Preparation and Characterization of Dense Nanohydroxyapatite/PLLA Composites. *Mater. Sci. Eng. C* **2009**, *29* (1), 172–177.
(136) Grinberg, O.; Binderman, I.; Bahar, H.; Zilberman, M. Highly Porous Bioresorbable Scaffolds with Controlled Release of Bioactive Agents for Tissue-Regeneration Applications. *Acta Biomater.* **2010**, *6* (4), 1278–1287.
(137) Zhang, P.; Wu, H.; Wu, H.; Lù, Z.; Deng, C.; Hong, Z.; Jing, X.; Chen, X. RGD-Conjugated Copolymer Incorporated into Composite of Poly(Lactide-Co-Glycotide)

and Poly(l-Lactide)-Grafted Nanohydroxyapatite for Bone Tissue Engineering. *Biomacromolecules* **2011**, *12* (7), 2667–2680.

(138) Guelcher, S. A. Biodegradable Polyurethanes: Synthesis and Applications in Regenerative Medicine. *Tissue Eng. Part B. Rev.* **2008**, *14* (1), 3–17.

(139) Temenoff, J. S.; Mikos, a G. Injectable Biodegradable Materials for Orthopedic Tissue Engineering. *Biomaterials* **2000**, *21* (23), 2405–2412.

(140) Kim, K.; Dean, D.; Mikos, A. G.; Fisher, J. P. Effect of Initial Cell Seeding Density on Early Osteogenic Signal Expression of Rat Bone Marrow Stromal Cells Cultured on Cross-Linked Poly(Propylene Fumarate) Disks. *Biomacromolecules* **2009**, *10* (7), 1810–1817.

(141) Clarke, B. Normal Bone Anatomy and Physiology. *Clin. J. Am. Soc. Nephrol.* **2008**, *3 Suppl 3*, 131–139.

(142) Chattopadhyay, S.; Raines, R. T. Collagen-Based Biomaterials for Wound Healing. *Biopolymers* **2015**, *101* (8), 821–833.

(143) Reagan, M. R.; Mishima, Y.; Glavey, S. V; Zhang, Y.; Manier, S.; Lu, Z. N.; Memarzadeh, M.; Zhang, Y.; Sacco, A.; Aljawai, Y.; et al. Investigating Osteogenic Differentiation in Multiple Myeloma Using a Novel 3D Bone Marrow Niche Model. *Blood* **2014**, *124* (22), 3250–3259.

(144) Vepari, C.; Kaplan, D. L. Silk as a Biomaterial. *Progress in Polymer Science (Oxford)*. 2007, pp 991–1007.

(145) Thein-Han, W.; Xu, H. H. K. Prevascularization of a Gas-Foaming Macroporous Calcium Phosphate Cement Scaffold via Coculture of Human Umbilical Vein Endothelial Cells and Osteoblasts. *Tissue Eng. Part A* **2013**, *19* (15–16), 1675–1685.

(146) Annabi, N.; Fathi, A.; Mithieux, S. M.; Martens, P.; Weiss, A. S.; Dehghani, F. The Effect of Elastin on Chondrocyte Adhesion and Proliferation on Poly (E{open}-Caprolactone)/Elastin Composites. *Biomaterials* **2011**, *32* (6), 1517–1525.

(147) Akar, B.; Jiang, B.; Somo, S. I.; Appel, A. A.; Larson, J. C.; Tichauer, K. M.; Brey, E. M. Biomaterials with Persistent Growth Factor Gradients in Vivo Accelerate Vascularized Tissue Formation. *Biomaterials* **2015**, *72*, 61–73.

(148) Zhang, J.; Zhou, H.; Yang, K.; Yuan, Y.; Liu, C. RhBMP-2-Loaded Calcium Silicate/Calcium Phosphate Cement Scaffold with Hierarchically Porous Structure for Enhanced Bone Tissue Regeneration. *Biomaterials* **2013**, *34* (37), 9381–9392.

(149) Fereshteh, Z.; Fathi, M.; Bagri, A.; Boccaccini, A. R. Preparation and Characterization of Aligned Porous PCL/Zein Scaffolds as Drug Delivery Systems via Improved Unidirectional Freeze-Drying Method. *Mater. Sci. Eng. C* **2016**, *68*, 613–622.

(150) Vanderburgh, J.; Sterling, J. A.; Guelcher, S. A. 3D Printing of Tissue Engineered Constructs for In Vitro Modeling of Disease Progression and Drug Screening. *Annals of Biomedical Engineering*. 2017, pp 164–179.

(151) Lee, S.-J.; Nowicki, M.; Harris, B.; Zhang, L. G. Fabrication of a Highly Aligned Neural Scaffold via a Table Top Stereolithography 3D Printing and Electrospinning. *Tissue Eng. Part A* **2016**, *00* (00), ten.TEA.2016.0353.

(152) Li, G.; Cuidi, L.; Fangping, C.; Changsheng, L. Fabrication and Characterization of Toughness-Enhanced Scaffolds Comprising Beta-TCP/POC Using the Freeform Fabrication System with Micro-Droplet Jetting. *Biomed. Mater.* **2015**, *10* (3), 035009 (10 pp.)-035009 (10 pp.).

(153) Bancroft, G. N.; Sikavitsas, V. I.; van den Dolder, J.; Sheffield, T. L.; Ambrose, C.

G.; Jansen, J. A.; Mikos, A. G. Fluid Flow Increases Mineralized Matrix Deposition in 3D Perfusion Culture of Marrow Stromal Osteoblasts in a Dose-Dependent Manner. *Proc. Natl. Acad. Sci. U. S. A.* **2002**, *99* (20), 12600–12605.

(154) Krishnan, V.; Vogler, E. A.; Mastro, A. M. Three-Dimensional in Vitro Model to Study Osteobiology and Osteopathology. *J. Cell. Biochem.* **2015**, *116* (12), 2715–2723.

(155) Talukdar, S.; Nguyen, Q. T.; Chen, A. C.; Sah, R. L.; Kundu, S. C. Effect of Initial Cell Seeding Density on 3D-Engineered Silk Fibroin Scaffolds for Articular Cartilage Tissue Engineering. *Biomaterials* **2011**, *32* (34), 8927–8937.

(156) Talukdar, S.; Kundu, S. C. Engineered 3D Silk-Based Metastasis Models: Interactions between Human Breast Adenocarcinoma, Mesenchymal Stem Cells and Osteoblast-like Cells. *Adv. Funct. Mater.* **2013**, *23* (42), 5249–5260.

(157) Mastro, A. M.; Gay, C. V.; Welch, D. R.; Donahue, H. J.; Jewell, J.; Mercer, R.; DiGirolamo, D.; Chislock, E. M.; Guttridge, K. Breast Cancer Cells Induce Osteoblast Apoptosis: A Possible Contributor to Bone Degradation. *J. Cell. Biochem.* **2004**, *91* (2), 265–276.

(158) Subia, B.; Dey, T.; Sharma, S.; Kundu, S. C. Target Specific Delivery of Anticancer Drug in Silk Fibroin Based 3D Distribution Model of Bone-Breast Cancer Cells. *ACS Appl. Mater. Interfaces* **2015**, *7* (4), 2269–2279.

(159) Lynch, M. E.; Chiou, A. E.; Lee, M. J.; Marcott, S. C.; Polamraju, P. V.; Lee, Y.; Fischbach, C. Three-Dimensional Mechanical Loading Modulates the Osteogenic Response of Mesenchymal Stem Cells to Tumor-Derived Soluble Signals. *Tissue Eng. Part A* **2016**, *22* (15–16), 1006–1015.

(160) Zhu, W.; Holmes, B.; Glazer, R. I.; Zhang, L. G. 3D Printed Nanocomposite Matrix for the Study of Breast Cancer Bone Metastasis. *Nanomedicine Nanotechnology, Biol. Med.* **2016**, *12* (1), 69–79.

(161) Wang, Y.; Pivonka, P.; Buenzli, P. R.; Smith, D. W.; Dunstan, C. R. Computational Modeling of Interactions between Multiple Myeloma and the Bone Microenvironment. *PLoS One* **2011**, *6* (11), e27494.

(162) Araujo, A.; Cook, L. M.; Lynch, C. C.; Basanta, D. An Integrated Computational Model of the Bone Microenvironment in Bone-Metastatic Prostate Cancer. *Cancer Res.* **2014**, *74* (9), 2391–2401.

CHAPTER 3

III. FABRICATION OF TRABECULAR BONE-TEMPLATED TISSUE-ENGINEERED CONSTRUCTS BY 3D INKJET PRINTING AND INCORPORATION INTO PERFUSION BIOREACTOR MODEL OF TIBD

3.1. Fabrication of Trabecular Bone-Templated Tissue-Engineered Constructs by 3D Inkjet Printing

Adapted from:
Vanderburgh, JP, Fernando, SJ, Merkel, AR, Sterling, JA, Guelcher, SA. "Fabrication of Trabecular Bone-Templated Tissue-Engineered Constructs by 3D Inkjet Printing." *Adv Healthc Mater*. 2017;6(22):1700369.

3.1.1. Abstract

3D printing enables the creation of scaffolds with precisely controlled morphometric properties for multiple tissue types, including musculoskeletal tissues such as cartilage and bone. Computed tomography (CT) imaging has been combined with 3D printing to fabricate anatomically scaled patient-specific scaffolds for bone regeneration. However, anatomically scaled scaffolds typically lack sufficient resolution to recapitulate the <100 micrometer-scale trabecular architecture essential for investigating the cellular response to the morphometric properties of bone. In this study, it is hypothesized that the architecture of trabecular bone regulates osteoblast differentiation and mineralization. To test this hypothesis, human bone-templated 3D constructs are fabricated via a new micro-CT/3D inkjet printing process. It is shown that this process reproducibly fabricates bone-templated constructs that recapitulate the anatomic site-specific morphometric properties of trabecular bone. A significant

correlation is observed between the structure model index (a morphometric parameter related to surface curvature) and the degree of mineralization of human mesenchymal stem cells, with more concave surfaces promoting more extensive osteoblast differentiation and mineralization compared to predominately convex surfaces. These findings highlight the significant effects of trabecular architecture on osteoblast function.

3.1.2. Introduction

The development of three-dimensional (3D) *in vitro* drug screening tools and disease models offers the potential to significantly advance fundamental understanding of disease, drug discovery, and patient-specific precision medicine.[1–5] Recent advances in 3D fabrication techniques have enabled studies on how properties such as matrix rigidity, surface chemistry, porosity, and curvature contribute to molecular mechanisms involved in disease progression.[6–9] Additive manufacturing (AM), also known as 3D printing or rapid prototyping, offers the advantage of creating 3D objects with precisely controlled geometries and topological properties for multiple tissue types, including musculoskeletal tissues such as cartilage and bone. Properties of the bone microenvironment, including matrix rigidity[7], surface curvature, and pore geometry[6,10], regulate bone cell activity and the bone remodeling process that can be disrupted in a diseased state, which highlights the need to recapitulate the physicochemical, mechanical, and morphometric properties of bone in tissue-engineered models. In this work, we hypothesized that the anatomic site-specific architecture of trabecular bone regulates osteoblast differentiation and mineralization. To test this hypothesis, we fabricated human bone-templated 3D constructs via a new micro-computed tomography (μCT)/3D inkjet printing process. We show that this process reproducibly fabricates tissue-engineered bone constructs (TEBCs) that recapitulate the anatomic site-specific morphometric and mechanical properties of trabecular bone. A significant correlation was observed between the Structure Model Index (SMI, a morphometric parameter related to surface curvature) and the degree of mineralization of human mesenchymal stem cells (hMSCs), with more concave surfaces promoting more extensive osteoblast differentiation and mineralization compared to predominately convex surfaces.

Recent studies have combined CT imaging with AM to fabricate patient-specific bone scaffolds at the anatomic scale. These studies highlight the potential of AM for fabricating anatomically-scaled bone scaffolds with tissue-matched mechanical properties that incorporate multiple cell types and integrate with host tissue in animal models.[11–14] However, anatomically-scaled 3D-printed scaffolds typically lack sufficient resolution to recapitulate the <100 micron-scale trabecular architecture essential for investigating the cellular response to the morphometric properties of bone. A limited number of recent studies utilizing 3D-printed scaffolds with controlled microstructure have reported that matrix rigidity, pore size, and pore shape regulate angiogenesis and osteogenesis *in vitro*.[7,15–19] However, the effects of the anatomic site-specific morphometric properties of trabecular bone on osteoblast activity have not been investigated. Bone-templated scaffolds must also be fabricated from biomaterials that support bone cell function, which is challenging due to the limited number of substrates that can be printed.[20,21] In this study, we used a templating approach in which 3D-printed wax molds were filled with a reactive, flowable, and settable poly(ester urethane)-nanocrystalline hydroxyapatite (PUR-nHA) hybrid polymer with bone-like strength. We have shown that this organic-inorganic hybrid polymer promotes osteoblast differentiation and mineralization, supports osteoclast-mediated resorption, and remodels to form new bone *in vivo*.[22,23]

3.1.3. Materials and Methods

Fabrication of TEBCs from Micro-computed Tomography Images: Human cadaver samples of the femoral head, proximal tibia, and vertebral body obtained from the Vanderbilt Anatomical Donation Program were scanned in a Scanco® μCT50. Resulting image files were then inverted and converted to STL files using Scanco® Image Processing Language (IPL). STL files were subsequently converted to Solidscape® 3Z Analysis software-compatible files and sent to a Solidscape® 3Z Studio Inkjet 3D printer to print a mold from the build material wax, a proprietary blend of sulfonamide derivatives. The resulting wax molds were submerged in leaching oil (Bioact VSO) to remove the support material, leaving behind the finished trabecular bone molds. The bone molds were then filled with a PUR-nHA hybrid composite material consisting of lysine diisocyanate (LDI)-grafted nHA and poly(caprolactone) triol (300 g mol^{-1}, Sigma) to yield a PUR-nHA network upon addition of FeAA catalyst, mixing, and curing at 50°C overnight. The wax mold was then leached from the PUR-nHA TEBCs by immersion in acetone. 2D PUR-nHA films with layer thicknesses representative of the 3D inkjet printer were cast into printed flat molds, cured, and leached in the same manner as previously described. TEBCs were soaked in ethanol overnight and placed under UV light for 30 minutes to sterilize prior to cell culture.

Contact Angle: Static water contact angle of 2D PUR-nHA films with characteristic 3D-printed surface roughness were compared to that of dentin using a contact angle goniometer. Contact angle was measured in 4 different locations on each film, and average values were calculated and compared between groups.

Mechanical Testing: TEBCs were tested in uniaxial compression mode using an Instron DynaMight 8800 Servohydraulic Test System (Norwood, MA) and operated in accordance with ASTM standard D695. The displacement rate was kept at a constant 1.3 mm/min, and compression was continued until failure.

Cell Culture: hMSCs (Extem Biosciences) were maintained in Mesenchymal Stem Cell Growth Medium 2 (PromoCell). Cells were detached at confluency by trypsin EDTA (Ethylenediaminetetraacetic acid, 0.25%) and resuspended at 1.67x10^6 cells mL^{-1} in same medium and seeded on TEBCs (30 µL scaffold^{-1}) pre-soaked in fibronectin solution (4 µg mL^{-1}) at 4°C for 24 h. After seeding, TEBCs were incubated for 3 h (5% CO_2 and 37 °C) in 96-well plates before moving to new wells and adding 200 µL complete medium to facilitate cell attachment to the surface. Cell metabolism was measured by MTS Tetrazolium assay (CellTiter 96 Aqueous Non-Radioactive Cell Proliferation Assay, Promega). Absorbance values measured at optical density (OD) 490 nm were normalized to values measured for the t-FDM scaffolds on day 1 and reported as fold-change.

Osteogenic Gene Expression: hMSCs were seeded on TEBCs as described previously and cultured in Mesenchymal Stem Cell Growth Medium 2 (PromoCell) for 3 days, at which time the media was changed to osteogenic differentiation media (PromoCell). TEBCs were removed and immersed in 1 mL TRIzol (ThermoFisher) at D3, D5, and D8 after transfer to differentiation medium. RNA was isolated from TRIzol reagent by phase separation by addition of chloroform and subsequent RNA precipitation via addition of isopropanol. The resulting RNA pellet was washed in 70% ethanol, air-dried, and re-suspended in RNAse-free water. cDNA was synthesized from purified total RNA via iScript Reverse Transcription Supermix (Biorad). qPCR (Quant Studio 5, ThermoFisher) was used to assess expression of the osteogenic genes *ALP* and *OPN*. *ALP* (Hs01029144_m1) and *OPN* (Hs00959010_m1) primers were purchased from ThermoFisher. All reactions were run in triplicate and expression levels of *ALP* and *OPN* were normalized to 18s (ThermoFisher).

Mineralization: TEBCs seeded with hMSCs as described previously were cultured in osteogenic media for up to 10 days. They were then washed with phosphate-buffered saline (PBS, Thermofisher), fixed in 10% formalin for 45 min, and stained with 20 mM Alizarin Red S for 5 min. After staining, TEBCs were washed ten times with DI water, and Alizarin Red S was extracted with 5% sodium dodecyl sulfate (SDS) for 1 hr. Absorbance of the extracted dye was read on a plate reader (OD, optical density = 540 nm), and dye extracted from cell-free TEBCs served as blank controls. For SEM, TEBCs were fixed in 5% glutaraldehyde, washed with DI water, fixed in 2% osmium tetraoxide, and subsequently dried in increasing concentrations of ethanol and vacuum dried overnight. Samples were then cut to expose a variety of surfaces and mounted on a stub covered with carbon tape. Samples were gold sputter-coated (108 Auto Sputter Coater; TedPella, Redding, CA) and imaged using scanning electron microscopy (Carl Zeiss Inc, Thornwood, NY). Mineral nodule clusters were counted (> 50 clusters from > 20 SEM images) and characterized for average diameter using ImageJ software.

Statistical Analysis: The statistical analysis was performed by a one- or two-way analysis of variance (ANOVA). Graphs report the mean and standard deviation unless indicated otherwise. $P < 0.05$ is considered statistically significant with $n \geq 3$ for all experiments. All statistical analysis was performed using Prism 7 software.

3.1.4. Results and Discussion

TEBCs were fabricated by a process utilizing μCT technology in tandem with a Solidscape® 3Z Studio inkjet 3D printer (**Figure 3.1A**). Human cadaver samples of the femoral head (FH), proximal tibia (PT), and vertebral body (VB) were scanned by μCT and the images inverted and converted to the STL file format compatible with the 3D printer. These three anatomic sites exhibit different morphometric properties, thereby enabling testing of the hypothesis that the surface curvature of trabecular bone regulates hMSC proliferation, differentiation, and mineralization. Specific sites within the cadaver specimens were chosen such that the morphometric parameters were within the range of previously established literature values for each anatomic site.[24] A reactive polyurethane-hydroxyapatite (PUR-nHA) hybrid composite composed of lysine methyl ester diisocyanate (LDI), nanocrystalline hydroxyapatite (nHA), polycaprolactone triol (PCL 300), and iron catalyst (5% iron acetylacetonate (FeAA) in ε-caprolactone), was poured into and drawn through the 3D wax templates under vacuum. The resulting hybrid polymer consisted of 52 wt% nHA, which falls in the range of the hydroxyapatite component of bone (50-70 wt%).[25] After curing overnight at 50°C, the wax was leached from the TEBCs by immersion in acetone and the resulting PUR-nHA scaffolds scanned by μCT to assess their similarity to the host bone template (**Figure 3.1B-C**). The bone morphometric parameters Bone Volume/Total Volume (BV/TV), Trabecular Separation (Tb.Sp.), Trabecular Number (Tb.N.), and Structure Model Index (SMI) were calculated for the host bone templates and the printed TEBCs (**Figure 3.1C**). Structure model index is a measure of the relative prevalence of plates (SMI = 0) versus rods (SMI = 3)[26] and is thus a measure of surface convexity, since regions of bone containing enclosed cavities can have negative SMI values. Bone morphometric parameters for the host bone and TEBCs followed similar trends. Furthermore, TEBCs printed from different anatomic sites showed significant differences ($p < 0.0001$) in morphometric parameters as determined by one-way ANOVA.

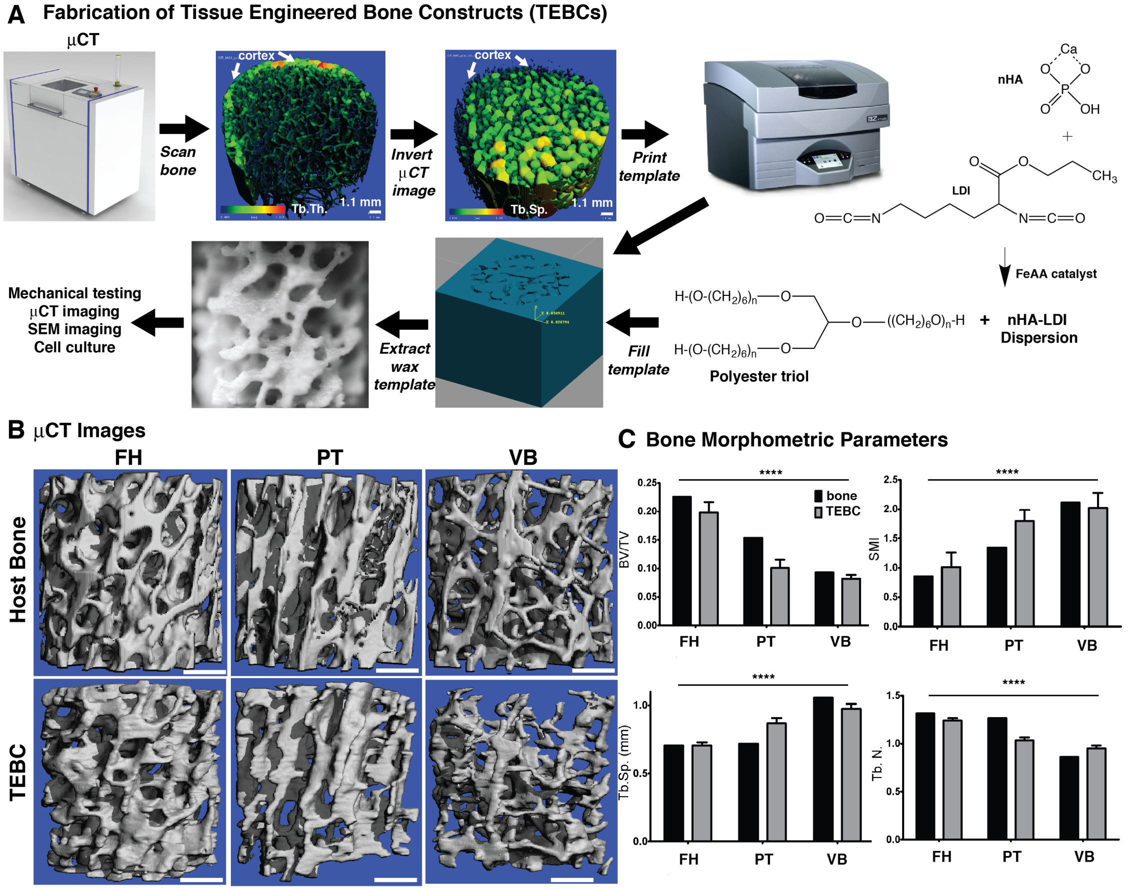

Figure 3.1. Bone-templated constructs recapitulate the morphometric properties of human bone. (A) Micro-computed tomography (µCT) images of human bone samples from three anatomical sites were inverted, segmented, converted to .stl files, and printed by a Solidscape® 3Z Studio inkjet printer to create wax template of human trabecular bone. Lysine methyl ester diisocyanate (LDI) was mixed with hydroxyapatite nanoparticles (nHA) and iron acetylacetonate (FeAA) catalyst to form an nHA-LDI dispersion that was subsequently mixed with a polyester triol and poured into the wax templates. After curing overnight, the wax templates were dissolved in acetone and the resulting constructs were washed in ethanol and subsequently DI water prior to characterization and cell culture. (B) µCT images of the femoral head (FH), proximal tibia (PT), and vertebral body (VB) human bone templates (top row) and the TEBCs (bottom row). Scale bar represents 1 mm. (C) The morphometric parameters bone volume density (BV/TV), structure model index (SMI), trabecular separation (Tb. Sp.), and trabecular number (Tb. N.) were measured for host bone and TEBCs by µCT. **** denotes statistical significance ($p < 0.0001$) measured by one-way ANOVA ($n = 8$).

Scanning electron microscopy (SEM) was used to image trabecular interconnectivity and surface roughness of the TEBCs (**Figure 3.2A**). SEM images revealed the presence of curved and interconnected trabeculae. Parallel ridges ~25 µm apart were also observed, which were conjectured to result from the layer-by-layer fabrication of the wax templates. Optical profilometry was used to measure surface roughness compared to a dentin control (**Figure 3.2B**). Dentin was chosen as a control due to its frequent use as a bone-like substrate for *in vitro* cell culture as well as its more reproducible surface properties compared to cortical bone.[27–29] Flat molds were created using CAD software to allow for the printing of 2D PUR-nHA discs with layer thickness (and therefore surface roughness) comparable to that of the 3D TEBCs. The average surface roughness and water contact angle of the PUR-nHA films did not significantly differ from those of dentin, suggesting that the surface properties of the TEBCs are similar to those of bone (Fig. 2C). Fibronectin adsorption was significantly (two-fold) higher on dentin compared to the PUR-nHA film (**Figure 3.2C**), which may be due to the absence of a collagen component in PUR-nHA.[30] Bulk modulus, compressive strength, and yield strain of the TEBCs were measured by quasi-static mechanical testing in compression mode using an Instron® Testing System. Force-displacement curves were obtained from quasi-static compression testing of FH-, PT-, and VB-TEBCs and converted to stress-strain curves to determine bulk modulus, compressive strength, and yield strain (**Figure 3.2D**). The bulk modulus of FH-TEBCs was within the range of values reported for trabecular bone from the proximal femur (21 – 965 MPa[31]) and significantly higher that of PT- and VB-TEBCs (**Figure 3.2E**). The bulk moduli of PT- and VB-TEBCs were comparable to trabecular bone from the proximal tibia (5 – 552 MPa) and vertebral bodies (1.1 – 428 MPa).[31] Since substrate modulus (E_s) could not be directly measured, it was calculated from the bulk modulus of each TEBC (K), polymer density ($\rho_s = 1.76$ g cm^{-3}), and TEBC bulk density (ρ):[32]

$$E_s = \frac{K}{\left(\rho / \rho_s\right)^2} \qquad (1)$$

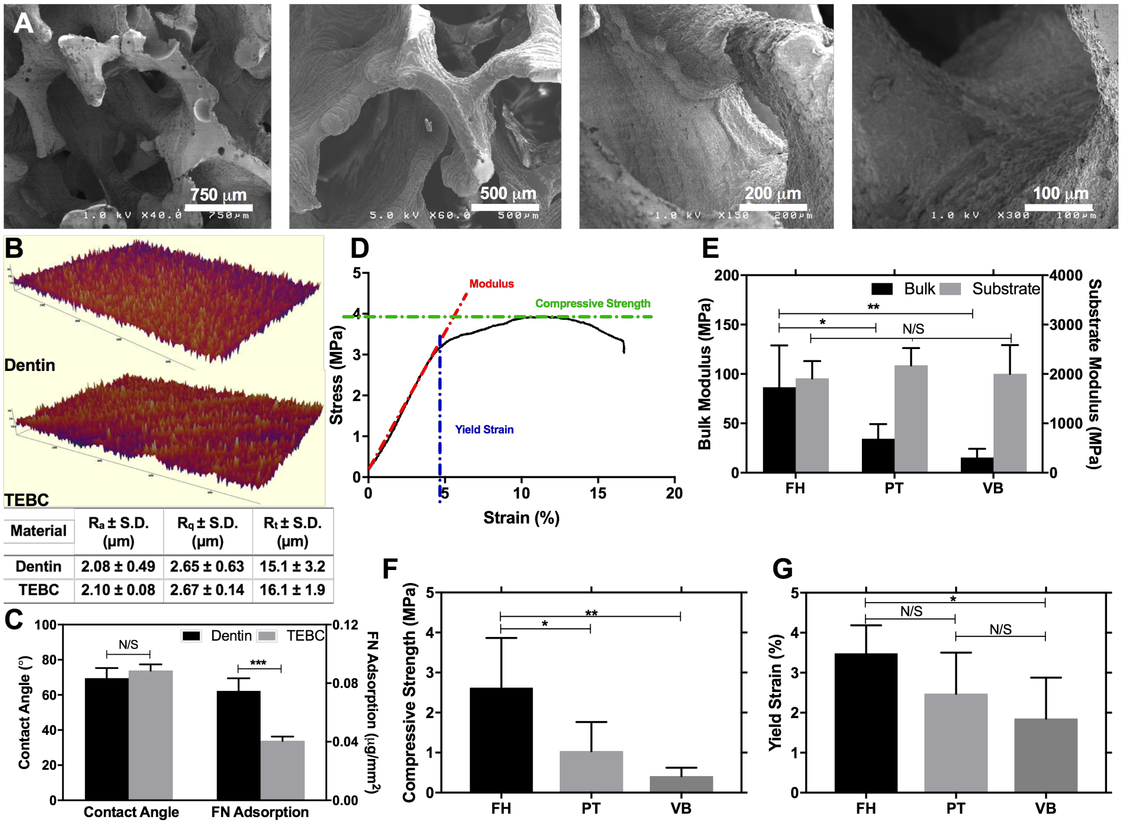

Material	R_a ± S.D. (µm)	R_q ± S.D. (µm)	R_t ± S.D. (µm)
Dentin	2.08 ± 0.49	2.65 ± 0.63	15.1 ± 3.2
TEBC	2.10 ± 0.08	2.67 ± 0.14	16.1 ± 1.9

Figure 3.2. TEBCs recapitulate the surface and mechanical properties of human bone. (A) Representative SEM images of the TEBC trabecular structure at increasing magnification from left to right. (B) Optical profilometer topographical maps of dentin and TEBC surface (axes in µm) and comparison of surface roughness between dentin and TEBC. Arithmetic average roughness (R_a), quadratic average roughness (Rq) and max roughness height (R_t) were calculated from the optical profilometry data. (C) Water contact angle (measured by contact angle goniometer) and fibronectin adsorption on TEBCs compared to dentin control. (D) Example stress-strain curve of TEBCs under quasi-static compression testing. Elastic modulus, compressive strength, and yield strain were calculated as indicated. (E) Bulk (left y-axis) and substrate (right y-axis) moduli of TEBCs measured for each anatomic site. (F) Compressive strength and (G) yield strain of TEBCs templated from trabecular bone from different sites. ** ($p < 0.01$) and * ($p < 0.05$) denote statistical significance determined by one-way ANOVA ($n = 4$).

The calculated substrate moduli exhibited no significant differences between anatomic sites (**Figure 3.2E**) and exceeded values measured for trabecular bone by nanoindentation (365±223 MPa).[31,33] This result suggests that the templating process does not adversely affect the microstructure of the PUR-nHA hybrid polymer, since the substrate modulus is independent of morphometric properties. Compressive strength (**Figure 3.2F**) showed similar trends to that of the bulk modulus, with the femoral head exhibiting the highest compressive strength (~3 MPa), and all TEBCs falling within the range of reported compressive strength of trabecular bone (0.2 - 15 MPa). While yield strain followed similar trends (**Figure 3.2G**), statistical significance was only observed between FH- and VB-TEBCs. Yield strains also fell within reported measurements of human bone and the specific anatomic sites (0.3-3%).[34]

Cell culture experiments were performed to assess the ability of the TEBCs to support hMSC proliferation and osteogenic differentiation and determine the effects of morphometric properties on cell behavior. hMSCs were suspended in growth medium (PromoCell), seeded on scaffolds in 30 μL droplets (5×10^4 cells per TEBC), allowed to adhere for 3 hours prior to immersion in media, and cultured at 37°C for 24 h. Adherent cells were fixed and imaged by SEM, which showed cells attached and spread on all three anatomic sites. The MTS metabolic assay was conducted to compare cell proliferation and activity on the different TEBCs as well as 3D t-FDM scaffolds (**Figure 3.3A**), which were used as a control due to their controlled pore size and geometry (**Figure 3.3H**). Metabolic activity increased across all groups over a 5-day period; however, there were significant differences in activity between the groups. Metabolic activity was higher for anatomic sites with lower BV/TV, higher SMI, and higher Tb.Sp. (PT- and VB-TEBCs), with the PT-TEBCs showing significantly higher activity compared to FH-TEBCs and t-FDM scaffolds at all three time points. These findings suggest that the morphometric properties of trabecular bone regulate proliferation of osteoprogenitor cells.

Osteogenic differentiation of hMSCs was assessed by measuring expression of osteogenic genes using quantitative real-time PCR (polymerase chain reaction). Gene expression was assessed on D3, D5, and D8 after transfer to osteogenic differentiation medium (PromoCell) for the early marker of osteoblast differentiation alkaline phosphatase (*ALP)* and late-stage marker osteopontin (*OPN*) to investigate how morphometric properties regulate osteogenic differentiation. *ALP* expression significantly increased on D8 for hMSCs seeded on the more rod-like (more convex) PT- and VB-TEBCs, while those cultured on the more plate-like (less convex) FH-TEBCs and t-FDM scaffold showed decreasing *ALP* expression from D5 to D8 (**Figure 3.3B**). The late increase in *ALP* expression on the more rod-like PT- and VB-TEBCs compared to the more plate-like FH-TEBCs suggests that osteogenic differentiation is delayed for cells seeded on scaffolds with more convex surfaces. The late-stage marker *OPN* peaked at D8 for all constructs, indicating that the cells are approaching osteoblast maturation (**Figure 3.3C**).[35] Furthermore, the largest fold change was observed for the t-FDM scaffolds. Concentrations of secreted osteocalcin (OCN), another late-stage osteoblast marker, were measured by ELISA (enzyme-linked immunosorbent assay) to further assess differences in osteogenic differentiation between anatomic sites (**Figure 3.3D**). A significant increase in OCN concentration was observed for VB-TEBCs on D8, while the other groups showed a decreasing trend by D8. This observation is in agreement with the *ALP* expression data suggesting that hMSCs cultured on the more convex VB-TEBCs exhibit delayed osteogenic differentiation compared to the less convex t-FDM scaffolds and FH-TEBCs.

Matrix mineralization was assessed to investigate how morphometric properties regulate osteoblast activity. Matrix mineralization after 7 and 10 days of culture in osteogenic medium was assessed by SEM (**Figure 3.3E**). D7 images indicate that cells are depositing matrix, but mineral nodules were observed only on t-FDM scaffolds and not the TEBCs. By D10, the SEM images exhibited extensive mineral nodules on t-FDM scaffolds and TEBCs. A representative high-magnification image of a nodule is shown in **Figure 3.3F**, from which the average diameter was measured and compared to literature values. The average nodule size was found to be 8.7 ± 6.4 μm, which is within the reported range of nodule sizes (~10 μm) at the early stages of mineralization.[36] To provide further evidence of mineralization, TEBCs were stained on D7 and D10 by Alizarin Red, which reacts with calcium to form an Alizarin Red S-calcium complex. Cells were fixed in 10% formalin, stained, and extracted with 5% SDS (sodium dodecyl sulfate) detergent to recover the stain. Absorbance of the extract was measured at 540 nm. As indicated by Alizarin Red absorbance, mineralization of t-FDM scaffolds on D7 was significantly higher ($p < 0.0001$) compared to the other groups, which showed minimal absorbance (**Figure 3.3G**). On D10, significant differences in mineralization were observed over time and between anatomic sites. From D7 to D10, significant increases in absorbance were observed for all groups except the VB-TEBCs, and the D10 absorbance was significantly different between each of the groups except the PT-TEBCs and VB-TEBCs ($p = 0.069$). These observations suggest that mineralization occurred between D7 and D10 for the TEBCs and that the degree of mineralization by D10 is dependent on scaffold architecture. Thus, the Alizarin Red staining data are consistent with the SEM images. Interestingly, mineralization on D10 (assessed by Alizarin Red absorbance) decreased significantly ($p < 0.01$) with increasing SMI (**Figure 3.3H**). SEM images of t-FDM scaffolds revealed the presence of completely enclosed concave pores (**Figure 3.3I**). Consequently, the SMI of t-FDM scaffolds is close to zero as anticipated for structures with enclosed cavities.[26,37] The observed increases in osteoblast differentiation and mineralization with decreasing surface convexity is consistent with previous studies reporting that the rate of new tissue formation on concave surfaces is significantly larger compared to convex or planar surfaces.[38–40] While earlier studies have shown that surface curvature regulates osteogenesis *in vitro*[41] and *in vivo*[42], the effects of the anatomic site-specific morphometric properties of human trabecular bone on osteogenic differentiation have not been previously reported.

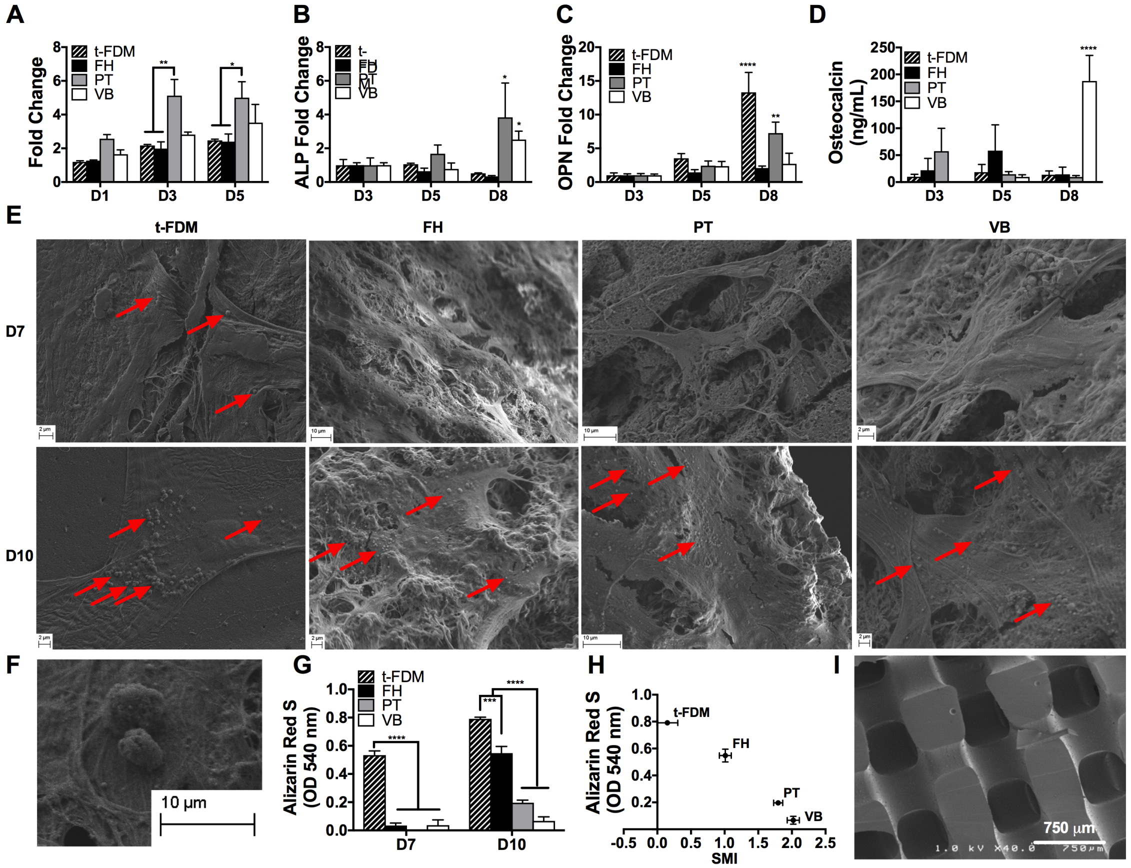

Figure 3.3. Human bone marrow-derived stem cells (hMSCs) attach, proliferate, and differentiate toward an osteoblastic phenotype on TEBCs. (A) hMSCs were cultured on TEBCs for up to 5 days and metabolic activity determined by the MTS assay. Data are plotted as fold-change in absorbance at an optical density (OD) of 490 nm. (B-C) Expression of (B) *ALP* (early osteoblast marker) and (C) *OPN* (late osteogenic marker) measured by qRT-PCR for hMSCs cultured on TEBCs for up to 8 days. (D) Concentration of secreted osteocalcin (measured by ELISA) for hMSCs cultured on TEBCs for up to 8 days. (E) SEM images of hMSCs cultured in osteogenic medium for 7 days (top row) show adherent cells and mineral nodules (red arrows) on t-FDM constructs, but no mineral nodules were observed on the TEBCs. At day 10 (bottom row), all scaffolds showed evidence of mineralization. (F) Representative SEM image of mineral nodule on t-FDM scaffolds on day 10. (G) Absorbance of the Alizarin Red dye extracted from the mineralizing matrix on days 7 and 10. (H) Correlation of the degree of mineralization (assessed by Alizarin Red absorbance on day 10) with structure model index (SMI) of the TEBCs (Pearson's correlation coefficient; $r = -0.9916$, $p < 0.01$). (I) Low-magnification images of t-FDM scaffolds reveal the presence of enclosed cavities. All graphs show mean and SEM. * ($p < 0.05$), ** ($p < 0.01$), *** ($p < 0.001$), **** ($p < 0.0001$) determined by two-way ANOVA ($n = 3$).

3.1.5. Conclusion

In summary, we report a new 3D inkjet printing process to fabricate anatomic site-specific TEBCs that recapitulate the morphometric and mechanical properties of human trabecular bone. Similar to bone, TEBCs comprised > 50% nanocrystalline hydroxyapatite. The morphometric parameters BV/TV, Tb.Sp., Tb.N. and SMI of TEBCs were comparable to the bone templates from which they were fabricated. Bulk modulus, compressive strength, and yield strain of the TEBCs were within the range of human bone, and the surface roughness was comparable to that of dentin. hMSCs cultured on TEBCs exhibited significantly different metabolic activities, osteogenic differentiation, and mineralization depending on the anatomic site. Proliferation increased with decreasing BV/TV and increasing Tb.Sp., while differentiation and mineralization increased with increasing BV/TV and decreasing Tb.Sp. The SMI, a measure of surface convexity, was identified as an important predictor of osteoblast mineralization. Taken together, these findings highlight the relative contribution of anatomic site-specific properties to osteoblast differentiation and mineralization, thereby supporting the need for anatomically relevant *in vitro* models. By recapitulating the morphometric properties of trabecular bone at specific anatomic sites in individual patients, bone-templated TEBCs will potentially provide a new platform technology for precision medicine approaches to treating diseases of the skeleton.

3.2. Incorporation of TEBCs into Perfusion Bioreactor Model

3.2.1. Introduction

Many cancer patients experience tumor-induced bone disease (TIBD). When cancer metastasizes to bone, patients experience an increased risk of pathologic fracture, a reduction in mobility, and severe bone pain.[43] Unfortunately, it is not currently possible to predict which tumors will metastasize nor how these tumors will respond to therapeutics. Conventional two-dimensional (2D) well-plate cell culture and animal models have been critical in understanding the underlying mechanisms that contribute to human disease, including TIBD. However, traditional 2D cell culture techniques are often unable to capture the complex 3D tissue microenvironment that is known to interact with cells and affect disease progression.[15] Animal models, on the other hand, are able to better recapitulate human tissue, however genetic and phenotypic differences between animal and human tissue thwart efficient clinical translatability. Therefore, there remains a compelling need for 3D *in vitro* models that can bridge the gap between traditional 2D cell culture and animal models.

In this work, we incorporate the TEBCs into a perfusion bioreactor with a coculture of human osteoblasts, osteoclasts, and tumor cells to recapitulate the human bone-tumor microenvironment and tumor-induced bone resorption *in vitro.* After establishing proof-of-concept trials on 2D discs comprising the composite nHA-PUR material used in the TEBCs, relevant cell populations were seeded on TEBCs and incorporated into a perfusion bioreactor for 30 days. We hypothesized that a coculture with bone cells and tumor would lead to significant TEBC resorption after 30 days of perfusion culture compared to TEBCs cultured with only bone cells.

3.2.2. Materials and Methods

Cell lines and reagents: Bone-metastatic variants of the human breast cancer cell line MDA-MB-231 were generated in our laboratory as previously published.[44–46] RAW264.7 and MC3T3-E1 cells were purchased from ATCC. MDA-MB-231-bone clones and RAW264.7 cells were maintained in DMEM (Cellgro) and MC3T3-E1 cells maintained in α-MEM (Cellgro), supplemented with 10% fetal bovine serum (FBS; Hyclone Laboratories) and 1% penicillin/streptomycin (P/S; Mediatech). Human mesenchymal stem cells (hMSCs; Extem Biosciences) were maintained in Mesenchymal Stem Cell Growth Medium 2 (PromoCell). All other reagents were purchased from Sigma Aldrich (St. Louis, MO, USA) unless otherwise specified.

Synthesis of PUR-nHA discs: PUR-nHA hybrid composite material consisting of lysine diisocyanate (LDI)-grafted nHA and poly(caprolactone) triol (300 g mol^{-1}, Sigma) were poured into cylindrical mixing cups to yield a PUR-nHA network upon addition of FeAA catalyst, mixing, and curing at 50°C overnight. The cylinder was then cut on a low speed saw (Buehler IsoMet) to create discs of PUR-nHA material.

2D PUR-nHA coculture: PUR-nHA discs were sterilized by soaking in 70% ethanol overnight and exposure to UV light for 30 min. Discs were then soaked in fibronectin (5 μg/mL) for 4 hours prior to cell seeding. MC3T3-E1 cells were seeded onto PUR-nHA discs at 50,000 cells/disc in α-MEM supplemented with ascorbic acid (50 μg/mL), dexamethasone (10 nM) and β-glycerophosphate (10 mM) for one week to allow for osteoblast differentiation. RAW264.7 cells were then seeded onto discs at 50,000 cells/disc in same osteogenic differentiation media. 48 hr after RAW264.7 introduction, MDA-MB-231 cells were added to one cohort of discs at 10,000 cells/disc. The cells were then cultured for 28 days with media changes once every 3 days. At the end of the experiment, discs were removed from culture and sonicated for 2 min in 0.25 M ammonium hydroxide to remove cells.

Resorption pitting analysis: Resorption pitting was observed by toluidine blue staining and scanning electron microscopy (SEM). For toluidine blue stain, discs were stained for 5 min in 0.05% toluidine blue in 40% methanol and air-dried. Discs were then observed on a stereoscope (Leica) for dark blue stains indicating pits. For SEM, discs were dehydrated in increasing concentrations of ethanol and allowed to air dry overnight. Discs were then gold sputter-coated (108 Auto Sputter Coater; TedPella, Redding, CA) and imaged using scanning electron microscopy (Carl Zeiss Inc, Thornwood, NY).

Gravimetric resorption analysis: Discs were weighed after vacuum drying overnight on an analytical balance prior to cell-seeding and the initial disc mass was recorded. After cell culture and subsequent cell-removal, discs were vacuum-dried and weighed again on an analytical balance. The mass difference before and after cell culture was then calculated.

Generation of human osteoclasts from peripheral blood: Human osteoclasts (hOC) were generated from discarded, de-identified blood samples as previously described.[47] Briefly, peripheral blood mononuclear cells (PBMCs) were separated from peripheral blood via Ficoll-Paque (GE Healthcare) separation per manufacturer instructions. PBMCs were then cultured in α-MEM supplemented with M-CSF (25 ng/mL) for 6 days to allow for macrophage expansion. RANKL (50 ng/mL) was then added to the expanded macrophages along with M-CSF to promote hOC formation. hOCs were counted via tartrate-resistant acid phosphatase (TRAP) staining at prescribed time points using TRAP kit (Sigma) and counterstained with hematoxylin. TRAP positive cells containing 3 or more nuclei were counted as OCs.

3D TEBC coculture: Femoral head TEBCs (FH-TEBCs) were sterilized by soaking in 70% ethanol overnight and exposure to UV light for 30 min. FH-TEBCs were then soaked in fibronectin (5 μg/mL) for 4 hours prior to cell seeding. hMSCs were seeded onto FH-TEBCs at 100,000 cells/TEBC in α-MEM supplemented with ascorbic acid (50 μg/mL), dexamethasone (10 nM), β-glycerophosphate (10 mM) and vitamin D (10 nM) for one week in static (well-plate) culture to allow for osteoblast differentiation. hOCs were then seeded onto TEBCs in static culture at 100,000 cells/TEBC in same osteogenic differentiation media with added RANKL and M-CSF. 48 hr after hOC introduction, MDA-MB-231 cells were added to TEBCs in static culture at 100,000 cells/TEBC. After 24 hr, TEBCs were then transferred into a perfusion bioreactor (Biodynamic TA Electroforce, TA Instruments) and cultured for 28 days in same media. Three experimental groups were compared in order to measure resorption: TEBCs seeded with all three cell types (OB+OC+T), TEBCs seeded with just bone cells (OB+OC), and a no cell control (No Cell). Cells remaining in the well plate were also cultured for the duration of the study with media changes every 3 days. At the end of the experiment, TEBC were removed from culture and either fixed with 10% neutral buffered formalin or sonicated for 2 min in 0.25 M ammonium hydroxide to remove cells. Tartrate-resistant acid phosphatase (TRAP) staining was conducted on cocultures remaining in the well-plate after 28 days culture using a TRAP kit (Sigma) per the manufacturer instructions and counterstained with hematoxylin.

Scanning Electron Microscopy (SEM): FH-TEBCs after 28-days culture in perfusion bioreactor were fixed in 5% glutaraldehyde solution for 2 hr. FH-TEBCs were then washed and fixed with 2% osmium tetroxide for 1 h, after which they were dehydrated in increasing concentrations of ethanol, and dried overnight. Samples were then cut to expose a variety of surfaces and mounted on a stub covered with carbon tape. Samples were gold sputter-coated (108 Auto Sputter Coater; TedPella, Redding, CA) and imaged using scanning electron microscopy (Carl Zeiss Inc, Thornwood, NY).

Resorption Analysis: FH-TEBC samples were vacuum-dried prior to cell seeding and weighed on an analytical balance. Samples were then scanned by micro-computed tomography (μCT). Tomographic images were acquired at 70 kVp with an isotropic voxel size of 10 μm and at an integration time of 300 ms. μCT images were reconstructed, filtered (σ = 0.2, support = 1.0) and thresholded at 110. Samples were then contoured using the Scanco software algorithm to encompass the entire TEBC. Images were then reconstructed using the Scanco Medical Imaging software. After perfusion culture, samples were again vacuum-dried after cell removal, weighed, and again scanned by μCT. Before and after uCT renderings were then overlaid using Scanco ® Image Processing Language (IPL). First, the uCT files were co-registered in order to save them in the same orientation. The files were then transformed and concatenated to create a linked, overlaid image with the "before" rendering labeled in green, and the "after" rendering labeled in red, and the sections with no change labeled in purple.

3.2.3. Results and Discussion

In order to confirm PUR-nHA material supported bone and tumor cell coculture and osteoclast-mediated resorption, preliminary 2D PUR-nHA disc studies were conducted. MDA-MB-231 human breast cancer cells were co-cultured with MC3T3 pre-osteoblasts and RAW 264.7 macrophages on 2D PUR-nHA discs. At 28 days, substrates were stained with toluidine blue, which revealed the presence of resorption pits (**Fig. 3.4A**). Resorption pitting was further confirmed by SEM analysis (**Figure 3.4B**). PUR-nHA discs cultured with tumor cells showed a net mass loss compared to discs cultured without tumor cells (**Fig. 3.4C**), indicating that the tumor cells stimulated PUR-nHA resorption.

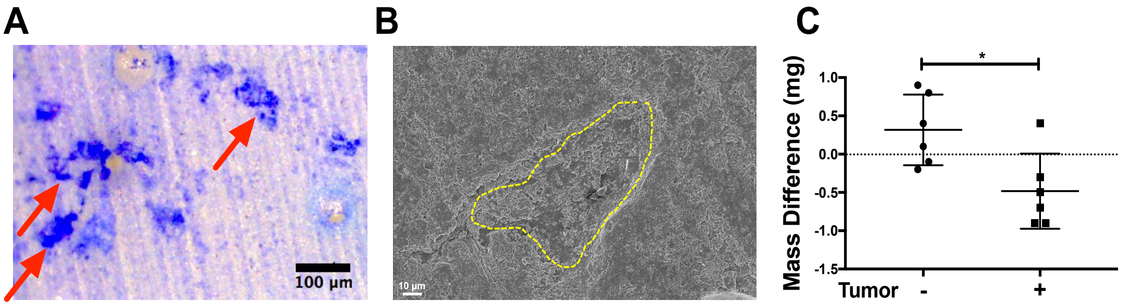

Figure 3.4. **2D osteoblast/osteoclast/tumor cell culture assay**. (A) Resorption pits stained with toluidine blue. (B) SEM of resorption pit on PUR-nHA substrate (outlined in yellow). (C) Substrates showed mass loss in the presence of tumors.

In order to humanize the model, a method for generating hOCs from human peripheral blood was optimized based on a previously established method.[47] Human PBMCs were isolated from peripheral blood and differentiated toward macrophages by stimulation with M-CSF. hOCs are a transient cell population that are only active for approximately 2 weeks.[48] In order to observe the time-course of hOC differentiation to inform subsequent coculture studies, expanded macrophages were seeded in well-plates and stimulated with RANKL to promote hOC maturation. TRAP stain at predetermined time points indicated that number of osteoclasts (N.Oc.) steadily increased over 21-day period (**Figure 3.5A-B**). Expanded macrophages were then seeded on PUR-nHA discs to confirm PUR-nHA material supports hOC maturation and activity. TRAP stain on PUR-nHA discs demonstrates significant hOC formation on material (**Figure 3.5C**) and SEM further confirmed the hOCs are able to resorb PUR-nHA, as indicated by hOC pitting (**Figure 3.5D**).

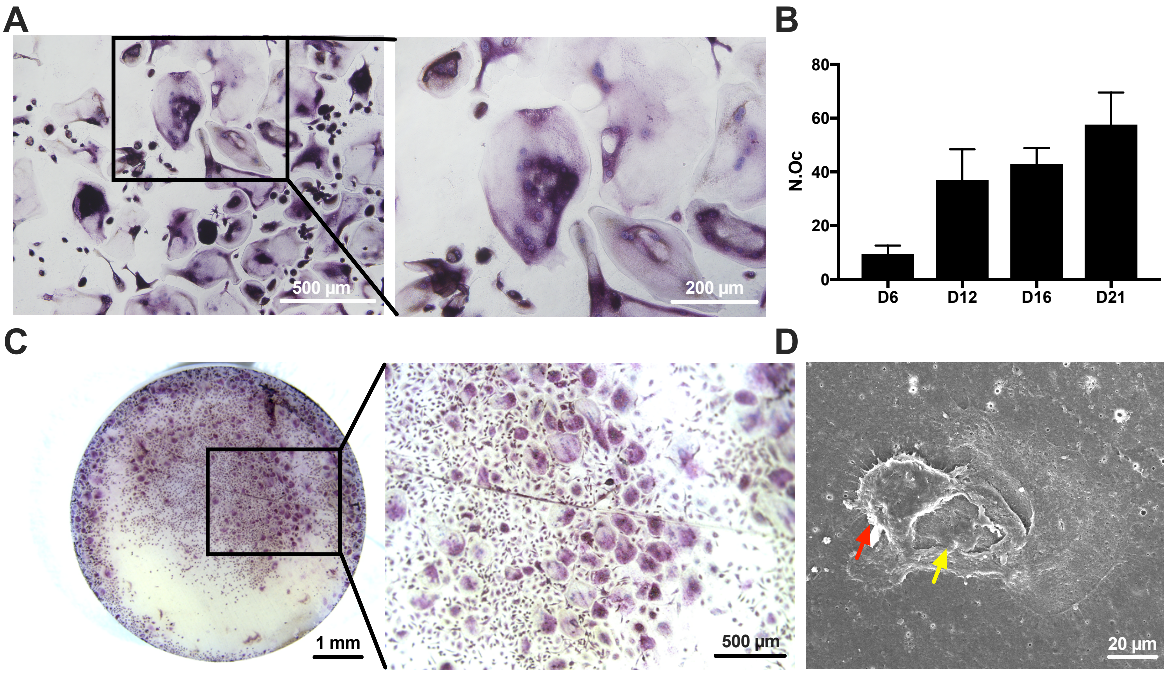

Figure 3.5. **Generation of hOCs and culture on PUR-nHA**. (A) TRAP stain of human peripheral blood mononuclear cells (PBMCs) supplemented with M-CSF and RANKL after 21 days culture. (B) Time-course hOC counts over 21-day period. (C) TRAP stain of PBMC-derived macrophages seeded on PUR-nHA discs after 14-day culture. (D) Representative SEM image of hOC (red arrow) creating resorption pit (yellow arrow) on PUR-nHA material.

A 3D *in vitro* resorption assay was developed utilizing TEBCs cocultured with human osteoblast (OB) and OC precursors and tumor cells (T) in a perfusion bioreactor to closely mimic the *in vivo* milieu of the bone-tumor microenvironment (**Figure 3.6A**). Human mesenchymal stem cells (hMSCs) were seeded on TEBCs in static culture and allowed to differentiate toward OBs for 7 days in osteogenic media. At day 7, hOCs were introduced onto the TEBCs cultured for 2 additional days in static culture with RANKL and M-CSF. MDA-MB-231 tumor cells were then introduced to the TEBCs and TEBCs were subsequently placed into a perfusion bioreactor. Perfusion culture was then allowed to proceed for 28 days. After bioreactor shutdown, a cohort of cells were fixed and observed by SEM (**Figure 3.6B**). SEM images showed that TEBC surfaces were covered in cells and ECM, suggesting that bone and tumor cells adhere, proliferate, and survive extended perfusion bioreactor culture. TRAP stain of cells remaining in well-plate culture also demonstrated significant TRAP staining in the OB+OC+T group, suggesting tumor cells are driving osteoclastogenesis (**Figure 3.6C**). Previous hOC studies demonstrated that hOCs behave similarly on PUR-nHA material as they do on tissue-culture plastic, thus we hypothesized that hOCs were viable and active in perfusion culture on the TEBCs. Decellularized TEBCs were weighed before and after perfusion culture in order to measure mass loss attributed to OC-mediated resorption (**Figure 3.6D**). TEBCs cultured with OB+OC+T demonstrated a significant 1% mass loss compared to the OB+OC and no cell control groups, suggesting tumor cells are driving resorption. TEBCs were also scanned by μCT before and after perfusion culture in order to observe changes to TEBC structure (**Figure 3.6E**). μCT reconstructions of the TEBCs before and after perfusion culture were overlaid using Scanco imaging processing software. Reconstructions were assigned different colors in order to distinguish between before and after scans (red: before, green: after, purple: no change). Red areas in the overlaid reconstruction indicate areas of resorption, green indicate areas of new mineralization, and purple areas indicate where there was no net change. These renderings are hypothesized to be informative in observing spatial heterogeneity in cellular activity within the TEBCs. With further optimization of the image registration process in order to minimize image manipulation during concatenation, we hypothesize the μCT measurements could also be a second readout for resorption by bone volume loss.

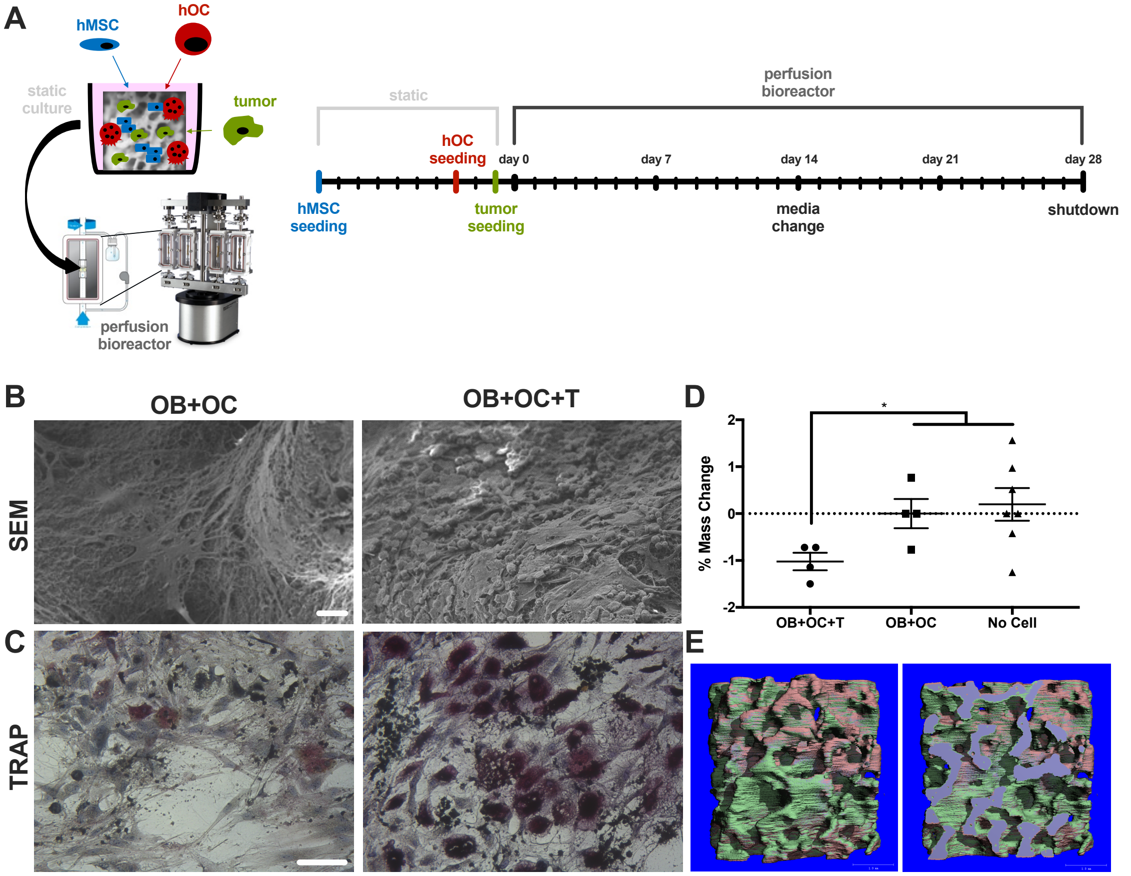

Figure 3.6. **3D perfusion bioreactor resorption model**. (A) Timeline for cell seeding and bioreactor culture. (B) Representative SEM images of OB+OC and OB+OC+T cohorts on TEBCs after 28 days culture. Scale bar: 20 µm. (C) TRAP stain of OB+OC and OB+OC+T cohorts after 28 days culture. (D) Percent mass change of TEBCs before and after perfusion bioreactor culture. (E) Representative overlaid µCT image of TEBCs before (red) and after (green) cell culture. Purple color indicates area of no change.

Taken together, these findings support that we have developed a viable method for mimicking key cell types and their behavior in TIBD *in vitro*. Others have reported 3D *in vitro* models for studying cancer in bone.[49,50] These models, however, utilize either animal-derived scaffolds[49] or 3D-printed scaffolds[50] with lattice-type architectures that do not recapitulate trabecular bone. Our TEBC model, on the other hand, recapitulates human trabecular bone and the key cell types and is reproducible such that different trabecular bone architectures may be studied systematically. Further, the PUR-nHA material is resorbable and thus provides a functional output beyond traditional cellular outputs such as gene expression and histological analysis.

3.2.4. Conclusion

In summary, a fully-humanized 3D *in vitro* model of TIBD was developed that mimics the key cell types and bone-specific features of the *in vivo* TIBD milieu. 2D resorption assays demonstrated that the PUR-nHA supports coculture of bone and tumor cells and subsequent osteoclast-mediated resorption. In order to humanize the model, hOCs were isolated from peripheral blood and preliminary differentiation studies demonstrated these PBMC-derived hOCs exhibit hOC behavior on both tissue-culture plastic and PUR-nHA. TEBCs were then incorporated into a perfusion bioreactor after sequential seeding of hMSCs, hOC precursors, and MDA-MB-231 tumor cells. After 28 days perfusion culture, SEM analysis demonstrated cells spread over TEBC surface and remained viable over 28-day period. TRAP histological analysis and resorption analysis further demonstrated there was osteoclast-mediated resorption of TEBCs in the presence of tumor. Further in-depth analyses of gene expression, flow cytometry, and other functional assays such as Alizarin Red staining for mineralization could make this model a powerful tool for studying TIBD disease progression. Incorporation of patient tumor cells into the model could also provide a means to assess patients’ risk of developing TIBD.

References

(1) Fischbach, C.; Chen, R.; Matsumoto, T.; Schmelzle, T.; Brugge, J. S.; Polverini, P. J.; Mooney, D. J. Engineering Tumors with 3D Scaffolds. *Nat. Methods* **2007**, *4* (10), 855–860.

(2) Gurski, L. A.; Petrelli, N. J.; Jia, X.; Farach-Carson, M. C. 3D Matrices for Anti-Cancer Drug Testing and Development. *Oncol. Issues* **2010**, *25* (February), 20–25.

(3) Yamada, K. M.; Cukierman, E. Modeling Tissue Morphogenesis and Cancer in 3D. *Cell* **2007**, *130* (4), 601–610.

(4) Griffith, L. G.; Swartz, M. A. Capturing Complex 3D Tissue Physiology in Vitro. *Nat. Rev. Mol. Cell Biol.* **2006**, *7* (3), 211–224.

(5) Schuessler, T. K.; Chan, X. Y.; Chen, H. J.; Ji, K.; Park, K. M.; Roshan-Ghias, A.; Sethi, P.; Thakur, A.; Tian, X.; Villasante, A.; et al. Biomimetic Tissue-Engineered Systems for Advancing Cancer Research: NCI Strategic Workshop Report. *Cancer Res.* **2014**, *74* (19), 5359–5363.

(6) Zadpoor, A. A. Bone Tissue Regeneration: The Role of Scaffold Geometry. *Biomater. Sci.* **2015**, *3* (2), 231–245.

(7) Guo, R.; Lu, S.; Page, J. M.; Merkel, A. R.; Basu, S.; Sterling, J. A.; Guelcher, S. A. Fabrication of 3D Scaffolds with Precisely Controlled Substrate Modulus and Pore Size by Templated-Fused Deposition Modeling to Direct Osteogenic Differentiation. *Adv. Healthc. Mater.* **2015**, *4* (12), 1826–1832.

(8) Malda, J.; Woodfield, T. B. F.; van der Vloodt, F.; Wilson, C.; Martens, D. E.; Tramper, J.; van Blitterswijk, C. A.; Riesle, J. The Effect of PEGT/PBT Scaffold Architecture on the Composition of Tissue Engineered Cartilage. *Biomaterials* **2005**, *26* (1), 63–72.

(9) Sanz-Herrera, J. A.; Moreo, P.; García-Aznar, J. M.; Doblaré, M. On the Effect of Substrate Curvature on Cell Mechanics. *Biomaterials* **2009**, *30* (34), 6674–6686.

(10) Ferlin, K. M.; Prendergast, M. E.; Miller, M. L.; Kaplan, D. S.; Fisher, J. P. Influence of 3D Printed Porous Architecture on Mesenchymal Stem Cell Enrichment and Differentiation. *Acta Biomater.* **2016**, *32*, 161–169.

(11) Kang, H. W.; Lee, S. J.; Ko, I. K.; Kengla, C.; Yoo, J. J.; Atala, A. A 3D Bioprinting System to Produce Human-Scale Tissue Constructs with Structural Integrity. *Nat. Biotechnol.* **2016**, No. October 2015.

(12) Jakus, A. E.; Rutz, A. L.; Jordan, S. W.; Kannan, A.; Mitchell, S. M.; Yun, C.; Koube, K. D.; Yoo, S. C.; Whiteley, H. E.; Richter, C.-P.; et al. Hyperelastic "Bone": A Highly Versatile, Growth Factor–Free, Osteoregenerative, Scalable, and Surgically Friendly Biomaterial. *Sci. Transl. Med.* **2016**, *8* (358), 358ra127 LP-358ra127.

(13) Temple, J. P.; Hutton, D. L.; Hung, B. P.; Huri, P. Y.; Cook, C. a.; Kondragunta, R.; Jia, X.; Grayson, W. L. Engineering Anatomically Shaped Vascularized Bone Grafts with HASCs and 3D-Printed PCL Scaffolds. *J. Biomed. Mater. Res. - Part A* **2014**, 4317–4325.

(14) Holmes, B.; Zhu, W.; Li, J.; Lee, J. D.; Zhang, L. G. Development of Novel Three-Dimensional Printed Scaffolds for Osteochondral Regeneration. *Tissue Eng. Part A* **2015**, *21* (1–2), 403–415.

(15) Vanderburgh, J.; Sterling, J. A.; Guelcher, S. A. 3D Printing of Tissue Engineered Constructs for In Vitro Modeling of Disease Progression and Drug Screening.

Annals of Biomedical Engineering. 2017, pp 164–179.

(16) Albritton, J. L.; Miller, J. S. 3D Bioprinting: Improving in Vitro Models of Metastasis with Heterogeneous Tumor Microenvironments. *Dis. Model. Mech.* **2017**, *10* (1), 3–14.

(17) Jang, J.; Yi, H.-G.; Cho, D.-W. 3D Printed Tissue Models: Present and Future. *ACS Biomater. Sci. Eng.* **2016**, *2* (10), 1722–1731.

(18) VanBael, S.; Chai, Y. C.; Truscello, S.; Moesen, M.; Kerckhofs, G.; Van Oosterwyck, H.; Kruth, J. P.; Schrooten, J. The Effect of Pore Geometry on the in Vitro Biological Behavior of Human Periosteum-Derived Cells Seeded on Selective Laser-Melted Ti6Al4V Bone Scaffolds. *Acta Biomater.* **2012**, *8* (7), 2824–2834.

(19) Sun, L.; Parker, S. T.; Syoji, D.; Wang, X.; Lewis, J. A.; Kaplan, D. L. Direct-Write Assembly of 3D Silk/Hydroxyapatite Scaffolds for Bone Co-Cultures. *Adv. Healthc. Mater.* **2012**, *1* (6), 729–735.

(20) Jakus, A. E.; Rutz, A. L.; Shah, R. N. Advancing the Field of 3D Biomaterial Printing. *Biomed. Mater.* **2015**, *014102* (In press.), 14102.

(21) Pedde, R. D.; Mirani, B.; Navaei, A.; Styan, T.; Wong, S.; Mehrali, M.; Thakur, A.; Mohtaram, N. K.; Bayati, A.; Dolatshahi-Pirouz, A.; et al. Emerging Biofabrication Strategies for Engineering Complex Tissue Constructs. *Adv. Mater.* **2017**, *29* (19), 1–27.

(22) Lu, S.; McGough, M. A. P.; Rogers, B. R.; Wenke, J. C.; Shimko, D.; Guelcher, S. A. Resorbable Nanocomposites with Bone-like Strength and Enhanced Cellular Activity. *J. Mater. Chem. B* **2017**, *5* (22), 4198–4206.

(23) Mcenery, M. A. P.; Lu, S.; Gupta, M. K.; Zienkiewicz, K. J.; Wenke, J. C.; Kalpakci, K. N.; Shimko, D. A.; Duvall, L.; Guelcher, S. A. Oxidatively Degradable Poly(Thioketal Urethane)/Ceramic Composite Bone Cements with Bone-like Strength. *R. Soc. Chem. Adv.* **2016**, *6*, 109414–109424.

(24) Hildebrand, T.; Laib, A.; Müller, R.; Dequeker, J.; Rüegsegger, P. Direct Three-Dimensional Morphometric Analysis of Human Cancellous Bone: Microstructural Data from Spine, Femur, Iliac Crest, and Calcaneus. *J. Bone Miner. Res.* **1999**, *14* (7), 1167–1174.

(25) Clarke, B. Normal Bone Anatomy and Physiology. *Clin. J. Am. Soc. Nephrol.* **2008**, *3 Suppl 3*, 131–139.

(26) Hildebrand, T.; Rüegsegger, P. Quantification of Bone Microarchitecture with the Structure Model Index. *Comput. Methods Biomech. Biomed. Engin.* **1997**, *1* (1), 15–23.

(27) Bozogullari, N.; Inan, O.; Usumez, A. Bond Strength of Adhesively Luted Ceramic Discs to Different Core Materials. *J. Biomed. Mater. Res. - Part A* **2009**, *89* (2), 466–471.

(28) Danilin, S.; Merkel, A. R.; Johnson, J. R.; Johnson, R. W.; Edwards, J. R.; Sterling, J. A. Myeloid-Derived Suppressor Cells Expand during Breast Cancer Progression and Promote Tumor-Induced Bone Destruction. *Oncoimmunology* **2012**, *1* (9), 1484–1494.

(29) Vandooren, B.; Melis, L.; Veys, E. M.; Tak, P. P.; Baeten, D. In Vitro Spontaneous Osteoclastogenesis of Human Peripheral Blood Mononuclear Cells Is Not Crucially Dependent on t Lymphocytes. *Arthritis Rheum.* **2009**, *60* (4), 1020–1025.

(30) An, B.; Abbonante, V.; Yigit, S.; Balduini, A.; Kaplan, D. L.; Brodsky, B. Definition of the Native and Denatured Type II Collagen Binding Site for

Fibronectin Using a Recombinant Collagen System. *J. Biol. Chem.* **2014**, *289* (8), 4941–4951.

(31) Goldstein, S. A. The Mechanical Properties of Trabecular Bone: Dependence on Anatomic Location and Function. *J. Biomech.* **1987**, *20* (11–12), 1055–1061.

(32) Gibson, L. J.; Ashby, M. F. *Cellular Solids: Structure and Properties*, 2nd ed.; Cambridge University Press: Cambridge, UK, 1997.

(33) Smith, K. E.; Hyzy, S. L.; Sunwoo, M.; Gall, K. A.; Schwartz, Z.; Boyan, B. D. The Dependence of MG63 Osteoblast Responses to (Meth)Acrylate-Based Networks on Chemical Structure and Stiffness. *Biomaterials* **2010**, *31* (24), 6131–6141.

(34) Røhl, L.; Larsen, E.; Linde, F.; Odgaard, A.; Jørgensen, J. Tensile and Compressive Properties of Cancellous Bone. *J. Biomech.* **1991**, *24* (12), 1143–1149.

(35) Beck, G.; Zerler, B.; Moran, E. Phosphate Is a Specific Signal for Induction of Osteopontin Gene Expression. *Proc. Natl. Acad. Sci.* **2000**, *97* (15), 8352–8357.

(36) Ghita, A.; Pascut, F. C.; Sottile, V.; Notingher, I. Monitoring the Mineralisation of Bone Nodules in Vitro by Space- and Time-Resolved Raman Micro-Spectroscopy. *Analyst* **2014**, *139* (1), 55–58.

(37) Bouxsein, M. L.; Boyd, S. K.; Christiansen, B. A.; Guldberg, R. E.; Jepsen, K. J.; Müller, R. Guidelines for Assessment of Bone Microstructure in Rodents Using Micro-Computed Tomography. *J. Bone Miner. Res.* **2010**, *25* (7), 1468–1486.

(38) Bidan, C. M.; Kommareddy, K. P.; Rumpler, M.; Kollmannsberger, P.; Fratzl, P.; Dunlop, J. W. C. Geometry as a Factor for Tissue Growth: Towards Shape Optimization of Tissue Engineering Scaffolds. *Adv. Healthc. Mater.* **2013**, *2* (1), 186–194.

(39) Rumpler, M.; Woesz, A.; Dunlop, J. W. .; van Dongen, J. T.; Fratzl, P. The Effect of Geometry on Three-Dimensional Tissue Growth. *J. R. Soc. Interface* **2008**, *5* (27), 1173–1180.

(40) Bianchi, M.; Urquia Edreira, E. R.; Wolke, J. G. C.; Birgani, Z. T.; Habibovic, P.; Jansen, J. A.; Tampieri, A.; Marcacci, M.; Leeuwenburgh, S. C. G.; Van Den Beucken, J. J. J. P. Substrate Geometry Directs the in Vitro Mineralization of Calcium Phosphate Ceramics. *Acta Biomater.* **2014**, *10* (2), 661–669.

(41) Wilkinson, A.; Hewitt, R. N.; McNamara, L. E.; McCloy, D.; Dominic Meek, R. M.; Dalby, M. J. Biomimetic Microtopography to Enhance Osteogenesis in Vitro. *Acta Biomater.* **2011**, *7* (7), 2919–2925.

(42) Ripamonti, U.; Roden, L. C.; Renton, L. F. Osteoinductive Hydroxyapatite-Coated Titanium Implants. *Biomaterials* **2012**, *33* (15), 3813–3823.

(43) Coleman, R. E. Skeletal Complications of Malignancy. *Cancer* **1997**, *80* (8 Suppl), 1588–1594.

(44) Johnson, R. W.; Nguyen, M. P.; Padalecki, S. S.; Grubbs, B. G.; Merkel, A. R.; Oyajobi, B. O.; Matrisian, L. M.; Mundy, G. R.; Sterling, J. A. TGF-Beta Promotion of Gli2-Induced Expression of Parathyroid Hormone-Related Protein, an Important Osteolytic Factor in Bone Metastasis, Is Independent of Canonical Hedgehog Signaling. *Cancer Res.* **2011**, *71* (3), 822–831.

(45) Johnson, R. W.; Merkel, A. R.; Page, J. M.; Ruppender, N. S.; Guelcher, S. A.; Sterling, J. A. Wnt Signaling Induces Gene Expression of Factors Associated with Bone Destruction in Lung and Breast Cancer. *Clin. Exp. Metastasis* **2014**, *31* (8), 945–959.

(46) Sterling, J. a.; Oyajobi, B. O.; Grubbs, B.; Padalecki, S. S.; Munoz, S. a.; Gupta, A.;

Story, B.; Zhao, M.; Mundy, G. R. The Hedgehog Signaling Molecule Gli2 Induces Parathyroid Hormone-Related Peptide Expression and Osteolysis in Metastatic Human Breast Cancer Cells. *Cancer Res.* **2006**, *66* (15), 7548–7553.

(47) Henriksen, K.; Karsdal, M. A.; Taylor, A.; Tosh, D.; Coxon, F. P. Generation of Human Osteoclasts from Peripheral Blood. *Methods Mol. Biol.* **2012**.

(48) Manolagas, S. C. Birth and Death of Bone Cells: Basic Regulatory Mechanisms and Implications for the Pathogenesis and Treatment of Osteoporosis. *Endocr. Rev.* **2000**, *21* (2), 115–137.

(49) Villasante, A.; Marturano-Kruik, A.; Robinson, S. T.; Liu, Z.; Guo, X. E.; Vunjak-Novakovic, G. Tissue-Engineered Model of Human Osteolytic Bone Tumor. *Tissue Eng. Part C Methods* **2017**, *23* (2), 98–107.

(50) Zhu, W.; Holmes, B.; Glazer, R. I.; Zhang, L. G. 3D Printed Nanocomposite Matrix for the Study of Breast Cancer Bone Metastasis. *Nanomedicine Nanotechnology, Biol. Med.* **2016**, *12* (1), 69–79.

CHAPTER 4

IV. SYSTEMIC DELIVERY OF A GLI INHIBITOR VIA POLYMERIC NANOCARRIERS BLOCKS TUMOR-INDUCED BONE DISEASE

Adapted from:
Vanderburgh, JP*, Kwakwa, KA*, Werfel, TA, Merkel, AR, Gupta, MK, Johnson, RW, Guelcher, SA, Duvall, CL, Rhoades Sterling, JA. “Systemic Delivery of a Gli Inhibitor via Polymeric Nanocarriers Blocks Tumor-Induced Bone Disease.”

4.1. Abstract

Solid tumors frequently metastasize to bone and induce bone destruction leading to severe pain, fractures, and other skeletal-related events (SREs). Osteoclast inhibitors such as bisphosphonates delay SREs but do not prevent skeletal complications or improve overall survival. Because bisphosphonates can cause adverse side effects and are contraindicated for some patients, we sought an alternative therapy to reduce tumor-associated bone destruction. Our previous studies identified the transcription factor Gli2 as a key regulator of parathyroid hormone-related protein (PTHrP), which is produced by bone metastatic tumor cells to promote osteoclast-mediated bone destruction. In this study, we focused on testing the promising Gli antagonist GANT58, which inhibits Gli2 nuclear translocation and PTHrP expression in tumor cells *in vitro*. In initial testing, GANT58 did not have efficacy *in vivo* due to its low water solubility and poor bioavailability. We therefore developed a micellar nanoparticle (NP) to encapsulate and colloidally stabilize GANT58, providing a fully aqueous, intravenously injectable formulation based on the polymer poly(propylene sulfide)$_{135}$-*b*-poly[(oligoethylene glycol)$_9$ methyl ether acrylate]$_{17}$ (PPS$_{135}$-*b*-POEGA$_{17}$). POEGA forms the hydrophilic NP surface while PPS forms the hydrophobic NP core that sequesters GANT58. In response to reactive oxygen species (ROS), PPS becomes hydrophilic and degrades to enable drug release. In an intratibial model of breast cancer bone metastasis, treatment with GANT58-NPs decreased bone lesion area by 49% ($p < 0.01$) and lesion number by 38% ($p < 0.05$) and resulted in a 2.5-fold increase in trabecular bone volume ($p < 0.001$). Similar results were observed in intracardiac and intratibial models of breast and lung cancer bone metastasis, respectively. Importantly, GANT58-NPs reduced tumor cell proliferation but did not alter mesenchymal stem cell proliferation or osteoblast mineralization *in vitro*, nor was there evidence of cytotoxicity after repeated *in vivo* treatment. Thus, inhibition of Gli2 using GANT58-NPs is a potential therapy to reduce bone destruction while limiting bone toxicity in patients with tumor-induced bone disease (TIBD).

4.2. Introduction

Despite advances in early screening and adjuvant therapy, metastatic disease remains a leading cause of cancer patient morbidity and mortality. One of the most common metastatic sites is the skeleton. Approximately 70–80% of patients with breast or prostate cancer and 30–40% of patients with lung or renal cancer who die from disease develop bone metastases.[1,2] Patients with bone metastases experience complications including severe bone pain, pathological fractures, and other skeletal-related events (SREs) that significantly reduce their quality of life.[2,3]

Once established in bone, cancer cells disrupt normal bone remodeling to initiate a vicious cycle of tumor-induced bone disease (TIBD).[4] Specifically, tumor cells in the bone microenvironment secrete parathyroid hormone-related protein (PTHrP), which increases osteoblast expression of receptor activator of nuclear factor kappa-B ligand (RANKL) and subsequent osteoclast-mediated bone resorption.[5,6] Current treatment strategies for TIBD include the antiresorptive therapies denosumab (RANKL inhibitor) and bisphosphonates (osteoclast inhibitor).[1,2,7] However, these drugs are associated with increased risk of atypical femoral fractures and osteonecrosis of the jaw.[8–12] Conventional chemotherapy and radiation therapies suppress bone marrow cells, resulting in adverse hematologic events and poor bone quality.[13,14] Tumor-targeted therapies that reduce SREs while minimizing damage to the bone are currently unavailable.

The Hedgehog (Hh) signaling pathway is a key regulator of embryonic development with essential roles in cell differentiation and proliferation, tissue polarity, and stem cell maintenance[15,16] but has limited activity in the healthy adult skeleton. Aberrant Hh signaling in adults has been implicated in the development and progression of breast, prostate, and lung cancer.[17–20] However, pharmacological inhibitors of the Hh receptor Smoothened (Smo) failed to show significant clinical benefit in patients with advanced solid tumors[21–23] due to acquired mutations in Smo and/or non-canonical Hh pathway activation.[24–27] Small molecule inhibitors that target the Hh transcription factor Gli2 downstream of Smo circumvent these resistance mechanisms.[28,29] Our previous studies demonstrated that Gli2 stimulates PTHrP expression in bone-destructive tumor cells[30,31] and that genetic inhibition of Gli2 attenuates the ability of cancer cells to colonize bone and induce osteolysis *in vivo.*[26] The small molecule Gli-antagonists GANT58 and GANT61 have shown promising anti-tumor effects *in vitro* and in xenograft models,[28,32–34] but their low water solubility and poor pharmacokinetics (PK) has limited their testing to less translationally-relevant studies using direct injection into subcutaneous tumors. Thus, while Gli2 is a promising therapeutic target for TIBD, small molecule Gli inhibitors have not been tested using systemic delivery nor in models of bone metastasis.

Nanoparticle (NP) drug delivery systems have emerged in recent years as a promising approach to overcome PK and toxicity limitations of otherwise promising drug candidates. Cancer nanomedicines have been widely reported as carriers for chemotherapeutics.[35,36] However, molecularly targeted agents (MTAs) offer multiple benefits over conventional chemotherapies.[37–39] Most notably, their selectivity reduces normal tissue toxicity, thereby improving the therapeutic index.[40] GANT58 is a therapeutically promising MTA with limited bioavailability, and thus is an excellent candidate for development in a nanoparticle formulation to improve its PK *in vivo.* Polymer-based micellar nanoparticles have been shown to enhance the solubility and systemic PK of hydrophobic compounds *in vivo* and have also seen clinical success in cancer treatment.[41–46] Further, advances in polymer science toward environmentally-responsive, “smart" polymer formulations have improved target-specific drug delivery.[47–50]

Herein, we employ polymeric nanoparticles to encapsulate GANT58 (GANT58-NPs) to enable systemic delivery with distribution to breast and lung cancer bone metastases. Following NP characterization, evaluation of *in vitro* toxicity, and *in vivo* biodistribution and PK studies, we tested GANT58-NPs in mouse models of bone metastasis in order to investigate its therapeutic efficacy and safety. We hypothesized that GANT58-NPs delivered intravenously (i.v.) in a fully-aqueous formulation would reduce tumor-induced bone destruction with minimal effects on bone marrow progenitors.

4.3. Materials and Methods

Cell lines and reagents: Bone-metastatic variants of the human breast cancer cell line MDA-MB-231 and human squamous non-small cell lung carcinoma cell line RWGT2 were generated in our laboratory as previously published.[26,27,30,51] MDA-MB-231-bone and RWGT2-bone clones were maintained in DMEM (Cellgro) and α-MEM (Cellgro) respectively, supplemented with 10% fetal bovine serum (FBS; Hyclone Laboratories) and 1% penicillin/streptomycin (P/S; Mediatech). Human mesenchymal stem cells (hMSCs; Extem Biosciences) were maintained in Mesenchymal Stem Cell Growth Medium 2 (PromoCell). GANT58 was purchased from Santa Cruz Biotechnology (Dallas, TX, USA). All other reagents were purchased from Sigma Aldrich (St. Louis, MO, USA) unless otherwise specified.

Immunohistologic staining of patient tumor samples: Bone metastatic (n = 17) and soft tissue (n = 3) tumor biopsies were obtained from the Cooperative Human Tissue Network (CHTN) Western Division in accordance with our Institutional Review Board (IRB #151700)-approved protocol and upon informed consent from patients undergoing surgical resection. All patient information was deidentified prior to receipt by investigators to protect subject privacy. The clinical features of the patient samples are summarized in **Table S1**. Briefly, fresh tissue samples were fixed in 10% formalin (Fisher Scientific) for 48 hr and stored in 70% ethanol at 4°C before being processed and embedded in paraffin. Serial sections (5-μm thickness) were placed on slides, deparaffinized in xylene, and rehydrated with graded alcohol solutions, followed by antigen retrieval in 10 mM sodium citrate buffer at 80°C for 30 min. Sections were then blocked with 5% goat serum in phosphate-buffered saline (PBS)/0.1% Tween-20 for 30 min and incubated with rabbit polyclonal anti-Gli2 primary antibody (1:500, Novus Biologicals) overnight at 4°C. The VECTASTAIN Elite ABC HRP Kit (Vector Laboratories) with biotinylated goat anti-rabbit secondary antibody and the ImmPACT NovaRED Peroxidase Substrate Kit (Vector Laboratories) were both used according to the manufacturer's protocol. After counterstaining with hematoxylin, tumor sections were mounted with Cytoseal XYL (Thermo Scientific) and imaged using an Olympus BX41 microscope equipped with an Olympus DP71 camera. Gli2-positive staining was quantified using Metamorph software (Molecular Devices, Inc.).

In silico analyses of patient tumors: The Gene Expression Omnibus (GEO) database was queried on 11 October 2018 for the GEO accession number GSE14017 to obtain the gene expression profiling dataset of 29 human breast cancer metastases in different organs, which was generated by X.H. Zhang, et al.[52] For the purposes of their study, the authors used the Affymetrix Human Genome U133 Plus 2.0 Array (https://www.ncbi.nlm.nih.gov/geo/query/acc.cgi?acc=GSE14017).[52] To determine Gli2 expression in bone, brain, and lung cancer metastases of breast cancer patients, the identifiers corresponding to Gli2 (207034_s_at, 228537_at, 208057_s_at) were located on the platform record, and gene expression values across dataset samples were retrieved. One brain metastasis (GSM352120) and one lung metastasis (GSM352127) sample from the microarray dataset were omitted from final statistical analyses after performing the Grubb's test for outliers (GraphPad Software, Inc.).

Polymer synthesis and characterization: The diblock copolymer poly(propylene sulfide)$_{135}$-*b*-poly[(oligoethylene glycol)$_9$ methyl ether acrylate]$_{17}$ (PPS$_{135}$-*b*-POEGA$_{17}$) was synthesized via a combination of anionic and reversible addition-fragmentation chain transfer (RAFT) polymerization as previously published.[41,42] Briefly, the PPS block was synthesized via anionic polymerization to a degree of polymerization of approximately 135 (10 kDa), conjugated to the RAFT macro-chain transfer agent, and chain-extended with POEGA to a degree of polymerization of approximately 17 (8 kDa). Polymer structure was confirmed by ^{1}H-NMR. Fluorophore-grafted polymers were synthesized by adding a small amount of the amine-reactive intermediate pentafluorophenyl acrylate (PFPA) into the reaction mixture with POEGA at a 1:1 mole ratio (PFPA:PPS-ECT). The reaction was allowed to proceed for 24 h at 70ºC. The reaction was dialyzed against methanol and dried under vacuum. The resulting polymer (0.021 mmol) was reacted with Cy7-amine or Cy5-amine fluorophores (0.042 mmol) in DMSO for 24 hr at 50ºC. The reaction mixture was again dialyzed against methanol and dried under vacuum.

GANT58-NP preparation and characterization: GANT58-loaded PPS_{135}-*b*-$POEGA_{17}$ micellar nanoparticles (GANT58-NPs) were formed by the bulk solvent evaporation method. PPS_{135}-*b*-$POEGA_{17}$ (10 mg) was co-dissolved with GANT58 (2.5 mg) in chloroform (0.1 mL) and added dropwise to a vial containing vigorously-stirring PBS (1 mL). The oil-in-water biphasic solution was left stirring overnight to evaporate the chloroform and allow for micelle formation. The resulting micelle solution was passed through a 0.45 μm syringe filter producing the final GANT58-NP formulation. The same technique, excluding addition of GANT58, was used to create empty PPS_{135}-*b*-$POEGA_{17}$ micellar nanoparticles (Empty-NPs). Dynamic light scattering (DLS) was used to measure the hydrodynamic diameter (D_h) and zeta potential (ζ) of the GANT58-NPs and Empty-NPs via a Malvern Zetasizer Nano-ZS (Malvern Instruments Ltd., Worcestershire, UK) equipped with a 4 mW He-Ne laser operating at $\lambda = 632.8$ nm. Transmission electron microscopy (TEM) samples were prepared as previously described.[42] Briefly, 5 μL of GANT58-NPs were added to a pure carbon TEM grid (Ted Pella, Inc., Redding, CA, USA), blotted dry after 60 s, and counterstained with 3% uranyl acetate for 20 s. After vacuum drying, the grids were imaged on an FEI Tecnai Osiris microscope operating at 200 kV for TEM. GANT58 loading was quantified utilizing the fluorescence properties of GANT58. Aliquots of GANT58-NPs in PBS (50 μL) were added in triplicate to a 96-well plate and dissolved by adding an equal volume of DMF. On the same plate, a standard of GANT58 in the same solvent (1:1 DMF:PBS) was prepared. Fluorescence intensity of GANT58 (ex. 485 nm, em. 590 nm) was measured on a micro-plate reader (Tecan Infinite 500, Tecan Group Ltd., Mannedorf, Switzerland) and GANT58 concentration was calculated from the standard curve.

Critical micelle concentration (CMC) determination: The CMC was determined as previously described.[41,42] Nile Red (NR) was substituted for GANT58 as the loaded species due to its unique fluorescence properties and its similar molecular weight to GANT58. NR is highly fluorescent in hydrophobic environments yet non-fluorescent in polar, aqueous environments, making it ideal for characterizing self-assembly properties. Briefly, NR-loaded PPS_{135}-*b*-$POEGA_{17}$ micelles (NR-NPs) were prepared by the described bulk solvent evaporation method. NR loading was measured as described for GANT58. Different dilutions of the NR-NPs were prepared in PBS, and NR fluorescence (ex. 535 nm, em. 612 nm) was read on a micro-plate reader (Tecan Infinite 500, Tecan Group Ltd., Mannedorf, Switzerland). The CMC was defined as the intersection point on the plot of NR fluorescence versus polymer concentration as previously described.[41,42]

Hydrogen peroxide (H_2O_2)-dependent drug release: The ROS-responsive behavior of the PPS_{135}-b-$POEGA_{17}$ NPs was assessed as described previously, using H_2O_2 as the ROS-species.[42] Briefly, NR-NPs prepared as described were exposed to a range of concentrations (0-1.5 M) of H_2O_2. Fluorescence intensity of NR was monitored in a 96-well plate using a micro plate reader (Tecan Infinite 500, Tecan Group Ltd., Mannedorf, Switzerland). Release of the NR due to NP oxidation and destabilization was assessed over time based on disappearance of NR fluorescence. The loss of fluorescence for each sample at each time point was determined by subtracting the fluorescent value from that of the sample prior to H_2O_2 addition, and the percent fluorescence remaining was determined by normalization to the same value (before addition of H_2O_2). This value for percent fluorescence remaining was subtracted from 100% and expressed as a percent release for each sample at each time point.

Quantitative real-time polymerase chain reaction (qPCR): Total RNA was extracted from MDA-MB-231 bone cells after 48 hr GANT58 (0-20 µM) treatment with the RNeasy Mini Kit (Qiagen) as per manufacturer's instructions. Complimentary DNA (cDNA) was synthesized from 1 µg RNA using the qScript cDNA SuperMix (Quanta Biosciences) and serially diluted to create a standard curve. qPCR was performed on a 7500 Real-Time PCR System (Applied Biosciences) using TaqMan Universal PCR Master Mix (Applied Biosystems) and the TaqMan primers for eukaryotic 18S rRNA (4352930E, Applied Biosystems) or human PTHLH (Hs00174969_m1, Thermo Fisher) under the following conditions: 10 min at 95°C, (15 s at 95°C, 1 min at 60°C) x 40 cycles. Three technical replicates were run for each biological replicate. Quantification was performed using the absolute quantitative method using 18S as an internal control.

Western blotting: Nuclear and cytoplasmic protein lysates were isolated from MDA-MB-231 bone cells after 72 hr treatment with GANT58 (0-20 µM) using NE-PER Nuclear and Cytoplasmic Extraction Reagents (Thermo Scientific) supplemented with Halt Protease and Phosphatase Inhibitor Cocktail (Thermo Scientific). Protein concentrations were quantified using the Pierce BCA Protein Assay Kit (Thermo Scientific). Protein samples (20 µg/well) were separated on a 4–20% Mini-PROTEAN TGX polyacrylamide gel (Bio-Rad) by SDS-PAGE prior to being transferred to a nitrocellulose membrane (Bio-Rad) with the Trans-Blot Turbo Transfer System (Bio-Rad). Membranes were then blocked for 1 hr in 1X TBS containing 0.1% Tween-20 and 5% w/v BSA and incubated with the following primary antibodies at 4°C overnight: anti-Gli2 (1:500, Novus Biologicals), anti-TATA binding protein (TBP) (1:1000, Cell Signaling), or anti-Glyceraldehyde 3-phosphate dehydrogenase (GAPDH) (1:5000, Cell Signaling). Following incubation with anti-rabbit IgG HRP-linked secondary antibody (Cell Signaling) at room temperature for 1 hr, protein bands were developed by Western Lightning Plus-ECL (Perkin Elmer) and imaged on a ChemiDoc MP Imaging System (Bio-Rad). The intensity of each band was determined by densitometry using ImageJ software.

Tumor cell proliferation assay: MDA-MB-231-bone cells were seeded in a 96-well plate at 2,000 cells/well in quadruplicate. Vehicle (DMSO), free GANT58, Empty-NPs, or GANT58-NPs were introduced to wells after 24 hr and media was replenished every other day for 7 days. Cell proliferation was determined by 3-(4,5-dimethylthiazol-2-yl)-5-(3-carboxymethoxyphenyl)-2-(4-sulfophenyl)-2H-tetrazolium (MTS) assay using the CellTiter 96 Aqueous Non-Radioactive Cell Proliferation Assay kit (Promega) per the manufacturer's instructions. Absorbance values were measured on a plate reader at optical density (OD) 450 nm.

hMSC proliferation assay: hMSCs were seeded in a 96-well plate at 50,000 cells/mL (5,000 cells/well). Vehicle (DMSO), free GANT58, Empty-NPs, or GANT58-NPs were introduced to the wells after 24 hr. As described, cell proliferation was determined using the CellTiter 96 Aqueous Non-Radioactive Cell Proliferation Assay kit (Promega) per manufacturer's instructions. Absorbance values were measured at OD 490 nm.

Fluorescence microscopy: MDA-MB-231-bone cells were seeded in a 4-chamber well slide at 20,000 cells/well. After 24 hr, media was replaced with media containing treatments. For NP uptake experiments, GANT58-Cy5NPs were added and incubated for 12 hr after treatment. Cells were then stained with DAPI and viewed on a Nikon Eclipse TI confocal microscope for Cy5 and DAPI fluorescence. For Gli2 immunofluorescence, cells were incubated with 20 μM GANT58, 20 μM GANT58-NP, Empty-NP, or DMSO control for 72 hr, fixed with 4% neutral-buffered formalin, and washed with Tris-buffered saline (TBS). The cells were then blocked and permeabilized with TBS containing 2.5% BSA, 0.1%

Tween, and 0.2% Triton-X for 5 min. Gli2 antibody (1:500, Novus Biologicals) was then incubated in permeabilization buffer overnight at 4ºC. Cells were then washed again with TBS and incubated with secondary Alexa-488 anti-rabbit antibody (1:2000, Thermo Fisher) for 90 min. The cells were then stained with DAPI for 10 min, washed, and mounted with a cover slip. Cells were imaged using an Olympus BX60 fluorescence microscope for DAPI and Alexa-488 fluorescence. ImageJ was used to calculate the Manders coefficient to quantify Gli2 nuclear colocalization.

Cell viability, cytotoxicity, and apoptosis: MDA-MB-231 bone cells were seeded in a 96-well plate (5,000 cells/well) and treated with GANT58 (0-80 μM) for 24 hr and viability, cytotoxicity, and apoptosis were measured using the ApoTox-Glo Triplex Assay (Promega) according to the manufacturer's instructions. Briefly, 20 μL of Viability/Cytotoxicity Reagent was added to 100 μL of media in each well and incubated for 30 min at 37ºC. Fluorescence intensity was then measured for viability (ex. 400 nm, em. 505 nm) and cytotoxicity (ex. 485 nm, em. 520 nm). Luminescence was measured for apoptosis (caspase 3/7 activation) following the addition of 100 μL of Caspase-Glo 3/7 Reagent and 30 min incubation at room temperature.

Mineralization assay: hMSCs were seeded at 25,000 cells/mL (50,000 cells/well) in a 24-well plate and allowed to grow to confluency for 48 hr in MSC Growth Medium 2 (PromoCell) as we have described previously.[53] Cells were then induced with MSC Osteogenic Differentiation Medium (PromoCell) treated with vehicle (DMSO), free GANT58, Empty-NPs, or GANT58-NPs. Cells were cultured for 14 days and media was changed every third day. A cohort of wells remained in MSC Growth Media and served as a control. Cells were then washed with PBS and fixed in 10% formalin for 45 min, and stained with Alizarin Red S (80 mM) for 30 min. After staining, cells were washed five times with deionized (DI) water and imaged under an inverted microscope. Alizarin dye was then extracted with 5% SDS for 1 hr. Absorbance of the extracted dye was read on a plate reader at OD 405 nm.

Osteoclastogenesis assay: Mouse bone marrow-derived stromal cells were obtained from C57BL/6J mice and used in an osteoclastogenesis coculture assay as previously described.[54,55] Briefly, femora and tibiae were dissected, and both ends cut off. Bone marrow cells were flushed out and collected via centrifugation, suspended in α-MEM with 10% FBS, and plated in 100 mm culture dishes. After 2 hr, nonadherent cells were harvested and pelleted. The non-adherent bone marrow cells (500,000 cells/well) and MDA-MB-231-bone cells supplemented with 10 ng/mL TGF-β (1000 cells/well) were plated in 48-well plates in 300 μL α-MEM (day 1). Treatments with Free GANT58, Empty-NPs, and GANT58-NPs started on day 1. On day 2, 300 μL of fresh α-MEM supplemented with treatments was added to each well, and 300 μL was replaced with fresh, treatment supplemented media each subsequent day until fixation. On day 6, cells were fixed and stained for TRAP using a TRAP kit (Sigma) and counterstained with hematoxylin. TRAP-positive cells with 3 or more nuclei were counted as osteoclasts. Vitamin D_3 was used as a positive control for osteoclast formation, whereas absence of MDA-MB-231-bone cells and vitamin D_3 was used as a negative control.

NP cargo biodistribution: Athymic female nude mice (4-6 weeks old, Envigo) were intratibially inoculated with GFP-expressing MDA-MB-231-bone tumor cells and given 14 days to progress into tumors. Two independent experiments were performed to assess the biodistribution of the NP cargo and of the NP polymer. For biodistribution of the NP cargo, the near-IR fluorophore Cy7 was loaded into the NP formulation via the bulk solvent evaporation method to serve as the surrogate fluorescent loading species. Cy7-loaded NPs were then injected via tail vein injection (1 mg/kg Cy7). Mice were then imaged on a Pearl Near-IR imager (Licor) immediately, 2 hr, 6 hr, and 24 hr after injection and the images analyzed using region of interest (ROI) analysis in the Licor software. For biodistribution of the NP polymer, Cy7-grafted GANT58-NPs were injected via tail vein injection (8 mg/kg GANT58). Mice were then sacrificed at 1, 4, and 24 hr post NP-injection. Organs and long bones were imaged on a Pearl Near-IR imager (Licor) and the images analyzed using ROI analysis in the Licor software.

Pharmacokinetics: Rag 2-/- mice were injected with Cy5-grafted GANT58-NPs via retroorbital injection (8 mg/kg GANT58, 100 μL injection) under isoflurane anesthesia. Immediately post-injection, 15 min, 30 min, 1 hr, 2 hr, 4 hr, 12 hr, and 24 hr, a small volume of blood (< 5 μL) was drawn via tail-nick into a heparinized capillary tube and deposited into PCR tubes. PCR tubes containing whole blood samples were then frozen until analysis. Blood samples were thawed at time of analysis and diluted 40x in PBS. Samples were then read on a Take3 microvolume plate (Biotek) and a Synergy H1 fluorescence plate reader (Biotek) and background fluorescence was subtracted. NP concentration was calculated via a standard curve made by doping Cy5-grafted NPs into fresh mouse blood that was then frozen until time of analysis, at which time it was also diluted 40x.[56]

Free GANT58 intratibial mouse model of late bone metastasis: Athymic female nude mice (4-6 weeks old, Harlan) were injected with 2.5 x 10^5 GFP-expressing MDA-MB-231-bone cells in 10 μL PBS into the left tibia under isoflurane anesthesia as previously described.[57] As a control, the contralateral limb was injected with 10 μL PBS. GANT58 was reconstituted in a 4:1 Cremophor EL:ethanol solution to solubilize the drug. GANT58 treatments started 4 days post-tumor inoculation to allow for tumor establishment (n = 8, GANT58; n = 8, vehicle). Mice were then treated 3 days/week with 50 mg/kg GANT58 via subcutaneous, 100 µL injection. Mice were imaged weekly to track tumor progression and sacrificed at 4 weeks.

GANT58-NP intratibial mouse model of late bone metastasis: Athymic female nude mice (4-6 weeks old, Envigo) were injected with 2.5 x 10^5 GFP-expressing MDA-MB-231-bone or RWGT2-bone cells in 10 µL PBS into the left tibia under isoflurane anesthesia as previously described.[57] As a control, the contralateral limb was injected with 10 µL PBS. GANT58-NP and Empty-NP treatment started 4 days post-tumor inoculation to allow for tumor establishment (n = 12, GANT58-NP; n = 12, Empty-NP). Mice were then treated 5 days/week with 8 mg/kg GANT58 in the GANT58-NP formulation or an equivalent polymer dose of Empty-NPs in 100 µL of PBS via tail vein injection. Mice were imaged weekly to track tumor progression and sacrificed at 4 weeks or 6 weeks post-tumor injection for the MDA-MB-231 and RWGT2 experiments respectively.

GANT58-NP intracardiac mouse model of early bone metastasis: Athymic female nude mice (4-6 weeks old, Envigo) were anesthetized by continuous isoflurane and inoculated with 1 x 10^5 GFP-expressing MDA-MB-231-bone cells resuspended in PBS via intracardiac injection into the left cardiac ventricle using a 27-gauge needle, as previously described.[26,30,57] Mice were then divided into two cohorts: one group which was treated immediately post-tumor inoculation with GANT58-NPs (8 mg/kg, n = 12) or Empty-NPs (equivalent polymer dose, n = 12), and the remaining group started the same treatment 7 days post-tumor inoculation. Mice were imaged weekly to track tumor progression and sacrificed at 4 weeks.

Radiographic imaging: Mice were radiographically imaged weekly beginning 1-week post-tumor cell inoculation using a Faxitron LX-60. Specifically, mice were anesthetized with isoflurane and laid in a prone position on the imaging platform. Images were acquired at 35 kVp for 8 seconds. Using a freehand selection tool, osteolytic lesions in each image were manually outlined and total lesion area and number were measured using the quantitative image analysis software Metamorph (Molecular Devices, Inc.). All data are represented as mean lesion area and number per mouse.

Micro-computed tomography (μCT): Tibiae and femora were analyzed using a high-resolution benchtop μCT 40 system (Scanco Medical). Tomographic images were acquired at 70 kVp with an isotropic voxel size of 12 μm and at an integration time of 300 ms. Scans were acquired with hindlimbs in 70% ethanol. μCT images were reconstructed, filtered (σ = 0.2, support = 1.0) and thresholded at 230. Tibiae and femora were then contoured using the Scanco software algorithm starting 10 slices below the growth plate and continued 100 slices in the distal direction. Images were then reconstructed using the Scanco Medical Imaging software. The software was also used to calculate the bone morphometric parameters bone volume/total volume (BV/TV, ratio of segmented bone volume to the total volume of interest), trabecular separation (Tb.Sp., mean distance between trabeculae), trabecular thickness (Tb.Th., mean thickness of trabeculae), and trabecular number (Tb.N., measure of the average number of trabeculae per unit length) of the segmented bone.

Histology/histomorphometry: Tibiae and femora were removed during autopsy and fixed in 10% neutral-buffered formalin (Fisher Scientific) for 48 hr at room temperature after which they were stored at 4ºC in 70% ethanol. Bone specimens were decalcified in 10% EDTA for 2 weeks at 4°C and embedded in paraffin wax. Bone sections (5-μm thickness) were stained with hematoxylin & eosin (H&E), orange G, and phloxine. Tumor burden was examined under a microscope and quantified using Metamorph software (Molecular Devices, Inc.). Specifically, tumors were manually outlined as ROIs using a freehand selection tool and the total tumor area was measured as a percentage of the total bone marrow area.

Ethics statement: All animal protocols were approved by Vanderbilt University Institutional Animal Care and Use Committee (IACUC) and were conducted according to National Institutes of Health (NIH) guidelines for care and use of laboratory animals.

Statistical analyses: All statistical analyses were performed using Prism version 7 (GraphPad Software, Inc.). Values are presented as mean ± SEM and p-values determined using one-way ANOVA unless otherwise specified where $*p < 0.05$, $**p < 0.01$, $***p < 0.001$, and $****p < 0.0001$.

4.4. Results and Discussion

Our previous data have established that Gli2 regulates PTHrP expression and is strongly correlated with bone-destructive tumor cells.[26,30] To test our hypothesis that Gli2 is overexpressed in patients with bone metastases, we collected 20 human biopsies through the CHTN (**Table S1**) and evaluated Gli2 expression in bone-metastatic tumors from a mix of primary origins. Three of the 20 biopsies were from non-metastatic soft tissue sarcomas and were tested as controls. Patient bone metastases expressed significantly higher levels of Gli2 by IHC compared to soft tissue sarcomas (6-fold increase) (**Figure 4.1A-B**). To further show that Gli2 is overexpressed in bone metastases, we queried the GEO database to obtain Gli2 expression values among 29 human breast cancer metastases in different organs.[52] Gli2 gene expression was significantly higher in bone metastases compared to brain and lung metastases from breast cancer patients (**Figure 4.1C**). Together, these observations suggest that overexpression of Gli2 is a characteristic of bone metastases and therefore represents a promising therapeutic target for TIBD.

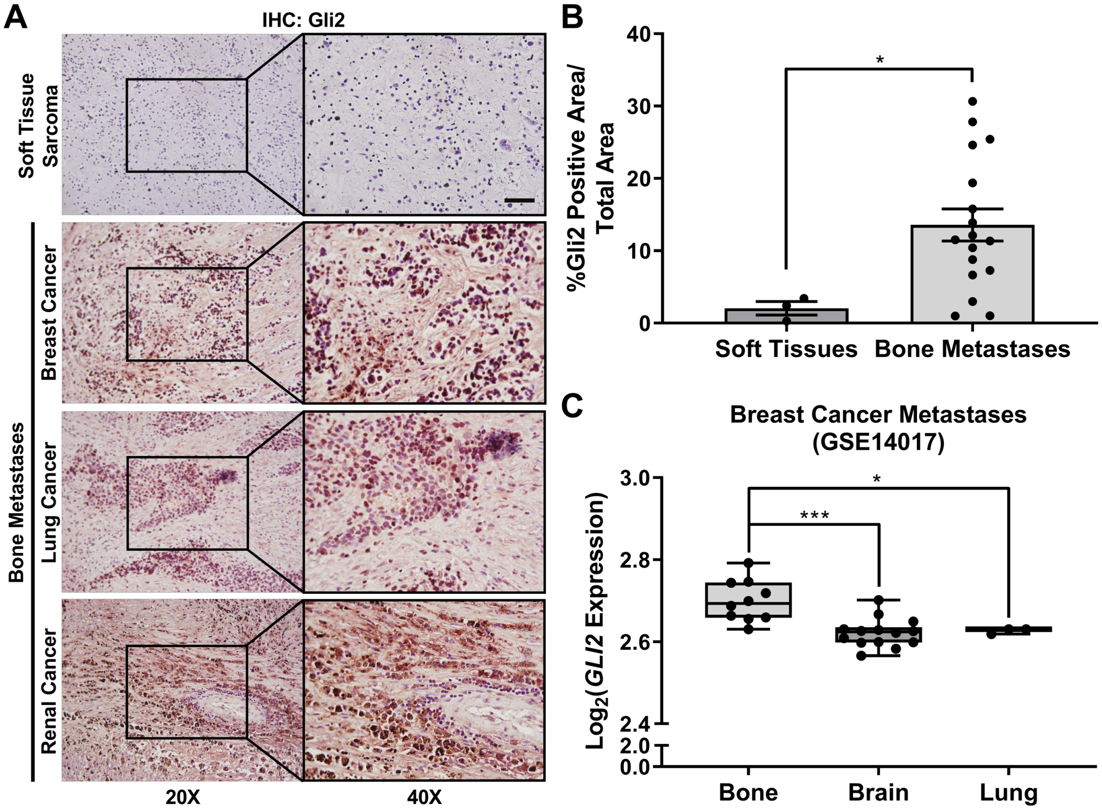

Figure 4.1. Gli2 is overexpressed in patient bone-metastatic tumors. (A) Representative images of Gli2 IHC for patient soft tissue sarcomas (n = 3) and bone-metastatic tumors (n = 17) from different primary origins. Scale bar: 50 µm. (B) Quantification of Gli2-stained patient tumor samples. Groups were statistically compared using student's unpaired t-test. (C) Gli2 gene expression in human breast cancer metastases from bone (n = 10), brain (n = 14), and lung (n = 3) [52]. Minima = 25th percentile, maxima = 75th percentile, centers = median.

To evaluate GANT58 as a therapeutic for TIBD, mice were treated with GANT58 (4:1 Cremophor EL:ethanol). Cremophor EL was chosen due to its widespread use for various poorly-water soluble drugs such as paclitaxel.[58] Athymic nude mice were inoculated with MDA-MB-231 cells into the left tibiae and were then treated 3 days/week with 50 mg/kg GANT58 or vehicle control via subcutaneous injection (**Figure 4.2A**).

Radiographic imaging of the mice over the time course of the study showed that by week 3 both the GANT58 and vehicle-treated groups exhibited severe osteolytic lesions, which significantly worsened by week 4, at which time the mice were sacrificed. Further, the mice showed an adverse response to the injections, presenting with scabs and chemical burns as early as week 2. Radiographic analysis showed that there was no significant difference between GANT58 and control mice in lesion area or lesion number, with both groups exhibiting numerous lesions in the tumor-bearing tibia (**Figure 4.2B-D**). To further investigate the bone outcomes in these mice, μCT was conducted on the tibiae after sacrifice (**Figure 4.2E**). BV/TV was significantly reduced in all tumor bearing animals and was comparable for vehicle- and GANT58-treated tumor-bearing tibiae (**Figure 4.2F**). Similarly, Tb.Sp. was comparable for vehicle-and GANT58-treated tumor-bearing tibiae and both were significantly higher than the non-tumor controls (**Figure 4.2G**). Histological analysis showed that in both treated and control mice, the average tumor area (%) measured by histomorphometry was 60-70%, indicating that tumor had effectively invaded the entire marrow space of the tibia (**Figure 4.2H-I**). These findings demonstrate that delivery of free GANT58 at high doses using standard clinical formulation techniques is not effective in blocking TIBD, highlighting the need for delivery strategies that solubilize the drug and improve its PK profile to enable bone tumor delivery.

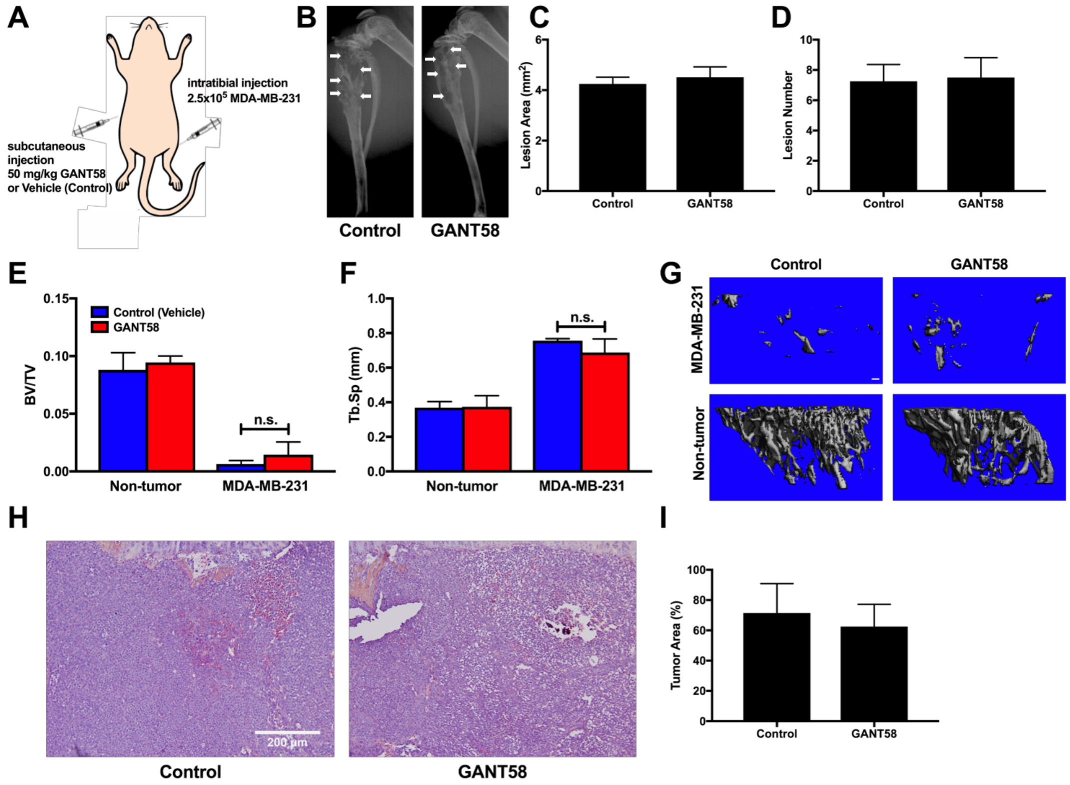

Figure 4.2. GANT58 treatment does not block tumor-induced osteolysis when delivered via Cremophor EL vehicle. (A) Tumor inoculation and subcutaneous treatment scheme for intratibial model of bone metastasis. (B) Representative radiographic images of vehicle (control) and GANT58 treated mice at 4-weeks post-tumor (MDA-MB-231) inoculation. Arrows indicate osteolytic bone lesions. (C) Lesion area and (D) lesion number as assessed by radiographic analysis exhibit no significant difference between vehicle and treatment groups. (E & F) µCT analysis of tibiae bone volume fraction (BV/TV) and trabecular separation (Tb. Sp.) showed no significant difference in mice treated with GANT58 versus those treated with Cremophor EL vehicle. (G) Representative µCT reconstructions of vehicle-treated, GANT58-treated, and contralateral, non-tumor bearing tibiae. (H) Representative H&E stained sections and (I) histomorphometric analysis of tumor area in vehicle-treated and GANT58-treated mice inoculated with MDA-MB-231 cells. Scale bar: 200 µm.

A diblock copolymer comprising PPS and POEGA was synthesized via RAFT polymerization (**Figure 4.3A, Figure S4.1A-B**). PPS was chosen as the core-forming hydrophobic block primarily due to its promise from other studies in our lab that showed excellent encapsulation and retention of hydrophobic small molecules.[42,50,59] Furthermore, the sulfide group in PPS reacts with oxygen radicals to create sulfoxides and sulfones. This reaction causes a hydrophobic to hydrophilic phase transition in the polymer which potentially contributes to both drug release at sites of oxidative stress and ultimate systemic clearance of the polymer. Previous studies have also reported that PPS is a potent ROS-scavenger, which is hypothesized to impart beneficial antioxidant properties to the GANT58-NPs.[60,61] The POEGA hydrophilic block forms a brush-like conformation of 9 repeating units of ethylene glycol pendant to the hydrocarbon backbone. POEGA was chosen as the NP surface-forming block because this graft polymer architecture has been shown to improve circulation time over linear PEG.[62–64]

Nanoparticles were formed by the bulk solvent evaporation method to create either GANT58-loaded PPS_{135}-*b*-$POEGA_{17}$ nanoparticles (GANT58-NPs) or unloaded PPS_{135}-*b*-$POEGA_{17}$ nanoparticles (Empty-NP) (**Figure 4.3B**). GANT58 (**Figure S4.1C**) was introduced into the organic phase resulting in an average loading content of 11.4% (mg drug/mg polymer) and an encapsulation efficiency of 51.8%. The hydrodynamic diameter of both the GANT58-NPs and Empty-NPs were assessed by DLS. The GANT58-NPs have an average hydrodynamic diameter of 93.3 ± 4.1 nm, while the Empty-NPs have a slightly smaller diameter of 73.5 ± 3.4 nm. TEM shows the NPs exhibit a spherical morphology (**Figure 4.3C**). Both the GANT58-NPs and Empty-NPs were monodispersed with an average PDI of 0.22 and 0.18, respectively, and a relatively low ζ-potential (-1.33 mV and -1.20 mV, respectively). The critical micelle concentration (CMC) of the GANT58-NPs was 0.079 mg/mL as determined by the Nile Red (NR) method (**Figure 4.3D**).[41] This CMC is almost an order of magnitude lower than the initial NP concentration after i.v. administration (~0.5 mg/mL) and remains lower than the NP blood concentration after 12 hr of circulation (~0.15 mg/mL) as indicated by circulation time measurements. The ROS-responsive behavior of the NPs was investigated *in vitro* using H_2O_2 as the model ROS species and NR-loaded NPs (**Figure S4.2**). Incubation of Cy5-labeled GANT58-NPs with MDA-MB-231-bone cells revealed that cells readily uptake the NPs into the cytoplasm. The Cy5-labeled NPs (red) exhibit close proximity to DAPI-stained nuclei (blue), indicating uptake of the NPs within the cells (**Figure 4.3E**).

The authors of the manuscript on the original drug screen that identified GANT58 hypothesized that it primarily acts at the nuclear level,[28] but the molecular mechanism has not been reported. To test the hypothesis that GANT58 inhibits nuclear translocation of Gli2, MDA-MB-231-bone cells were treated with 20 μM GANT58 or GANT58-NP for 72 hr. Immunofluorescent analyses revealed significantly reduced colocalization of Gli2 with DAPI-stained nuclei in cells treated with GANT58 or GANT58-NPs compared to the Empty-

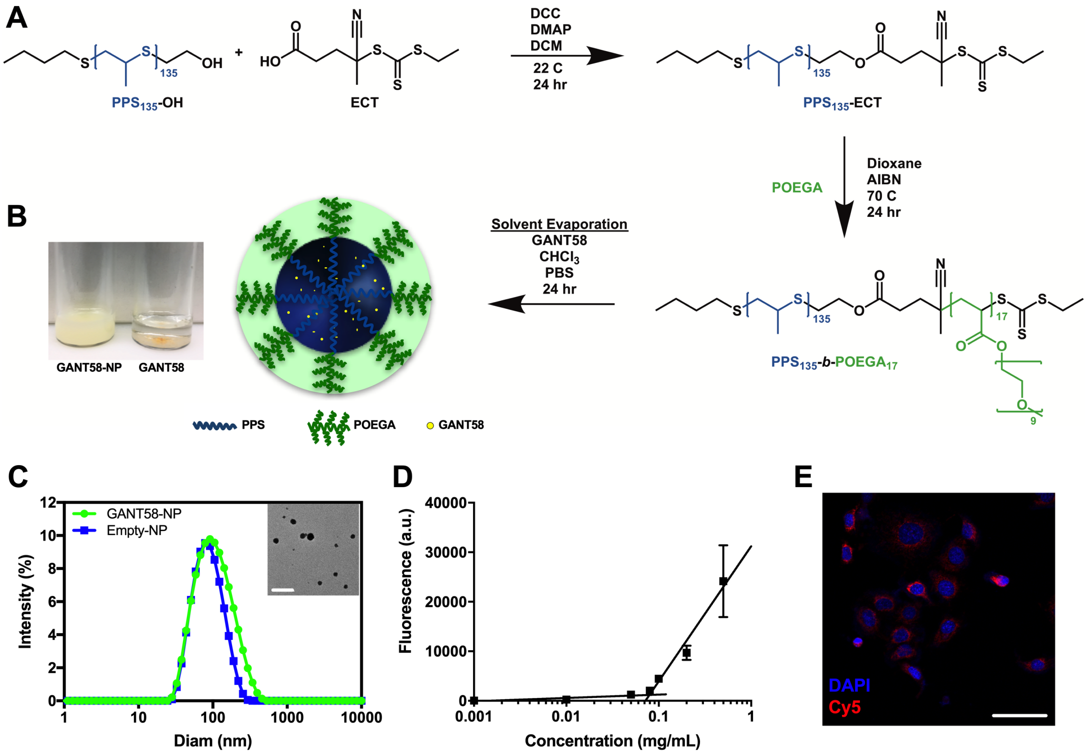

Figure 4.3. GANT58-NP fabrication and characterization. (A) Synthesis of PPS$_{135}$-b-POEGA$_{17}$ polymer and nanoparticle fabrication. (B) GANT58-NPs (2 mg/mL GANT58) are dispersed in PBS while insoluble free GANT58 (2 mg/mL) precipitates from solution. (C) Particle size distribution of GANT58-NPs and Empty-NPs measured by dynamic light scattering (DLS) indicate that both loaded and unloaded formulations have an average diameter < 100 nm. A TEM image (inset) reveals the spherical morphology of GANT58-NPs. Scale bar: 500 nm. (D) Critical micelle concentration (CMC) determined by Nile red assay. (E) Fluorescence microscopy image of MDA-MB-231-bone cells after 3 hr treatment with Cy5-labeled GANT58-NPs indicating significant NP uptake into cytoplasm of tumor cells.

NP control (**Figure 4.4A**). Additionally, MDA-MB-231-bone cells treated with increasing concentrations of free GANT58 or GANT58-NPs showed reduced nuclear Gli2 protein levels as shown by immunoblotting (**Figure 4.4B**). Nuclear protein levels of Gli2 in cells treated with 20 μM GANT58 or GANT58-NP was 48% and 57% of the control, respectively. Inhibition of Gli2 nuclear translocation by GANT58 significantly reduced PTHrP mRNA levels (**Figure 4.4C**). In contrast, Gli2 protein levels in the cytoplasm did not decrease in a dose-dependent manner following treatment with GANT58 or GANT58-NP, but cytoplasmic Gli2 protein levels were reduced (67 - 69% of the control) at the highest GANT58 dose tested (20 μM) (**Figure S4.3**). These findings show that GANT58 blocks translocation of Gli2 into the nucleus and consequent transcription of PTHrP.

To determine the effect of GANT58-NPs on tumor cell proliferation and viability, MDA-MB-231-bone cells treated with increasing drug concentrations were cultured up to 7 days. Cell proliferation assessed by MTS assay demonstrated that treatment with GANT58 or GANT58-NP significantly reduced tumor cell growth rate *in vitro* (**Figure 4.4D**). GANT58 and GANT58-NP also reduced cell viability and increased activation of caspase 3/7 (which is indicative of apoptosis) compared to vehicle-treated cells in the ApoTox-Glo assay (**Figure 4.4E**).

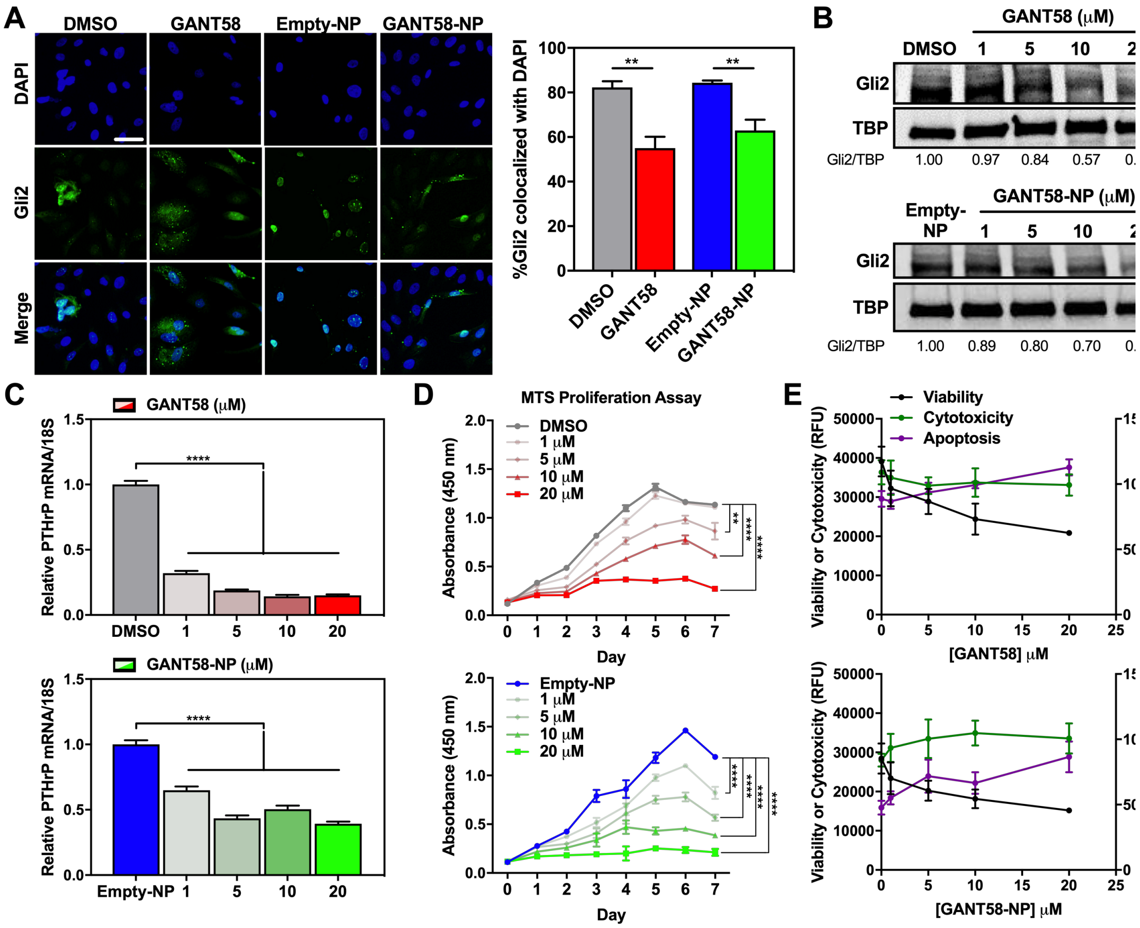

Figure 4.4. GANT58-NP treatment inhibits nuclear translocation of Gli2 and tumor cell proliferation. (A) Representative immunofluorescent images of Gli2 nuclear translocation *(left)* with quantification as measured by the Manders coefficient *(right)* after treatment with 20 μM GANT58 or GANT58-NP for 72 hr. Scale bar: 50 μm. (B) Nuclear Gli2 protein levels in MDA-MB-231-bone cells at 72 hr. (C) Expression of PTHrP mRNA for MDA-MB-231-bone cells treated with varying concentrations of free GANT58 (red), Empty-NP (blue), or GANT58-NP (green) for 48 hr. Gradient colors indicate varying doses: 1 μM (transparent), 5 μM, 10 μM, to 20 μM (opaque). (D) Tumor cell proliferation as assessed by MTS assay after treatment with free GANT58 or GANT58-NPs for 7 d. Gradient colors detailed above. (E) Viability, cytotoxicity, and apoptosis of MDA-MB-231-bone cells treated with free GANT58 or GANT58-NPs for 24 hr measured by ApoTox-Glo assay.

The effect of GANT58-NPs on hMSC proliferation and osteoblast differentiation was assessed to ensure that GANT58-NPs do not negatively impact osteoblast function and behavior. Proliferation (assessed by MTS assay) was not significantly affected by free GANT58, Empty-NPs, or GANT58-NPs at concentrations up to 20 μM (**Figure 4.5A**). Deposition of mineralized matrix by osteoblasts was assessed via Alizarin Red stain after 14 d culture in osteogenic media. Neither the DMSO vehicle nor free GANT58 significantly reduced Alizarin red staining compared to no treatment, and NP treatment had no negative effects on osteoblast mineralization (**Figure 4.5B**). Representative images of the Alizarin Red-stained cells show the deposition of mineralized matrix by the NP-treated osteoblasts (**Figure 4.5C**).

While GANT58 is an antagonist of Gli2 within tumor cells, its functional effect is to reduce secretion of PTHrP protein, which stimulates osteoblasts to express RANKL, a transmembrane protein that stimulates osteoclast differentiation. In order to investigate the effect of GANT58-NPs on osteoclast differentiation, an osteoclastogenesis assay utilizing a coculture of mouse bone marrow-derived stromal cells and MDA-MB-231s was performed. Osteoclast number was counted after 7 d culture in the presence of free GANT58, Empty-NP, and GANT58-NP via TRAP stain (**Figure 4.5D**). Osteoclasts were counted at 40x magnification and identified as TRAP+ (red/pink stain), multinucleated (≥ 3 nuclei) cells (**Figure 4.5E**). Osteoclast number showed a GANT58 dose-dependent decrease in osteoclasts for both the free GANT58 and GANT58-NP, while the Empty-NP had no effect on osteoclastogenesis. Representative 10x magnification images of the coculture show very few osteoclasts in the (-) vitamin D negative control and 20 μM GANT58-NP group, whereas the untreated tumor group exhibited extensive osteoclast maturation (**Figure 4.5F**).

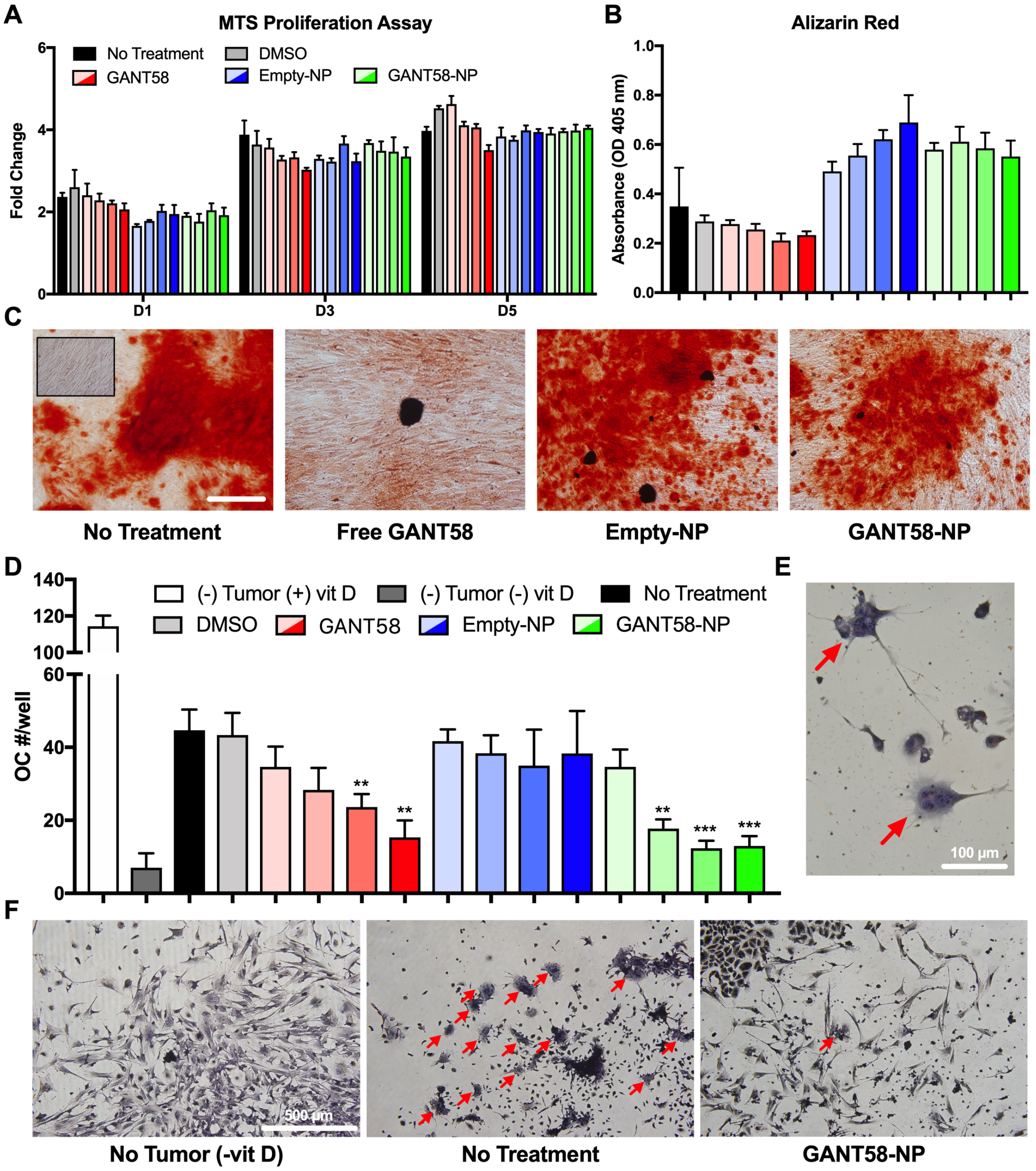

Figure 4.5. GANT58-NP treatment does not inhibit osteoblast function but reduces tumor-mediated osteoclastogenesis *in vitro*. (A) hMSCs treated with varying concentrations of free GANT58 (red), Empty-NP (blue), or GANT58-NP (green) were cultured for 1, 3, and 5 days (D1, D3, D5) and proliferation assessed by MTS assay. Gradient colors indicate varying doses: 1 µM (transparent), 5 µM, 10 µM, to 20 µM (opaque). (B) hMSCs were cultured in osteogenic medium treated with same dosage scheme described in (A). Deposition of mineralized matrix by osteoblasts was determined by absorbance of extracted Alizarin Red stain after 14 d of culture in osteogenic media. (C) Representative images of Alizarin Red staining of treated osteoblasts after 14 d culture in osteogenic media. Inset image shows hMSCs cultured in non-osteogenic media. Scale bar: 200 µm. (D) Number of osteoclasts (OC)/well in coculture treated with varying doses of GANT58, Empty-NP, and GANT58-NP after 6 days culture with MDA-MB-231 cells. (E) Multinucleated (3 or more nuclei) and TRAP positive cells were counted as OCs. Red arrows: OCs. (F) Representative images of negative control group (no tumor, -vitD), no treatment group, and 20 µM GANT58-NP treatment group. Red arrows: OCs.

After validation of *in vitro* efficacy, the biodistribution and pharmacokinetics (PK) of the PPS_{135}-b-$POEGA_{17}$ NPs and its cargo was evaluated via near-IR fluorescent dye grafting and loading (for NP and cargo tracking, respectively) of the micelles. First, Cy7 fluorophore-loaded PPS_{135}-b-$POEGA_{17}$ NPs (Cy7-NPs) were administered via i.v. tail vein injection to tibial tumor-bearing athymic nude mice to evaluate NP cargo biodistribution and PK of in tumor and organs of interest. Cy7 was chosen as the surrogate compound for GANT58 due to its strong near-IR fluorescence and solubility properties similar to that of GANT58. *In vivo* biodistribution was assessed in mice over time to observe Cy7 cargo localization in the tumor-bearing tibia site versus control tibia (**Figure 4.6A**). Near-IR *in vivo* imaging and Pearl image analysis software were used to quantify Cy7 fluorescence intensity in both the tumor and control ROI. Cy7 fluorescence intensity was significantly higher in the tumor-bearing tibia at each time point, indicating that the Cy7 cargo was preferentially localizing in the tumor bearing site.

Next, Cy7-grafted GANT58-NPs (GANT58-Cy7NPs) were administered via tail vein injection to track GANT58-Cy7NP biodistribution over time. Mice were sacrificed at predetermined time points and Cy7 fluorescence was measured in organs of interest *ex vivo*. At 24 hr post-injection, the tumor-bearing left hindlimb (LHL) had significantly increased uptake over the other long bones, while the liver and kidneys had the highest intensity as expected due to clearance by the mononuclear phagocyte system (MPS) (**Figure 4.6B**). Cy7 fluorescence steadily decreased over time in all long bones aside from the tumor-bearing hindlimb, indicating stable accumulation only in the bone-tumor site (**Figure 4.6C**). Similarly, there was a steady decrease in Cy7 fluorescence in all soft tissues aside from liver and kidney, whereas there was an increase in intensity as expected as the NPs were cleared from circulation (**Figure 4.6D**). To further validate the findings that the NPs are preferentially accumulating in the tumor, GFP intensity from the MDA-MB-231 cells was measured and spatially compared to the Cy7 fluorescence (**Figure 4.6E**). A strong colocalization was observed, suggesting the NP accumulation is primarily within the tumor site.

The PK profile of the GANT58-NPs was next investigated by measuring the blood circulation time of Cy5-grafted GANT58-NPs (GANT58-Cy5NPs). The findings from the biodistribution study suggested a significant concentration of NPs are still in circulation after 12 hr due to the increased NP accumulation in tumor, liver, and kidneys at the 24 hr time point. We designed the circulation time experiment to encompass both short (< 30 min) and long (> 12 hr) time periods for accurate measurement of the α and β phase circulation half-lives. After retroorbital injection of the GANT58-Cy5NPs, a tail nick method was used to draw small volumes (< 5 μL) of blood immediately post-injection (t=0) and at subsequent predetermined intervals up to 24 hr. These small blood volumes were then measured for Cy5 fluorescence intensity on a micro-volume plate using a fluorescence plate reader and NP concentration calculated from a standard curve. A rapid α-phase distributive half-life of 12.3 min was observed, after which there was a more gradual β-phase with a 28 hr half-life (**Figure 4.6F**). Even after 24 hr, roughly 15% of the initial NP dose was still in circulation, which supports the biodistribution findings showing increased uptake in tumor and clearance organs at 24 hr.

The promising *in vitro* results and preferential uptake in the tumor site presented compelling evidence that GANT58-NPs would successfully block tumor-induced bone destruction *in vivo* and possibly reduce tumor burden. To test this hypothesis, MDA-MB-231-bone cells were inoculated into the left tibiae of female athymic nude mice. After 4 days to allow tumor establishment, mice were treated daily with GANT58-NPs (8 mg/kg GANT58) or Empty-NPs via tail vein injection (**Figure 4.7A**). Empty-NPs were chosen as the control due to the *in vitro* results suggesting the positive effect the Empty-NPs may have on osteoblast differentiation.

Substantial osteolytic lesions were observed radiographically in the mice treated only with the Empty-NPs after 4 weeks, while smaller and fewer lesions were visible in mice treated with GANT58-NP (**Figure 4.7B**). Quantitative assessment of both lesion area and

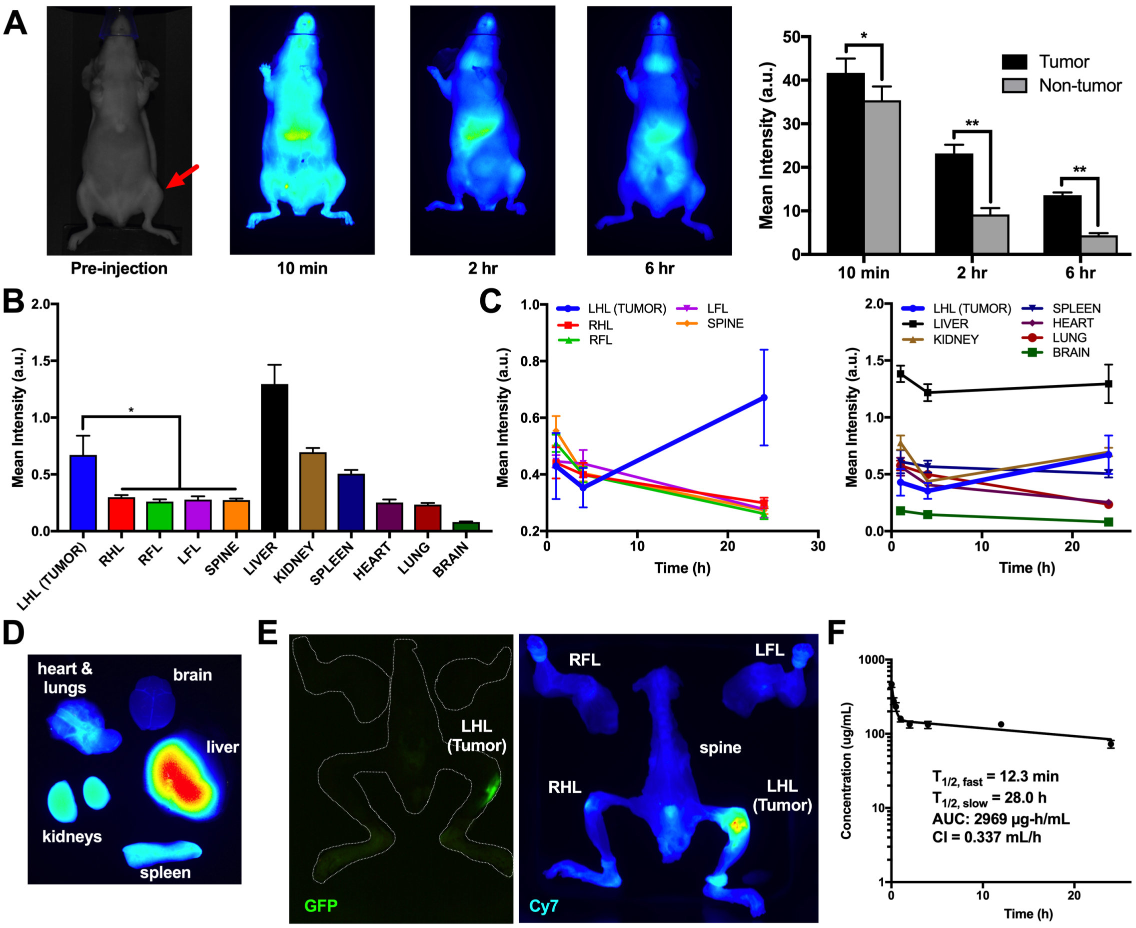

Figure 4.6. GANT58-NPs accumulate in tumor and demonstrate prolonged blood circulation. (A) Cy7-loaded NPs (Cy7-NPs) time course biodistribution in tumor-bearing mice. Cy7 fluorescence is significantly higher in the tumor-bearing tibia (red arrow) compared to the contralateral control. (B) Cy7-grafted GANT58-NPs biodistribution *ex vivo* analysis at 24 hr shows significantly higher Cy7 fluorescence in the tumor-bearing hindlimb compared to other long bones. L(R)HL = left (right) hindlimb; L(R)FL = left (right) forelimb. (C) Time-course *ex vivo* analysis of Cy7-grafted GANT58-NPs shows that NPs slowly accumulate in tumor over 24 hr period. (D) Representative soft tissue Cy7 fluorescence at 24 hr post-NP injection. (E) GFP imaging (tumor) and Cy7 fluorescence (NP) confirm colocalization of NPs within the tumor site. (F) Circulation time of Cy5-grafted GANT58-NPs as assessed by tail nick method.

number confirmed that the osteolytic lesions in the GANT58-NP-treated mice were significantly smaller and fewer (**Figure 4.7C-D**).

After sacrifice, mouse tibiae were examined by μCT to assess the effects of the drug on bone morphometric properties. Mice treated with the GANT58-NPs had 2.5-fold higher ($p < 0.001$) BV/TV than those treated with Empty-NPs and 22% lower ($p < 0.05$) BV/TV than the untreated control (**Figure 4.7E**). Tb.Sp. in the GANT58-NP group was 34% lower ($p < 0.05$) than the Empty-NP group and 48% higher ($p < 0.05$) than the untreated control (**Figure 4.7F**). Similarly, trabecular number (Tb.N.) in the GANT58-NP group trended higher than the Empty-NP group and was 28% lower than the untreated control (**Figure 4.7G**). 3D μCT renderings of representative tibiae from each group further demonstrate the significant tumor-induced bone destruction in the mice treated with Empty-NPs compared to those treated with GANT58-NPs (**Figure 4.7H**). Histomorphometric analysis of the tibiae showed no significant differences in tumor burden between groups (**Figure 4.7I-J**).

In order to establish the rigor of these findings, another human osteolytic cancer cell line was tested in the same intratibial model. In this experiment, a bone-metastatic variant of a squamous non-small cell lung carcinoma line, RWGT2-bone, was used and the same bone outcomes were assessed. Again, BV/TV was significantly higher in the mice treated with GANT58-NPs than those treated with Empty-NPs (**Figure 4.7K**). Radiograph analysis also showed significant reduction in lesion area and number in GANT58-NP-treated mice (**Figure S4.4A**). Further, there was no significant difference in BV/TV in GANT58-NP-treated mice and the non-tumor-bearing control tibiae (**Figure 4.7K**). Other morphometric parameters, however, were not significantly different between the GANT58-NP and Empty-NP groups (**Figure S4.4B**). 3D μCT renderings of representative tibiae from each group again demonstrate the tumor-induced bone destruction in the mice treated with Empty-NPs compared to those treated with GANT58-NPs (**Figure 4.7L**). It is important to note that the RWGT2-bone cell line was not as aggressive as the MDA-MB-231-bone line, as indicated by the higher BV/TV in the RWGT2-bone Empty-NP group compared to the same group in the MDA-MB-231-bone experiment. This lower tumor burden could explain the diminished significance in μCT outcomes for the GANT58-NP treatment group relative to controls for this study relative to the MDA-MB-231 study.

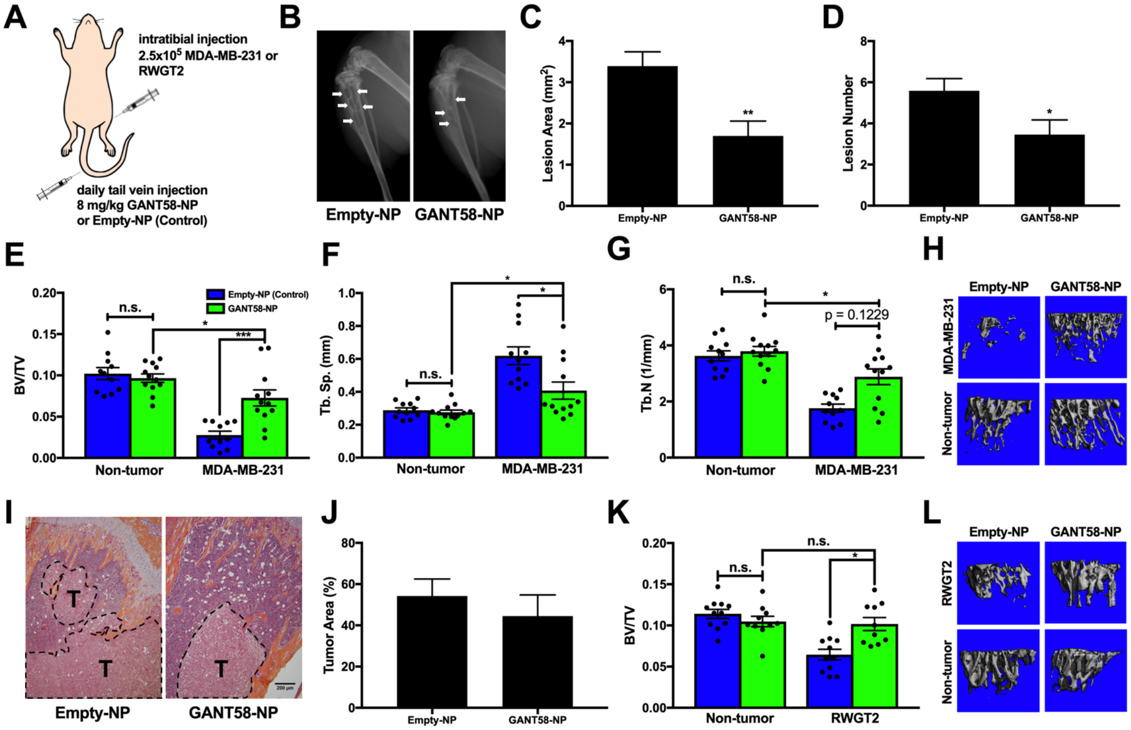

Figure 4.7. GANT58-NP treatment reduces tumor-induced osteolysis in mouse model of late bone metastasis in multiple tumor cell lines. (A) Tumor-inoculation and treatment scheme for intratibial model of bone metastasis. (B) Representative radiographic images of control (Empty-NP) and GANT58-NP treated mice at 4-weeks post-tumor (MDA-MB-231) inoculation. Arrows indicate osteolytic bone lesions. (C) Lesion area and (D) lesion number as assessed by radiographic analysis are significantly reduced in GANT58-NP treated mice. (E-G) μCT analysis of tibiae bone volume fraction (BV/TV), trabecular separation (Tb. Sp.), and trabecular number (Tb. N.) showed significantly improved bone quality in mice treated with GANT58-NPs. (H) Representative μCT reconstructions of GANT58-NP-treated, Empty-NP-treated, and contralateral, non-tumor bearing tibiae. (I) Representative H&E stained sections and (J) histomorphometric analysis of tumor area (indicated by T) in Empty-NP-treated and GANT58-NP-treated in mice inoculated with MDA-MB-231 cells. Scale bar: 200 μm. (K) Intratibial model repeated with RWGT2 cell line, and BV/TV again showed improved bone quality in GANT58-NP treated mice. (L) Representative μCT reconstructions of GANT58-NP-treated, Empty-NP-treated, and contralateral, non-tumor bearing tibiae.

The intratibial model of bone metastasis was informative in showing that GANT58 is effective in blocking bone destruction induced by established tumors, but its effect on tumor metastasis could not be elucidated using this model. Therefore, an intracardiac model of bone metastasis was used in order to investigate the effect of GANT58-NPs on blocking tumor metastasis in addition to bone destruction. In this experiment, mice were injected with MDA-MB-231 cells via intracardiac injection and were subsequently divided into two cohorts. The first cohort, denoted the "immediate" group, was then divided into treatment and control subgroups and immediately treated via tail vein injection with either GANT58-NPs (treatment) or Empty-NPs (control). The second cohort of mice, denoted the "delayed" group, was also divided into treatment and control subgroups, but was allowed 7 days for tumor establishment before starting treatment (**Figure 4.8A**).

Tibiae and femurs were scanned by μCT after sacrifice, and subsequent observation of histological sections showed that tumor presence was more substantial in the femur than in the tibia. Thus, the femur was chosen for thorough μCT and histological analysis. μCT analysis revealed that there was significantly higher BV/TV and Tb. Th. in the mice that were treated with GANT58-NPs, indicating reduced bone destruction and improved bone quality in GANT58-NP-treated mice. However, there was no significant difference between the mice treated immediately and the mice that received delayed treatment (**Figure 4.8B**). Histological analysis, however, showed no significant reduction in tumor burden across all groups (**Figure 4.8C**). Taken together, these findings are consistent with those of the intratibial model where GANT58-NP treatment significantly improved bone outcomes, but tumor burden was not significantly affected. While more studies are needed to further characterize potential effects on tumor growth, these studies strongly demonstrate that GANT58-NPs reduce tumor-induced bone destruction in two mouse models of bone metastasis.

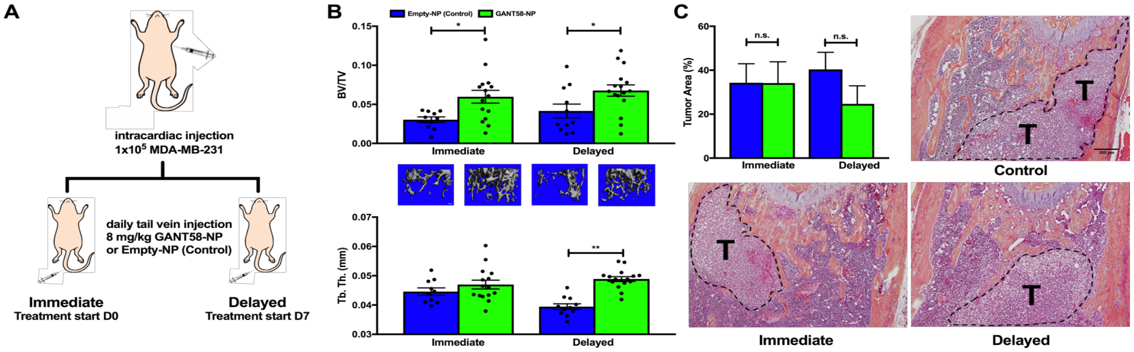

Figure 4.8. GANT58-NP treatment reduces tumor-induced osteolysis in early metastasis model of tumor-induced bone disease. (A) Tumor-inoculation and treatment scheme for intracardiac model of bone metastasis. (B) µCT analysis of tibiae bone volume fraction (BV/TV) and trabecular thickness (Tb. Th.) showed significantly improved bone quality in mice treated with GANT58-NPs. (C) Representative H&E stained sections histomorphometric analysis of tumor area (indicated by T) in Empty-NP-treated and GANT58-NP-treated in mice inoculated with MDA-MB-231 cells. Scale bar: 200 µm.

In addition to efficacy, successful clinical translation of the GANT58-NPs hinges upon safety of the treatment at therapeutic doses. To test the safety profile of the GANT58-NPs, blood was drawn at time of sacrifice for the cohort of mice in the intratibial study after having received GANT58-NP or Empty-NP treatment daily at 8 mg/kg GANT58 (or equivalent dose of Empty-NP) for 4 weeks. Biochemical analysis of blood serum markers for liver and kidney toxicity was performed. There was no significant increase in aspartate aminotransferase (AST), alanine aminotransferase (ALT), or blood urea nitrogen (BUN) levels above two standard deviations from average levels reported by the animal supplier (Envigo) (**Figure S4.5A**). Further, histological sections of the liver and kidney of the same mice were observed by a blinded, board certified pathologist and there was no evident toxicity in either group (**Figure S4.5B**). Metastatic disease accounts for over 90% of cancer-related deaths and therefore remains a major clinical concern.[65] In patients with bone metastases, standard-of-care RANKL and osteoclast inhibitors improve quality of life but do not target tumor-specific aberrations in signaling that cause TIBD. We identified Gli2 as a promising therapeutic target for bone metastases based on our previous studies establishing its overexpression in bone-destructive cell lines.[26,30] While free GANT58 did not inhibit bone resorption *in vivo* due to its poor solubility and PK, GANT58-NPs significantly reduced bone resorption in intracardiac and intratibial injection models of TIBD using bone-metastatic breast and lung cancer cell lines.

Since RANKL and osteoclast inhibitors target osteoclast function throughout the body, osteoblast activity, which is tightly coupled with and triggered by bone resorption, is also decreased, which severely impairs bone remodeling and fracture healing.[66,67] Consistent with these findings, other studies have reported dose-dependent inhibitory effects of bisphosphonates on osteoblast proliferation, differentiation, and mineralization.[68,69] In contrast, the tumor-targeted MTA GANT58 did not inhibit osteoblast hMSC proliferation or deposition of mineralized matrix by osteoblasts (**Fig. 5A-C**). GANT58 blocked nuclear translocation of Gli2 and consequent PTHrP expression (**Fig. 4A-C**). Considering that PTHrP stimulates expression of RANKL (a stimulator of osteoclast formation) by osteoblasts, we investigated the effects of GANT58 treatment on osteoclastogenesis *in vitro*. GANT58 treatment of mouse bone marrow-derived cells co-cultured with MDA-MB-231-bone tumor cells significantly inhibited osteoclastogenesis (**Fig. 5D-F**). These findings suggest that GANT58 blocks tumor-induced stimulation of osteoclastogenesis without impairing osteoblast differentiation.

While the current study establishes the therapeutic potential of Gli2 inhibition to block tumor-mediated bone destruction, other studies have previously utilized nanomedicine strategies for delivery of Hh pathway inhibitors to tumors. Delivery of Hedgehog Pathway Inhibitor-1 (HPI-1) has been investigated for treatment of medulloblastoma and hepatocellular carcinoma.[43,70] While these studies showed that HPI-1 nanoparticles inhibited systemic metastases in an orthotopic model of human hepatocellular carcinoma, the effects of Hh inhibition on bone metastases were not investigated.[43,70] Nanomedicine strategies have also been applied to inhibit bone metastases by delivering conventional chemotherapies to reduce bone tumor burden in the bone marrow.[71,72] These studies found that nanoencapsulated docetaxel and paclitaxel reduced tumor burden, but the effects of the drugs on bone were not investigated extensively *in vivo*. Other studies have reported that conventional chemotherapies cause DNA damage and apoptotic cell death in human bone marrow cells, and that these treatments negatively affect trabecular bone microarchitecture and mechanical properties.[73,74] Thus, targeted delivery of chemotherapies to tumors in bone is anticipated to have adverse effects on the bone microenvironment and warrants further investigation. In contrast, nanoencapsulated GANT58 blocked tumor-induced bone destruction in tumor-bearing bones, but the drug did not inhibit mineralization (**Fig. 5B-C**).

GANT58-NPs inhibited tumor proliferation (**Fig. 4D**) and viability (**Fig. 4E**) *in vitro*, but cytotoxicity showed only modest changes with increasing GANT58 dose (**Fig. 4E**). These data suggest that GANT58 inhibits tumor growth but is not cytotoxic to tumor cells, which is consistent with previous studies reporting that GANT58 and GANT61 inhibit tumor proliferation by inducing cytostasis (cell cycle arrest) and early phase apoptosis rather than direct cytotoxic killing.[28,33,75] Our previous study showed that genetic inhibition of Gli2 using an Engrailed repressor construct significantly attenuated the ability of cancer cells to colonize bone (only micrometastases were observed) and induce osteolysis *in vivo*.[26] However, GANT58-NPs did not significantly reduce tumor burden in either the intratibial or intracardiac models. Micellar nanoparticles are passively targeted to tumor sites via the enhanced permeability and retention (EPR) effect, which requires the tumor vasculature to be permeable or "leaky" in order for nanoparticles to accumulate within the tumoral interstitial space.[76] Thus, GANT58-NPs likely do not sufficiently accumulate at bone-tumor sites until larger, vascularized tumors are established. In future studies, we will evaluate the nanoparticle carrier to determine if conferring bone-binding affinity to the polymer chemistry will improve targeted delivery to bone and block initial bone tumor establishment.

There may also be spatial variation in the tumor cell responsiveness to GANT58 within the bone and bone marrow. Matrix rigidity in the bone microenvironment is a key mediator of Gli2 expression in bone-metastatic tumor cells. Gli2 expression was significantly increased in patient bone-metastatic tumors but not soft tissue tumors (**Fig. 1A-B**) or brain and lung metastases (**Fig. 1C**). Furthermore, Gli2 is not expressed on collagen-like (30 MPa) substrates but is overexpressed on bone-like (>100 MPa) substrates *in vitro.*[77] Considering the relatively low elastic modulus of bone marrow (0.25–24.7 kPa),[78] tumor cells growing in the marrow space are anticipated to express low levels of Gli2 and are therefore likely to be less sensitive to GANT58. However, as tumor cells approach bony trabeculae, they overexpress Gli2 and PTHrP in response to the rigid (>100 MPa) mineralized bone matrix.[77,79] Thus, GANT58 is anticipated to inhibit tumor cell proliferation, expression of PTHrP, and the transition to the bone-destructive phenotype in tumor cells within close proximity of bone but potentially have less direct impact on tumor cells in the marrow space.

Previous studies have also implied the importance of tumor-stromal interactions in promoting bone metastasis.[6] Recent work has elucidated new molecular mechanisms and therapeutic targets for prevention of bone metastasis and/or halting the vicious cycle of bone destruction. In addition to Hh signaling, Notch signaling has been implicated in bone metastasis, and the Notch ligand Jagged1 drives tumor progression in bone.[80] A subsequent study developed a Jagged1 antibody that not only reduced incidence of bone metastasis, but also sensitized the tumor to chemotherapy and reduced tumor recurrence.[81] Another recent study showed that crosstalk between ROR1-HER3 and the Hippo-YAP pathway promotes breast cancer bone metastasis and identified multiple new therapeutic targets for inhibition.[82] While these tumor-targeted approaches offer the potential of reducing tumor burden in bone, inter-patient heterogeneity may limit their ability to benefit all bone-metastatic cancer patients.[83] In patients with metastatic cancer, PTHrP is expressed in > 90% of bone-residing tumors compared to < 20% at non-bony sites.[84] Similarly, we show that Gli2 is also overexpressed in bone-metastatic tumors from various primary sites (**Fig. 1A-B**). The prevalence of Gli2 and PTHrP expression in bone suggests that GANT58 treatment is likely to be effective in a broad spectrum of patients suffering from bone metastases, which is supported by our observations of bone protection by GANT58-NPs across both breast and lung cancer models. Thus, combined delivery of GANT58, which blocks the transition to the bone-destructive phenotype, with targeted therapies or conventional chemotherapeutics that block tumor growth in the bone marrow could potentially slow the progress of TIBD and improve patient quality of life.

4.5. Conclusion

Polymeric NP encapsulation of GANT58 provided an injectable aqueous dispersion that significantly decreased bone lesions and increased trabecular bone volume in two breast cancer models of bone metastasis (intratibial and intracardiac). Importantly, GANT58-NPs did not alter hMSC proliferation or osteoblast mineralization, essential processes for bone remodeling and fracture repair in cancer patients. Pharmacokinetic and biodistribution analysis showed the GANT58-NPs exhibit an extensive circulation time, preferentially localize at the tumor site, and show no evidence of cytotoxicity in the liver or kidneys, the major organs through which the GANT58-NPs are cleared. Thus, the efficacy and safety profile of GANT58-NPs highlight its potential as a new therapy for patients with TIBD.

4.6. Supplementary Information

Table S4.1. Clinical features of patient tumor samples.

Patient ID	Age (years)	Gender	Primary Site	Histological Type	Metastatic Site	Chemo-therapy	Radio-therapy	Pathologic Fracture
45478	38	F	Soft Tissue	Myxoid sarcoma	-	Y	N	N
45479	69	M	Soft Tissue	Myxoid sarcoma	-	N	N	N
52086	22	M	Soft Tissue	Synovial sarcoma	-	Y	N	N
50892	58	F	Bone	Ewing's sarcoma	Kidney	Y	Y	N
48233	59	F	Breast	Carcinoma*	Humerus	N	Y	Y
48538	80	F	Breast	Carcinoma†	Femur	N	Y	Y
51392	69	F	Breast	Carcinoma‡	Femur	Y	Y	Y
48081	55	M	Kidney	Renal cell carcinoma	Femur	Y	Y	Y
48459	73	M	Kidney	Renal cell carcinoma	Humerus	N	N	N
48640	77	M	Kidney	Renal cell carcinoma	Femur	N	N	N
48641	77	M	Kidney	Renal cell carcinoma	Tibia	N	N	N
48909	50	M	Kidney	Renal cell carcinoma	Femur	N	N	Y
49652	63	F	Lung	Non-small cell carcinoma	Humerus	Y	Y	Y
53159	77	M	Lung	Non-small cell carcinoma	Humerus	Y	Y	N
52963	69	M	Lung	Squamous cell carcinoma	Humerus	N	N	Y
53107	67	M	Lung	Squamous cell carcinoma	Femur	Y	Y	Y
50080	80	M	Prostate	Adenocarcinoma	Femur	Y	N	N
48089	54	F	Thyroid	Follicular carcinoma	Pelvis	Y	Y	N
52766	69	M	Thyroid	Follicular carcinoma	Pelvis	N	N	Y
49224	29	F	Unknown	Squamous cell carcinoma	Fibula	Y	Y	Y

ER: estrogen receptor; PR: progesterone receptor; HER2: human epidermal growth factor receptor 2
*Receptor status unknown; †ER+/PR+; ‡ER+/PR-/HER2+

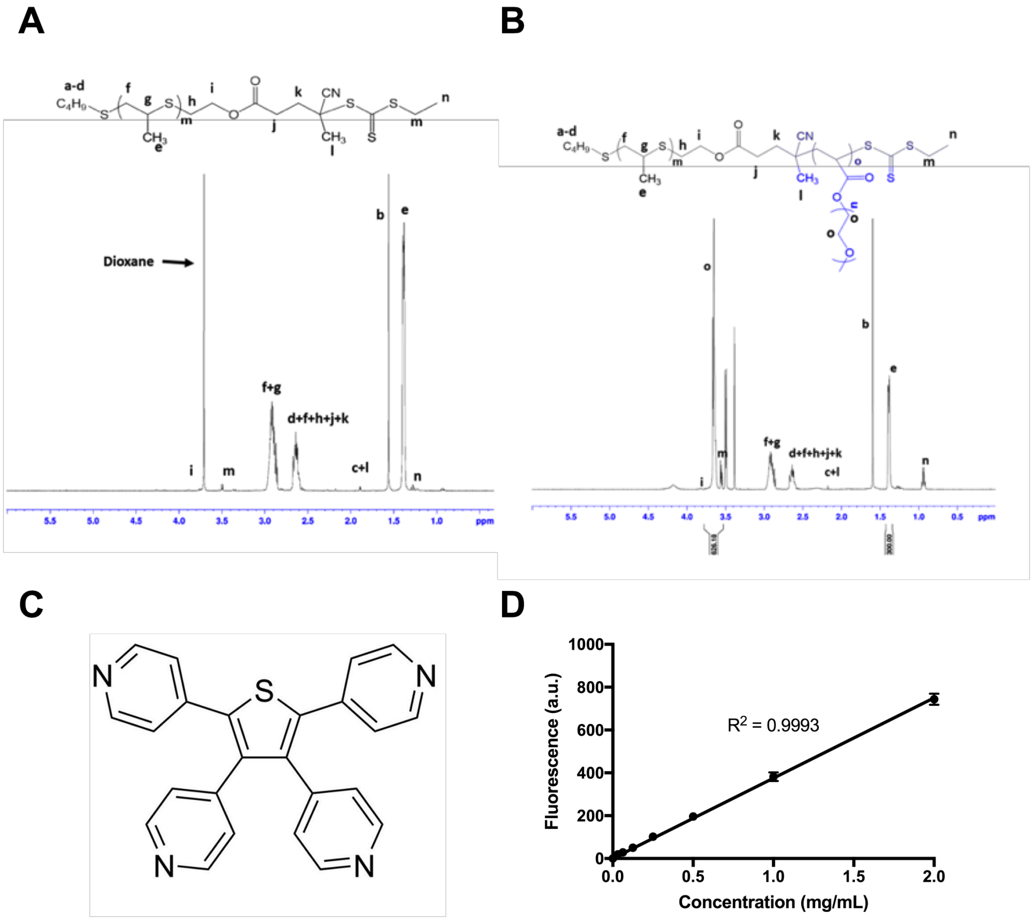

Figure S4.1. PPS135-b-POEGA17 synthesis and GANT58 characterization. (A) 1H-NMR of PPS135-ECT and (B) PPS135-b-POEGA17. (C) GANT58 chemical structure. (D) GANT58 fluorescence standard

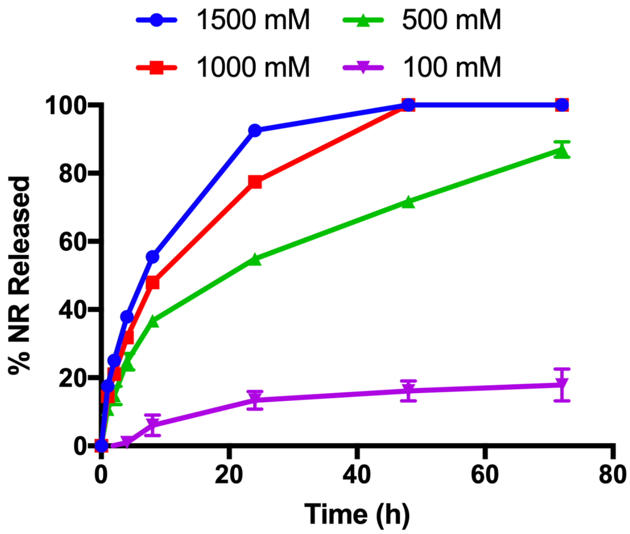

Figure S4.2. H_2O_2 concentration-dependent release of Nile red (NR) from NPs. H_2O_2 concentrations were chosen to include physiologically relevant ROS concentrations (~100-400 mM) based on calculations from published values for macrophage ROS generation rates.

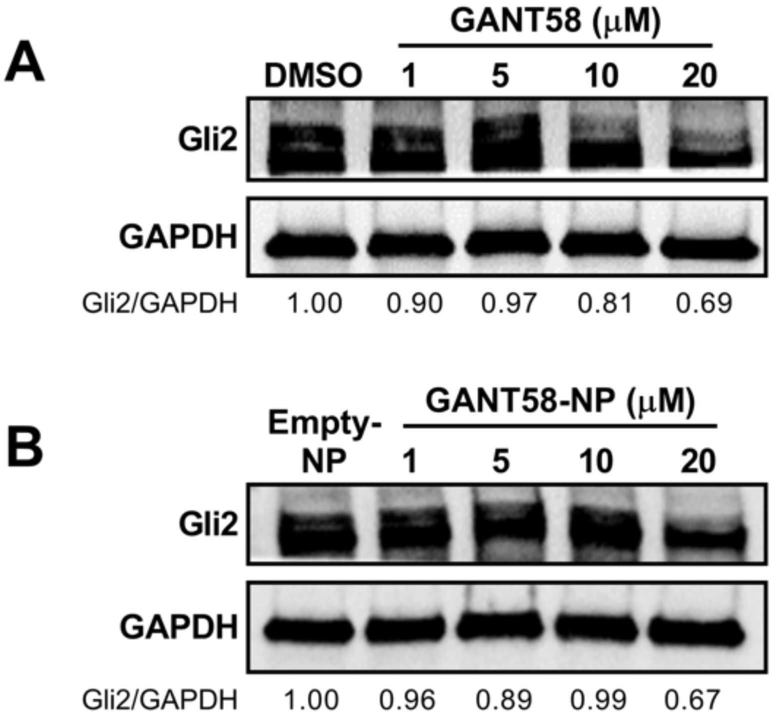

Figure S4.3. Western blots of Gli2 cytoplasmic protein after 72 hr treatment with (A) free GANT58 and (B) GANT58-NPs.

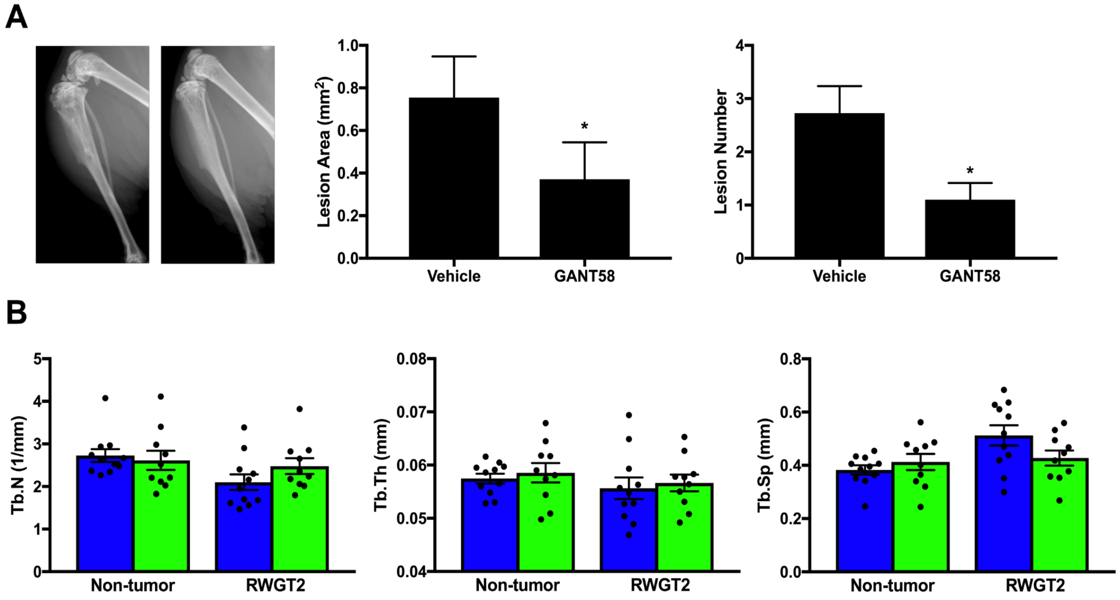

Figure S4.4. RWGT2 Faxitron and μCT analysis. (A) Representative radiographic images of control (Empty-NP) and GANT58-NP treated mice at 4-weeks post-tumor (RWGT2) inoculation. (B) μCT analysis of tibiae Tb. N., Tb. Th., and Tb. Sp. in mice treated with Empty-NPs (blue) or GANT58-NPs (green) after sacrifice at 4 weeks.

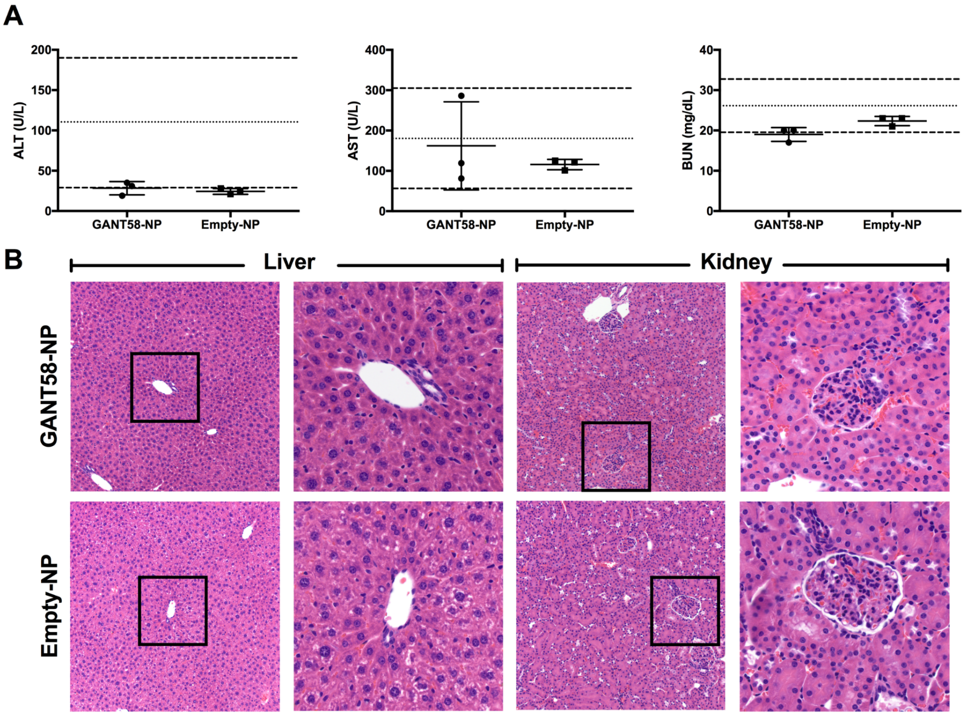

Figure S4.5. GANT58-NPs elicit minimal systemic toxicity. (A) Serum chemical markers of liver (ALT and AST) and kidney (BUN) toxicity measured after 8 mg/kg GANT58-NP i.v. treatment 5 days/week for 4 weeks. (B) Representative images of liver and kidney at 10x and 20x with GANT58-NP and Empty-NP treatment.

References

(1) Buijs, J. T.; van der Pluijm, G. Osteotropic Cancers: From Primary Tumor to Bone. *Cancer Lett.* **2009**, *273* (2), 177–193.

(2) Coleman, R. E. Clinical Features of Metastatic Bone Disease and Risk of Skeletal Morbidity. *Clin. Cancer Res.* **2006**, *12* (20 Pt 2), 6243s–6249s.

(3) Saad, F.; Lipton, A.; Cook, R.; Chen, Y.-M.; Smith, M.; Coleman, R. Pathologic Fractures Correlate with Reduced Survival in Patients with Malignant Bone Disease. *Cancer* **2007**, *110* (8), 1860–1867.

(4) Mundy, G. R. Mechanisms of Bone Metastasis. *Cancer* **1997**, *80* (8), 1546–1556.

(5) Sterling, J. A.; Edwards, J. R.; Martin, T. J.; Mundy, G. R. Advances in the Biology of Bone Metastasis: How the Skeleton Affects Tumor Behavior. *Bone*. 2011, pp 6–15.

(6) Weilbaecher, K. N.; Guise, T. A.; McCauley, L. K. Cancer to Bone: A Fatal Attraction. *Nat Rev Cancer* **2011**, *11* (6), 411–425.

(7) Sousa, S.; Clézardin, P. Bone-Targeted Therapies in Cancer-Induced Bone Disease. *Calcif. Tissue Int.* **2018**, *102* (2), 227–250.

(8) Edwards, B. J.; Sun, M.; West, D. P.; Guindani, M.; Lin, Y. H.; Lu, H.; Hu, M.; Barcenas, C.; Bird, J.; Feng, C.; et al. Incidence of Atypical Femur Fractures in Cancer Patients: The MD Anderson Cancer Center Experience. *J. Bone Miner. Res.* **2016**, *31* (8), 1569–1576.

(9) Yang, S. P.; Kim, T. W. B.; Boland, P. J.; Farooki, A. Retrospective Review of Atypical Femoral Fracture in Metastatic Bone Disease Patients Receiving Denosumab Therapy. *Oncologist* **2017**, *22* (4), 438–444.

(10) Bamias, A.; Kastritis, E.; Bamia, C.; Moulopoulos, L. A.; Melakopoulos, I.; Bozas, G.; Koutsoukou, V.; Gika, D.; Anagnostopoulos, A.; Papadimitriou, C.; et al. Osteonecrosis of the Jaw in Cancer after Treatment with Bisphosphonates: Incidence and Risk Factors. *J. Clin. Oncol.* **2005**, *23* (34), 8580–8587.

(11) Coleman, R.; Woodward, E.; Brown, J.; Cameron, D.; Bell, R.; Dodwell, D.; Keane, M.; Gil, M.; Davies, C.; Burkinshaw, R.; et al. Safety of Zoledronic Acid and Incidence of Osteonecrosis of the Jaw (ONJ) during Adjuvant Therapy in a Randomised Phase III Trial (AZURE: BIG 01--04) for Women with Stage II/III Breast Cancer. *Breast Cancer Res. Treat.* **2011**, *127* (2), 429–438.

(12) Smith, M. R.; Saad, F.; Coleman, R.; Shore, N.; Fizazi, K.; Tombal, B.; Miller, K.; Sieber, P.; Karsh, L.; Damião, R.; et al. Denosumab and Bone-Metastasis-Free Survival in Men with Castration-Resistant Prostate Cancer: Results of a Phase 3, Randomised, Placebo-Controlled Trial. *Lancet* **2012**, *379* (9810), 39–46.

(13) Fan, C.; Georgiou, K. R.; Morris, H. A.; McKinnon, R. A.; Keefe, D. M. K.; Howe, P. R.; Xian, C. J. Combination Breast Cancer Chemotherapy with Doxorubicin and Cyclophosphamide Damages Bone and Bone Marrow in a Female Rat Model. *Breast Cancer Res. Treat.* **2017**, *165* (1), 41–51.

(14) Green, D. E.; Rubin, C. T. Consequences of Irradiation on Bone and Marrow Phenotypes, and Its Relation to Disruption of Hematopoietic Precursors. *Bone* **2014**, *63*, 87–94.

(15) Ingham, P. W.; McMahon, A. P. Hedgehog Signaling in Animal Development: Paradigms and Principles. *Genes and Development*. 2001.

(16) Briscoe, J.; Therond, P. P. The Mechanisms of Hedgehog Signalling and Its Roles in

Development and Disease. *Nat. Rev. Mol. Cell Biol.* **2013**, *14* (7), 416–429.

(17) Pasca di Magliano, M.; Hebrok, M. Hedgehog Signalling in Cancer Formation and Maintenance. *Nat. Rev. Cancer* **2003**, *3* (12), 903–911.

(18) Kubo, M.; Nakamura, M.; Tasaki, A.; Yamanaka, N.; Nakashima, H.; Nomura, M.; Kuroki, S.; Katano, M. Hedgehog Signaling Pathway Is a New Therapeutic Target for Patients with Breast Cancer. *Cancer Res.* **2004**.

(19) Karhadkar, S. S.; Bova, G. S.; Abdallah, N.; Dhara, S.; Gardner, D.; Maitra, A.; Isaacs, J. T.; Berman, D. M.; Beachy, P. A. Hedgehog Signalling in Prostate Regeneration, Neoplasia and Metastasis. *Nature* **2004**, *431* (7009), 707–712.

(20) Yuan, Z.; Goetz, J. A.; Singh, S.; Ogden, S. K.; Petty, W. J.; Black, C. C.; Memoli, V. A.; Dmitrovsky, E.; Robbins, D. J. Frequent Requirement of Hedgehog Signaling in Non-Small Cell Lung Carcinoma. *Oncogene* **2007**, *26* (7), 1046–1055.

(21) LoRusso, P. M.; Rudin, C. M.; Reddy, J. C.; Tibes, R.; Weiss, G. J.; Borad, M. J.; Hann, C. L.; Brahmer, J. R.; Chang, I.; Darbonne, W. C.; et al. Phase I Trial of Hedgehog Pathway Inhibitor Vismodegib (GDC-0449) in Patients with Refractory, Locally Advanced or Metastatic Solid Tumors. *Clin. cancer Res. an Off. J. Am. Assoc. Cancer Res.* **2011**, *17* (8), 2502–2511.

(22) Jimeno, A.; Weiss, G. J.; Miller, W. H. J.; Gettinger, S.; Eigl, B. J. C.; Chang, A. L. S.; Dunbar, J.; Devens, S.; Faia, K.; Skliris, G.; et al. Phase I Study of the Hedgehog Pathway Inhibitor IPI-926 in Adult Patients with Solid Tumors. *Clin. Cancer Res.* **2013**, *19* (10), 2766–2774.

(23) Wagner, A. J.; Messersmith, W. A.; Shaik, M. N.; Li, S.; Zheng, X.; McLachlan, K. R.; Cesari, R.; Courtney, R.; Levin, W. J.; El-Khoueiry, A. B. A Phase I Study of PF-04449913, an Oral Hedgehog Inhibitor, in Patients with Advanced Solid Tumors. *Clin. Cancer Res.* **2015**, *21* (5), 1044–1051.

(24) Metcalfe, C.; de Sauvage, F. J. Hedgehog Fights Back: Mechanisms of Acquired Resistance against Smoothened Antagonists. *Cancer Res.* **2011**, *71* (15), 5057–5061.

(25) Atwood, S. X.; Sarin, K. Y.; Whitson, R. J.; Li, J. R.; Kim, G.; Rezaee, M.; Ally, M. S.; Kim, J.; Yao, C.; Chang, A. L. S.; et al. Smoothened Variants Explain the Majority of Drug Resistance in Basal Cell Carcinoma. *Cancer Cell* **2015**, *27* (3), 342–353.

(26) Johnson, R. W.; Nguyen, M. P.; Padalecki, S. S.; Grubbs, B. G.; Merkel, A. R.; Oyajobi, B. O.; Matrisian, L. M.; Mundy, G. R.; Sterling, J. A. TGF-Beta Promotion of Gli2-Induced Expression of Parathyroid Hormone-Related Protein, an Important Osteolytic Factor in Bone Metastasis, Is Independent of Canonical Hedgehog Signaling. *Cancer Res.* **2011**, *71* (3), 822–831.

(27) Johnson, R. W.; Merkel, A. R.; Page, J. M.; Ruppender, N. S.; Guelcher, S. A.; Sterling, J. A. Wnt Signaling Induces Gene Expression of Factors Associated with Bone Destruction in Lung and Breast Cancer. *Clin. Exp. Metastasis* **2014**, *31* (8), 945–959.

(28) Lauth, M.; Bergstrom, A.; Shimokawa, T.; Toftgard, R. Inhibition of GLI-Mediated Transcription and Tumor Cell Growth by Small-Molecule Antagonists. *Proc. Natl. Acad. Sci.* **2007**, *104* (20), 8455–8460.

(29) Hyman, J. M.; Firestone, A. J.; Heine, V. M.; Zhao, Y.; Ocasio, C. a; Han, K.; Sun, M.; Rack, P. G.; Sinha, S.; Wu, J. J.; et al. Small-Molecule Inhibitors Reveal Multiple Strategies for Hedgehog Pathway Blockade. *Proc. Natl. Acad. Sci. U. S. A.* **2009**, *106* (33), 14132–14137.

(30) Sterling, J. a.; Oyajobi, B. O.; Grubbs, B.; Padalecki, S. S.; Munoz, S. a.; Gupta, A.; Story, B.; Zhao, M.; Mundy, G. R. The Hedgehog Signaling Molecule Gli2 Induces Parathyroid Hormone-Related Peptide Expression and Osteolysis in Metastatic Human Breast Cancer Cells. *Cancer Res.* **2006**, *66* (15), 7548–7553.

(31) Cannonier, S. A.; Sterling, J. A. The Role of Hedgehog Signaling in Tumor Induced Bone Disease. *Cancers (Basel).* **2015**, *7* (3), 1658–1683.

(32) Neelakantan, D.; Zhou, H.; Oliphant, M. U. J.; Zhang, X.; Simon, L. M.; Henke, D. M.; Shaw, C. A.; Wu, M.-F.; Hilsenbeck, S. G.; White, L. D.; et al. EMT Cells Increase Breast Cancer Metastasis via Paracrine GLI Activation in Neighbouring Tumour Cells. *Nat. Commun.* **2017**, *8*, 15773.

(33) Gonnissen, A.; Isebaert, S.; McKee, C. M.; Dok, R.; Haustermans, K.; Muschel, R. J. The Hedgehog Inhibitor GANT61 Sensitizes Prostate Cancer Cells to Ionizing Radiation Both in Vitro and in Vivo. *Oncotarget* **2016**, *7* (51), 84286–84298.

(34) Huang, L.; Walter, V.; Hayes, D. N.; Onaitis, M. Hedgehog-GLI Signaling Inhibition Suppresses Tumor Growth in Squamous Lung Cancer. *Clin. Cancer Res.* **2014**, *20* (6), 1566–1575.

(35) Peer, D.; Karp, J. M.; Hong, S.; Farokhzad, O. C.; Margalit, R.; Langer, R. Nanocarriers as an Emerging Platform for Cancer Therapy. *Nat. Nanotechnol.* **2007**, *2* (12), 751–760.

(36) Wicki, A.; Witzigmann, D.; Balasubramanian, V.; Huwyler, J. Nanomedicine in Cancer Therapy: Challenges, Opportunities, and Clinical Applications. *J. Control. Release* **2015**, *200*, 138–157.

(37) Ashton, S.; Song, Y. H.; Nolan, J.; Cadogan, E.; Murray, J.; Odedra, R.; Foster, J.; Hall, P. A.; Low, S.; Taylor, P.; et al. Aurora Kinase Inhibitor Nanoparticles Target Tumors with Favorable Therapeutic Index in Vivo. *Sci. Transl. Med.* **2016**, *8* (325).

(38) Mizrachi, A.; Shamay, Y.; Shah, J.; Brook, S.; Soong, J.; Rajasekhar, V. K.; Humm, J. L.; Healey, J. H.; Powell, S. N.; Baselga, J.; et al. Tumour-Specific PI3K Inhibition via Nanoparticle-Targeted Delivery in Head and Neck Squamous Cell Carcinoma. *Nat. Commun.* **2017**, *8*.

(39) Schmid, D.; Park, C. G.; Hartl, C. A.; Subedi, N.; Cartwright, A. N.; Puerto, R. B.; Zheng, Y.; Maiarana, J.; Freeman, G. J.; Wucherpfennig, K. W.; et al. T Cell-Targeting Nanoparticles Focus Delivery of Immunotherapy to Improve Antitumor Immunity. *Nat. Commun.* **2017**, *8* (1), 1–11.

(40) Kwak, E. L.; Clark, J. W.; Chabner, B. Targeted Agents: The Rules of Combination. *Clin. Cancer Res.* **2007**, *13* (18), 5232–5237.

(41) Gupta, M. K.; Meyer, T. a.; Nelson, C. E.; Duvall, C. L. Poly(PS-b-DMA) Micelles for Reactive Oxygen Species Triggered Drug Release. *J. Control. Release* **2012**, *162* (3), 591–598.

(42) Uddin, M. J.; Werfel, T. A.; Crews, B. C.; Gupta, M. K.; Kavanaugh, T. E.; Kingsley, P. J.; Boyd, K.; Marnett, L. J.; Duvall, C. L. Fluorocoxib A Loaded Nanoparticles Enable Targeted Visualization of Cyclooxygenase-2 in Inflammation and Cancer. *Biomaterials* **2016**, *92*, 71–80.

(43) Chenna, V.; Hu, C.; Pramanik, D.; Aftab, B. T.; Karikari, C.; Campbell, N. R.; Hong, S.-M.; Zhao, M.; Rudek, M. A.; Khan, S. R.; et al. A Polymeric Nanoparticle Encapsulated Small-Molecule Inhibitor of Hedgehog Signaling (NanoHHI) Bypasses Secondary Mutational Resistance to Smoothened Antagonists. *Mol. Cancer Ther.* **2012**, *11* (1), 165–173.

(44) Blanco, E.; Shen, H.; Ferrari, M. Principles of Nanoparticle Design for Overcoming Biological Barriers to Drug Delivery. *Nat. Biotechnol.* **2015**, *33* (9), 941–951.

(45) Wei, T.; Chen, C.; Liu, J.; Liu, C.; Posocco, P.; Liu, X.; Cheng, Q.; Huo, S.; Liang, Z.; Fermeglia, M.; et al. Anticancer Drug Nanomicelles Formed by Self-Assembling Amphiphilic Dendrimer to Combat Cancer Drug Resistance. *Proc. Natl. Acad. Sci.* **2015**, *112* (10), 2978–2983.

(46) Kim, D.-W.; Kim, S.-Y. S.-W.; Kim, H.-K.; Shin, S. W.; Kim, J. S.; Park, K.; Lee, M. Y.; Heo, D. S. Multicenter Phase II Trial of Genexol-PM, a Novel Cremophor-Free, Polymeric Micelle Formulation of Paclitaxel, with Cisplatin in Patients with Advanced Non-Small-Cell Lung Cancer. *Ann. Oncol.* **2007**, *18* (12), 2009–2014.

(47) Ramasamy, T.; Ruttala, H. B.; Gupta, B.; Poudel, B. K.; Choi, H. G.; Yong, C. S.; Kim, J. O. Smart Chemistry-Based Nanosized Drug Delivery Systems for Systemic Applications: A Comprehensive Review. *J. Control. Release* **2017**, *258*, 226–253.

(48) Joshi, R. V; Nelson, C. E.; Poole, K. M.; Skala, M. C.; Duvall, C. L. Dual PH- and Temperature-Responsive Microparticles for Protein Delivery to Ischemic Tissues. *Acta Biomater.* **2013**, *9* (5), 6526–6534.

(49) Li, H.; Miteva, M.; Kirkbride, K. C.; Cheng, M. J.; Nelson, C. E.; Simpson, E. M.; Gupta, M. K.; Duvall, C. L.; Giorgio, T. D. Dual MMP7-Proximity-Activated and Folate Receptor-Targeted Nanoparticles for SiRNA Delivery. *Biomacromolecules* **2015**, *16* (1), 192–201.

(50) Poole, K. M.; Nelson, C. E.; Joshi, R. V; Martin, J. R.; Gupta, M. K.; Haws, S. C.; Kavanaugh, T. E.; Skala, M. C.; Duvall, C. L. ROS-Responsive Microspheres for on Demand Antioxidant Therapy in a Model of Diabetic Peripheral Arterial Disease. *Biomaterials* **2015**, *41*, 166–175.

(51) Guise, T. A.; Yin, J. J.; Taylor, S. D.; Kumagai, Y.; Dallas, M.; Boyce, B. F.; Yoneda, T.; Mundy, G. R. Evidence for a Causal Role of Parathyroid Hormone-Related Protein in the Pathogenesis of Human Breast Cancer-Mediated Osteolysis. *J Clin Invest* **1996**, *98* (7), 1544–1549.

(52) Zhang, X. H.-F.; Wang, Q.; Gerald, W.; Hudis, C. A.; Norton, L.; Smid, M.; Foekens, J. A.; Massague, J. Latent Bone Metastasis in Breast Cancer Tied to Src-Dependent Survival Signals. *Cancer Cell* **2009**, *16* (1), 67–78.

(53) Guo, R.; Lu, S.; Merkel, a. R.; Sterling, J. a.; Guelcher, S. a. Substrate Modulus Regulates Osteogenic Differentiation of Rat Mesenchymal Stem Cells through Integrin Β1 and BMP Receptor Type IA. *J. Mater. Chem. B* **2016**, 3584–3593.

(54) Mbalaviele, G.; Chen, H.; Boyce, B. F.; Mundy, G. R.; Yoneda, T. The Role of Cadherin in the Generation of Multinucleated Osteoclasts from Mononuclear Precursors in Murine Marrow. *J. Clin. Invest.* **1995**.

(55) Michigami, T.; Shimizu, N.; Williams, P. J.; Niewolna, M.; Dallas, S. L.; Mundy, G. R.; Yoneda, T. Cell-Cell Contact between Marrow Stromal Cells and Myeloma Cells via VCAM-1 and Alpha(4)Beta(1)-Integrin Enhances Production of Osteoclast-Stimulating Activity. *Blood* **2000**.

(56) Tietjen, G. T.; DiRito, J.; Pober, J. S.; Saltzman, W. M. Quantitative Microscopy-Based Measurements of Circulating Nanoparticle Concentration Using Microliter Blood Volumes. *Nanomedicine Nanotechnology, Biol. Med.* **2017**, *13* (6), 1863–1867.

(57) Wright, L. E.; Ottewell, P. D.; Rucci, N.; Peyruchaud, O.; Pagnotti, G. M.; Chiechi, A.; Buijs, J. T.; Sterling, J. A. Murine Models of Breast Cancer Bone Metastasis.

Bonekey Rep. **2016**, *5*, 804.

(58) Sparreboom, A.; Zuylen, L. Van; Brouwer, E.; Loos, W. J.; Bruijn, P. De; Gelderblom, H.; Pillay, M.; Nooter, K.; Stoter, G.; Verweij, J. Cremophor EL-Mediated Alteration of Paclitaxel Distribution in Human Blood : Clinical Pharmacokinetic Implications Advances in Brief Cremophor EL-Mediated Alteration of Paclitaxel Distribution in Human Blood : Clinical Pharmacokinetic Implications. **1999**, 1454–1457.

(59) Gupta, M. K.; Martin, J. R.; Werfel, T. A.; Shen, T.; Page, J. M.; Duvall, C. L. Cell Protective, ABC Triblock Polymer-Based Thermoresponsive Hydrogels with ROS-Triggered Degradation and Drug Release. *J. Am. Chem. Soc.* **2014**, *136* (42), 14896–14902.

(60) O'Grady, K. P.; Kavanaugh, T. E.; Cho, H.; Ye, H.; Gupta, M. K.; Madonna, M. C.; Lee, J.; O'Brien, C. M.; Skala, M. C.; Hasty, K. A.; et al. Drug-Free ROS Sponge Polymeric Microspheres Reduce Tissue Damage from Ischemic and Mechanical Injury. *ACS Biomater. Sci. Eng.* **2018**, *4* (4), 1251–1264.

(61) Dollinger, B. R.; Gupta, M. K.; Martin, J. R.; Duvall, C. L. Reactive Oxygen Species Shielding Hydrogel for the Delivery of Adherent and Nonadherent Therapeutic Cell Types<sup/>. *Tissue Eng. Part A* **2017**, *23* (19–20), 1120–1131.

(62) Monfardini, C.; Schiavon, O.; Caliceti, P.; Morpurgo, M.; Veronese, F. M.; Harris, J. M. A Branched Monomethoxypoly(Ethylene Glycol) for Protein Modification. *Bioconjug. Chem.* **1995**, *6* (1), 62–69.

(63) Gao, W.; Liu, W.; Mackay, J. A.; Zalutsky, M. R.; Toone, E. J.; Chilkoti, A. In Situ Growth of a Stoichiometric PEG-like Conjugate at a Protein's N-Terminus with Significantly Improved Pharmacokinetics. *Proc. Natl. Acad. Sci. U. S. A.* **2009**, *106* (36), 15231–15236.

(64) Gao, W.; Liu, W.; Christensen, T.; Zalutsky, M. R.; Chilkoti, A. In Situ Growth of a PEG-like Polymer from the C Terminus of an Intein Fusion Protein Improves Pharmacokinetics and Tumor Accumulation. *Proc. Natl. Acad. Sci. U. S. A.* **2010**, *107* (38), 16432–16437.

(65) Chaffer, C. L.; Weinberg, R. A. A Perspective on Cancer Cell Metastasis. *Science* **2011**, *331* (6024), 1559–1564.

(66) Baron, R.; Ferrari, S.; Russell, R. G. G. Denosumab and Bisphosphonates: Different Mechanisms of Action and Effects. *Bone*. 2011, pp 677–692.

(67) Shane, E.; Burr, D.; Abrahamsen, B.; Adler, R. A.; Brown, T. D.; Cheung, A. M.; Cosman, F.; Curtis, J. R.; Dell, R.; Dempster, D. W.; et al. Atypical Subtrochanteric and Diaphyseal Femoral Fractures: Second Report of a Task Force of the American Society for Bone and Mineral Research. *J. Bone Miner. Res.* **2014**, *29* (1), 1–23.

(68) Pozzi, S.; Vallet, S.; Mukherjee, S.; Cirstea, D.; Vaghela, N.; Santo, L.; Rosen, E.; Ikeda, H.; Okawa, Y.; Kiziltepe, T.; et al. High-Dose Zoledronic Acid Impacts Bone Remodeling with Effects on Osteoblastic Lineage and Bone Mechanical Properties. *Clin. Cancer Res.* **2009**, *15* (18), 5829–5839.

(69) Idris, A. I.; Rojas, J.; Greig, I. R.; Van't Hof, R. J.; Ralston, S. H. Aminobisphosphonates Cause Osteoblast Apoptosis and Inhibit Bone Nodule Formation in Vitro. *Calcif. Tissue Int.* **2008**, *82* (3), 191–201.

(70) Xu, Y.; Chenna, V.; Hu, C.; Sun, H. X.; Khan, M.; Bai, H.; Yang, X. R.; Zhu, Q. F.; Sun, Y. F.; Maitra, A.; et al. Polymeric Nanoparticle-Encapsulated Hedgehog Pathway Inhibitor HPI-1 (NanoHHI) Inhibits Systemic Metastases in an Orthotopic

Model of Human Hepatocellular Carcinoma. *Clin. Cancer Res.* **2012**, *18* (5), 1291–1302.

(71) Ross, M. H.; Esser, A. K.; Fox, G. C.; Schmieder, A. H.; Yang, X.; Hu, G.; Pan, D.; Su, X.; Xu, Y.; Novack, D. V.; et al. *Bone-Induced Expression of Integrin B3 Enables Targeted Nanotherapy of Breast Cancer Metastases*; 2017; Vol. 77.

(72) Yamashita, S.; Katsumi, H.; Hibino, N.; Isobe, Y.; Yagi, Y.; Tanaka, Y.; Yamada, S.; Naito, C.; Yamamoto, A. Development of PEGylated Aspartic Acid-Modified Liposome as a Bone-Targeting Carrier for the Delivery of Paclitaxel and Treatment of Bone Metastasis. *Biomaterials* **2018**, *154*, 74–85.

(73) Hu, W.; Sung, T.; Jessen, B. A.; Thibault, S.; Finkelstein, M. B.; Khan, N. K.; Sacaan, A. I. Mechanistic Investigation of Bone Marrow Suppression Associated with Palbociclib and Its Differentiation from Cytotoxic Chemotherapies. *Clin. Cancer Res.* **2016**, *22* (8), 2000–2008.

(74) Fonseca, H.; Carvalho, A.; Esteves, J.; Esteves, V. I.; Moreira-Gonï¿½alves, D.; Duarte, J. A. Effects of Doxorubicin Administration on Bone Strength and Quality in Sedentary and Physically Active Wistar Rats. *Osteoporos. Int.* **2016**, *27* (12), 3465–3475.

(75) Mazumdar, T.; DeVecchio, J.; Agyeman, A.; Shi, T.; Houghton, J. A. Blocking Hedgehog Survival Signaling at the Level of the GLI Genes Induces DNA Damage and Extensive Cell Death in Human Colon Carcinoma Cells. *Cancer Res.* **2011**, *71* (17), 5904–5914.

(76) Torchilin, V. Tumor Delivery of Macromolecular Drugs Based on the EPR Effect. *Adv. Drug Deliv. Rev.* **2011**, *63* (3), 131–135.

(77) Page, J. M.; Merkel, A. R.; Ruppender, N. S.; Guo, R.; Dadwal, U. C.; Cannonier, S. A.; Basu, S.; Guelcher, S. A.; Sterling, J. A. Matrix Rigidity Regulates the Transition of Tumor Cells to a Bone-Destructive Phenotype through Integrin B3 and TGF-β Receptor Type II. *Biomaterials* **2015**, *64*, 33–44.

(78) Jansen, L. E.; Birch, N. P.; Schiffman, J. D.; Crosby, A. J.; Peyton, S. R. Mechanics of Intact Bone Marrow. *J. Mech. Behav. Biomed. Mater.* **2015**, *50*, 299–307.

(79) Ruppender, N. S.; Merkel, A. R.; Martin, T. J.; Mundy, G. R.; Sterling, J. A.; Guelcher, S. A. Matrix Rigidity Induces Osteolytic Gene Expression of Metastatic Breast Cancer Cells. *PLoS One* **2010**, *5* (11), 1–10.

(80) Sethi, N.; Dai, X.; Winter, C. G.; Kang, Y. Tumor-Derived Jagged1 Promotes Osteolytic Bone Metastasis of Breast Cancer by Engaging Notch Signaling in Bone Cells. *Cancer Cell* **2011**, *19* (2), 192–205.

(81) Zheng, H.; Bae, Y.; Kasimir-Bauer, S.; Tang, R.; Chen, J.; Ren, G.; Yuan, M.; Esposito, M.; Li, W.; Wei, Y.; et al. Therapeutic Antibody Targeting Tumor- and Osteoblastic Niche-Derived Jagged1 Sensitizes Bone Metastasis to Chemotherapy. *Cancer Cell* **2017**, *32* (6), 731–747.e6.

(82) Li, C.; Wang, S.; Xing, Z.; Lin, A.; Liang, K.; Song, J.; Hu, Q.; Yao, J.; Chen, Z.; Park, P. K.; et al. A ROR1-HER3-LncRNA Signalling Axis Modulates the Hippo-YAP Pathway to Regulate Bone Metastasis. *Nat. Cell Biol.* **2017**, *19* (2), 106–119.

(83) Wan, L.; Pantel, K.; Kang, Y. Tumor Metastasis: Moving New Biological Insights into the Clinic. *Nat. Med.* **2013**, *19* (11), 1450–1464.

(84) Powell, G. J.; Southby, J.; Danks, J. A.; Stillwell, R. G.; Hayman, J. A.; Henderson, M. A.; Bennett, R. C.; John Martin, T. Localization of Parathyroid Hormone-Related Protein in Breast Cancer Metastases: Increased Incidence in Bone Compared with

Other Sites. *Cancer Res.* **1991**, *51* (11), 3059–3061.

CHAPTER 5

V. BONE-TARGETED POLYMERIC NANOCARRIERS IMPROVE EFFICACY OF GLI-INHIBITOR IN BLOCKING TUMOR-INDUCED BONE DESTRUCTION

Adapted from:
Vanderburgh, JP, Gupta, MK, Wang, SK, Moyer, KE, Merkel, AR, Guelcher, SA, Rhoades, JA, Duvall, CL. “Bone-Targeted Polymeric Nanocarriers Improve Efficacy of Gli-Inhibitor in Combatting Tumor-Induced Bone Disease.”

5.1. Abstract

Breast cancer patients are often at high risk for bone metastasis. Metastatic bone disease is a major clinical problem that leads to a reduction in mobility, increased risk of pathologic fracture, severe bone pain, and other skeletal-related events (SREs). Our previous studies have demonstrated that the small molecule Gli-antagonist GANT58 is a potent inhibitor of parathyroid hormone-related protein (PTHrP) – a major driver of osteoclast-mediated bone destruction – and systemic delivery in a nanoparticle formulation significantly reduced tumor-induced bone destruction in mouse models of bone metastasis. *In vitro* studies suggested GANT58 would also reduce tumor burden *in vivo*, however no effect on tumor burden was observed. In this study, we designed a bone-targeted nanoparticle formulation (BTNP) comprising an amphiphilic diblock copolymer of poly(propylene sulfide)-*b*-poly(alendronate-*co*-dimethylacrylamide) (PPS-*b*-P(Aln-*co*-DMA) to encapsulate and preferentially deliver GANT58 to bone. Development of a GANT58-BTNP combinatorial library yielded a lead candidate formulation with optimal bone-binding *in vivo*, with the lead candidate formulation exhibiting a 2-fold increase in bone localization over the non-targeted formulation. In an intracardiac model of breast cancer bone metastasis, GANT58-BTNPs treatment led to a 3-fold decrease in lesion area and 2.5-fold increase in bone volume fraction in the tibiae of mice. Histological analysis revealed spatial heterogeneity in Gli2 expression in the bone-tumor microenvironment, with significantly higher Gli2 expression in tumor near the epiphyseal plate over

tumor in the distal tibia. These findings suggest GANT58-BTNPs act as a potent tumor-mediated osteoclast inhibitor; however spatial heterogeneity limits its efficacy as an antitumor treatment. Thus, GANT58-BTNP is a potential therapy for blocking tumor-induced bone destruction in bone-metastatic patients.

5.2. Introduction

Breast cancer remains the second leading cause of cancer-related deaths among female cancer patients.[1] Despite advances in early screening and adjuvant therapy, many breast cancer subtypes remain elusive and currently lack any targeted therapies. Metastasis is the major prognostic factor for breast cancer patient survival, and breast tumors have a striking propensity for metastasis to bone with over 70% of patients presenting with bone metastases at post-mortem.[2] Patients presenting with bone metastases often experience significant skeletal complications including bone pain, increased risk of pathological fracture, and a reduction in mobility that significantly reduce quality of life, and thus treating tumor-induced bone disease (TIBD) remains a large clinical challenge.[3] Current treatment strategies for TIBD include antiresorptives such as bisphosphonates and the RANKL inhibitor, denosumab. While these agents inhibit osteoclast activity and subsequent bone resorption, they have no effect on tumor burden nor do they selectively obstruct the vicious cycle, and thus do not improve overall survival.[4–6] Therefore, there remains a compelling need for treatments that target the tumor directly to reduce tumor burden and tumor-induced bone destruction while limiting off-target effects.

Once established in bone, breast cancer cells disrupt normal bone remodeling to initiate a vicious cycle of TIBD.[7] Specifically, tumor cells in the bone microenvironment secrete parathyroid hormone-related protein (PTHrP) which increases osteoblast expression of receptor activator of nuclear factor kappa-B ligand (RANKL) and drives subsequent osteoclast-mediated resorption of the bone matrix. Consequently, the release of matrix-bound growth factors like transforming growth factor beta (TGF-β) further stimulate tumor growth and osteolytic bone destruction, thus propagating the cycle.[8]

Multifunctional polymeric nanoparticles (NPs) have emerged as effective carriers that improve the pharmacokinetic (PK) profile of small molecule drugs over conventional formulations. Polymeric carriers have seen clinical success in cancer therapy due to their ability improve circulation time and more recently, the ability to selectively target tumors.[9] Advances in polymer science toward environmentally-responsive and tunable polymer formulations have improved target-specific drug delivery and broadened the frontiers of nanomedicine applications. Cancer nanomedicines have been widely reported in literature as carriers for chemotherapeutics, however more recent research has demonstrated their potential as delivery vehicles for molecularly targeted agents (MTAs) and RNA interference (RNAi) therapies.[10–16] These targeted therapies offer multiple benefits over traditional cytotoxic agents. Most notably, their selectivity for inhibiting tumor-associated molecular entities, or genetic sequences in the case of RNAi, often leads to minimal normal tissue toxicity, thus improving the therapeutic index (TI), the ratio of the amount of agent that causes therapeutic effect to the amount that causes toxicity.[17] Efficient bone-targeting of nanomedicines has also been successfully implemented using myriad chemistries including bisphosphonates[18–21], anionic peptides[22–24], carboxylic acids[25], and other phosphate-containing moieties.[26]

Previous work from our lab demonstrated that encapsulation of the small molecule Gli-inhibitor GANT58 – which blocks PTHrP expression and obstructs the vicious cycle of TIBD – in an NP formulation improved protection from tumor-induced bone destruction upon systemic administration in mouse models of bone metastasis. Further, GANT58 was found to obstruct tumor proliferation *in vitro*, however these findings did not translate *in vivo*.

In this work, we hypothesized that conferring bone-affinity to the NP corona could improve therapeutic efficiency of GANT58 by localizing GANT58 to the bone-tumor site. We further hypothesized that if GANT58 was present in sufficient concentration at the bone site prior to tumor establishment, GANT58 could prevent tumor establishment and subsequent growth *in vivo*. To this end, we developed and characterized a bone-targeted nanoparticle (BTNP) chemistry and tested the new formulation in a mouse model of bone metastasis for its ability to block both bone destruction and tumor burden.

5.3. Materials and Methods

Cell Lines and Reagents: The human breast cancer cell line MDA-MB-231 was obtained from ATCC and a bone metastatic variant generated in our lab was used for all *in vitro* and *in vivo* experiments, as previously published.[59,60] Human mesenchymal stem cells (hMSCs, Extem Biosciences) were maintained in Mesenchymal Stem Cell Growth Medium 2 (PromoCell). MDA-MB-231 cells were maintained in DMEM (Cell-gro) plus 10% Fetal Bovine Serum (FBS; Hyclone Laboratories) and 1% penicillin/streptomycin (P/S; Mediatech). All cell lines are routinely tested for changes in cell growth and gene expression. GANT58 was purchased from Santa Cruz Biotechnology (Dallas, TX, USA), all other reagents were purchased from Sigma Aldrich (St. Louis, MO, USA) unless otherwise specified.

Synthesis of hydroxyl end-functionalized poly(propylene sulfide) (PPS_{135}-OH): A terminal hydroxyl end functional poly(propylene sulfide) polymer was synthesized by anionic ring polymerization of three membered cyclic propylene sulfide monomer using DBU/1-buthane thiol followed by an end-functionalization with 2-iodoethanol. In brief, 1,8-diazabicyclo[5.4.0]undec 7-ene (DBU) (3 mmol, 0.46 g, 0.45 mL) in dry THF (15 mL) was transferred to a heat dried and nitrogen flushed 100 mL round bottomed flask and degassed for 30 min. The flask was submerged into an ice bath, and a degassed solution of 1-butane thiol (1 mmol, 0.122 g, 0.138 mL) in THF (10 mL) was added drop wise at 0 °C. After 30 min, freshly dried, distilled, and degassed propylene sulfide (135 mmol, 9.99 g, 10.56 mL) monomer was added to the reaction mixture, and temperature was maintained at 0 °C for another 30 min. The polymerization was carried for another 150 min, quenched by addition of degassed 2-iodoethanol (4 mmol, 0.68 g, 0.311 mL), and stirred overnight at RT. The next day, the polymer mixture was filtered to remove precipitated salt, and the filtered solution was concentrated under vacuum. The crude polymer was purified by three precipitations into cold methanol (100 mL) from dichloromethane (10 mL) before being vacuum-dried to yield a colorless viscous polymer. The formation of polymer with a terminal hydroxyl functionality was characterized by 1H NMR and GPC. ^{1}H NMR (400 MHz; $CDCl_3$): δ(ppm) 1.3-1.4 (s, CH_3), 2.5-2.8 (s, -CH), 2.8-3.1 (s, CH_2), 3.72 (q, CH_2-OH). (PPS_{135}-OH, Mn = 9,700 g/mol, PDI =1.32).

Synthesis of poly(propylene sulfide)-4-cyano-4-(ethylsulfanylthiocarbonyl) sulfanylpentanoic acid (PPS_{135}-ECT): The PPS-based reversible addition−fragmentation chain-transfer (RAFT) macro chain transfer agent (CTA) was prepared using a Steglich esterification reaction between carboxyl-terminated ECT (RAFT agent) and the terminal hydroxyl groups of the PPS_{135}-OH. To a dried flask, PPS_{135}-OH (6.0 g, 0.6 mmol), ECT (0.628 g, 2.4 mmol), and 4-dimethylaminopyridine (DMAP, 0.021 g, 0.18 mmol) were transferred and dissolved in DCM and degassed for 15 min. To this flask, N,N'-

dicyclohexylcarbodiimide (DCC, 0.495 g, 2.4 mmol) was added and stirred at RT for 24h. The polymer mixture was filtered to remove precipitated dicyclohexyl urea and concentrated under vacuum. The crude polymer mixture was diluted with DCM (10 mL) and subsequently purified by three precipitations into 250 mL of cold methanol. ^{1}H NMR (400 MHz; $CDCl_3$): δ(ppm) 1.35 (t, 3H, $-S-CH_2-CH_3$), 1.3-1.4 (s, 3H, CH_3), 1.88 (s,$-C(CN)-CH_3$), 2.4−2.67 (m, 4H, $-CH_2-CH_2-S$), 2.5-2.8 (broad s, S-CH), 2.8- 3.1 (broad s, 2H, CH_2), 3.34 (q, $-S-CH_2-CH_3$), 4.2 (t, $-OCH_2-CH_2$). (PPS_{135}-ECT, $M_{n,GPC}$ = 9,900 g/mol, PDI =1.32).

Synthesis of poly(propylene sulfide)-b-poly(pentafluorophenyl acrylate-co-dimethylacrylamide) PPS_{135}-b-P($PFPA_x$-co-DMA_y)$_{150}$: The diblock copolymer PPS_{135}-*b*-P($PFPA_x$-*co*-DMA_y)$_{150}$ was synthesized via RAFT polymerization using AIBN as the initiator at a 5:1 molar ratio of PPS_{135}-ECT to AIBN. In a 10 mL round-bottom reaction flask, PPS_{135}-ECT (0.3 g, 0.03 mmol) was co-dissolved with stoichiometric amounts of pentafluorophenyl acrylate (PFPA) and dimethylacrylamide (DMA) in 1:1 DMF to 1,4-dioxane (4 mL) to achieve a final second block chain length of 150, where the PFPA amount was varied from 0 to 100% PFPA in the 150-unit second block with the balance DMA. A solution of AIBN (0.98 mg, 0.006 mmol) in 1,4-dioxane was added to the reaction mixture and degassed for 15 min by bubbling ultrahigh purity nitrogen through the reaction mixture. The reaction flask was then submerged in a 70ºC oil bath and polymerization was allowed to proceed for 24 h. The final polymerization mixture was precipitated twice in cold diethyl ether and dried under vacuum overnight to yield a light-yellow polymer.

Synthesis of PPS_{135}-b-P(Aln_x-co-DMA_y)$_{150}$ and fluorescent PPS_{135}-b-P(Aln_x-co-DMA_y)$_{150}$: The amine-reactive PFPA group of PPS_{135}-*b*-P($PFPA_x$-*co*-DMA_y)$_{150}$ was used to graft alendronate (Aln), an amine-terminated bisphosphonate, to the polymer backbone. PPS_{135}-*b*-P($PFPA_x$-*co*-DMA_y)$_{150}$ (0.013 mmol, 0.3 g), triethylamine (0.013 mmol, 1.8 µL), Aln (10% excess of PFPA molar content) were added to a dry round-bottom flask and dissolved in DMSO (4 mL) and submerged in a 50ºC oil bath. The amine-conjugation was allowed to proceed for 24 h at 50ºC. The reaction contents were then dialyzed against deionized water for 48 h followed by lyophilization. For fluorescent-labeling of polymers, Cy7-amine or Cy5-amine (0.013 mmol) was added to the reaction flask prior to Aln addition and reaction allowed to proceed 24 h. To the same reaction flask, Aln was then added and reaction proceeded as described. The resulting polymer was then dialyzed first against methanol for 48 h until disappearance of fluorophore color and then against deionized water for 48 h.

GANT58-BTNP synthesis and characterization: GANT58-loaded nanoparticles (GANT58-BTNPs) were formed by either the bulk solvent evaporation method or nanoprecipitation method. PPS_{135}-*b*-$P(Aln_x\text{-co-}DMA_y)_{150}$ was co-dissolved with GANT58 in chloroform (solvent evaporation) or methanol (nanoprecipitation) and added dropwise to a vial containing vigorously-stirring phosphate-buffered saline (PBS, 1 mL). For the solvent evaporation method, the oil-in-water biphasic solution was left stirring overnight to evaporate the chloroform and allow for micelle formation. For nanoprecipitation, the solution was allowed to stir for 1 h, after which the methanol was removed from the solution via rotary evaporation. The resulting micelle solution was passed through a 0.45 µm syringe filter producing the final GANT58-BTNP formulation. The same technique, excluding addition of GANT58, was used to create empty PPS_{135}-*b*-$P(Aln_x\text{-co-}DMA_y)_{150}$ micellar nanoparticles (Empty-BTNPs). Dynamic light scattering (DLS) was used to measure the hydrodynamic diameter (D_h) and zeta potential (ζ) of the GANT58-BTNPs and Empty-BTNPs via a Malvern Zetasizer Nano-ZS (Malvern Instruments Ltd., Worcestershire, UK) equipped with a 4 mW He-Ne laser operating at $\lambda = 632.8$ nm. Transmission electron microscopy (TEM) samples were prepared as previously described.[29] Briefly, 5 μL of GANT58-NPs were added to a pure carbon TEM grid (Ted Pella, Inc., Redding, CA, USA), blotted dry after 60 s, and counterstained with 1% uranyl acetate for 20 s. After vacuum drying, the grids were imaged on an FEI Tecnai Osiris microscope operating at 200 kV for TEM and Scanning Transmission Electron Microscopy Energy Dispersive X-ray Spectroscopy (STEM-EDS).

GANT58 loading and encapsulation was quantified utilizing the fluorescence properties of GANT58. Aliquots of GANT58-BTNPs in PBS (50 μL) were added in triplicate to a 96-well plate and dissolved by adding an equal volume of DMF. On the same plate, a standard of GANT58 in the same solvent (1:1 DMF:PBS) was prepared. Fluorescence intensity of GANT58 (ex. 485 nm, em. 590 nm) was measured on a micro plate reader (Synergy H1, Biotek, Winooski, VT) and GANT58 concentration was calculated from the standard curve.

Critical micelle concentration (CMC) determination: The critical micelle concentration was determined as previously described.[29,30] Nile Red (NR) was substituted for GANT58 as the loaded species due to its lipophilic fluorescence properties and its similar molecular weight to GANT58. NR is ideal for identifying intact micelles due to its fluorescence in hydrophobic environments and minimal fluorescence in aqueous environments. Nile Red (NR)-loaded PPS_{135}-*b*-$P(Aln_x\text{-co-}DMA_y)_{150}$ micelles (NR-BTNPs) were prepared by the described bulk solvent evaporation method. Serial dilutions of the NR-NPs were prepared in PBS and NR fluorescence (ex. 535 nm, em. 612 nm) was read on a micro plate reader (Synergy H1, Biotek, Winooski, VT). The CMC was defined as the intersection point on the semi-log plot of NR fluorescence versus polymer concentration as previously described.[30]

BTNP Stability Measurements: BTNP stability was tracked by measuring BTNP hydrodynamic diameter in salt and serum using DLS. BTNPs were incubated at a concentration of 100 μg/mL in solutions of NaCl (0.5M) or fetal bovine serum (FBS, 50% in PBS) and incubated for 2 h prior to DLS measurements. Hydrodynamic diameters were compared to control BTNP solutions prepared in PBS. Serum stability was further investigated using a Forster resonance energy transfer (FRET) based assay described previously.[29,61] Briefly, BTNPs were co-loaded with the FRET pair DiI and DiO and incubated in 50% FBS. Fluorescence measurements were taken at emission wavelengths of 517 nm and 573 nm after excitation at 480 nm over an 8 h time period on a fluorescence micro plate reader. FRET efficiency was calculated as

$$\% \text{ FRET} = \frac{I_{573}}{I_{573}+I_{517}} \times 100$$

Macrophage Uptake: RAW 264.7 macrophages were seeded at 25,000 cells/well in a 24-well plate. After 24 h, cells were incubated with DMEM containing 1 mg/mL Cy5-grafted GANT58-BTNPs for 4 h. Cells were then washed 3x with PBS containing 1% bovine serum albumin (BSA), harvested using a cell scraper, and pelleted. Cell pellets were resuspended in PBS containing 0.04% trypan blue and run through a flow cytometer (BD LSR Fortessa, BD Biosciences, Franklin Lakes, NJ, USA). Cy5 fluorescence (ex. 640 em. 670) was monitored and 1,000 cells collected for each measurement and mean Cy5 fluorescence was normalized to original BTNP solution fluorescence. Untreated RAW 264.7 cells were used as negative controls.

Hydrogen peroxide- (H_2O_2-) dependent drug release: The ROS-responsive behavior of the BTNPs was assessed as described previously, using H_2O_2 as the ROS-species.[29] Briefly, NR-BTNPs prepared as described were exposed to a range of concentrations (1-2000 mM) of H_2O_2. Fluorescence intensity of NR was monitored in a 96 well plate using a micro plate reader (Synergy H1, Biotek, Winooski, VT). Release of the NR due to NP oxidation and destabilization was assessed over time based on disappearance of NR fluorescence. The loss of fluorescence for each sample at each time point was determined by subtracting the fluorescent value from that of the sample prior to H_2O_2 addition, and the percent fluorescence remaining was determined by normalization to the same value (before addition of H_2O_2). This value for percent fluorescence remaining was subtracted from 100% and expressed as a percent release for each sample at each time point.

Biodistribution: Athymic female nude mice (4-6 weeks old, Envigo) were injected with GANT58-loaded Cy7-grafted PPS_{135}-*b*-P(Aln_{15}-co-DMA_{135}) (GANT58-Cy7BTNPs) via tail vein injection (8 mg/kg GANT58). Mice were then sacrificed at 8h post NP-injection. Organs and long bones (forelimbs, hindlimbs, and spine) were imaged on a Pearl Near-IR imager (Licor) and the images were analyzed using ROI analysis in the Licor software.

Orthotopic Mouse Model of Late Bone Metastasis: Athymic female nude mice (4-6 weeks old, Envigo) were anesthetized by continuous isoflurane and inoculated with $1x10^5$ GFP-expressing MDA-MB-231 cells resuspended in PBS via intracardiac injection into the left cardiac ventricle using a 27-gauge needle, as previously described.[62] Mice were then treated 5x per week via 100 μL tail vein injections with GANT58-BTNPs (10% Aln formulation, 8 mg/kg, n=12), GANT58-NPs (0% Aln formulation, 8 mg/kg, n=12), unloaded BTNPs of the same formulations (10% Aln and 0% Aln, n=12 per group), or PBS (control). Mice were imaged weekly to track tumor progression and sacrificed at 4 weeks.

Radiographic Imaging: Mice were radiographically imaged weekly beginning 1-week post-tumor cell inoculation using a Faxitron LX-60. Specifically, mice were anesthetized with isoflurane laid in a prone position on the imaging platform. Images were acquired at 35 kVp for 8 seconds. Lesion area and number were measured using quantitative image analysis software (Metamorph, Molecular Devices, Inc.) by region of interest analysis. All data are represented as mean lesion area and number per mouse.

Micro-Computed Tomography: Tibiae were analyzed using a high-resolution µCT 50 system (Scanco Medical). Tomographic images were acquired at 70 kVp with an isotropic voxel size of 12 µm and at an integration time of 300 ms. Scans were acquired with hindlimbs in 70% ethanol. µCT images were reconstructed, filtered ($\sigma = 0.2$, support = 1.0) and thresholded at 230. Tibiae and femur were contoured using the Scanco software algorithm starting 10 slices below the growth plate and continued 100 slices in the distal direction. Images were analyzed using the Scanco Medical Imaging software to determine the morphometric parameters.

Bone Histomorphometry: Tibiae were removed during autopsy and fixed in 10% neutral-buffered formalin (Fisher Scientific) for 48 hours at room temperature, after which they were stored at 4ºC in 70% ethanol. Bone specimens were decalcified in 10% EDTA for 2 weeks at 4°C and embedded in paraffin. Bone sections (5-µm thickness) were stained with hematoxylin & eosin (H&E), orange G, and phloxine. Tumor burden in the tibiae was examined under a microscope and quantified using Metamorph software (Molecular Devices, Inc.) and region of interest analysis. For osteoclast analysis, bone sections were stained for Tartrate-Resistant Acid Phosphatase (TRAP) utilizing a substrate incubation step (0.2 mg/mL Napthol AS-BI) followed by a color reaction (25 mg/mL Pararosaniline dye) to form a bright red stain in TRAP-positive cells. Sections were then counterstained with hematoxylin, coverslipped, and examined under a microscope and quantified using OsteoMeasure software (OsteoMetrics, Decatur, GA, USA).

Immunohistochemistry: Bone sections (5-µm thickness) were deparaffinized in xylene and rehydrated with graded alcohol solutions, followed by antigen retrieval in 10 mM sodium citrate buffer at 80°C for 30 min. Sections were then blocked with VECTASTAIN Elite ABC blocking buffer (Vector Laboratories) in phosphate-buffered saline (PBS)/0.1% Tween-20 for 1 hr and incubated with rabbit polyclonal anti-Gli2 primary antibody (1:500, Novus Biologicals) overnight at 4°C. The VECTASTAIN Elite ABC HRP Kit with biotinylated goat anti-rabbit secondary antibody and the ImmPACT NovaRED Peroxidase Substrate Kit (Vector Laboratories) were both used according to the manufacturer's protocol. After counterstaining with hematoxylin, tumor sections were mounted with Cytoseal XYL (Thermo Scientific) and imaged using an Olympus BX41 microscope equipped with an Olympus DP71 camera. Gli2-positive staining was quantified using Metamorph software (Molecular Devices, Inc.). Ki67 immunohistochemical staining was performed by the Vanderbilt Translational Pathology Shared Resource (TPSR) per established protocols.

Proliferation Assay: MDA-MB-231-bone cells were seeded in a 96-well plate at 2,000 cells/well in triplicate. Half of wells were pre-coated with 0.5 mm GelMA as a compliant substrate. Vehicle (DMSO) or GANT58 (40 μM) were introduced to wells after 24 hr. Cell proliferation was determined by MTS assay using the CellTiter 96 Aqueous Non-Radioactive Cell Proliferation Assay kit (Promega) per the manufacturer's instructions. Absorbance values were measured on a plate reader at optical density (OD) 490 nm and normalized to no cell controls in the respective GelMA coated and uncoated wells.

5.4. Results and Discussion

Five diblock copolymers were synthesized comprising a core-forming block of polypropylene sulfide (PPS) to a degree of polymerization of approximately 135 (10 kDa). PPS has previously been shown to efficiently encapsulate hydrophobic small molecules and elicit minimal toxicity upon systemic administration, and was thus chosen as the hydrophobic block.[27–30] Further, PPS is responsive to reactive oxygen species (ROS), which is prevalent in inflamed tissues such as tumor.[31,32] The sulfide in PPS reacts with radical oxygen provided by ROS to create sulfoxides and sulfones. This causes a phase transition of the polymer from hydrophobic to hydrophilic, resulting in disassembly of the micelle and subsequent cargo release. The PPS block was synthesized via anionic polymerization and conjugated to the RAFT chain transfer agent (CTA) 4-cyano-4-(ethylsulfanylthiocarbonyl) sulfanylpentanoic acid (ECT) as previously described to create the RAFT macro-CTA PPS_{135}-ECT.[28–30]

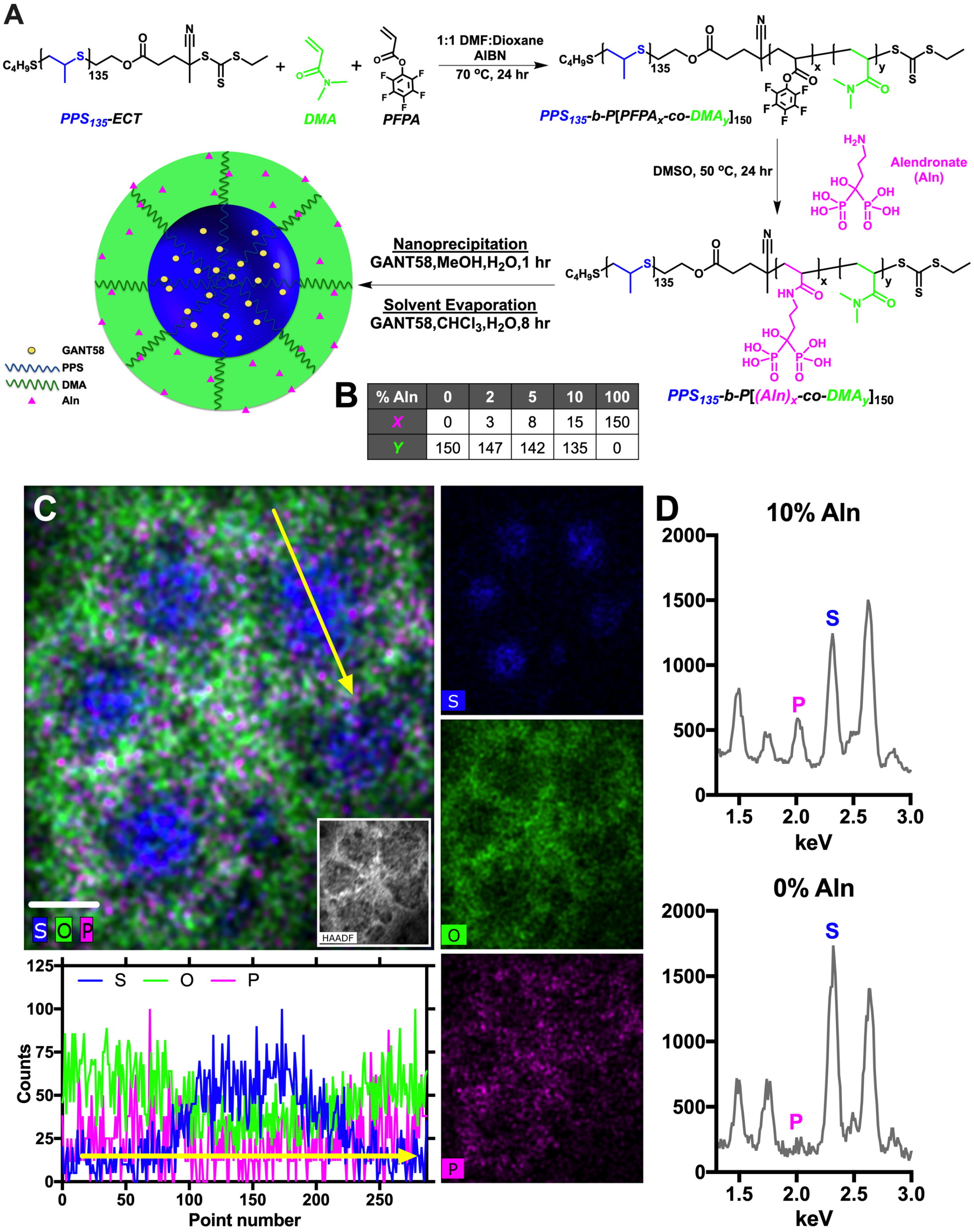

% Aln	0	2	5	10	100
X	0	3	8	15	150
Y	150	147	142	135	0

Figure 5.1. GANT58-BTNP synthesis, fabrication and TEM characterization. (A) Synthesis of PPS$_{135}$-b-P(Aln-co-DMA)$_{150}$ polymer and subsequent BTNP micelle fabrication. (B) Aln (X, magenta):DMA (Y, green) content in polymer formulations synthesized for analysis. Resulting formulations denoted by their %Aln in the coronal block (0%Aln, 2%Aln, 5%Aln, 10%Aln, 100%Aln) (C) STEM-EDS characterization of 10%Aln formulation using chemical mapping and EDS line scan over length of single micelle (yellow arrow, analysis on bottom left). Sulfur (blue), oxygen (green), phosphorus (magenta) used as signatures for PPS, DMA, and Aln, respectively. (D) EDS spectra of 10%Aln and 0%Aln formulation and respective sulfur (S) and phosphorus (P) characteristic peaks.

The PPS_{135}-ECT was then employed for the RAFT polymerization of a second, hydrophilic block consisting of a random copolymer of dimethylacrylamide (DMA) and pentafluorophenyl acrylate (PFPA) intermediate which was subsequently reacted with the bone-binding bisphosphonate, alendronate (Aln), resulting in PPS_{135}-*b*-$P(Aln_x\text{-co-}DMA_y)_{150}$ (**Figure 5.1A**). DMA was chosen due to its hydrophilicity, low toxicity, and its short pendant chain length so as to not sterically hinder the activity of the bone-targeting ligand.[33] PFPA was incorporated into the hydrophilic block to act as a reactive intermediate for grafting the bone-targeting ligand due to its highly amine-reactive pentafluorophenyl group. This second block consisting of DMA and PFPA was chain-extended to the PPS block to a total degree of polymerization of approximately 150 (14 kDa). The stoichiometric ratio of DMA:PFPA in the coronal block was varied to create five diblock copolymer formulations: 150:0 (0% PFPA), 49:1 (2% PFPA), 19:1 (5% PFPA), 9:1 (10% PFPA), and 0:150 (100% PFPA). The Aln was then grafted to the coronal block via the amine-reactive PFPA intermediate and the primary amine of Aln. Aln was chosen as the bone-targeting moiety due to its well-documented bone-binding affinity and its accessible terminal primary amine for reactivity with the PFPA group.[18,19,34,35] While it was not chosen for its therapeutic activity, it is important to note that alendronate is a clinically-approved osteoclast inhibitor.[36] The final Aln content was dependent on the PFPA content in the polymer precursor, and resulted in the five final polymer formulations denoted by the Aln content in the coronal block: 0%, 2%, 5%, 10%, and 100%Aln (**Figure 5.1B**). For fluorescently-labeled BTNPs, a 1:1 mol ratio (dye:polymer) of Cy5-amine or Cy7-amine fluorescent dyes were grafted to the PFPA block prior to addition of Aln.

Nanoparticles were formed by a bulk solvent evaporation method or a nanoprecipitation method to create GANT58-loaded PPS_{135}-*b*-$P(Aln\text{-co-}DMA)_{150}$ bone-targeted nanoparticles

(GANT58-BTNPs). The GANT58-BTNPs were observed via transmission electron microscope (TEM) in order to confirm the GANT58-BTNPs assume the hypothesized micellar morphology. TEM images indicate the GANT58-BTNPs have a spherical morphology and a diameter of approximately 60 nm in their dehydrated form, and approximately 100 nm in hydrodynamic diameter as measured by dynamic light scattering (DLS) (**Figure S5.1**). Chemical mapping using Energy Dispersive X-Ray Spectroscopy (EDS) in scanning TEM (STEM) was used to assess chemical content of the BTNPs. Sulfur (blue) was used as the chemical signature for PPS, oxygen (green) for DMA and Aln, and phosphorus (magenta) for Aln. Using these chemical signatures, the BTNP morphology of the 10%Aln formulation was shown to have a sulfur-rich core, and a corona rich in oxygen and sparsely-decorated with phosphorus, suggesting the Aln is randomly interspersed throughout the coronal block (**Figure 5.1C**). Further, the EDS spectra demonstrates that the 10%Aln formulation has a significant phosphorus peak, whereas the 0%Aln formulation (**Figure S5.2A**) lacks a significant phosphorus peak (**Figure 5.1D, Figure S5.2B**). This suggests the phosphorus signature is indicative of Aln and that it is only present in formulations consisting Aln.

Using the five polymer formulations, the two fabrication methods and varying drug:polymer ratios, a BTNP library was created to identify an optimal formulation based on size, zeta potential, and drug loading (**Figure 5.2**). The hydrodynamic diameter and zeta potential of the BTNPs were assessed by DLS and GANT58 loading was measured by GANT58 fluorescence (ex. 485 nm em. 590 nm) and calculated via a standard curve. GANT58-BTNPs of all polymer formulations exhibited hydrodynamic diameters of approximately 100 nm aside from the 100%Aln formulation which exhibited diameters of approximately 200 nm (**Figure 5.2A**). As expected, BTNPs formed by the nanoprecipitation method exhibited, on average, smaller diameters (96.9 ± 23.5 nm) than the solvent evaporation method (115.1 ± 21.6 nm) and drug loading had no significant effect on particle size. The surface charge of the BTNPs, as measured by zeta potential, was Aln content-dependent, with increasing Aln content leading to more negative surface charge due to the electronegativity of the constituent phosphate groups in Aln (**Figure 5.2B**). GANT58 was loaded at drug:polymer ratios of 1:2 (high), 1:4, and 1:10 (low) into the organic phase during micelle fabrication, and GANT58 loading and encapsulation efficiency was measured by GANT58 fluorescence (ex. 485 nm em. 590 nm) and calculated via a standard curve (**Figure 5.2C&D**). The average loading and encapsulation efficiency were significantly higher in BTNPs synthesized via the solvent evaporation method across all drug:polymer ratios. We surmised that despite the marginally smaller size of the nanoprecipitation-prepared BTNPs, the increased loading achieved in the BTNPs prepared by solvent evaporation rendered it the optimal fabrication method. Thus, we prepared BTNPs via the solvent evaporation method for all subsequent experiments.

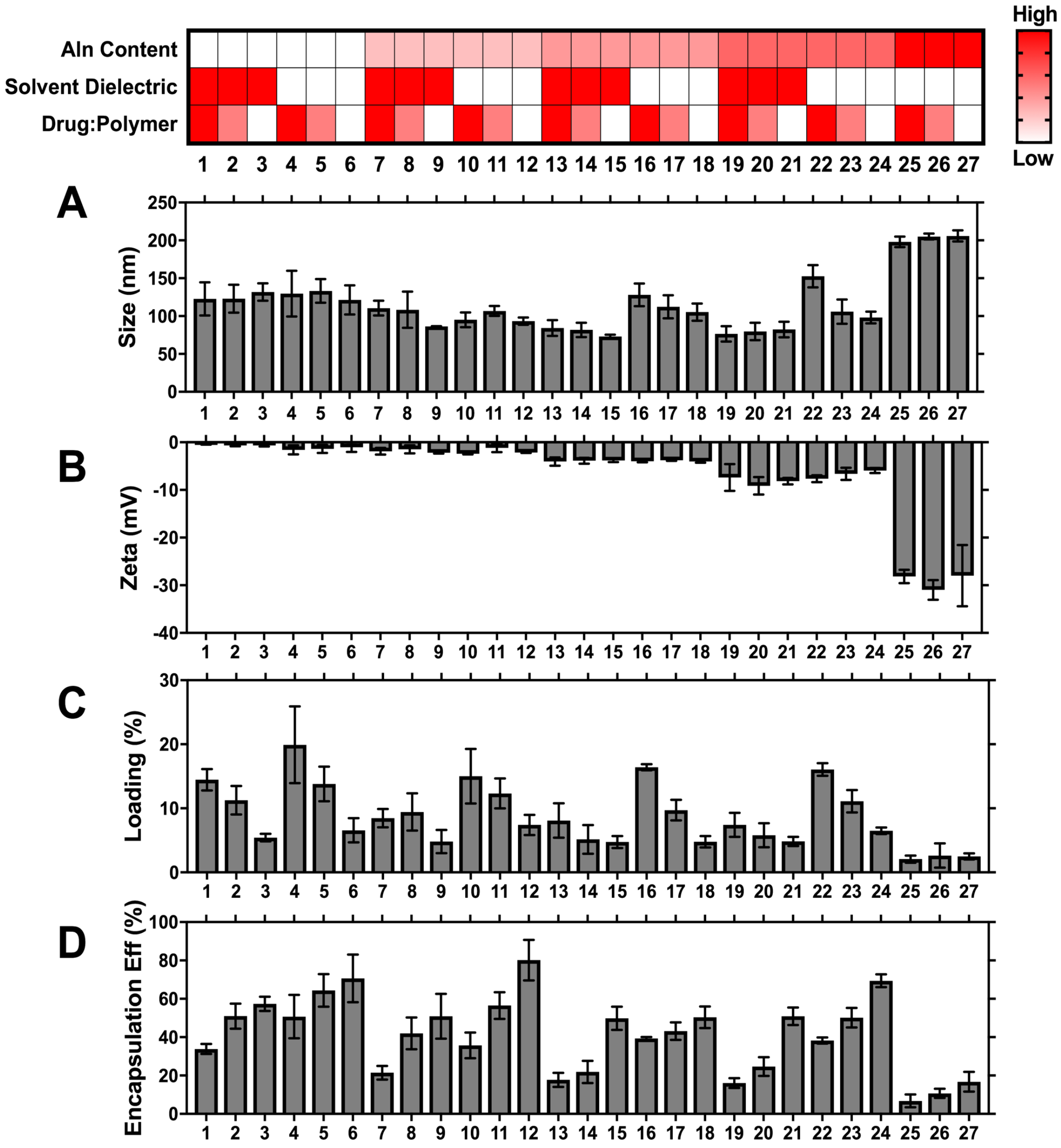

Figure 5.2. BTNP combinatorial library comparing BTNPs with varying Aln content, fabrication methods, and drug:polymer ratios. (A) BTNP hydrodynamic diameter and (B) zeta potential as measured by DLS. (C) BTNP GANT58 loading and (D) encapsulation efficiency as measured by GANT58 fluorescence.

Nanoparticle stability *in vivo* is essential to maximizing nanoparticle circulation time and subsequent accumulation in the bone. Dilution of the nanoparticles upon systemic administration can lead to nanoparticle disassembly due to NP concentration dropping below the critical micelle concentration (CMC).[37,38] To confirm the CMC of the BTNPs was lower than the initial NP blood concentration, the CMC was determined by the Nile Red (NR) method (**Figure 5.3A**).[30] The BTNPs were determined to be approximately 0.07 mg/mL for all BTNP formulations which is almost an order of magnitude lower than the initial NP concentration after i.v. administration (~0.5 mg/mL). Each BTNP formulation was also stable in high salt concentrations (0.5M NaCl) as measured by DLS, suggesting that the combination of electrostatic and steric repulsions in the P(Aln-co-DMA) corona is resistant to salt destabilization (**Figure 5.3B**).

Nanoparticle stability is also affected *in vivo* by opsonization of serum proteins leading to rapid macrophage clearance.[39–41] Thus, BTNP serum stability was investigated by measuring both NP size and drug retention when challenged with high serum (50% fetal bovine serum, FBS) conditions. DLS measurements showed that BTNP size was largely unaffected by serum incubation in all Aln contents aside from 100%Aln, where the average size increased from ~210 nm to ~330 nm (**Figure 5.3C**). We hypothesize that this is due to opsonization of serum proteins to the negatively charged surface (-35 mV) of the 100%Aln corona. To measure drug retention in the presence of serum, the FRET pair DiI and DiO were co-loaded into BTNPs and incubated in 50% FBS (**Figure 5.3D**). We found that drug retention was dependent on Aln content in the coronal block, with the 100%Aln formulation exhibiting the fastest loss of encapsulated species, further demonstrating its instability in serum conditions. Incubation of BTNPs in lower FBS concentrations (0, 10, 25% FBS) resulted in similar yet less pronounced trends, with the BTNPs exhibiting high stability in saline (0% FBS) conditions (**Figure S5.3**). Notably, the 10%Aln formulation exhibited the highest stability amongst all formulations.

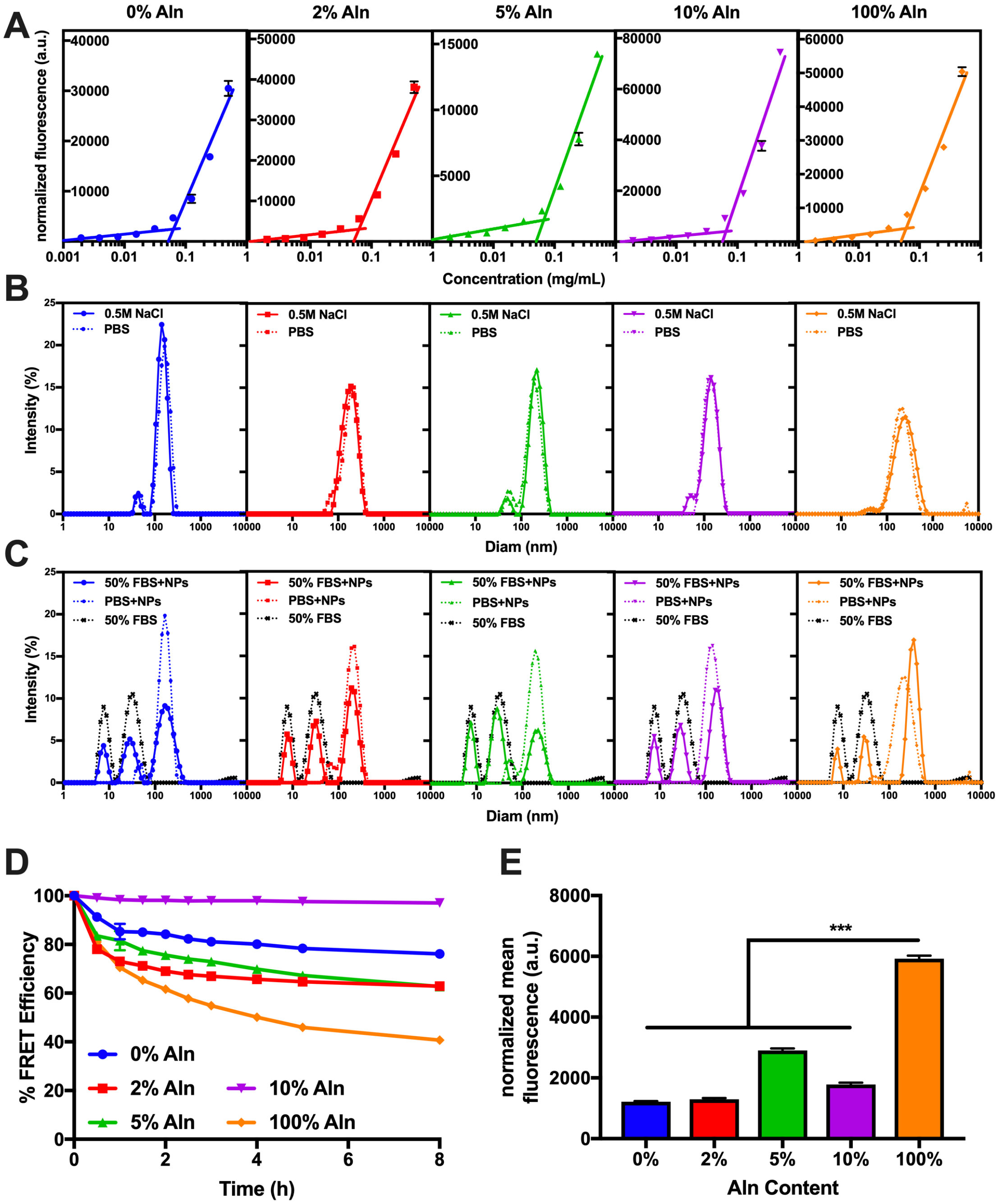

Figure 5.3. GANT58-BTNP stability and macrophage uptake. (A) Critical micelle concentration of each BTNP formulation as measured by Nile Red method. (B) Salt stability of BTNPs in high salt concentrations (0.5M NaCl) as measured by DLS. (C) Serum stability of BTNPs in high serum concentrations (50% FBS) as measured by DLS and (D) FRET efficiency for drug retention in high serum conditions. (E) Macrophage uptake assay performed using Cy5-labeled BTNPs incubated with RAW 264.7 macrophages for three hours and analyzed for cell uptake by flow cytometry.

Nanoparticle clearance is often initiated *in vivo* by uptake into the mononuclear phagocytic system (MPS).[42] Thus, macrophage uptake has been implicated as a preliminary indication of nanoparticle pharmacokinetics (PK) *in vivo*.[43,44] *In vitro* macrophage uptake experiments showed that the 100%Aln formulation BTNPs exhibit significantly higher macrophage uptake than the lower Aln content formulations, suggesting significant opsonization occurs on the 100%Aln formulation, leading to increased uptake (**Figure 5.3E**). Interestingly, the 10%Aln formulation exhibits significantly less uptake than the 5%Aln and 100%Aln formulations. This result aligns with the drug retention findings that showed the 10%Aln is more stable in serum than the other Aln formulations. We hypothesize that the combination of steric and electrostatic repulsion in the 10%Aln formulation leads to improved drug retention and shielding from macrophage uptake. Other studies have shown that slightly anionic micelles avoid non-specific organ uptake and a surface charge < 15 mV leads to minimal macrophage uptake and longer circulation times.[40,45,46]

The bone-binding kinetics of the BTNPs were assessed *in vitro* using nanocrystalline hydroxyapatite (nHA) as a bone substitute. An Aln-dependent binding of BTNPs to nHA was observed, with increasing Aln content leading to higher equilibrium nHA binding (**Figure 5.4A**). Notably, the 10% Aln formulation exhibited similar binding kinetics to the 100% Aln formulation, suggesting there is a saturation concentration of Aln in the coronal block that leads to optimal BTNP bone binding. This finding, along with the results from the combinatorial NP library and the stability studies, led us to choose the 10% Aln formulation as our lead candidate for *in vivo* studies. After incubation with nHA, 10%Aln and 0%Aln formulations were further investigated for nHA affinity using chemical mapping in EDS-STEM. Sulfur (blue) and calcium (white) were used as the chemical signatures for BTNPs and nHA respectively. 10% Aln BTNPs exhibited significant binding to nHA whereas the 0%Aln BTNPs showed no specificity or binding to nHA (**Figure 5.4B, Figure S5.4**).

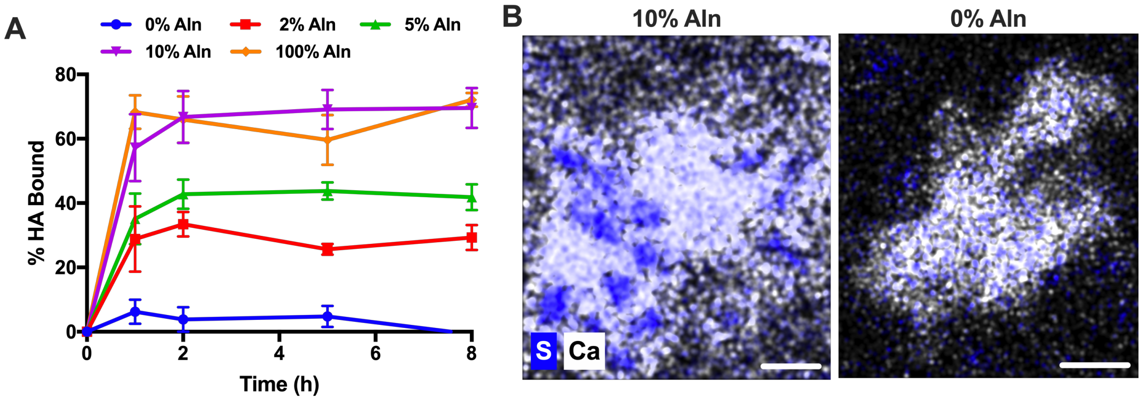

Figure 5.4. GANT58-BTNPs demonstrate high binding affinity to hydroxyapatite. (A) BTNP nHA binding kinetics. Nile Red-loaded BTNPs were incubated with nHA and % nHA bound was measured by loss in Nile Red fluorescence over time. (B) Chemical mapping in STEM-EDS demonstrates 10%Aln BTNPs physically binds to nHA using sulfur (blue) as a chemical signature for BTNPs and calcium (white) as signature for nHA. 0%Aln formulation demonstrates minimal nHA binding.

The ROS-responsive behavior of the NPs was investigated *in vitro* using H_2O_2 as the model ROS species and Nile Red (NR)-loaded BTNPs. The NR cargo was released in an H_2O_2 concentration-dependent manner with minimal cargo release at low H_2O_2 concentrations (**Figure S5.5**). Interestingly, the ROS-release was also dependent on Aln content, with higher Aln content in the corona leading to slower drug release. We hypothesize this is due to the electronegative Aln repelling radical oxygens that would normally penetrate and react with the core sulfide groups.

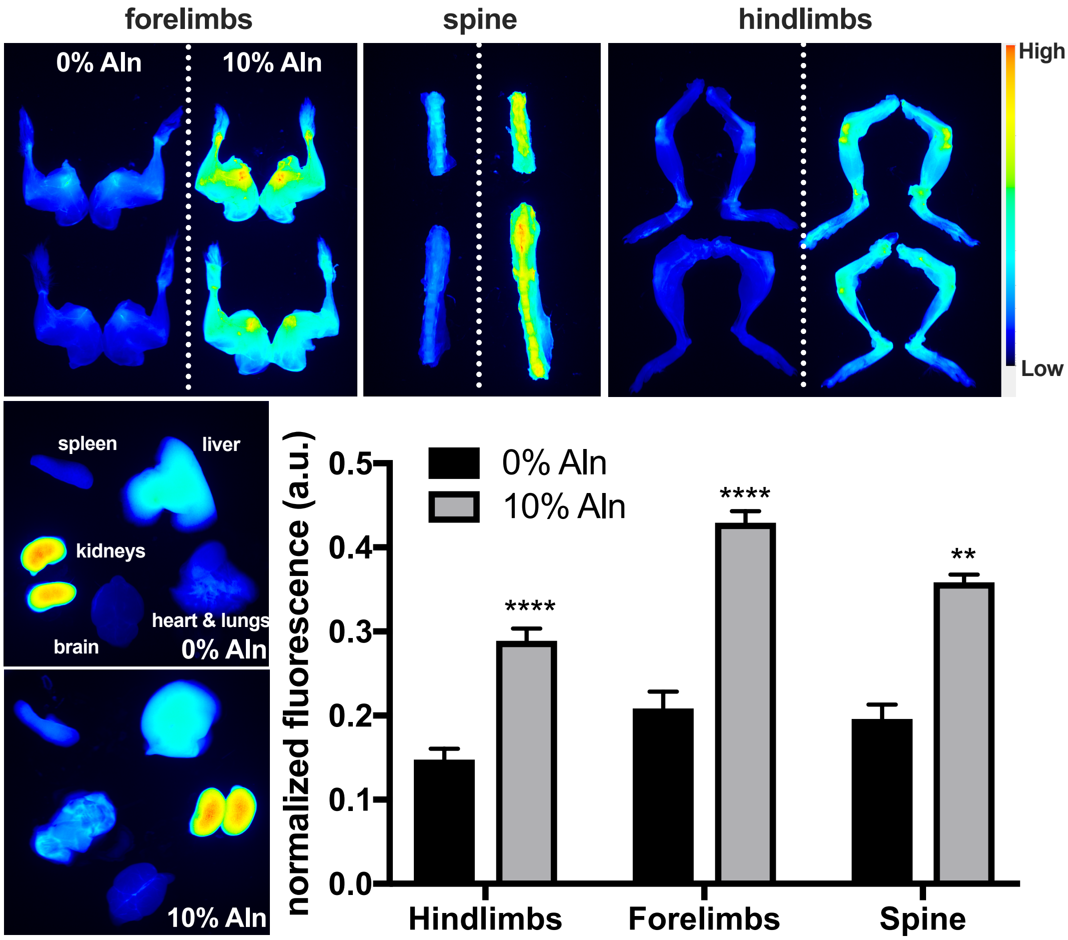

Figure 5.5. GANT58-BTNP Pharmacokinetics and Biodistribution. Near-IR imaging and quantification of Cy7 fluorescence in forelimbs, spine, hindlimbs, and soft tissue of mice treated with Cy7-grafted BTNPs via i.v. injection after 8h circulation.

The biodistribution of the GANT58-BTNPs for the 10% and 0% Aln formulations was first evaluated via fluorescently labeled BTNPs. Cy7-grafted GANT58-BTNPs were administered via intravenous (i.v.) tail vein injection to Rag2 -/- mice. After 8 h, mice were sacrificed and long bones (forelimbs, spine, and hindlimbs) were imaged using a near-IR Pearl imager (**Figure 5.5**). Pearl image analysis software was used to quantify Cy7 fluorescence intensity in the long bones normalized to soft tissue. Cy7 fluorescence intensity in the forelimbs, spine, and hindlimbs was > 2 fold higher in mice treated with the 10% Aln formulation over the 0% Aln formulation.

Based on the biodistribution studies, it was hypothesized that GANT58-BTNPs could provide a pretreatment platform for not only blocking bone destruction, but also tumor establishment by localizing GANT58 to bone prior to tumor metastasis. To test this hypothesis, female athymic nude mice were treated via tail vein injection with either GANT58-BTNPs (10%Aln-GANT58, 8 mg/kg GANT58), unloaded BTNPs (10%Aln), non-targeted GANT58-BTNPs (0%Aln-GANT58, 8 mg/kg GANT58), non-targeted unloaded BTNPs (0%Aln), or no treatment control (Control) starting 3 days prior to tumor inoculation. MDA-MB-231-bone cells were then inoculated via intracardiac injection at day 0 and treatments continued 5 times/week for 4 weeks (**Figure 5.6A**).

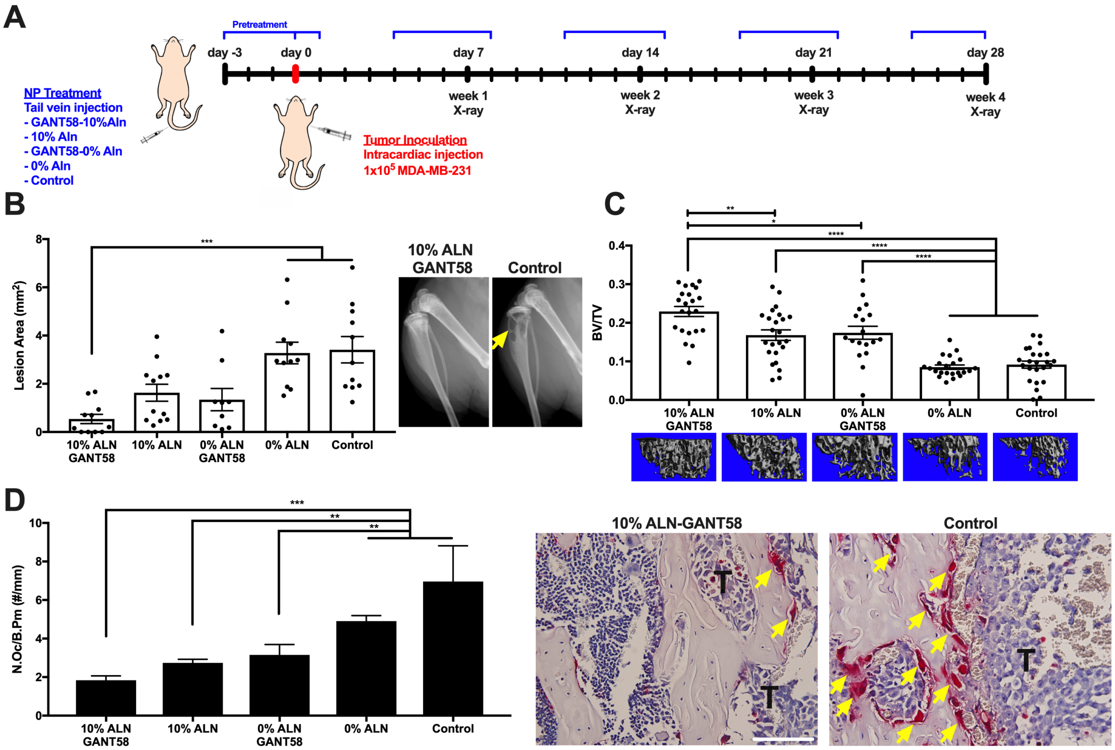

Figure 5.6. GANT58-BTNP treatment reduces tumor-induced osteolysis in mouse model of early bone metastasis. (A) Tumor-inoculation and treatment timeline for intracardiac model of bone metastasis. (B) Lesion area as assessed by radiographic analysis is significantly reduced in GANT58-BTNP treated mice. Yellow arrows indicate osteolytic lesions (C) µCT analysis of tibiae bone volume fraction (BV/TV) showed significantly improved bone quality in mice treated with GANT58-BTNPs. (D) Tartrate-resistant acid phosphatase (TRAP) histomorphometric analysis of osteoclast (OC) number shows significantly decreased OC number per bone perimeter in GANT58-BTNP treated mice. Yellow arrows indicate OCs. Scale bar: 100 µm.

Radiographic imaging was used to track tumor progression in the hindlimbs of mice by visualization of osteolytic lesions. Radiographic analysis prior to sacrifice at week 4 showed the 10%Aln-GANT58 treated mice exhibited smaller and fewer lesions compared to the 0%Aln treated and control mice (**Figure 5.6B, Figure S5.6**). To further assess the bone quality in these mice, micro-computed tomography (µCT) was conducted on the tibiae after sacrifice (**Figure 5.6C**). Mice treated with 10%Aln-GANT58, 10%Aln, and 0%Aln-GANT58 had significantly higher bone volume fraction (BV/TV) than the 0%Aln and control mice. These findings demonstrate that the 10%Aln BTNPs alone have a therapeutic effect, hypothesized to be due to the osteoclast-inhibiting bisphosphonate, Aln, in the corona. Notably, the 10%Aln-GANT58 treated mice exhibited significantly higher BV/TV than 10%Aln and 0%Aln-GANT58 treated mice, suggesting the effects of the of the GANT58 and Aln are additive. Measurement of other morphometric parameters including connectivity density (Conn.D), trabecular number (Tb.N), trabecular separation (Tb.Sp), and trabecular thickness (Tb.Th) also demonstrated that 10%Aln-GANT58 treatment significantly improved bone quality (**Figure S5.7**) The functional effect of both GANT58 and Aln treatment is to reduce osteoclastogenesis. To determine whether the improved bone outcomes are due to a reduction in osteoclasts, tartrate-resistant acid phosphatase (TRAP) histological staining was conducted on the tibia samples after µCT analysis (**Figure 5.6D**). TRAP staining showed that the 10%Aln-GANT58, 10%Aln, and 0%Aln-GANT58 treated mice exhibited significantly fewer osteoclasts per bone perimeter (N.Oc/B.Pm) than 0%Aln-treated and control mice.

Previous studies have shown that Gli2-inhibition blocks tumor growth *in vitro* and even *in vivo* when Gli2 is molecularly repressed in bone metastatic cancer cells lines. This led to the hypothesis that blocking Gli-activity in metastatic breast tumors could obstruct their potential to establish in bone and adopt a bone-destructive phenotype. However, histomorphometric analysis of the tibiae showed no significant decrease in tumor burden in 10%Aln-GANT58 treated mice, whereas bone area quantification followed the same trends observed in μCT (**Figure 5.7A, Figure S5.8**). It is important to note the large variability in tumor burden inherent to the intracardiac model as evidenced by the large standard error. Even with this variability in consideration, there is significant tumor burden in the 10%Aln-GANT58 treated mice despite high BV/TV. Based on a previous study from our lab that demonstrated that increased matrix rigidity drives Gli2 expression in bone metastatic cancer cell lines, we hypothesized that GANT58-BTNP treatment is having a significant effect at the bone interface, yet minimal effect on tumor cells in the marrow space due to a gradient in Gli2 expression as tumor cells approach the rigid bone matrix. To test this hypothesis, immunohistochemistry (IHC) was used to spatially investigate Gli2 protein expression in the tibiae (**Figure 5.7B**). Gli2 expression significantly decreased as distance from the growth plate increased, suggesting the trabecular bone-rich microenvironment in the metaphysis near epiphyseal plate is driving Gli2 expression. This finding further led us to hypothesize that GANT58-BTNP treatment could be reducing proliferation in cells that have adopted a bone-destructive phenotype and increased Gli2 expression. To this end, we conducted IHC for the proliferation marker Ki67 to investigate spatial heterogeneity in tumor cell proliferation (**Figure 5.7C**). It was observed that Ki67 expression was significantly lower at the bone interface compared to the marrow space in the 10%Aln-GANT58 treated mice, whereas there was no observed gradient in the control mice. To further investigate these findings, an *in vitro* proliferation assay was conducted on MDA-MB-231 cells cultured on rigid, tissue culture plastic and compliant gelatin methacrylate (GelMA) gels and treated with GANT58 (**Figure 5.7D**). The proliferation assay supported the *in vivo* findings showing that GANT58 was effective in slowing proliferation of cells on rigid substrates, yet was ineffective on compliant substrates. Taken together, these findings support the hypothesis that the GANT58-BTNP treatment has minimal effects on tumor burden due to the spatial heterogeneity of Gli2 expression within the bone-tumor microenvironment. However, effects at the bone interface, including reduction of both osteoclast number and tumor cell proliferation, are significant due to the high Gli2 expression near bone and high concentration of GANT58 due to the bone-affinity of the treatment.

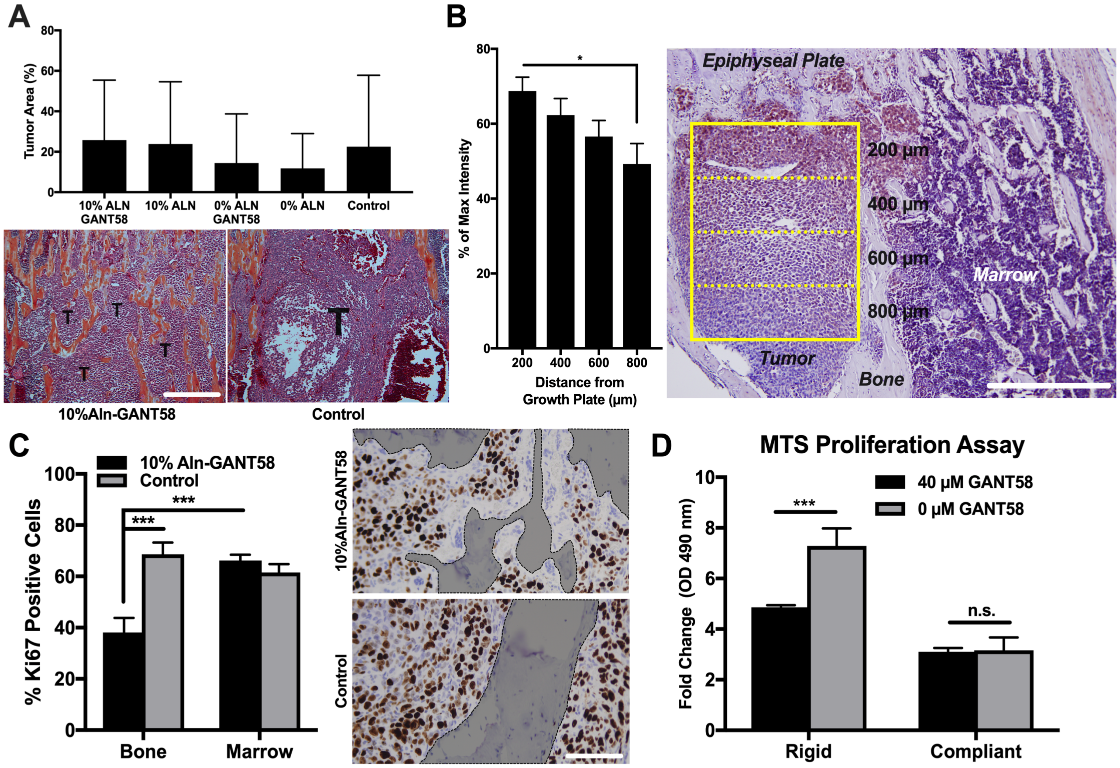

Figure 5.7. GANT58-BTNP treatment effect on tumor burden in mouse model of early bone metastasis. (A) Hematoxylin and Eosin (H&E) histomorphometry demonstrates there is no significant change in tumor burden in GANT58-BTNP treated mice over control. Scale bar: 500 µm. (B) Gli2 immunohistochemistry shows there is a gradient in Gli2 expression as the distance from the growth plate increases. Yellow box denotes tumor region of interest (ROI) analyzed and binned distances from growth plate. Scale bar: 500 µm. (C) Spatial quantification of Ki67 immunohistochemistry shows there is a decrease in % Ki67 positive cells at the bone interface when treated with GANT58-BTNPs. Shaded and outlined regions denote bone. Scale bar: 200 µm. (D) *In vitro* MTS proliferation assay at day 3 after drug treatment shows GANT58 treatment is effective on cells grown on rigid substrates but not on compliant substrates.

Toxicological safety of the GANT58-BTNPs after treatment at therapeutic doses is key to clinical translatability. To test the toxicological profile of the GANT58-BTNPs, blood was drawn at time of sacrifice for the cohort of mice in the intracardiac model study after having received 10%Aln-GANT58, 10%Aln, 0%Aln-GANT58, 0%Aln treatment or no treatment control daily at 8 mg/kg GANT58 (or equivalent dose of unloaded-BTNPs) for 4 weeks. Biochemical analysis of blood serum markers for liver (ALT and AST) and kidney (BUN) toxicity was performed. There was no significant increase in AST, ALT, or BUN levels above two standard deviations from average levels reported by the animal supplier (Envigo) (**Figure S5.9**).

This study built on previous findings that showed encapsulation of GANT58 into polymeric nanoparticles enabled its efficacy in blocking tumor-induced bone destruction *in vivo*, however there was no observed effect on tumor burden. Based on conclusions drawn from the aforementioned study, it was hypothesized that conferring bone-binding affinity to the nanoparticle chemistry could improve site-specific delivery of GANT58 to bone prior to tumor establishment to enable GANT58 to block both bone destruction and tumor proliferation. However, the combined results from the bone and tumor outcomes of the intracardiac model study in this work indicate that GANT58-BTNPs serve as an effective tumor-mediated antiresorptive therapy, but with negligible antitumor activity *in vivo*.

Tissues – including tumor – are known to respond to the stiffness of their microenvironment.[47] These responses in tumor can result in phenotypic changes that alter gene expression and cell behavior causing spatial heterogeneity within the tumor site. Intratumor spatial heterogeneity causes complications in therapeutic targeting and has precluded advances in personalized medicine due to unrepresentative single-tumor biopsies in the clinic.[48] Previous research in our lab has demonstrated that Gli2 expression in bone metastatic cell lines is regulated by matrix rigidity, and thus we hypothesized that Gli2 expression in the bone metastatic tumors could be spatially heterogeneous, with most Gli2 expression being localized near trabecular bone.[49,50] Indeed, Gli2 IHC demonstrated there is a gradient of Gli2 expression within the metaphysis of the tibia (Figure 7B). The spatial gradient suggests that, in addition to rigidity effects, there is an additional component involved in driving Gli2 expression, considering the gradient is a function of distance from the growth plate, not distance from bone. We hypothesize the high concentration of trabecular bone and active bone cells – which cause release of growth factors including TGF-β that is known to drive Gli2 expression – near the epiphysis combine to create a fertile environment for tumor cells to adopt a bone-destructive phenotype. Further, Ki67 staining demonstrated that GANT58-BTNP treatment has an effect on blocking proliferation at the bone-interface, yet no effect on cells in the marrow space (Figure 7C). Collectively, these findings suggest the lack of GANT58-BTNP antitumor activity *in vivo* is driven by intratumor heterogeneity in Gli2 expression.

Developing a GANT58 formulation that was highly stable in circulation and promoted aggregation in bone in the absence of tumor were two key elements to the design of the BTNP platform. Most polymer chemistries used in NP drug delivery systems are inherently tunable and myriad design parameters including size, shape, surface charge and functionalization are known to play a role in NP behavior *in vivo*.[51] Previous studies have demonstrated the utility of developing combinatorial NP libraries using NP characterization techniques and *in vitro* screening to identify optimal NP formulations for use *in vivo*.[43,52] Here, the development of a combinatorial BTNP library was critical to identifying an optimal formulation for *in vivo* studies based on BTNP size, surface charge and drug loading in addition to bone-binding affinity *in vitro*. The lead 10%Aln formulation overcomes sole reliance on the enhanced permeation and retention (EPR) effect – the debated phenomenon in which established, vascularized tumors allow for nanoparticle extravasation through leaky tumor vessels[53] – for NP accumulation in the bone-tumor microenvironment through its bone-affinity. Conferring bone-binding affinity to nanoparticle chemistries is an area of active research with many successful examples that has been reviewed extensively.[19,34,54] Much of this work, however, has focused on the delivery of traditional chemotherapeutics – such as doxorubicin, paclitaxel, and cisplatin – to bone.[21,23,55,56] The bone marrow microenvironment is extremely sensitive to chemotherapeutics, so targeting these chemotherapies specifically to bone with the goal of minimizing off-target effects can lead to significant toxicity to healthy bone cells and bone itself.[57,58] GANT58-BTNPs, on the other hand, are designed to inhibit the aberrantly activated Gli2 protein that is known to drive bone destruction. The specificity of GANT58 for Gli2 had a two-fold impact: the treatment selectively targeted a major driver of the vicious cycle to block bone destruction, and this selectivity mitigated the systemic toxicity that is common among chemotherapies. Further, we show the added bone-affinity of the BTNPs led to improved protection from tumor-induced bone destruction over the non-targeted GANT58-loaded formulation. These findings make GANT58-BTNPs a strong candidate for clinical translation as an alternative to pan-osteoclast inhibitors, or as a combination therapy with other antitumor therapeutics to improve bone quality and patient quality of life.

5.5. Conclusion

Synthesis of BTNP polymers and development of a combinatorial NP library yielded a GANT58-loaded lead candidate formulation that significantly reduced bone destruction in an intracardiac mouse model of bone metastasis. The lead candidate 10%Aln formulation BTNPs demonstrated significant bone-binding *in vivo* and elicited minimal systemic toxicity upon i.v. administration with an aggressive treatment schedule. Histological analysis elucidated spatial heterogeneity in Gli2 expression and GANT58-BTNP effect on tumor cell proliferation, and thus provided insight into the role the bone microenvironment plays in driving tumor progression. Collectively, these findings suggest GANT58-BTNP is a potential therapy for TIBD patients, however combination therapy with antitumor agents should be investigated to improve both patient quality of life and survival.

5.6. Supplementary Information

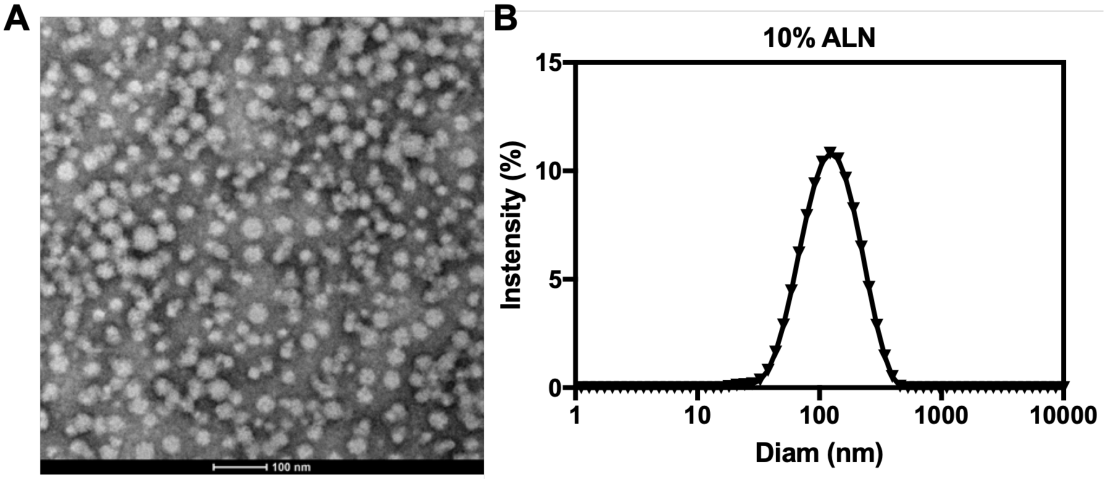

Figure S5.1. GANT58-BTNP size characterization. (A) Representative TEM image demonstrates the 10%Aln micelles exhibit a spherical morphology. (B) Dynamic light scattering (DLS) of 10%Aln micelles shows the micelles have an average hydrodynamic diameter of ~100 nm.

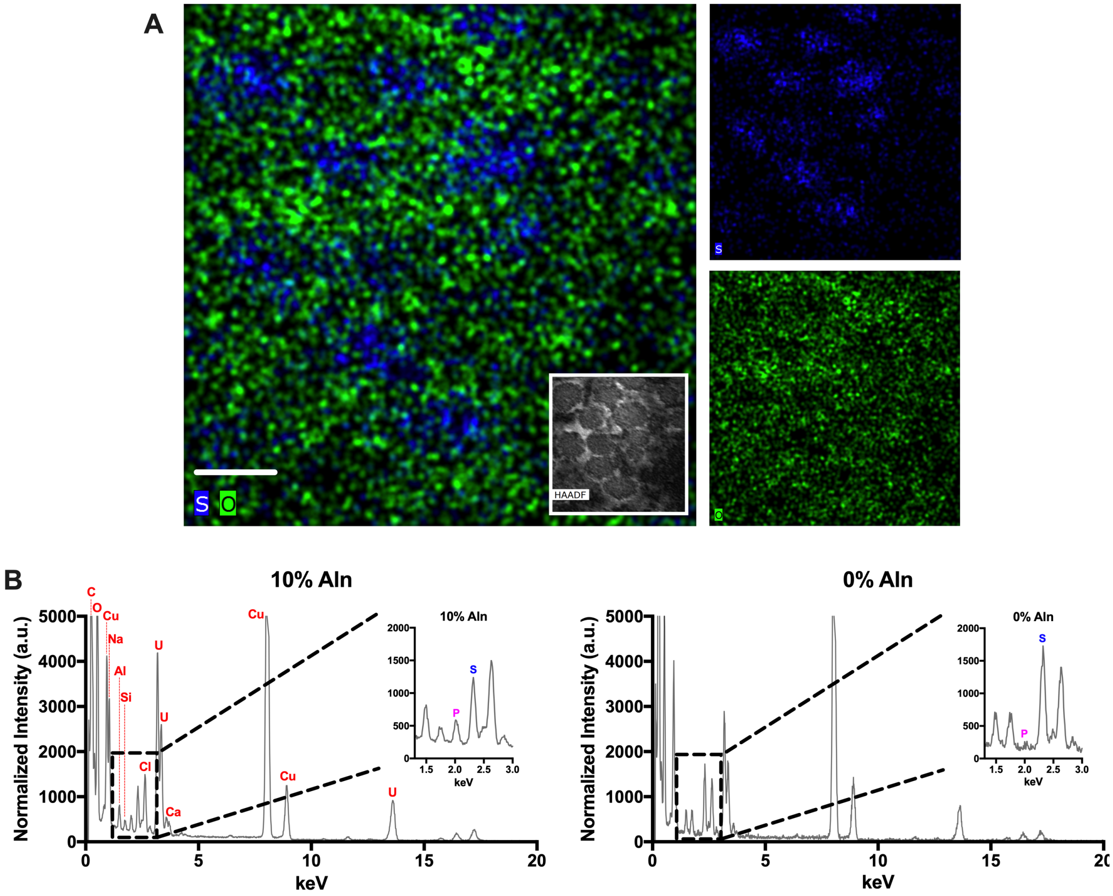

Figure S5.2. BTNP STEM-EDS characterization. (A) 0%Aln formulation chemical mapping using sulfur (blue) and oxygen (green) as signatures for PPS and DMA shows a sulfur-rich core and oxygen-rich corona. Scale bar: 40 nm. (B) Full EDS spectra of both the 10%Aln and 0% Aln formulations. Other characteristic EDS peaks of relevant elements (from TEM grid and buffer) labeled in red.

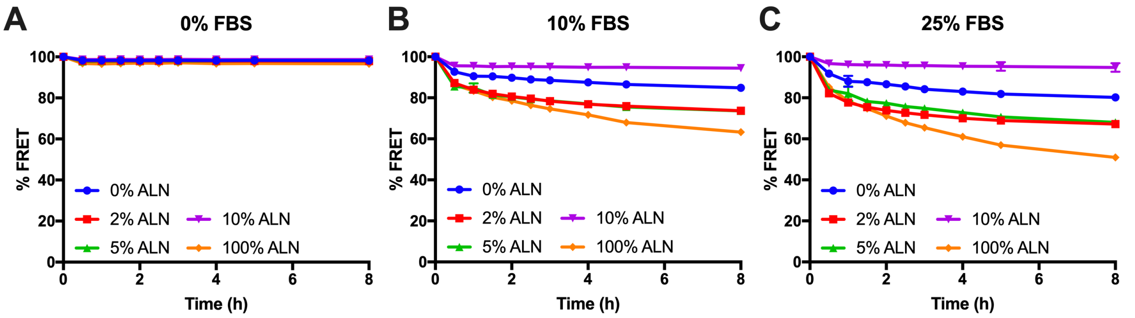

Figure S5.3. GANT58-BTNP cargo retention in serum. FRET pair DiI-DiO were loaded into BTNPs and FRET efficiency was measured at prescribed times after incubation in (A) 0% fetal bovine serum (FBS), (B) 10% FBS, and (C) 25% FBS.

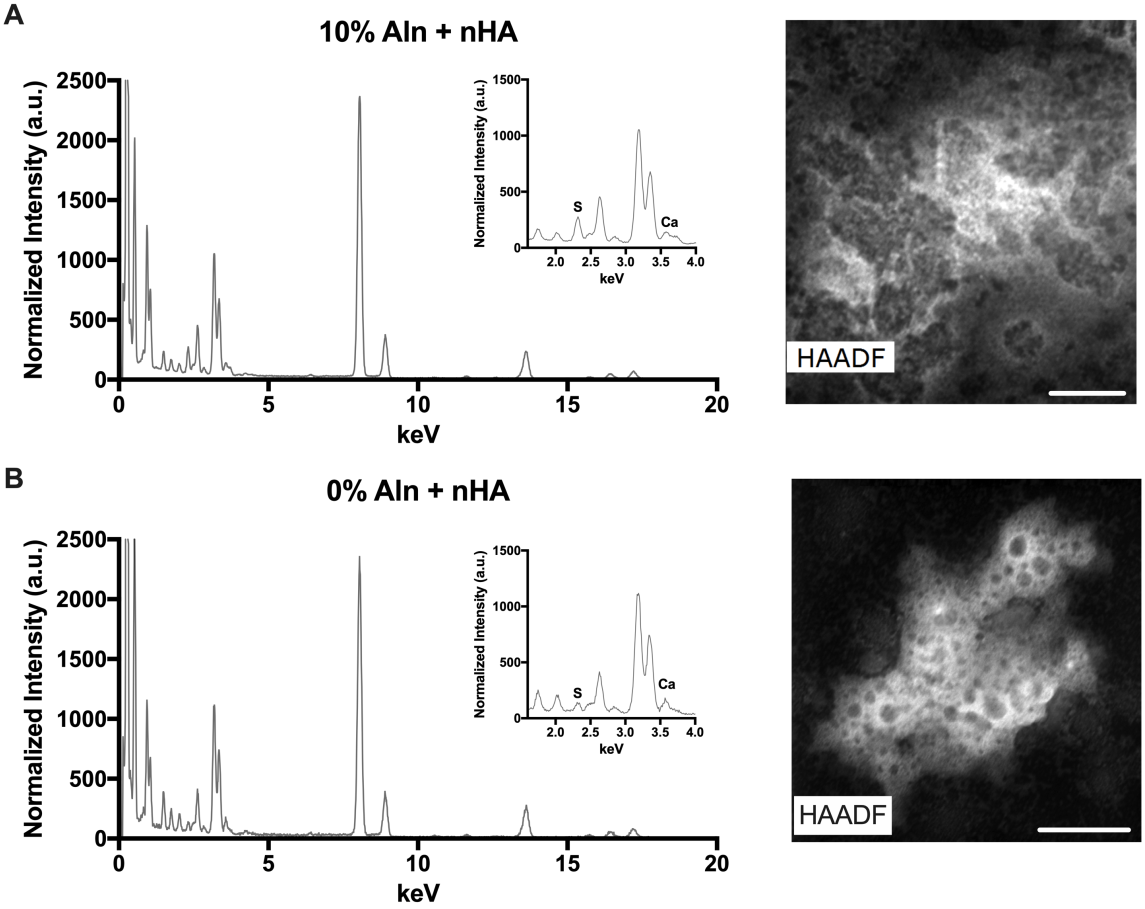

Figure S5.4. STEM-EDS characterization of *in vitro* nHA binding of BTNPs. (A) 10%Aln formulation and (B) 0%Aln formulation EDS spectra exhibit significant sulfur peak (inset images) only in 10%Aln formulation. Original HAADF images from which EDS spectra was analyzed on right. Scale bar: 50 nm.

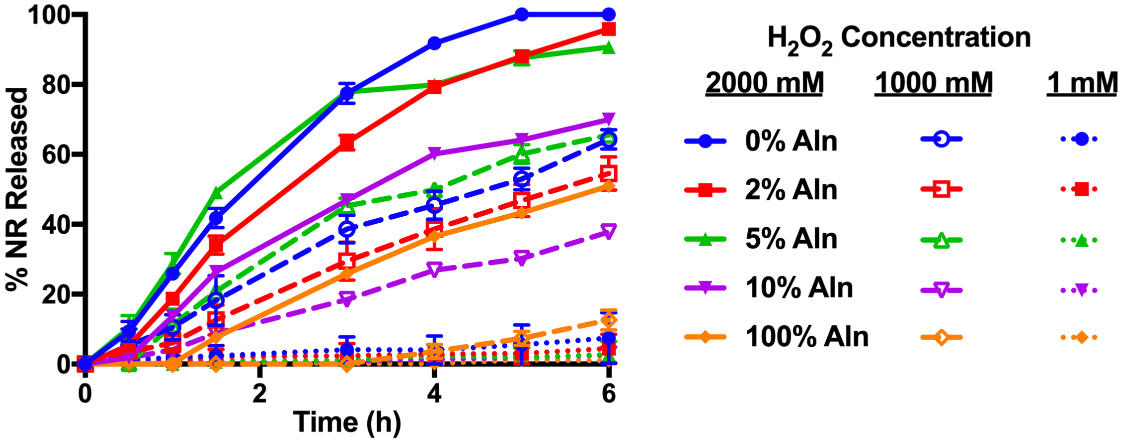

Figure S5.5. GANT58-BTNP ROS-mediated release characterization. H_2O_2 concentration-dependent release of encapsulated species from BTNPs as measured by Nile Red method.

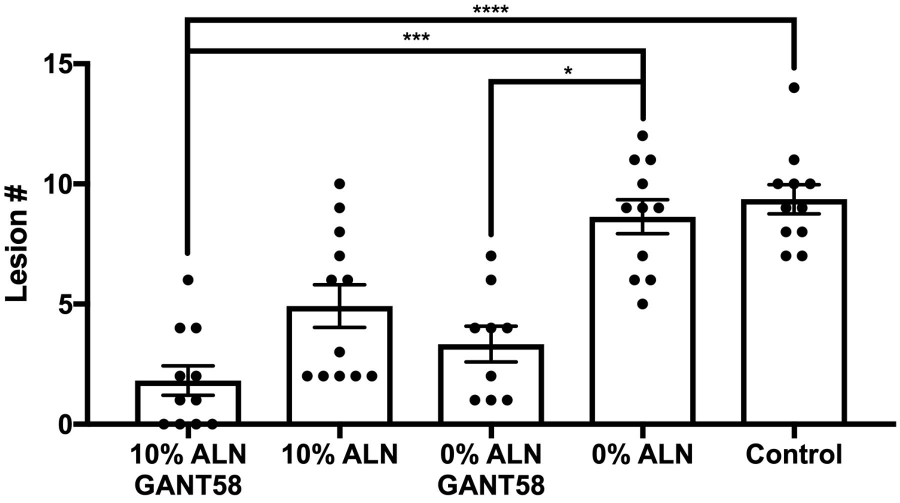

Figure S5.6. GANT58-BTNPs reduced osteolytic lesion number in mouse model of early bone metastasis. Radiographic analysis at 4 weeks post-tumor inoculation indicates mice treated with GANT58-BTNPs have significantly reduced number of osteolytic lesions.

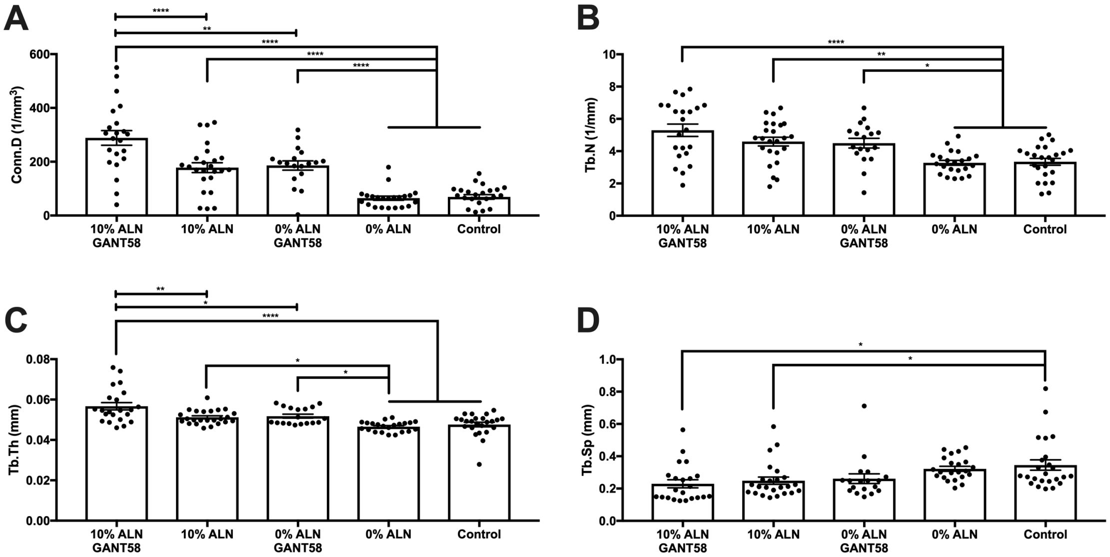

Figure S5.7. GANT58-BTNPs reduced bone destruction in mouse model of early bone metastasis. *Ex vivo* µCT analysis at 4 weeks post-tumor inoculation indicates mice treated with GANT58-BTNPs have (A) significantly increased connectivity density (Conn.D), (B) trabecular number (Tb.N), (C) trabecular thickness (Tb.Th), and (D) significantly decreased trabecular spacing (Tb.Sp).

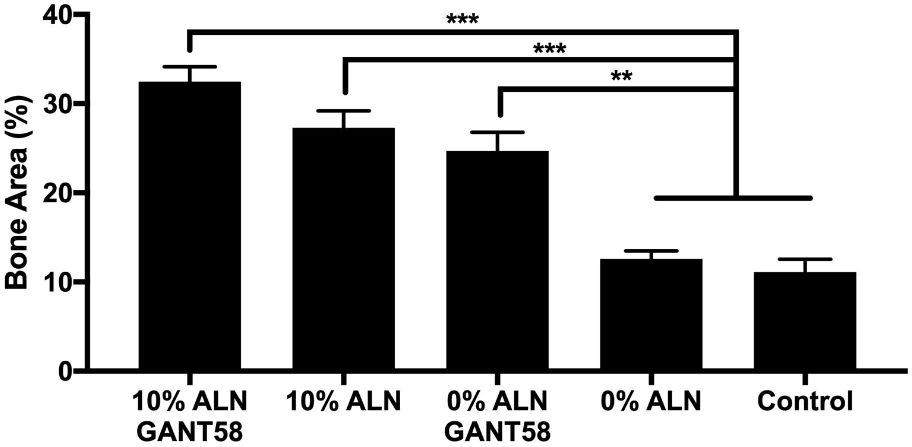

Figure S5.8. GANT58-BTNPs treatment reduces bone destruction as measured by histomorphometric analysis in mouse model of early bone metastasis. Hematoxylin and Eosin (H&E) histomorphometric analysis of bone area supports µCT findings that GANT58-BTNP treatment significantly increases trabecular bone volume in tumor-bearing mice.

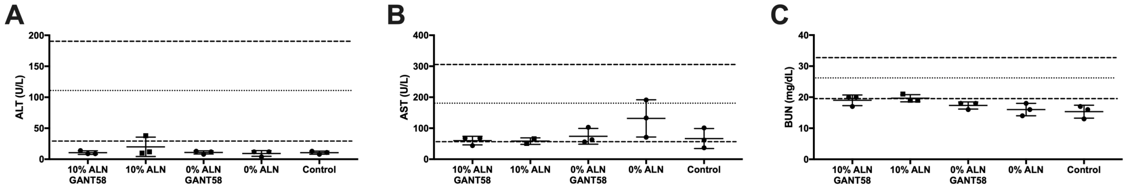

Figure S5.9. GANT58-BTNPs elicit minimal systemic toxicity. Biochemical analysis of serum markers of liver toxicity (A) ALT and (B) AST, and kidney toxicity (C) BUN after 8 mg/kg GANT58-BTNP treatment 5x/week for 4 weeks.

References

(1) American Cancer Society. Breast Cancer Facts & Figures 2017-2018. *Atlanta: American Cancer Society, Inc.* 2017, pp 1–44.

(2) GD, R. Mechanisms of Bone Metastasis. *N Engl j Med* **2004**, *350* (16), 1655–1664.

(3) Onishi, T.; Hayashi, N.; Theriault, R. L.; Hortobagyi, G. N.; Ueno, N. T. Future Directions of Bone-Targeted Therapy for Metastatic Breast Cancer. *Nature Reviews Clinical Oncology*. 2010.

(4) Gnant, M.; Pfeiler, G.; Dubsky, P. C.; Hubalek, M.; Greil, R.; Jakesz, R.; Wette, V.; Balic, M.; Haslbauer, F.; Melbinger, E.; et al. Adjuvant Denosumab in Breast Cancer (ABCSG-18): A Multicentre, Randomised, Double-Blind, Placebo-Controlled Trial. *Lancet* **2015**, *386* (9992), 433–443.

(5) Fusco, V.; Galassi, C.; Berruti, A.; Ciuffreda, L.; Ortega, C.; Ciccone, G.; Angeli, A.; Bertetto, O. Osteonecrosis of the Jaw after Zoledronic Acid and Denosumab Treatment. *Journal of Clinical Oncology*. 2011.

(6) Bamias, A.; Kastritis, E.; Bamia, C.; Moulopoulos, L. A.; Melakopoulos, I.; Bozas, G.; Koutsoukou, V.; Gika, D.; Anagnostopoulos, A.; Papadimitriou, C.; et al. Osteonecrosis of the Jaw in Cancer after Treatment with Bisphosphonates: Incidence and Risk Factors. *J. Clin. Oncol.* **2005**, *23* (34), 8580–8587.

(7) Mundy, G. R. Mechanisms of Bone Metastasis. *Cancer* **1997**, *80* (8), 1546–1556.

(8) Yin, J. J.; Selander, K.; Chirgwin, J. M.; Dallas, M.; Grubbs, B. G.; Wieser, R.; Massagué, J.; Mundy, G. R.; Guise, T. A. TGF-β Signaling Blockade Inhibits PTHrP Secretion by Breast Cancer Cells and Bone Metastases Development. *J. Clin. Invest.* **1999**.

(9) Peer, D.; Karp, J. M.; Hong, S.; Farokhzad, O. C.; Margalit, R.; Langer, R. Nanocarriers as an Emerging Platform for Cancer Therapy. *Nat. Nanotechnol.* **2007**, *2* (12), 751–760.

(10) Ashton, S.; Song, Y. H.; Nolan, J.; Cadogan, E.; Murray, J.; Odedra, R.; Foster, J.; Hall, P. A.; Low, S.; Taylor, P.; et al. Aurora Kinase Inhibitor Nanoparticles Target Tumors with Favorable Therapeutic Index in Vivo. *Sci. Transl. Med.* **2016**, *8* (325).

(11) Mizrachi, A.; Shamay, Y.; Shah, J.; Brook, S.; Soong, J.; Rajasekhar, V. K.; Humm, J. L.; Healey, J. H.; Powell, S. N.; Baselga, J.; et al. Tumour-Specific PI3K Inhibition via Nanoparticle-Targeted Delivery in Head and Neck Squamous Cell Carcinoma. *Nat. Commun.* **2017**, *8*.

(12) Schmid, D.; Park, C. G.; Hartl, C. A.; Subedi, N.; Cartwright, A. N.; Puerto, R. B.; Zheng, Y.; Maiarana, J.; Freeman, G. J.; Wucherpfennig, K. W.; et al. T Cell-Targeting Nanoparticles Focus Delivery of Immunotherapy to Improve Antitumor Immunity. *Nat. Commun.* **2017**, *8* (1), 1–11.

(13) Schultheis, B.; Strumberg, D.; Santel, A.; Vank, C.; Gebhardt, F.; Keil, O.; Lange, C.; Giese, K.; Kaufmann, J.; Khan, M.; et al. First-in-Human Phase I Study of the Liposomal RNA Interference Therapeutic Atu027 in Patients with Advanced Solid Tumors. *J. Clin. Oncol.* **2014**, *32* (36), 4141–4148.

(14) Tabernero, J.; Shapiro, G. I.; LoRusso, P. M.; Cervantes, A.; Schwartz, G. K.; Weiss, G. J.; Paz-Ares, L.; Cho, D. C.; Infante, J. R.; Alsina, M.; et al. First-in-Humans Trial of an RNA Interference Therapeutic Targeting VEGF and KSP in Cancer Patients with Liver Involvement. *Cancer Discov.* **2013**, *3* (April), 406–417.

(15) Xu, X.; Wu, J.; Liu, Y.; Saw, P. E.; Tao, W.; Yu, M.; Zope, H.; Si, M.; Victorious, A.; Rasmussen, J.; et al. Multifunctional Envelope-Type SiRNA Delivery Nanoparticle Platform for Prostate Cancer Therapy. *ACS Nano* **2017**, *11* (3), 2618–2627.

(16) Werfel, T. A.; Wang, S.; Jackson, M. A.; Kavanaugh, T. E.; Joly, M. M.; Lee, L. H.; Hicks, D. J.; Sanchez, V.; Ericsson, P. G.; Kilchrist, K. V.; et al. Selective MTORC2 Inhibitor Therapeutically Blocks Breast Cancer Cell Growth and Survival. *Cancer Res.* **2018**, *78* (7),

1845–1858.

(17) Kwak, E. L.; Clark, J. W.; Chabner, B. Targeted Agents: The Rules of Combination. *Clin. Cancer Res.* **2007**, *13* (18), 5232–5237.

(18) Swami, A.; Reagan, M. R.; Basto, P.; Mishima, Y.; Kamaly, N.; Glavey, S.; Zhang, S.; Moschetta, M.; Seevaratnam, D.; Zhang, Y.; et al. Engineered Nanomedicine for Myeloma and Bone Microenvironment Targeting. *Proc. Natl. Acad. Sci. U. S. A.* **2014**, *111* (28), 10287–10292.

(19) Cole, L. E.; Vargo-Gogola, T.; Roeder, R. K. Targeted Delivery to Bone and Mineral Deposits Using Bisphosphonate Ligands. *Adv. Drug Deliv. Rev.* **2016**, *99*, 12–27.

(20) Qiao, H.; Cui, Z.; Yang, S.; Ji, D.; Wang, Y.; Yang, Y.; Han, X.; Fan, Q.; Qin, A.; Wang, T.; et al. Targeting Osteocytes to Attenuate Early Breast Cancer Bone Metastasis by Theranostic Upconversion Nanoparticles with Responsive Plumbagin Release. *ACS Nano* **2017**, *11* (7), 7259–7273.

(21) Liu, P.; Sun, L.; Zhou, D.; Zhang, P.; Wang, Y.; Li, D.; Li, Q.; Feng, R.-J. Development of Alendronate-Conjugated Poly (Lactic-Co-Glycolic Acid)-Dextran Nanoparticles for Active Targeting of Cisplatin in Osteosarcoma. *Sci. Rep.* **2015**, *5* (December), 17387.

(22) Murphy, M. B.; Hartgerink, J. D.; Goepferich, A.; Mikos, A. G. Synthesis and in Vitro Hydroxyapatite Binding of Peptides Conjugated to Calcium-Binding Moieties. *Biomacromolecules* **2007**.

(23) Yamashita, S.; Katsumi, H.; Hibino, N.; Isobe, Y.; Yagi, Y.; Tanaka, Y.; Yamada, S.; Naito, C.; Yamamoto, A. Development of PEGylated Aspartic Acid-Modified Liposome as a Bone-Targeting Carrier for the Delivery of Paclitaxel and Treatment of Bone Metastasis. *Biomaterials* **2018**, *154*, 74–85.

(24) Wang, D.; Miller, S. C.; Shlyakhtenko, L. S.; Portillo, A. M.; Liu, X. M.; Papangkorn, K.; Kopečková, P.; Lyubchenko, Y.; Higuchi, W. I.; Kopeček, J. Osteotropic Peptide That Differentiates Functional Domains of the Skeleton. *Bioconjug. Chem.* **2007**, *18* (5), 1375–1378.

(25) Yamashita, S.; Katsumi, H.; Hibino, N.; Isobe, Y.; Yagi, Y.; Kusamori, K.; Sakane, T.; Yamamoto, A. Development of PEGylated Carboxylic Acid-Modified Polyamidoamine Dendrimers as Bone-Targeting Carriers for the Treatment of Bone Diseases. *J. Control. Release* **2017**, *262*, 10–17.

(26) Zhou, Z.; Fan, T.; Yan, Y.; Zhang, S.; Zhou, Y.; Deng, H.; Cai, X.; Xiao, J.; Song, D.; Zhang, Q.; et al. One Stone with Two Birds: Phytic Acid-Capped Platinum Nanoparticles for Targeted Combination Therapy of Bone Tumors. *Biomaterials* **2019**, *194*, 130–138.

(27) Poole, K. M.; Nelson, C. E.; Joshi, R. V.; Martin, J. R.; Gupta, M. K.; Haws, S. C.; Kavanaugh, T. E.; Skala, M. C.; Duvall, C. L. ROS-Responsive Microspheres for on Demand Antioxidant Therapy in a Model of Diabetic Peripheral Arterial Disease. *Biomaterials* **2015**, *41*, 166–175.

(28) Gupta, M. K.; Martin, J. R.; Werfel, T. A.; Shen, T.; Page, J. M.; Duvall, C. L. Cell Protective, ABC Triblock Polymer-Based Thermoresponsive Hydrogels with ROS-Triggered Degradation and Drug Release. *J. Am. Chem. Soc.* **2014**, *136* (42), 14896–14902.

(29) Uddin, M. J.; Werfel, T. A.; Crews, B. C.; Gupta, M. K.; Kavanaugh, T. E.; Kingsley, P. J.; Boyd, K.; Marnett, L. J.; Duvall, C. L. Fluorocoxib A Loaded Nanoparticles Enable Targeted Visualization of Cyclooxygenase-2 in Inflammation and Cancer. *Biomaterials* **2016**, *92*, 71–80.

(30) Gupta, M. K.; Meyer, T. a.; Nelson, C. E.; Duvall, C. L. Poly(PS-b-DMA) Micelles for Reactive Oxygen Species Triggered Drug Release. *J. Control. Release* **2012**, *162* (3), 591–598.

(31) Costa, A.; Scholer-Dahirel, A.; Mechta-Grigoriou, F. The Role of Reactive Oxygen Species and Metabolism on Cancer Cells and Their Microenvironment. *Seminars in Cancer Biology*. 2014.

(32) Szatrowski, T. P.; Nathan, C. F. Production of Large Amounts of Hydrogen Peroxide by Human Tumor Cells1. **1991**, 794–799.

(33) Šprincl, L.; Vacík, J.; Kopeček, J.; Lím, D. Biological Tolerance of Poly(N-substituted Methacrylamides). *J. Biomed. Mater. Res.* **1971**.

(34) Low, S. A.; Kopeček, J. Targeting Polymer Therapeutics to Bone. *Advanced Drug Delivery Reviews*. 2012.

(35) Leu, C. T.; Luegmayr, E.; Freedman, L. P.; Rodan, G. A.; Reszka, A. A. Relative Binding Affinities of Bisphosphonates for Human Bone and Relationship to Antiresorptive Efficacy. *Bone* **2006**.

(36) Baron, R.; Ferrari, S.; Russell, R. G. G. Denosumab and Bisphosphonates: Different Mechanisms of Action and Effects. *Bone*. 2011, pp 677–692.

(37) Lu, Y.; Zhang, E.; Yang, J.; Cao, Z. Strategies to Improve Micelle Stability for Drug Delivery. *Nano Res.* **2018**, *11* (10), 4985–4998.

(38) Kim, S.; Shi, Y.; Kim, J. Y.; Park, K.; Cheng, J.-X. Overcoming the Barriers in Micellar Drug Delivery: Loading Efficiency, *in Vivo* Stability, and Micelle–Cell Interaction. *Expert Opin. Drug Deliv.* **2010**.

(39) Gustafson, H. H.; Holt-Casper, D.; Grainger, D. W.; Ghandehari, H. Nanoparticle Uptake: The Phagocyte Problem. *Nano Today*. 2015.

(40) Kamaly, N.; Xiao, Z.; Valencia, P. M.; Radovic-Moreno, A. F.; Farokhzad, O. C. Targeted Polymeric Therapeutic Nanoparticles: Design, Development and Clinical Translation. *Chem. Soc. Rev.* **2012**, *41* (7), 2971–3010.

(41) Salvador-Morales, C.; Zhang, L.; Langer, R.; Farokhzad, O. C. Immunocompatibility Properties of Lipid-Polymer Hybrid Nanoparticles with Heterogeneous Surface Functional Groups. *Biomaterials* **2009**, *30* (12), 2231–2240.

(42) Bertrand, N.; Leroux, J. C. The Journey of a Drug-Carrier in the Body: An Anatomo-Physiological Perspective. *Journal of Controlled Release*. 2012.

(43) Valencia, P. M.; Pridgen, E. M.; Rhee, M.; Langer, R.; Farokhzad, O. C.; Karnik, R. Microfluidic Platform for Combinatorial Synthesis and Optimization of Targeted Nanoparticles for Cancer Therapy. *ACS Nano* **2013**, *7* (12), 10671–10680.

(44) Perry, J. L.; Reuter, K. G.; Kai, M. P.; Herlihy, K. P.; Jones, S. W.; Luft, J. C.; Napier, M.; Bear, J. E.; Desimone, J. M. PEGylated PRINT Nanoparticles: The Impact of PEG Density on Protein Binding, Macrophage Association, Biodistribution, and Pharmacokinetics. *Nano Lett.* **2012**, *12* (10), 5304–5310.

(45) He, C.; Hu, Y.; Yin, L.; Tang, C.; Yin, C. Effects of Particle Size and Surface Charge on Cellular Uptake and Biodistribution of Polymeric Nanoparticles. *Biomaterials* **2010**, *31* (13), 3657–3666.

(46) Yamamoto, Y.; Nagasaki, Y.; Kato, Y.; Sugiyama, Y.; Kataoka, K. Long-Circulating Poly(Ethylene Glycol)-Poly(D,L-Lactide) Block Copolymer Micelles with Modulated Surface Charge. *J. Control. Release* **2001**, *77* (1–2), 27–38.

(47) Discher, D. E. Tissue Cells Feel and Respond to the Stiffness of Their Substrate. *Science (80-.).* **2005**, *310* (5751), 1139–1143.

(48) Gerlinger, M.; Rowan, A. J.; Horswell, S.; Larkin, J.; Endesfelder, D.; Gronroos, E.; Martinez, P.; Matthews, N.; Stewart, A.; Tarpey, P.; et al. Intratumor Heterogeneity and Branched Evolution Revealed by Multiregion Sequencing. *N. Engl. J. Med.* **2012**, *366* (10), 883–892.

(49) Ruppender, N. S.; Merkel, A. R.; Martin, T. J.; Mundy, G. R.; Sterling, J. A.; Guelcher, S. A. Matrix Rigidity Induces Osteolytic Gene Expression of Metastatic Breast Cancer Cells. *PLoS One* **2010**, *5* (11), 1–10.

(50) Page, J. M.; Merkel, A. R.; Ruppender, N. S.; Guo, R.; Dadwal, U. C.; Cannonier, S. A.; Basu, S.; Guelcher, S. A.; Sterling, J. A. Matrix Rigidity Regulates the Transition of Tumor Cells to a Bone-Destructive Phenotype through Integrin B3 and TGF-β Receptor Type II.

Biomaterials **2015**, *64*, 33–44.

(51) Blanco, E.; Shen, H.; Ferrari, M. Principles of Nanoparticle Design for Overcoming Biological Barriers to Drug Delivery. *Nat. Biotechnol.* **2015**, *33* (9), 941–951.

(52) Werfel, T. A.; Jackson, M. A.; Kavanaugh, T. E.; Kirkbride, K. C.; Miteva, M.; Giorgio, T. D.; Duvall, C. Combinatorial Optimization of PEG Architecture and Hydrophobic Content Improves Ternary SiRNA Polyplex Stability, Pharmacokinetics, and Potency in Vivo. *J. Control. Release* **2017**, *255*, 12–26.

(53) Clark, A. J.; Wiley, D. T.; Zuckerman, J. E.; Webster, P.; Chao, J.; Lin, J.; Yen, Y.; Davis, M. E. CRLX101 Nanoparticles Localize in Human Tumors and Not in Adjacent, Nonneoplastic Tissue after Intravenous Dosing. *Proc. Natl. Acad. Sci.* **2016**, *113*, 3850–3854.

(54) Carbone, E. J.; Rajpura, K.; Allen, B. N.; Cheng, E.; Ulery, B. D.; Lo, K. W. H. Osteotropic Nanoscale Drug Delivery Systems Based on Small Molecule Bone-Targeting Moieties. *Nanomedicine Nanotechnology, Biol. Med.* **2017**, *13* (1), 37–47.

(55) Zhao, Y. P.; Ye, W. L.; Liu, D. Z.; Cui, H.; Cheng, Y.; Liu, M.; Zhang, B. Le; Mei, Q. B.; Zhou, S. Y. Redox and PH Dual Sensitive Bone Targeting Nanoparticles to Treat Breast Cancer Bone Metastases and Inhibit Bone Resorption. *Nanoscale* **2017**, *9* (19), 6264–6277.

(56) Li, C.; Zhang, Y.; Chen, G.; Hu, F.; Zhao, K.; Wang, Q. Engineered Multifunctional Nanomedicine for Simultaneous Stereotactic Chemotherapy and Inhibited Osteolysis in an Orthotopic Model of Bone Metastasis. *Adv. Mater.* **2017**, *29* (13).

(57) Sinder, B. P.; Zweifler, L.; Koh, A. J.; Michalski, M. N.; Hofbauer, L. C.; Aguirre, J. I.; Roca, H.; McCauley, L. K. Bone Mass Is Compromised by the Chemotherapeutic Trabectedin in Association With Effects on Osteoblasts and Macrophage Efferocytosis. *J. Bone Miner. Res.* **2017**, *32* (10), 2116–2127.

(58) Fan, C.; Georgiou, K. R.; Morris, H. A.; McKinnon, R. A.; Keefe, D. M. K.; Howe, P. R.; Xian, C. J. Combination Breast Cancer Chemotherapy with Doxorubicin and Cyclophosphamide Damages Bone and Bone Marrow in a Female Rat Model. *Breast Cancer Res. Treat.* **2017**, *165* (1), 41–51.

(59) Guise, T. A.; Yin, J. J.; Taylor, S. D.; Kumagai, Y.; Dallas, M.; Boyce, B. F.; Yoneda, T.; Mundy, G. R. Evidence for a Causal Role of Parathyroid Hormone-Related Protein in the Pathogenesis of Human Breast Cancer-Mediated Osteolysis. *J Clin Invest* **1996**, *98* (7), 1544–1549.

(60) Saito, H.; Tsunenari, T.; Onuma, E.; Sato, K.; Ogata, E.; Yamada-Okabe, H. Humanized Monoclonal Antibody against Parathyroid Hormone-Related Protein Suppresses Osteolytic Bone Metastasis of Human Breast Cancer Cells Derived from MDA-MB-231. *Anticancer Res.* **2005**, *25* (6 B), 3817–3823.

(61) Jackson, M. A.; Werfel, T. A.; Curvino, E. J.; Yu, F.; Kavanaugh, T. E.; Sarett, S. M.; Dockery, M. D.; Kilchrist, K. V.; Jackson, A. N.; Giorgio, T. D.; et al. Zwitterionic Nanocarrier Surface Chemistry Improves SiRNA Tumor Delivery and Silencing Activity Relative to Polyethylene Glycol. *ACS Nano* **2017**, *11* (6), 5680–5696.

(62) Johnson, R. W.; Nguyen, M. P.; Padalecki, S. S.; Grubbs, B. G.; Merkel, A. R.; Oyajobi, B. O.; Matrisian, L. M.; Mundy, G. R.; Sterling, J. A. TGF-Beta Promotion of Gli2-Induced Expression of Parathyroid Hormone-Related Protein, an Important Osteolytic Factor in Bone Metastasis, Is Independent of Canonical Hedgehog Signaling. *Cancer Res.* **2011**, *71* (3), 822–831.

CHAPTER 6

VI. SUMMARY AND CONCLUSIONS

In this work, a trabecular-bone templated tissue-engineered bone construct (TEBC) *in vitro* model was developed and polymeric nanoparticles were designed and synthesized to encapsulate and enable systemic efficacy of the small molecule Gli2-inhibitor GANT58 in blocking tumor-induced bone destruction. The results from the TEBC studies demonstrate that bone microstructure affects bone cell behavior and perfusion culture of bone and tumor cells on TEBCs can mimic dysregulated bone remodeling in the presence of tumor. Results from *in vivo* testing of GANT58-loaded polymer nanoparticles (GANT58-NPs) and bone-targeted nanoparticles (GANT58-BTNPs) showed that Gli-inhibition in the bone-tumor microenvironment can block tumor-induced bone destruction, however intratumor spatial heterogeneity in Gli2 expression thwarts the antitumor effects of GANT58. The findings from the *in vitro* model and drug delivery studies converge to demonstrate how matrix properties (e.g. rigidity and microstructure) can alter cellular behavior and subsequent response to therapeutics. These conclusions give impetus to further investigation into how spatial heterogeneity drives tumor progression in bone, and the tools developed in this dissertation provide a platform to facilitate this future work.

Development of TEBCs via a tandem μCT-3D printing method was crucial to mimicking human trabecular bone *in vitro* in order to investigate how bone microarchitecture affects cell behavior as described in Chapter 3. μCT analysis showed the TEBCs recapitulate the host bone from three anatomic sites with high fidelity. Assessment of surface and mechanical properties indicated the TEBCs had surface properties similar to dentin and mechanical properties within the reported range of human trabecular bone. Human mesenchymal stem cells (hMSCs) seeded on TEBCs differentiated toward osteoblasts (OBs) in an anatomic site-dependent manner, with more plate-like architectures promoting faster osteogenic differentiation than rod-like architectures. These findings underscored the importance of recapitulating trabecular structure in *in vitro* models. Incorporation of the TEBCs into a perfusion bioreactor demonstrated that the polyurethane-nanocrystalline hydroxyapatite (PUR-nHA) material was resorbable by osteoclasts (OCs) and extended coculture of OBs, OCs, and tumor cells resulted in measurable resorption of TEBCs. These studies lay the groundwork for using this TEBC model to investigate how patient tumors behave in the bone microenvironment and respond to therapeutics.

In Chapter 4, encapsulation of the small molecule Gli-inhibitor GANT58 in a polymeric nanocarrier (GANT58-NP) significantly improved its bioavailability and efficacy in blocking tumor-induced bone destruction in mouse models of bone metastasis. Characterization of the GANT58-NPs showed the micelles exhibit an ideal size for systemic delivery of approximately 100 nm in diameter and the GANT58-NPs were readily taken up by tumor cells. The reactive oxygen species (ROS)-responsive nature of the polypropylene sulfide (PPS) core was hypothesized to promote a tumor site-specific release of GANT58. GANT58-NPs significantly reduced PTHrP expression and proliferation in MDA-MB-231 cancer cells *in vitro*, yet had no negative effect on osteoblast activity. GANT58-NPs were then tested in intracardiac and intratibial models of bone metastasis. GANT58-NP treatment significantly reduced bone destruction in both models and in both breast (MDA-MB-231) and lung (RWGT2) cell lines, suggesting Gli-inhibition is efficacious in multiple metastatic solid tumor types. Importantly, GANT58-NPs elicited minimal systemic toxicity, further strengthening its potential for clinical translation.

Results from Chapter 4 led to the hypothesis that bone-targeting of GANT58 could enable GANT58 to block both bone destruction and tumor burden *in vivo*. In Chapter 5, GANT58-BTNPs were synthesized using the bisphosphonate alendronate (Aln) as the bone-targeting agent. A combinatorial NP library was developed to identify a lead candidate BTNP formulation based on BTNP size, surface charge, and GANT58 loading. Lead candidate BTNPs exhibited significant bone-binding *in vitro* and *in vivo* in addition to ROS-responsivity characteristic of the core-forming PPS. In an intracardiac model of bone metastasis, GANT58-BTNPs significantly reduced lesion area and improved bone volume fraction compared to non-targeted GANT58-loaded NPs and untreated mice suggesting the bone-targeting significantly improves GANT58 efficacy. Further, BTNPs elicited minimal systemic toxicity even after an aggressive treatment schedule. Bone-targeted GANT58 treatment was hypothesized to reduce tumor burden in addition to bone destruction, however no reduction in tumor burden was observed *in vivo*. Further immunohistochemical analysis demonstrated that Gli2 expression varied spatially within the tumor, with higher Gli2 expression near the epiphyseal plate. The high Gli2 expression near the epiphyseal plate was hypothesized to be due to the high concentration of rigid bone matrix and growth factors such as TGF-β that are known to drive Gli2 expression in that region. Ki67 immunohistochemical staining further showed that GANT58-BTNP treatment reduced tumor cell proliferation near the bone interface, suggesting Gli-inhibition was successfully blocking proliferation at sites of high Gli2 expression. Collectively, the results from Chapters 4 and 5 highlight that use of GANT58-BTNP as a tumor-targeted osteoclast inhibitor that has potential clinical translatability.

CHAPTER 7

VII. FUTURE DIRECTIONS

The work conducted in this dissertation not only provides tools that will facilitate future work toward understanding tumor progression in bone, but also provides valuable findings and insights that will guide such work. This chapter will first focus on future directions toward a more thorough and robust *in vitro* model using TEBCs as outlined in Chapter 3. In addition to building on the capabilities and outcomes of the current *in vitro* model, incorporation of the TEBCs into a mammary fat pad *in vivo* model and addition of a bone marrow component will be discussed to allow for study of immune cell populations and their interplay with bone cells. Next, enhancements to the bone-targeted nanoparticle chemistry will be proposed to improve the drug loading and retention and suggestions for alternative bone-targeting agents will be provided. Finally, future uses beyond TIBD for the BTNPs will be discussed.

7.1. TEBC *In Vitro* Model

Perfusion bioreactor culture of osteoblasts, osteoclasts, and tumor cells on TEBCs demonstrated TEBCs could support coculture of these three cell types and bone resorption could be measured gravimetrically. Future work will aim to enhance cell-mediated resorption of TEBCs by utilizing more actively cell-degradable biomaterials in the PUR composite. While a measurable mass loss was detected using the current PUR-nHA composite, we hypothesize that resorption greater than 2% of the original TEBC mass will improve reliability of the resorption measurement and will also facilitate using µCT as a secondary resorption outcome. µCT was implemented to qualitatively observe areas of bone resorption versus new matrix mineralization, however use as a quantitative measurement was precluded by µCT resolution and inconsistencies attributed to noise in the before and after µCT scan. We hypothesize that more significant TEBC resorption will overcome this obstacle, although optimization of scanning resolution and TEBC orientation during scanning will also be critical to realizing the use of μCT as a quantitative outcome of the *in vitro* model. ROS-responsive poly(thioketal urethanes) (PTKUR) and alternative pH-responsive poly(ester urethane) (PEUR) chemistries are hypothesized to enhance osteoclast-mediated resorption due to the high levels of ROS and produced by mature osteoclasts and the acidic environment promoted by resorbing osteoclasts, respectively.[1–4]

The resorption outcomes will also be coupled with other outcomes including gene expression via qRT-PCR, flow cytometry, and quantification of matrix mineralization via Alizarin Red staining to augment the utility of the model. qRT-PCR will be used to measure gene expression including tartrate-resistant acid phosphatase (*TRAP*) and cathepsin-K for osteoclast activity, alkaline phosphatase (*ALP*) and osteocalcin (*OCN*) for osteoblast activity, and *Gli2* and *PTHrP* as bone-destructive tumor markers. Flow cytometry will be used to sort cell types and allow for cell population analysis including tumor burden and osteoclast number after extended culture. Alizarin Red staining will allow for measurement of mineralization formed by osteoblasts which can be compared between tumor-bearing and non-tumor bearing groups.

Ultimately, after augmentation of the *in vitro* model outcomes, patient tumors will be introduced into the *in vitro* model. Tumor cells isolated from biopsies will be cultured and expanded prior to seeding in the TEBC coculture model. We hypothesize that by culturing primary tumors from patient biopsies in the model, some patient tumors will adopt a bone-destructive phenotype in the presence of the bone microenvironment which will be measured by gene and resorption outcomes. Thus, this model could be used as a diagnostic tool for assessing patient risk for developing bone metastases, and results could guide therapeutic strategies.

In vitro coculture on TEBCs captures the properties of trabecular bone and the behavior of osteoblasts, osteoclasts, and tumor cells in the vicious cycle of TIBD. However, the bone marrow component and other relevant cell populations – namely the immune populations – are omitted in the model. The bone marrow component is distinct from the rigid trabecular bone, and tumor cell phenotype can differ between the two, as demonstrated in Chapter 5. Further, the immune cell populations that localize in the marrow space are known to crosstalk with bone and tumor cells.[5–7] Therefore, future work will aim to incorporate these important components of the bone-tumor microenvironment by putting the TEBC model *in vivo*. TEBCs containing Matrigel as a marrow-like component have been successfully implanted in the mammary fat pad of immune-competent mice and Von Kossa staining demonstrated cells mineralizing matrix on the perimeter of the TEBCs after 30 days culture (**Figure 7.1**).

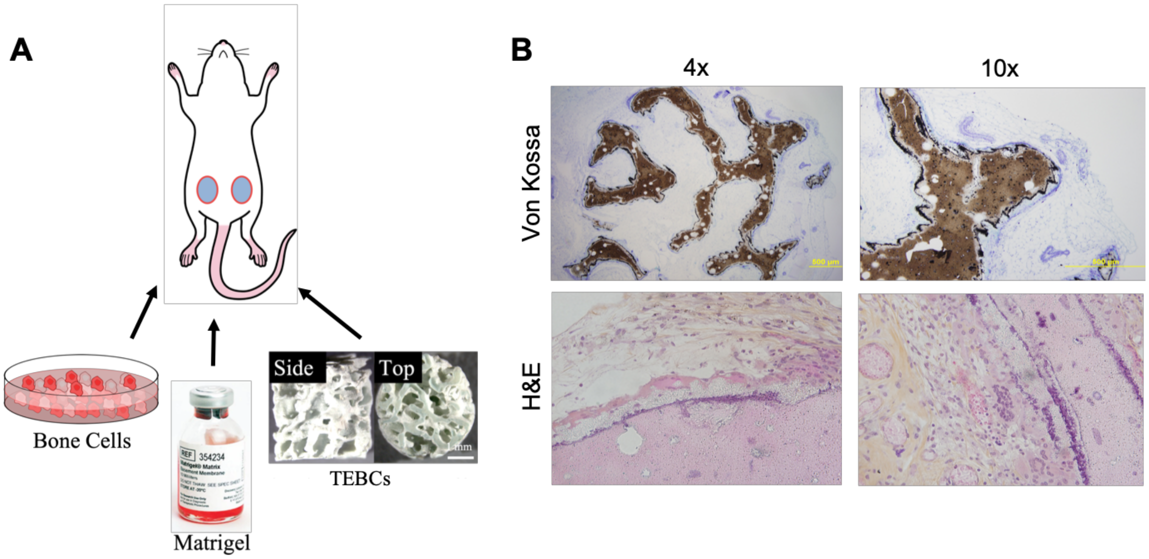

Figure 7.1. TEBC mammary fat pad *in vivo* model. (A) Mouse-derived bone marrow stromal cells were isolated from healthy mice and seeded onto TEBCs. Matrigel was added to the pores of the TEBCs to introduce a marrow-like component. Cell and Matrigel-seeded TEBCs were then implanted into the mammary fat pad. (B) Histological staining demonstrate osteoblast activity (Von Kossa) and cellular infiltration into the TEBCs. *Image provided by David Florian with permission.*

Future work will aim to assess cell populations that are infiltrating into the TEBCs after *in vivo* infiltration to confirm relevant immune cell populations are present. TEBCs are also hypothesized to resorb faster *in vivo* since osteoclast number is not restricted by seeding density. We therefore hypothesize that μCT scans of TEBCs before and after implantation could be a viable way to measure resorption. Finally, tumor cells will be locally injected into the TEBC site and assessment of tumor behavior and response to drugs will be assessed via immunohistochemistry, qRT-PCR, and flow cytometry.

7.2. Bone-Targeted Nanoparticles

An optimal BTNP formulation was identified in Chapter 5 via development of a combinatorial NP library. While the combinatorial library was crucial to identifying a lead candidate formulation based on the current chemistry, future work will aim to enhance the nanoparticle chemistry to improve drug loading and retention. Also, since alendronate, the bone-targeting agent used in this work, is a clinically approved bisphosphonate with known activity on osteoclasts, future work will also investigate new, inactive bone-targeting agents as alternatives to alendronate.

Two new core polymer additives are currently being investigated to improve GANT58 loading and retention (**Figure 7.2A**). Poly(benzoyloxypropyl methacrylamide) (PHPMA-Bz) is a biocompatible and biodegradable polymer that has been shown to promote π-π stacking with drug that contain aromatic rings that improves drug loading (**Figure 7.2B**).[8] Therefore, it was hypothesized that addition of PHPMA-Bz into the PPS core could improve GANT58 drug loading and retention due to the presence of thiophene rings in the structure of GANT58. β-cyclodextrin (CD) has also been used in drug delivery to improve drug retention by forming a drug-cyclodextrin inclusion complex (**Figure 7.2C**).[9,10] We have synthesized a dimethylacrylamide-*co*-CD (DMA-*co*-CD) that is hypothesized to improve drug retention of GANT58 and other hydrophobic small molecules. Preliminary drug retention studies have demonstrated that addition of up to 1:4 bone-targeted polymer:HPMA-Bz significantly improves drug retention in serum conditions (**Figure 7.2D-E**). Future studies will compare PHPMA-Bz and P(DMA-*co*-CD) for GANT58 drug loading and retention *in vitro*, as well as circulation time *in vivo*.

Alendronate is a potent bone-binding agent and was thus chosen in the current BTNP formulation. However, its therapeutic activity could possibly cause complications for further clinical translation. Therefore, future work will aim to identify other inactive bone-targeting agents for use in the BTNPs. The lead candidate for investigation is poly(aspartic acid) (Asp), due to previous studies showing its significant bone-binding affinity.[11,12] We hypothesize that a similar chemistry could be used to graft an amine-terminated Asp to the current BTNP formulation (**Figure 7.3**). These Asp-based BTNPs will then be compared to Aln-BTNPs *in vitro* and *in vivo* to compare both bone-binding affinity and efficacy in GANT58 delivery to the bone-tumor microenvironment.

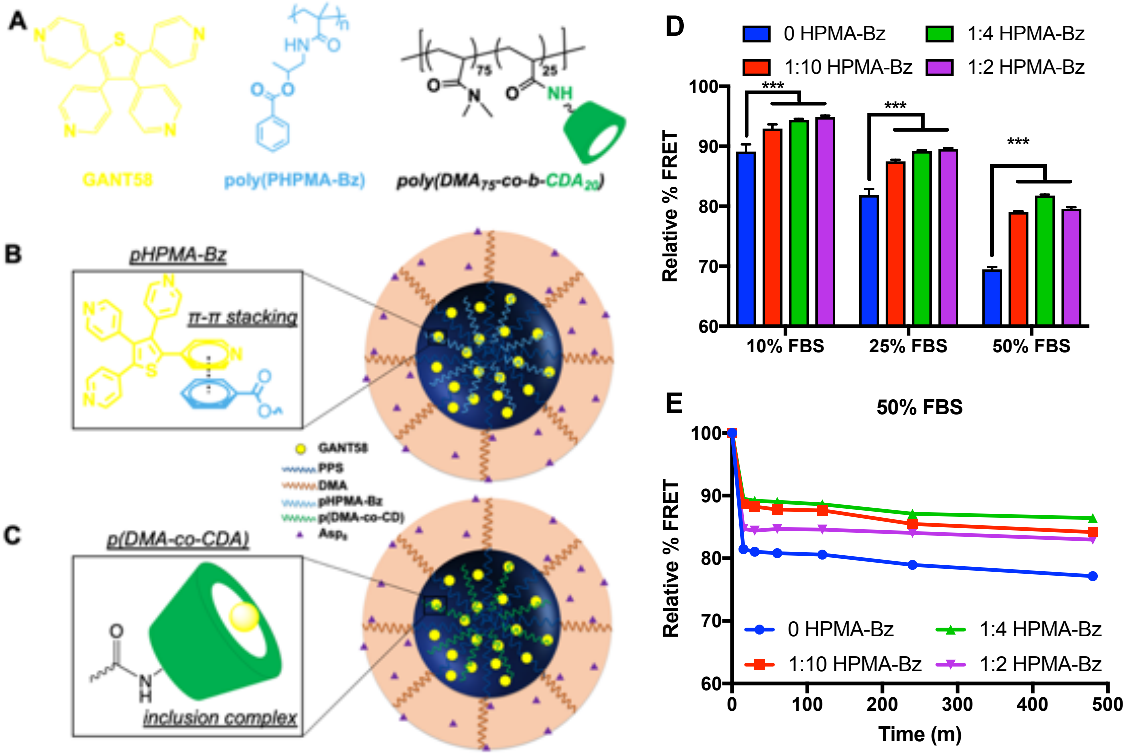

Figure 7.2. BTNP core additives. (A) Structure of GANT58 and the proposed core polymer additives PHPMA-Bz and P(DMA-co-CD). (B) π-π stacking of PHPMA-Bz with GANT58. (C) Inclusion complex formed with P(DMA-co-CD) and GANT58. (D) FRET-based drug retention studies demonstrate BTNPs with HPMA-Bz additive improve drug retention in presence of various serum concentrations. (E) FRET-based kinetic studies demonstrate HPMA-Bz additive improve retention over short time course in high serum conditions.

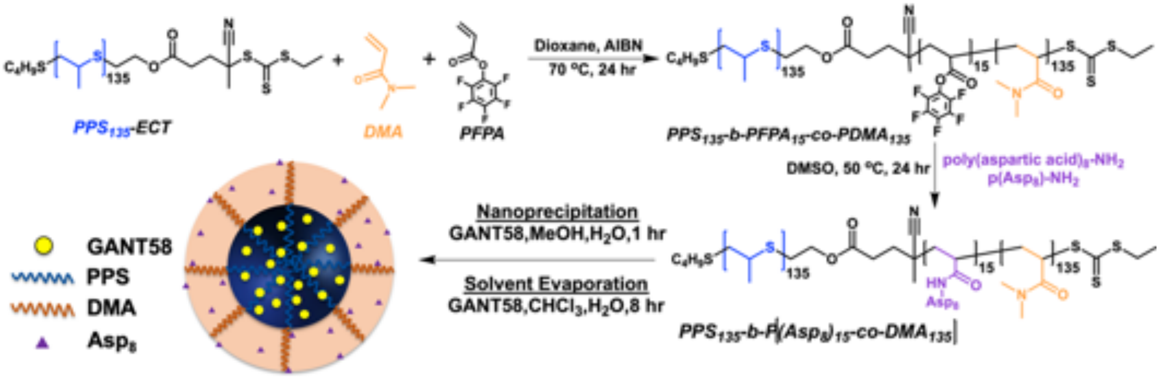

Figure 7.3. Proposed reaction scheme for poly(aspartic acid) (Asp)-based BTNPs.

GANT58 was an ideal candidate for encapsulation in a nanoparticle formulation due to its hydrophobic properties and low molecular weight. Hydrophobicity is a common property of small molecules that hinders their systemic bioavailability. We hypothesize that BTNPs could be a powerful platform for solubilization and bone-specific delivery of other hydrophobic small molecule therapeutics. Indeed, BTNPs are actively being utilized for delivery of therapeutics against osteomyelitis and cancer immunotherapy. The anionic properties of the BTNP corona are also hypothesized to give affinity to other cationic surfaces including the peptidoglycan in bacterial cell walls.[13] Thus, I believe there are abundant and varied potential new uses for BTNPs as carriers that can improve efficacy of hydrophobic small molecule therapeutic candidates.

References

(1) Lee, N. K.; Choi, Y. G.; Baik, J. Y.; Han, S. Y.; Jeong, D. W.; Bae, Y. S.; Kim, N.; Lee, S. Y. A Crucial Role for Reactive Oxygen Species in RANKL-Induced Osteoclast Differentiation. *Blood* **2005**, *106* (3), 852–859.

(2) Callaway, D. A.; Jiang, J. X. Reactive Oxygen Species and Oxidative Stress in Osteoclastogenesis, Skeletal Aging and Bone Diseases. *J. Bone Miner. Metab.* **2015**, *33* (4), 359–370.

(3) Anderson, R. E.; Woodbury, D. M.; Jee, W. S. S. Humoral and Ionic Regulation of Osteoclast Acidity. *Calcif. Tissue Int.* **1986**, *39* (4), 252–258.

(4) Silver, I. A.; Murrills, R. J.; Etherington, D. J. Microelectrode Studies on the Acid Microenvironment beneath Adherent Macrophages and Osteoclasts. *Exp. Cell Res.* **1988**, *175* (2), 266–276.

(5) Feder-Mengus, C.; Ghosh, S.; Reschner, A.; Martin, I.; Spagnoli, G. C. New Dimensions in Tumor Immunology: What Does 3D Culture Reveal? *Trends Mol. Med.* **2008**, *14* (8), 333–340.

(6) Roca, H.; McCauley, L. K. Inflammation and Skeletal Metastasis. *Bonekey Rep.* **2015**, *4*, 706.

(7) Nakashima, T.; Takayanagi, H. Osteoimmunology: Crosstalk between the Immune and Bone Systems. *J. Clin. Immunol.* **2009**, *29* (5), 555–567.

(8) Shi, Y.; Van Steenbergen, M. J.; Teunissen, E. A.; Novo, L.; Gradmann, S.; Baldus, M.; Van Nostrum, C. F.; Hennink, W. E. Π-Π Stacking Increases the Stability and Loading Capacity of Thermosensitive Polymeric Micelles for Chemotherapeutic Drugs. *Biomacromolecules* **2013**, *14* (6), 1826–1837.

(9) Gharib, R.; Greige-Gerges, H.; Fourmentin, S.; Charcosset, C.; Auezova, L. Liposomes Incorporating Cyclodextrin-Drug Inclusion Complexes: Current State of Knowledge. *Carbohydr. Polym.* **2015**, *129*, 175–186.

(10) García, A.; Leonardi, D.; Salazar, M. O.; Lamas, M. C. Modified β-Cyclodextrin Inclusion Complex to Improve the Physicochemical Properties of Albendazole. Complete in Vitro Evaluation and Characterization. *PLoS One* **2014**.

(11) Murphy, M. B.; Hartgerink, J. D.; Goepferich, A.; Mikos, A. G. Synthesis and in Vitro Hydroxyapatite Binding of Peptides Conjugated to Calcium-Binding Moieties. *Biomacromolecules* **2007**.

(12) Yamashita, S.; Katsumi, H.; Hibino, N.; Isobe, Y.; Yagi, Y.; Tanaka, Y.; Yamada, S.; Naito, C.; Yamamoto, A. Development of PEGylated Aspartic Acid-Modified Liposome as a Bone-Targeting Carrier for the Delivery of Paclitaxel and Treatment of Bone Metastasis. *Biomaterials* **2018**, *154*, 74–85.

(13) Boucard, J.; Boudjemaa, R.; Steenkeste, K.; Jacqueline, C.; Stephant, N.; Lefèvre, F.-X.; Laurent, A. D.; Lartigue, L.; Hulin, P.; Nedellec, S.; et al. Phosphonic Acid Fluorescent Organic Nanoparticles for High-Contrast and Selective Staining of Gram-Positive Bacteria. *ACS Omega* **2018**, *3* (12), 17392–17402.

APPENDIX

EXPERIMENTAL PROTOCOLS

Guelcher Lab **Standard Operating Procedure**

Oil-in-water (O/W) Single Emulsion Microsphere Synthesis

Before starting: Read and understand the MSDS of the reagents listed below

- Personal Protective and Safety Equipment required:
    - Disposable nitrile gloves
- Prep rotovap
    - Add liquid N_2 to cold trap and start cooling tower

Reagents:

- Polymer
- Drug/encapsulated species
- Organic solvent: $CHCl_3$ or DCM (not DMSO – slightly soluble in water)
- Aqueous solvent: 1% Polyvinyl alcohol (PVA) in H_2O
- diH_2O

Materials and Equipment:

- 2 mL microcentrifuge tubes
- 50 mL conical tubes
- 200 mL round-bottom flask
- Probe sonicator or homogenizer
- Rotovap
- Glass Pasteur pipettes
- Auto-pipetters

Procedure:

Organic/Aqueous Phase Prep

1. Weigh out approximately 20 mg of polymer into glass vial or 2mL microcentrifuge tube
2. Weigh out appropriate amount of drug (often 1:10 drug:polymer ratio) in separate vial
3. Add 1 mL organic solvent to polymer vial
    a. Vortex/sonicate to dissolve thoroughly
4. Add contents of polymer vial to vial containing drug
    a. Vortex to dissolve drug and polymer thoroughly and set aside
5. Add 6 mL 1% PVA to 50 mL conical tube

Emulsion

1. Set up probe sonicator/homogenizer with appropriate settings for desired emulsion
2. Add organic phase dropwise into 1% PVA aqueous phase conical tube using Pasteur pipette
3. Sonicate/homogenize for ~ 1 min to create oil-in-water emulsion
    a. Alter homogenization time/speed to control microparticle size
4. Transfer contents to 200 mL round-bottom flask and rotovap contents for 1 hr

Washing/Purification

1. Distribute resulting emulsion evenly between 6 microcentrifuge tubes (1 mL solution/tube)
2. Centrifuge @ 10000 rpm for 10 min
3. Extract and discard supernatant
4. Resuspend microparticle pellet in DI water (vortex/sonicate)
5. Repeat steps 2-4 twice
6. Freeze suspended particles in -80 for 20 min and lyophilize overnight

Clean-up:

1. Collect all glass waste (pipettes, vials, or broken glass) and dispose in the broken glass container (box)
2. Collect all sharps and dispose in the sharps waste container (red box)
3. Collect all solid waste and dispose in the solid waste container
4. Collect all liquid waste and dispose in the appropriate liquid waste container (acetone or halogenated)
5. Clean glassware:
    a. Wash with soap and water
    b. Rinse with acetone and dry in the oven

Guelcher Lab **Standard Operating Procedure**
PPS Microsphere ROS-Dependent Drug Release

Before starting: Read and understand the MSDS of the reagents listed below

- Personal Protective and Safety Equipment required:
    - Disposable nitrile gloves

Reagents:

- 1x PBS solution
- 30 wt% H_2O_2 solution in water
- Ethanol (or other solvent able to dissolve drug)[1]

Materials and Equipment:

- polypropylene sulfide (PPS) microspheres loaded with drug of interest
- 24-well plates (Fisher)
- 0.4 um pore transwell inserts for 24-well plates (Fisher)
- 50 mL centrifuge tubes
- 2 mL microcentrifuge tubes
- Incubator (37°) and shaker (30 rpm)
- Absorbance or Fluorescence Plate Reader (or HPLC)

Procedure:

6. Prepare absorbance/fluorescence standard curve
    a. Prepare solutions at appropriate drug concentrations in same buffer used for experiment (Appropriate H_2O_2 weight percent in PBS and Ethanol)
7. Prepare release buffer solutions
    a. Prepare ROS release buffers by mixing appropriate amounts of 30% H_2O_2 solution and 1x PBS to desired weight percent of H_2O_2. Make enough for entire study.
    b. Make initial release buffer solution based on amount of PBS used to resuspend microspheres (Need 0.6 mL initial release buffer/well total[2])
    c. Store release buffers in incubator for duration of study to ensure constant temperature
8. Well-plate preparation
    a. Weigh out lyophilized microspheres in 2 mL microcentrifuge tube
    b. Resuspend microspheres in 1x PBS solution by vortex and sonication (amount of PBS and time to resuspend will depend on mass of microspheres)
    c. Add 0.6 mL of initial release buffer to each of the appropriate wells
    d. Add transwell inserts into wells now containing initial release buffer
    e. Distribute microsphere/PBS solution evenly to each of the inserts, ideally 0.1 mL solution/insert

    f. Cover plate with parafilm and place in incubator at 37°under constant shaking at 30 rpm

9. Sample collection
    a. At desired time points, remove release buffer in each bottom chamber and add to individual 2 mL microcentrifuge tubes
        i. There will still be solution in the transwell insert at this point!
    b. Centrifuge the 24-well plate with transwell inserts still installed for 3 minutes at 2000 rpm on the plate centrifuge
        i. All solution should be in bottom chamber after centrifuge. If not, repeat centrifugation
    c. Remove remaining release buffer from bottom chamber and collect in same 2 mL microcentrifuge tubes as above
10. Solvent Wash
    a. Add 0.1 mL ethanol to each transwell insert, repeat centrifugation, and remove from bottom chamber. Add this solution to same 2 mL microcentrifuge tubes
    b. Move empty (except for microspheres) transwell inserts into unused wells and add 0.2 mL ethanol to each bottom chamber and place on shaker briefly (or shake gently by hand) to dissolve any remaining drug. Remove solution into same 2 mL microcentrifuge tubes
        i. At this point, each microcentrifuge tube should contain 1 mL of solution
11. Place transwell inserts back into appropriate wells and add 0.7 mL release buffer into each well
    a. 0.6 mL into bottom chamber, install inserts, then 0.1 mL into inserts
12. Cover with parafilm and place 24-well plate back into incubator
13. Prepare 96 well plate and run samples in triplicate on plate reader to determine drug concentration based on standard curve
14. Repeat sample collection at regular time intervals until desired drug release is evident

Notes:

1. Solvent should ideally dissolve drug and not the PPS polymer. If the solvent dissolves both, must refrain from step 5a and only add 0.3 mL to bottom chamber for the ethanol wash to ensure PPS remains in tact
2. Transwell insert manufacturer recommends these volumes (0.1 mL for insert and 0.6 mL for well) because the solution levels are equal in the well at these volumes, however this is not required since all release buffer will be removed at sample collection

Clean-up:

1. Collect all glass waste (pipettes, vials, or broken glass) and dispose in the broken glass container (box)
2. Collect all sharps and dispose in the sharps waste container (red box)
3. Collect all solid waste and dispose in the solid waste container
4. Collect all liquid waste and dispose in the appropriate liquid waste container (acetone or halogenated)
5. Clean glassware:
    a. Wash with soap and water
    b. Rinse with acetone and dry in the oven

Guelcher Lab **Standard Operating Procedure**

3D Printing of Bone-Templated Molds

Before starting: Read and understand the MSDS of the reagents listed below

- Personal Protective and Safety Equipment required:
    - o Disposable nitrile gloves

Reagents:

- 3z Build Material
- 3z Support Material

Materials and Equipment:

- uCT40 or uCT50
- Scanco IPL
- 3Z studio inkjet 3D printer
- 3Z Works/3Z Analyzer Software
- MeshLab and Netfabb Software (VA computer)

Procedure:

uCT Trabecular Image Selection – at VUIIS uCT room computers

15. Go to "SCAN" menu and select desired .isq file (raw image file)
16. Use left-hand toolbar to select circular area of interest
    a. Want large, interconnected trabeculae, likely near cortical wall
    b. For small scaffold size, create 200x200 pixel circle for 5 mm diameter
    c. *Note: computer mouse: left button = move circle, middle button = adjust size
17. Once circle of interest is in desired location
    a. Copy current circle (from edit tool bar)
    b. Paste circle 200 slices later (200 diam x 200 height)
18. Press C… (contour) button
    a. Select "All" then "Morph" to get cylinder through selected slices
19. Press T… (threshold) button
    a. Select appropriate script (Bone Templated Scaffolds, can also type 485)
    b. Settings: Gauss Sig: 0.8; Gauss Support: 2; Low Threshold: 375; High Threshold: 2718
    c. Units: mg HA/ccm
    d. VOI (volume of interest)
        i. Shows x and y locations of circle and dimensions
        ii. Create 25 pixel support wall around VOI
            1. Subtract 25 pixels from x and y
            2. Add 50 to each dimension
    e. Dilation script (optional) – enter Dilate, then select Shanik Dilate

            i. 3 is large, 5 makes solid block, normally stick with 1 or 2

20. Save file as GOBJ file
    a. Record seg aim and associated GOBJ file with time, date, SMI, and Tb. Th.
21. Open Command Prompt (DECTERM) window
    a. Enter "que" to see job status
    b. Will show when saving of GOBJ file is complete
22. microCT => DATA folder
    a. Check file name in scan mode
    b. *Note: File types seen in the DATA folder
        i. seg.aim: where thresholding has determined what is bone
        ii. .txt: shows bone morphometric parameters
        iii. sp.aim: map of trabecular spacing and thickness
23. At this point, can enter 3D menu (3D button in operator toolbar)
    a. Can open any of the created files to view structure

Scanco IPL Image Processing and Conversion to .stl

24. Type "ipl" in DECTERM
25. Type "read" into next prompt
    a. [in] = a
    b. [file name] = press middle button of mouse to copy seg.aim file & paste with same button
26. Type "cl_rank_extract" into prompt (this removes free-hanging trabeculae)
    a. [in] = a
    b. [cl] = b
    c. first[1] = 1
    d. last [1] = 1
    e. enter through rest
27. Type "set_val" into prompt (this inverts the file)
    a. [in] = b
    b. [127] = 0
    c. [0] = 127
28. Type "stl"
    a. [in] = b
    b. [tri] = c
    c. output file: paste file name (using middle button on mouse), delete old name to bracket and rename with initials, sample #, version, and **end with .stl**

Image Processing on VA computer (bootcamped with Mac and Windows) *password is bone
****Hold "option" at startup to switch between the two**

1. In Windows bootcamp
    a. microCT FTP program
        i. username: microct50
        ii. password: made1in2ch
        iii. Find sample # with .stl file
    b. Download and save to Google drive or flash drive
    c. Restart computer and open Mac operating system
2. In Mac Bootcamp
    a. 2 image software apps
        i. Meshlab
            1. Open file in meshlab
            2. Filters => cleaning and repairing => remove isolated pieces by diam
                a. standard = 10% and apply
            3. Save project
                a. file => export mesh as => .stl and indicate it as meshlab edit
        ii. Netfabb
            1. Open file (with meshlab edits)
            2. "!" within a triangle indicates an issue
            3. Press "analysis" button (next to "+" symbol in toolbar) => will indicate many shells
            4. Press "+" symbol => automatic repair and execute => apply repair and remove old parts
            5. Part => export part => as .stl => indicate as netfabb edit => "optimize" in dialog box => export
    b. Upload new file back to google drive/zip drive

    *****At this point, .stl file is ready for printing*****
3. In Windows Bootcamp
    a. Move file from Google drive to designated folder for finished .stl files
        i. Guelcher 3D => my documents => JPV
    b. Open 3Z Works app
        i. Open file from designated folder
        ii. Go to "move XYZ" and enter (this will automatically move it onto the platform)
        iii. Place object at desired location (i.e. X: 60 Y: 60) on platform using move object icon

        iv. Tools => fill model => select configurations
            1. Print 25 μm slices
            2. Extra cooling time: 5 sec
            3. Support perimeter: over entire part
            4. Support fill option: 0 cells support (can choose 1)
            5. Platform: 2 layers
        v. Output file => rename and enter, will calculate # of slices
        vi. Save in appropriate run folder
    c. Open 3Z Analyzer App
        i. *Will automatically open when done in 3z Works
        ii. Scroll through individual slices to find errors (look for overlapping colored lines)
        iii. If error is found:
            1. edit => fix up layer => options to use previous, next or delete layer
            2. Save fix up (indicate as fixup)
            3. Close out of old and open fix up
            4. Print using 4th button from left (copy destination)
            5. Select Network transfer => Print

Guelcher Lab **Standard Operating Procedure**

Polymer Micelle Synthesis

Before starting: Read and understand the MSDS of the reagents listed below

- Personal Protective and Safety Equipment required:
    - Disposable nitrile gloves
- Prep rotovap
    - Add liquid N_2 to cold trap and start cooling tower

Reagents:

- Polymer
- Drug/encapsulated species
- Organic solvent
    - Solvent evaporation: water-immiscible solvent ($CHCl_3$, DCM)
    - Nanoprecipitation: water-miscible solvent: (methanol, THF, acetone)
- Aqueous solvent: PBS

Materials and Equipment:

- 1.5 mL microcentrifuge tubes
- 4 mL glass vial (w/ cap)
- Small (0.5”) stir bar
- Rotovap (if nanoprecipitation used)
- Glass Pasteur pipettes
- Auto-pipettors
- 1 mL syringes
- 0.4 µm syringe filter

Procedure:

Organic/Aqueous Phase Prep

29. Weigh out approximately 10 mg of polymer into 1.5mL microcentrifuge tube
30. Weigh out appropriate amount of drug (often >1:10 drug:polymer ratio) in separate tube
31. Add 0.1 mL organic solvent to polymer tube
    a. Vortex/sonicate to dissolve thoroughly
32. Add contents of polymer tube to tube containing drug
    a. Vortex to dissolve drug and polymer thoroughly and set aside
33. Add 1 mL PBS to glass vial (can scale up, but keep 1:10 organic:aqueous solvent ratio, and 10 mg polymer/mL aqueous solvent)

Micelle Formation

5. Add organic phase dropwise to vigorously-stirring vial of PBS
6. Micelle formation:
    a. Solvent Evaporation: allow to stir overnight (>8h) to allow organic solvent to evaporate
    b. Nanoprecipitation: stir > 10 min, put glass vial on rotovap to remove organic solvent. If volatile solvent is used (e.g. acetone), same technique as solvent evaporation may be used

Filtration

7. Resulting solution should be just PBS + micelles. Although not required, it is recommended that the solution is filtered to remove unencapsulated drug and aggregates prior to use.
8. Take up solution with 1 mL syringe and pass through 0.4 µm syringe filter
9. If planning on long-term storage, freeze NP solution in -80 for 20 min and lyophilize overnight. Otherwise, fresh NPs are ready for use or may be stored in fridge for ~2 weeks.

Clean-up:

6. Collect all glass waste (pipettes, vials, or broken glass) and dispose in the broken glass container (box)
7. Collect all sharps and dispose in the sharps waste container (red box)
8. Collect all solid waste and dispose in the solid waste container
9. Collect all liquid waste and dispose in the appropriate liquid waste container (acetone or halogenated)
10. Clean glassware:
    a. Wash with soap and water
    b. Rinse with acetone and dry in the oven

Guelcher Lab **Standard Operating Procedure**
TEBC Mineralization – Alizarin Staining

Before starting: Read and understand the MSDS of the reagents listed below

- Personal Protective and Safety Equipment required:
  - Disposable nitrile gloves

Reagents:

- hMSCs
- MSC Growth Medium 2
- MSC Differentiation Medium
- PBS
- 20 mM Alizarin Red solution (pH: 4.1-4.3)
- 10% formalin
- 5% sodium dodecyl sulfate (SDS)
- 5 µg/mL fibronectin solution

Materials and Equipment:

- Plate Reader (absorbance) – 540 nm (or 405 nm)
- 96-well plate

Procedure:

TEBC Preparation

34. NOTE: Prepare enough TEBCs for cell-free controls – perform all the following procedures on the cell-free TEBCs and the resulting absorbance reading will be used as a background
35. Sterilize TEBCs by soaking in 70% EtOH for > 1h
36. Dry and place under UV light in cell culture hood 20 min
37. Soak in 5 µg/mL fibronectin solution at 4ºC overnight (or 3h in incubator)
38. Aspirate fibronectin solution and move scaffolds to new wells

Cell Seeding/Culture

39. Seed cells by applying 50,000 cells/scaffold in 30 µL growth medium (1.67×10^6 cells/mL) to center of the scaffolds
    a. Controls: Add same amount of media containing no cells to the control scaffolds
40. Place plate in incubator for 2h to facilitate cell attachment, then add remaining 170 µL of growth medium to wells
41. After 3 days of culture in growth medium to allow for sufficient proliferation, change to differentiation medium
42. Culture for appropriate amount of days (seen mineralization as early as 7d on TEBCs), changing media every 3d

Alizarin Staining

43. Wash wells containing TEBCs with PBS
44. Fix cells in 10% formalin for 45 min
45. Aspirate formalin and rinse with DI H_2O
46. Stain TEBCs with 20 mM Alizarin Red S solution (prepared in DI H_2O, pH: 4.1-4.3) for 5 min on orbital shaker. Cover plate with aluminum foil to protect from light.
47. Wash 10x with DI H_2O (until washes run clear)
48. Extract Alizarin dye bound to mineralized nodules by adding 200 µL of 5% SDS to wells.
49. Cover with aluminum foil and place on orbital shaker for 1h
50. Remove Alizarin-containing SDS solution from wells using micropipette and dispense in to new wells of 96-well plate.
    a. NOTE: Be careful not to introduce bubbles into the new well – this will obstruct absorbance reading
51. Read absorbance of Alizarin-containing SDS solution on plate reader at OD 540 nm (405 nm also works)
52. Subtract cell-free control absorbance readings to account for ceramic component of TEBCs

---

Guelcher Lab **Standard Operating Procedure**

GANT58 PK Quantification: Liquid-liquid Extraction/HPLC Method

---

Before starting: Read and understand the MSDS of the reagents listed below

- Personal Protective and Safety Equipment required:
  - Disposable nitrile gloves
- Clean homogenizer in 1% SDS solution, 70% ethanol, and 3 rinses in DI H_2O
- Prepare HPLC with mobile phase of 65/35 Acetonitrile/0.5 M Sodium Acetate Buffer

Reagents:

- GANT58-loaded NPs/Empty NPs
- PBS
- DCM/$CHCl_3$
- Acetonitrile
- 0.01 M Sodium Acetate buffer

Materials and Equipment:

- Tail-vein injection supplies: apparatus, insulin syringes, gauze, sterile wipes
- Tissue homogenizer and/or cryomill
- 5 mL polystyrene round-bottom tubes or cryomill tubes
- 0.45 µm PTFE syringe filter
- HPLC (C_{18} column)

Procedure:

NP injections and Tissue Harvest

53. Inject mice with appropriate dose(s) of GANT58-loaded NPs
54. At designated time point(s), sacrifice mouse by cervical separation after isoflurane or ketamine anesthesia
55. Harvest and weigh hindlimbs, forelimbs, spine, liver, and kidney and proceed to Step 4a for homogenizer procedure or Step 4b for cryomill procedure
56. Prepare tissue samples for homogenization
    a. Homogenizer
        i. Place tissues in 5 mL polystyrene round-bottom tube with 1 mL PBS
    b. Cryomill
        i. Immerse tissues in liquid nitrogen and keep frozen until processing
57. At this point, dope in known amount of GANT58 (dissolved in DCM) into tubes containing limbs of control mice (no treatment) for standard curve

Tissue homogenization

10. Homogenizer
    a. Start homogenizer at 30,000 RPM and immerse into PBS+tissue sample in bottom of round-bottom tube
    b. Continue until bone/tissue solution looks completely homogeneous

   - **c.** Move solution to 15 mL conical and put on ice

11. Cryomill
   - **a.** Fill cryomill with liquid nitrogen
   - **b.** Place frozen samples in polycarbonate cryomill tube
   - **c.** Run mill for 3 min at low speed (to avoid breaking tube)
   - **d.** Collect homogenized tissue into 15 mL conical tube immediately after removal from cryomill (to minimize condensation which will wet samples and make recovery difficult)
   - **e.** Weigh homogenized tissue prior to extraction

Liquid-liquid extraction

1. Add 6 mL DCM to 50 mL conical containing tissue homogenate
2. Vortex 2 min
3. Centrifuge tissue homogenates for 10 min @ 4000 rpm
4. Collect bottom (DCM) layer and pass through PTFE 0.45 μm syringe filter
5. Allow DCM to evaporate and for samples to dry O/N
6. Reconstitute samples in HPLC mobile phase (65/35 acetonitrile/acetate buffer)

HPLC

1. Inject 100 μL of reconstituted sample into HPLC (C18 column)
2. GANT58 peak at 7.97 min in mobile phase of 65/35 acetonitrile/acetate buffer